INTEGRATED ANALYSIS AND INTERPRETATION OF MICROSEISMIC MONITORING OF HYDRAULIC FRACTURING IN THE MARCELLUS SHALE

by

Erich Victor Zorn

Bachelor of Science – Geology, University of Pittsburgh, 2002

Master of Science – Geology, University of Pittsburgh, 2005

Submitted to the Graduate Faculty of

The Dietrich School of Arts and Sciences in partial fulfillment

of the requirements for the degree of

Doctor of Philosophy

University of Pittsburgh

2016

UNIVERSITY OF PITTSBURGH

DIETRICH SCHOOL OF ARTS AND SCIENCES

Geology and Environmental Science

This dissertation was presented

by

Erich Victor Zorn

It was defended on

March 28 2016

and approved by

Nadine McQuarrie, PhD, Assistant Professor

Michael Ramsey, PhD, Professor

Brian Stewart, PhD, Associate Professor

Andrew Bunger, PhD, Assistant Professor – Civil and Environmental Engineering

Dissertation Advisor: William Harbert, PhD, Professor of Geophysics

INTEGRATED ANALYSIS AND INTERPRETATION OF MICROSEISMIC MONITORING OF HYDRAULIC FRACTURING IN THE MARCELLUS SHALE

Erich Victor Zorn, PhD, PG

University of Pittsburgh, 2016

INTEGRATED ANALYSIS AND INTERPRETATION OF MICROSEISMIC MONITORING OF HYDRAULIC FRACTURING IN THE MARCELLUS SHALE

Erich Victor Zorn, PhD, PG

University of Pittsburgh, 2016

Abstract In 2012 and 2013, hydraulic fracturing was performed at two Marcellus Shale well pads, under the supervision of the Energy Corporation of America. Six lateral wells were hydraulically fractured in Greene County in southwestern Pennsylvania and one lateral well was fractured in Clearfield County in north-central Pennsylvania. During hydraulic fracturing operations, microseismic monitoring by strings of downhole geophones detected a combination of >16,000 microseismic events at the two sites. High quality traditional and geomechanical well logs were acquired at Clearfield County, as well as tomographic velocity profiles before and after stimulation. In partnership with the US Department of Energy's National Energy Technology Laboratory, I completed detailed analysis of these geophysical datasets to maximize the understanding of the engineering and geological conditions in the reservoir, the connection between hydraulic input and microseismic expression, and the geomechanical factors that control microseismic properties.

Additionally, one broad-band surface seismometer was deployed at Greene County and left to passively monitor site acoustics for the duration of hydraulic fracturing. Data from this instrument shows the presence of slow-slip or long period/long duration (LPLD) seismicity. In years prior to our investigation, lab-scale fracturing studies and broadband seismic monitoring of hydraulic fracturing had been completed by other researchers in unconventional shale and tight sand in Texas and Canada. This is the first study of LPLD seismicity in the Marcellus Shale and

reveals aseismic deformation during hydraulic fracturing that could account for a large portion of "lost" hydraulic energy input.

Key accomplishments of the studies contained in this dissertation include interpreting microseismic data in terms of hydraulic pumping data and vice versa, verifying the presence of LPLD seismicity during fracturing, establishing important geomechanical controls on the character of induced microseismicity, and extensive data integration toward locating a previously unmapped fault that appears to have exhibited significant control over well stimulation efforts at Clearfield.

TABLE OF CONTENTS

LIST OF TABLES

LIST OF FIGURES

LIST OF EQUATIONS

PREFACE

My time at the University of Pittsburgh spans the course of 18 years, starting with my freshman year in 1998, and ending with this. Punctuated by periods of soul-searching, personal growth, and career development outside the University totaling eight years, I found myself returning to continue both my MS and PhD studies for the same reasons: the belief that there is always more to learn, always a higher plateau of knowledge to reach for. I have had the privilege of collaborating with some truly sharp individuals and organizations over the last four years who have elevated my research and self-confidence to the levels required to complete my studies.

The journey to a PhD is not a solo endeavor. My Dissertation Adviser, Dr. William Harbert is a source of endless optimism and support, allowing me plenty of latitude to explore but enough input to keep me pointed toward fruitful ends. My committee members, Drs. Nadine McQuarrie, Brian Stewart, Michael Ramsey, and Andrew Bunger have increased my understanding of tectonics, Appalachian geology, geochemistry, remote sensing, geohazards, and hydraulic fracturing over the years. My committee as a whole offered invaluable input to the dissertation content and structure. Dr. Serge Shapiro's body of work, visits to the department, and conversations over coffee have inspired much of this dissertation. My former office-mate, Dr. Alan Mur (now at ikon Science) has been a source of many great rock physics and geomechanics discussions.

I need to thank the Department of Energy's National Energy Technology Laboratory (NETL) and their great people, including Richard Hammack, Jim Sams, Garret Veloski, and Dr. Abhash Kumar. Without the financial support and industry resources of NETL, none of this work would have been possible. Additionally, NETL librarian Bernie Kenney helped me immensely by tracking down many obscure publications. The Energy Corporation of America provided access to the Marcellus Shale well-pads and wells needed to perform the work in the first place. The Swanson School of Engineering's Center for Energy and the Richard K. Mellon Foundation provided two years of financial support with very few strings attached. For this I am grateful. The Chevron Energy Technology Company provided me with the opportunity to complete two summer internships in Houston, TX with the Reservoir Properties from Seismic team. These are some of the smartest people and one of the smartest companies I have ever had the privilege of working with, and I will carry this experience into the future.

My family has been and will always be the foundation upon which I build my successes. This is all for them. My wife Liz possesses the patience of a saint and confidence in me that pulled me through the roughest patches. She is glad this is over. My 20-month old daughter Cora could not care any less about my dissertation. Tearing me away from my computer a few times a day to play with puppets, toss a ball around, or gather sticks in the yards is better therapy than money could ever buy. My mother Jeanne, father Roger, and brothers Andy and Nick round out a short list of the most important people in my life. I am truly blessed.

Erich Victor Zorn – 14 April 2016

1.0 INTRODUCTION

Hydraulic fracturing of unconventional gas reservoirs has become an integral part of the national energy strategy in recent years. The potential to tap previously unavailable gas resources has resulted in lower energy costs, economic growth, and a drive to develop more advanced technology to maximize both the hydrocarbon and informational return on the investment. Advances in the science and engineering of hydraulic fracturing coupled with superior horizontal/directional well drilling abilities allow operators to reach farther and produce from more reservoir than ever before. With the ability to drill and stimulate a reservoir with pinpoint accuracy comes the environmental and economic obligation to do so responsibly and efficiently. Microseismic monitoring of hydraulic fracturing has played a critical role in this respect. The ability to locate micro-earthquakes and characterize induced brittle failure in the rock allows operators to monitor vertical and lateral growth of fractures. In addition, well trajectories can be adjusted with respect to the local stress conditions, leading to greater stimulated rock volume. Also, real time monitoring or microseismic data allows operators to shut down fluid injection if they see interaction with faults or undesirable out of zone activity, or optimize a technique that is working well.

From an academic perspective, the wealth of information contained within microseismic data is underutilized at best. Since 2012 and 2013, when the two Marcellus Shale microseismic datasets from Greene County and Clearfield County, respectively, were received for this study,

advanced microseismic processing has become more common. However, the "dots in a box" style of interpretation, i.e. (microseismic events) = (reservoir stimulation) and (no events) = (no stimulation) is still applied with a heavy hand. Microseismic data typically contains the microseismic event time, energy release, moment magnitude, and spatial coordinates, hydraulic pumping data, perforation shot coordinates, and a host of other attributes…an abundance of information left "on the cutting room floor". Additionally in these studies, geophysical well logs, passive surface seismic data, and a four-dimensional seismic velocity profile are available for integration. The goal of this dissertation is to showcase the increased understanding of both reservoir geology and the effects of hydraulic fracturing on an unconventional reservoir that can be achieved by integrating all available information to unveil powerful correlations and spatial relationships.

Table 1 and Table 2 introduce the reader to specialized language and equation variables used throughout the text. Next, a comprehensive history and background section covering the geology of the Marcellus Shale, the evolution of hydraulic fracturing technology, landmark microseismic studies in the last ~50 years, and an introduction to slow slip seismicity will prepare the reader for an in depth theory and methods discussion. Analysis of the Greene County dataset was made into a manuscript and presented at the Society of Petroleum Engineers – Hydraulic Fracturing Technology Conference in 2014. This manuscript, along with additional analysis of this dataset will follow the discussion of methods. All analysis of the Clearfield County dataset follows the Greene County manuscript. The Clearfield dataset contains geophysical well logs and a tomographic velocity profile, enabling integration with the microseismic data. A final summary and discussion section follows.

Table 1 – List of defined terms, abbreviations, and acronyms

Term / Abbreviation / Acronym	Definition
bbl	Blue Barrel (of oil) – 42 gallons
Borehole breakout	Stress-induced borehole deformation resulting in compressional and tensional vertical fractures along the borehole walls
b-value	Slope of the earthquake frequency versus magnitude plot above the magnitude of completeness; indicator of stress conditions and failure mechanism
Cross-plot	Plot of Y versus X values, usually colored or sized by a third parameter; common tool in rock physics / well log analysis
Cross-well velocity tomography	High resolution imaging of seismic velocity between two vertical wells, with one well as source host and the other well as receiver host
Detection bias	In seismology, the ability to detect smaller earthquakes as the proximity to the receiver array becomes closer, and vice-versa
D-value	Slope of the straight-line portion of the frequency versus earthquake-pair distance plot; indicator of point, line, plane, or cloud-shaped geometry
Fault block	Discrete, large block of relatively intact rock, bound by faults
Frac	Short for “hydraulic fracture” (noun) or “hydraulically fracture” (verb)
gpm	Gallons per minute; a measure of flow rate
hhp	Hydraulic horsepower; the energy transferred to the hydraulic fluid. Equals Pressure (psi) * Flow Rate (gpm) / 1714
Hz	Hertz; the frequency of waves or other phenomena in cycles per second
Lateral/directional/horizontal well	A well-bore drilled in a non-vertical direction; in oil and gas exploration, a well drilled laterally within a single reservoir to maximize contact
Leak-off	The pressure required to force fracturing fluid into the formation; the process of fluid being forced into the formation
Microseismic event	In seismology, a small earthquake of magnitude less than zero
Microseismic monitoring array	Geophones installed inside a well or on the surface for the purpose of detecting microseismic events
Microseismic moveout	The increase in distance between the leading edge of microseismicity and the injection point as a function of time
NY	New York, USA
OH	Ohio, USA
PA	Pennsylvania, USA
Passive seismic	The detection of natural earth frequencies from geologic phenomena such as fluid flow, tremors, and earthquakes. There is no active source of signal.
Perforation	Holes in the steel well casing through which fluid is injected into the geologic formation

Table 1 – Continued…

Power spectrum	A plot of the portion of a signal's power that falls within a bin of frequencies.
Proppant	Silica sand or ceramic particles injected along with fluid into a geologic formation during hydraulic fracturing to "prop" open dilated fractures
psi	Pounds per square inch; a measure of pressure
Receiver	A geophone, seismometer, or accelerometer used to detect seismic waves
Screen-out	A condition in which a perforation or fracture is clogged with proppant, inhibiting fluid flow and causing increased pressure
Seismogram	A record of ground motion, measured on a relative scale, as a function of time
Seismometer/geophone	A suspended magnetic mass within a coil of wire that moves in response to earth movement, generating voltage. Voltage is converted to the magnitude of earth movement.
S_{h_max}	Maximum horizontal stress; one of the three principal earth stresses
S_{h_min}	Minimum horizontal stress; one of the three principal earth stresses
Slow slip seismicity	Aseismic tremors or "creep" that emit infrasonic seismic signals, typically in the 0 to 20 Hz range
Source	The source of seismic signals; in passive seismic, an earthquake or similar occurrence; in active seismic, an explosion or weight-drop
Spectrogram	A record of the spectral strength of a signal as a function of time; represented as frequency versus time, colored by loudness
SRV	Stimulated Reservoir Volume
Stage	A discrete length of well-bore that is isolated and perforated in order to hydraulically fracture a desired portion of the reservoir
TOC	Total Organic Content or Total Organic Carbon; one measure of the hydrocarbon potential of an oil and/or gas reservoir
TSCF	Trillion Standard Cubic Feet (of natural gas)
Unconventional reservoir	An oil and/or gas reservoir that requires "unconventional" methods to recover the hydrocarbons such as hydraulic fracturing or steam injection, due to low natural formation permeability or fluid flowability. Includes oil and gas shale, tight gas sand, heavy oil/tar sand, and gas hydrates.
Well log	A record of geologic conditions along a well-bore, from geophysical measurements, direct physical measurements, observation of rock core, or observation of formation cutting and fluid in the drilling mud
Well shut-in	In hydraulic fracturing, the cessation of fluid flow into the well-bore and containment of downhole pressure
WV	West Virginia, USA

Table 2 – Table of Variables

Variable	Definition	Equation Reference
$N(m \geq M)$	Ordinate value, # events whose magnitude (m) is ≥ magnitude on abscissa (M)	Equation 1, Equation 16
a	Ordinate intercept on b and D-value plots	Equation 1, Equation 3, Equation 16, Equation 17
b	b-value, slope of frequency-magnitude distribution	Equation 1, Equation 16
M	Abscissa value, event magnitude	Equation 1, Equation 16
b_{est}	Maximum likelihood b-value	Equation 2
M_{avg}	Average magnitude of event catalog	Equation 2
M_c	Magnitude of completion of event catalog	Equation 2
$N(r < R)$	Ordinate value, # event pairs whose distance separation (r) is < distance on abscissa (R)	Equation 3, Equation 17
D	D-value, slope of frequency-distance distribution	Equation 3, Equation 17
R	Abscissa value, distance separation of an event pair	Equation 3, Equation 17
$r(a \rightarrow b)$	Distance between two points, a and b	Equation 4, Equation 20
x_a	x-coordinate of a	Equation 4, Equation 20
x_b	x-coordinate of b	Equation 4, Equation 20
y_a	y-coordinate of a	Equation 4, Equation 20
y_b	y-coordinate of b	Equation 4, Equation 20
z_a	z-coordinate of a	Equation 4, Equation 20
z_b	z-coordinate of b	Equation 4, Equation 20
P	Number of unique pairs	Equation 5, Equation 21
x	Total number of events in the microseismic catalog	Equation 5, Equation 21
$r_t(t)$	Triggering front distance as a function of time, event to perforation distance	Equation 6, Equation 18
D_{tf} D_{bf}	Triggering/Back-front diffusivity	Equation 6, Equation 7, Equation 18, Equation 19
t	Time between start of injection and occurrence of event	Equation 6, Equation 7, Equation 18
$r_b(t)$	Back-front distance as a function of time, event to perforation distance	Equation 7, Equation 19
d	Dimensionality of diffusion model, 1, 2, or 3	Equation 7, Equation 19
t_s	Time of well shut-in	Equation 7, Equation 19
E_{out}	Radiated seismic energy	Equation 8, Equation 12, Equation 13, Equation 22, Equation 23, Equation 24, Equation 25
M_w	Moment magnitude	Equation 8, Equation 9, Equation 12, Equation 13, Equation 22, Equation 23

Table 2 – Continued…

Variable	Definition	Equation Reference
M_o	Seismic moment	Equation 9, Equation 15
E_f	Fracture formation energy	Equation 10, Equation 27
P_d	Average fluid injection pressure	Equation 10, Equation 27
A_f	Area of the fracture	Equation 10, Equation 27
w	Fracture aperture	Equation 10, Equation 27
E_{in}	Hydraulic energy input	Equation 11, Equation 26
R	Average pumping rate	Equation 11, Equation 26
P	Average pumping pressure	Equation 11, Equation 26
t	Pumping duration	Equation 11, Equation 26
r	Seismogenic source radius	Equation 14, Equation 15
V_s	Shear wave velocity	Equation 14, Equation 33
f_o	Corner frequency of shear wave frequency spectrum	Equation 14
$\Delta\sigma$	Stress drop	Equation 15
E_s	Radiated shear wave energy	Equation 24, Equation 25
E_p	Radiated compressional wave energy	Equation 24, Equation 25
ε_{zz}	Vertical strain	Equation 28, Equation 29, Equation 31
ΔL	Change in vertical length	Equation 28
L	Original vertical length	Equation 28
E, YM	Young's modulus	Equation 29, Equation 36
σ_{zz}	Vertical stress	Equation 29
ε_{yy}	Lateral stress	Equation 30, Equation 31
ΔW	Change in lateral width	Equation 30
W	Original lateral width	Equation 30
v, PR	Poisson's ratio	Equation 31, Equation 36
μ	Mu, shear modulus	Equation 32
ρ	Rho, material density	Equation 32, Equation 33, Equation 35
SI	Shear impedance (V_s * density)	Equation 32, Equation 33, Equation 34
λ	Lambda, incompressibility	Equation 34
AI	Compressional impedance (V_p * density)	Equation 34, Equation 35
V_p	Compressional wave velocity	Equation 35
Brittleness	Elasticity-based brittleness	Equation 36

2.0 BACKGROUND AND HISTORY

2.1 MARCELLUS SHALE

The Marcellus Shale is very fine grained Middle Devonian black shale, located at varying depth and with varying thickness underneath PA, OH, WV, and NY (Figure 1). It is part of a succession of multiple Devonian black shales interbedded with sandstone, limestone, chert, and grey shale, including the overlying thick Huron and Rhinestreet shales, and thinner Middlesex, Geneseo, and Burket shales (Harper and Kostelnik 2011). The Marcellus is actually comprised of two black shales, the upper Oatka Creek or Upper Marcellus and the lower Union Springs or Lower Marcellus, separated by the Purcell/Cherry Valley Limestone. The Lower Marcellus is typically the target of exploration due to its higher Total Organic Content (TOC) (up to 20%) (Williams 2011). The Marcellus Shale is the lowest unit of the Devonian Hamilton Group at the bottom of the Appalachian Basin, and was deposited in relatively deep water at the onset of the Acadian foreland basin formation (Milici and Swezey 2006). During the Acadian orogeny, thick clastic sediments forming the main Catskill Delta were deposited on the shelf deposits (Figure 2) (Harper and Kostelnik 2011).

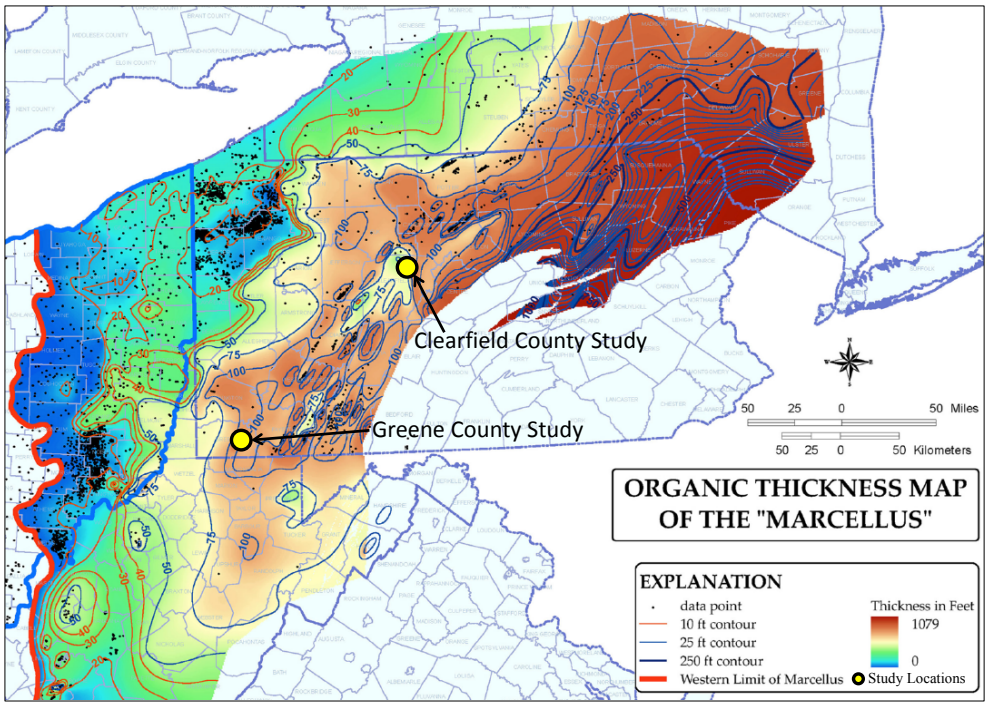

Figure 1 – Map of organic thickness of the Marcellus Shale with study locations for this thesis. Modified from Wickstrom, Perry et al. (2011).

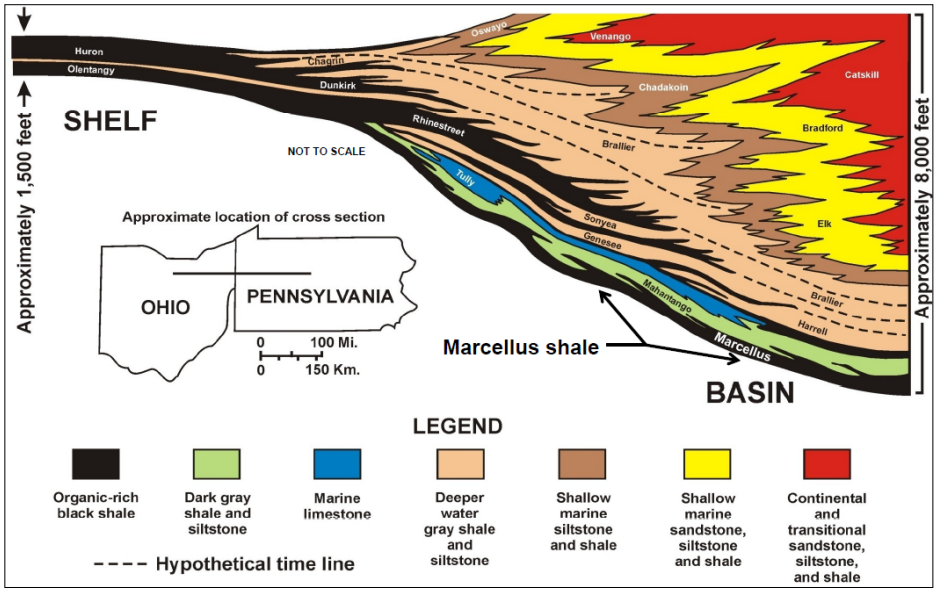

Figure 2 – Schematic cross section of the Appalachian Basin from Ohio into Pennsylvania, emphasizing the increasing thickness of sediments and depth of the basin from west to east. Modified from Harper and Kostelnik (2011).

Of critical importance to the success of hydrocarbon exploration in the Marcellus Shale and other Devonian black shales of the Appalachian Basin is the presence of two regional joint sets, known as J1 and the younger, cross-cutting J2 (Figure 3). These joints are natural hydraulic fractures formed at great depth by fluid pressure perturbations during the thermal maturation process. A third set of joints, known as J3, is of neotectonic origin and a result of the current-day stress field orientation. J1 and J3, by coincidence, are very closely aligned with each other; the difference being J1 is pre-tectonic and was folded and tilted, maintaining its normal incidence to bedding during the Acadian Orogeny and J3 is vertical, cross-cutting bedding at < 90° and other joint sets (Engelder, Lash et al. 2009).

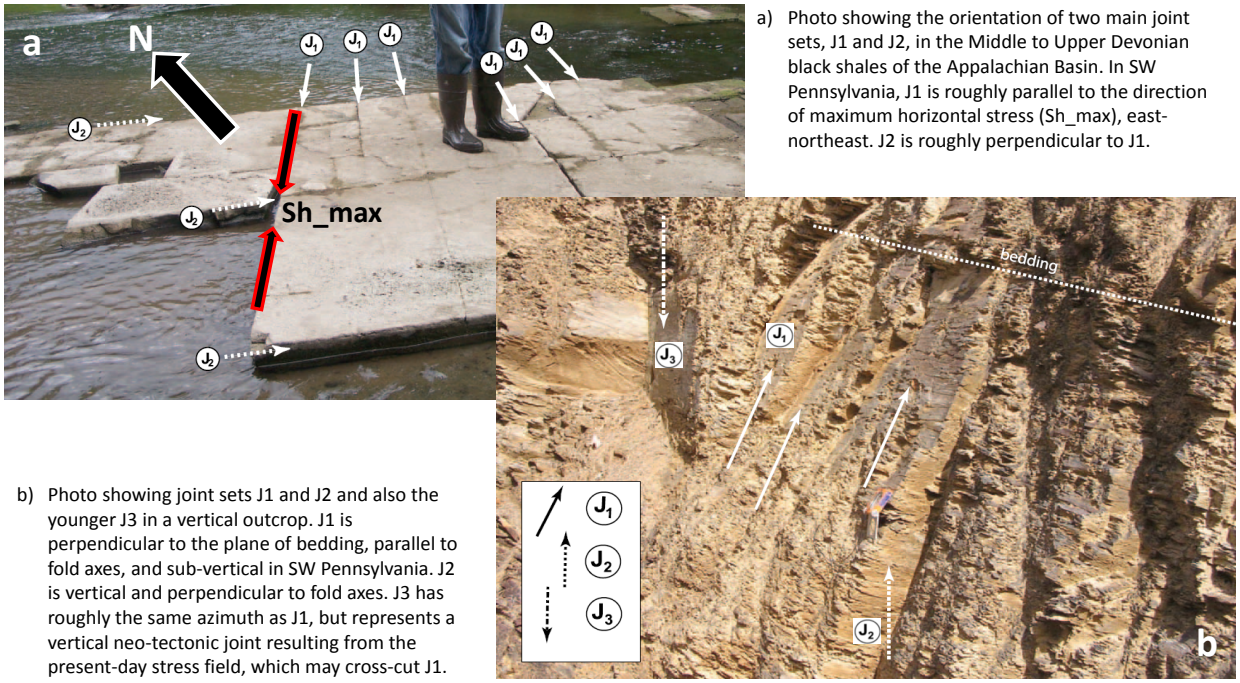

a) Photo showing the orientation of two main joint sets, J1 and J2, in the Middle to Upper Devonian black shales of the Appalachian Basin. In SW Pennsylvania, J1 is roughly parallel to the direction of maximum horizontal stress (Sh_max), east-northeast. J2 is roughly perpendicular to J1.

b) Photo showing joint sets J1 and J2 and also the younger J3 in a vertical outcrop. J1 is perpendicular to the plane of bedding, parallel to fold axes, and sub-vertical in SW Pennsylvania. J2 is vertical and perpendicular to fold axes. J3 has roughly the same azimuth as J1, but represents a vertical neo-tectonic joint resulting from the present-day stress field, which may cross-cut J1.

Figure 3 – The three regional joint sets present in Devonian organic shale of the Appalachian Basin. Modified from Engelder, Lash et al. (2009).

These joints play an important role in the exploitation of natural gas from the Marcellus Shale because they act as conduits through which gas can accumulate and flow (i.e. secondary porosity and permeability). Primary matrix permeability is extremely low in unconventional shale like the Marcellus and hydrocarbon production rates are directly linked to the abundance of secondary permeability (Duncan and Williams-Stroud 2009). Large-scale, multi-stage hydraulic fracturing (described below) in long horizontal wells has the capacity to stimulate all three of these joint sets where completed correctly. Hydraulic fractures have a tendency to propagate in the direction of maximum horizontal stress (S_{h_max}) due to the minimum resistance to tensile opening existing in the direction of minimum horizontal stress (S_{h_min}) (Figure 4). When a lateral well is drilled in the direction of S_{h_min} fractures propagate outward from the well bore, stimulating J1 and J3 joints on a first order and intersecting J2 joints in the process (Engelder, Lash et al. 2009).

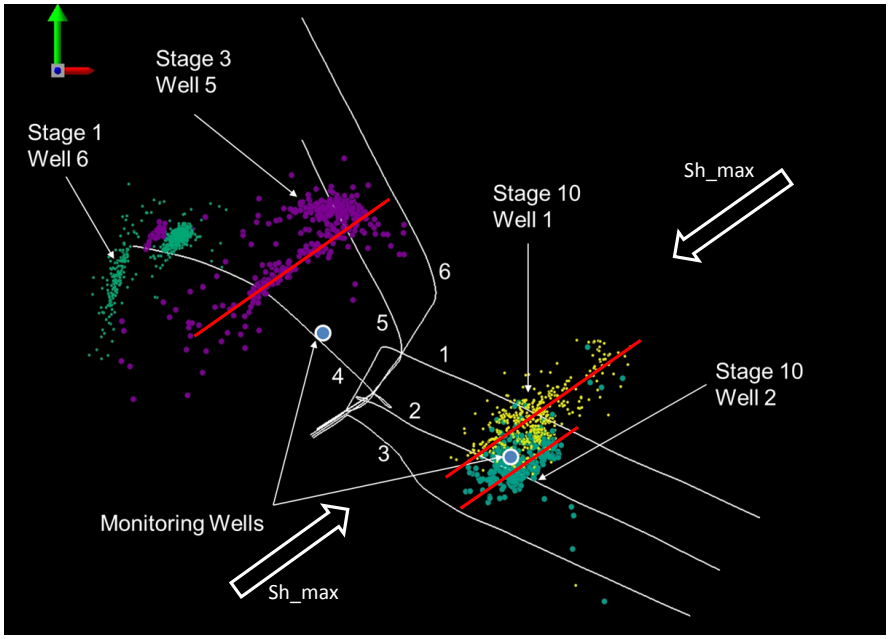

Figure 4 – Well layout at Greene County with microseismic events from four fracturing stages shown. Event clouds align with maximum horizontal stress direction (Zorn, Hammack et al. 2014).

2.2 HYDRAULIC FRACTURING

Slickwater hydraulic fracturing is the process of injecting a mix of water, chemicals, and sand at high pressure (hundreds up to 20,000 pounds/in² (psi)) into a borehole in order to dilate and fracture the surrounding rock formation and release hydrocarbons trapped in the micro pores and cracks. It has become a common practice in order to exploit shale gas in unconventional reservoirs. Exploration companies and geologists have known about the Marcellus Shale for quite some time, but the depth and low permeability nature of the formation have made it uneconomical to exploit until the practice of multi-stage hydraulic fracturing in vertical wells in 2004 (Fontaine, Johnson et al. 2008) and in horizontal, directionally drilled wells in 2006 (Engelder, Lash et al. 2009) (Figure 5), unlocked its potential as a major gas field (Abdalla, Drohan et al. 2011).

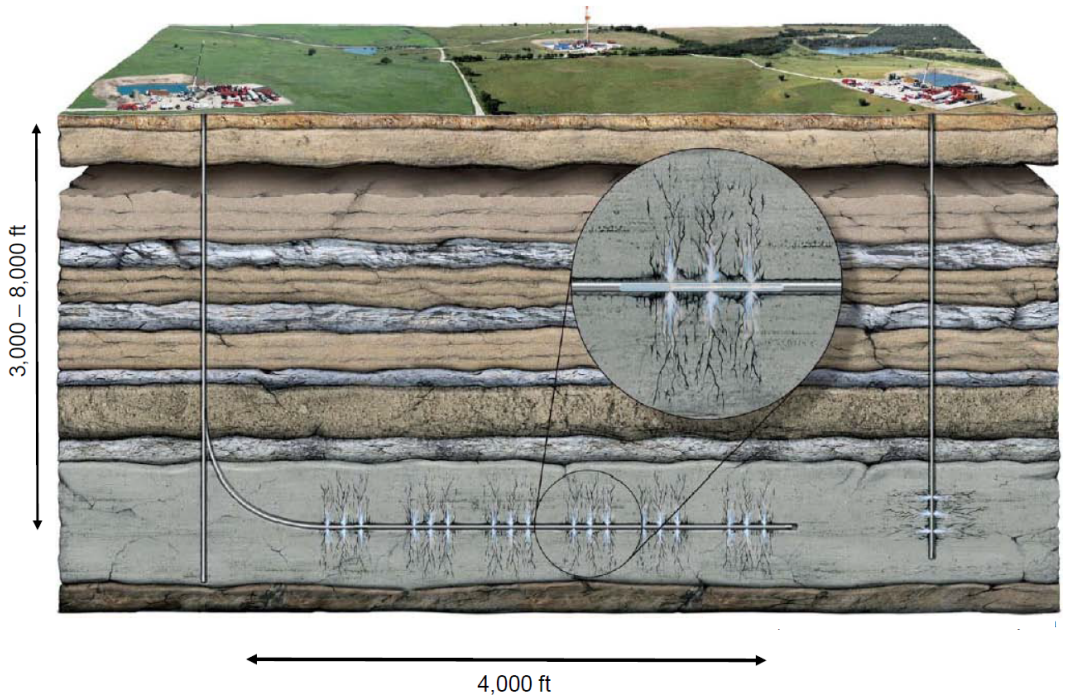

Figure 5 – Schematic diagram of horizontal and vertical well hydraulic fracturing. From Williams (2011).

In 1949 Floyd Harris of Stanolind Oil introduced modern hydraulic fracturing and since then, 2.5 million wells have been treated worldwide. Approximately 60% of all wells drilled today are hydraulically fractured at some point in their service life. Since the practice began, billions of bbls (Blue Barrels) of oil and hundreds of TSCF (Trillion Standard Cubic Feet) of gas, which would have been uneconomical to recover otherwise, have been added to the world supply of hydrocarbons (Montgomery and Smith 2010).

The idea of fracturing a product-bearing formation came about in the 1860s, when nitroglycerin was used to "shoot" wells, essentially rubblizing the formation, releasing oil, water, or gas. In the 1930s, the idea of injecting acid into the formation as a means of opening fractures and keeping them open through etching was introduced to the industry, with good results in carbonate rocks and carbonate-healed fractures. The relationship between formation breakdown and injection pressure had yet to be worked out. In the 1940s the concept of hydraulic fracturing came about, utilizing gelled gasoline or diesel as the fluid and in 1949 sand proppant was introduced to the mix, effectively creating what is known today as hydraulic fracturing. In 1953 water came into use a hydraulic fracturing fluid, which necessitated the addition of friction reducers, thickeners, surfactants, salts, "breakers", acids, biocides, and the other chemicals that are still used today in modern fracturing fluid. These chemicals and additives create what is known as "slickwater" (Montgomery and Smith 2010).

In order to fracture an in-place rock formation, possibly thousands of feet below ground and under tremendous confining pressure, greater pressure needs to be generated at the surface and transmitted down the borehole. Since 1949, the amount of hydraulic pressure available for fracturing operations has increased from ~75 hydraulic horsepower (hhp) to upwards of 10,000 hhp. The average hydraulic horsepower per fracturing treatment is currently ~1,500, able to

reach pressures of up to 20,000 psi (Montgomery and Smith 2010). The number of treatments/year peaked in the early 1950s and the early 1980s at 50,000/year and the current frequency is ~35,000/year. However, the complexity and magnitude of treatments has increased steadily since the inception of the process, from a few hundred gallons/treatment 60 years ago to ~4 million gallons/treatment today.

The importance of fracturing oil- and gas-bearing rock formations to facilitate recovery was recognized 150 years ago, so in that sense the theory and practice is well-established. However, the sophistication of the technology and the size of the treatments have increased exponentially since modern practices began. Directional drilling of multiple horizontal wells from one well-point coupled with millions of gallons of engineered fracturing fluids injected through multiple discrete stages has allowed us to explore for and recover resources considered unrecoverable just ten years ago.

2.3 MICROSEISMIC MONITORING

Microseismic monitoring of waste injection, hydraulic fracturing operations, geothermal development, and background seismicity has a relatively short but successful history of increasing the understanding of structural geology, earth stresses, and fracture networks. The first focused study of the presence of microseismicity during fluid injection took place between 1967 and 1969 at Oak Ridge National Laboratory in Tennessee (McClain 1971). Many landmark studies followed in the subsequent 40+ years that served to improve the technology and understanding required to identify, locate, and interpret microseismicity resulting from fluid injection at depth; these will be discussed in some detail in the following subsections (Table 3).

Table 3 – Landmark studies in microseismic monitoring.

Date	Location	Purpose	Reference
1967-1969	Oak Ridge National Laboratory, TN	Nuclear waste disposal - waveform detection and mapping	McClain 1971
Nov-72	Wharton Gas Storage, PA	Fluid and gas injection - waveform detection only	Hardy etal 1975
Jul-73	Morgantown Energy Research Center, Bradford, PA	Hydraulic fracturing - waveform detection and mapping	Shuck 1974
Dec-73	San Juan Basin, NM (El Paso N.G. Co. et al)	Hydraulic fracturing - waveform detection and mapping	Power et al 1976
Sep-74	Green River Basin, Pinedale, WY (El Paso N.G. Co. et al)	Hydraulic fracturing - waveform detection and mapping	Power et al 1976
Sep-76	Geysers Geothermal Field, Northern CA	Explosion and hydraulic fracturing - waveform detection and mapping	Majer and McEvilly 1979
1974-1995	Fenton Hill Hot Dry Rock Geothermal, NM	Geothermal development - microseismic mapping and stimulated volume estimates	Aki et al 1982; Brown 1995
1981-1988	DOE Multi-Well Experiment (MWX), Piceance Basin, Rulison Field, CO	Hydraulic fracturing of tight gas sandstone - microseismic fracture mapping	Northrop et al 1989
1988-1995	Hijiori Hot Dry Rock Geothermal, Japan	Geothermal development - microseismic mapping and stimulated volume estimates	Sasaki and Kaieda 2002
1989-2001	KTB Superdeep Borehole, Germany	Study fluid injection-induced seismicity at great depth	Zobackand Harjes 1997; Shapiro et al 1997; Brudy et al 1997; Baisch et al 2002
1993-1997	M-Site, Piceance Basin, Rulison Field, CO	Hydraulic fracturing of tight gas sandstone - microseismic fracture mapping	Warpinski et al 1998
1997	Cotton Valley Sands, East TX	Hydraulic fracturing of tight gas sandstone - microseismic fracture mapping	Walker 1997; Rutledge and Phillips 2003

The ability to resolve linear and/or planar features representing hydraulic fractures, faults, or joint sets using seismic waves from micro-earthquakes generated during fluid injection is critical to the continued fine-tuning and success of fracturing treatments in unconventional reservoirs. Before the advent of microseismic monitoring, operators were less informed with respect to how effective their fracturing treatment was; one well may produce above expectations while another nearby is a failure in comparison. Hydraulic fracture modelling offers a starting point for the design of the fluid, pumping, rate, and proppant schedules. Sound inputs about reservoir geology, geomechanics, and stress conditions are critical to producing a good model. While fracturing, pumping pressure and rate can start to give clues about what is happening at reservoir level; large fluctuations in pressure or an inability to maintain a high injection pressure could indicate interaction with open fracture systems or faults that are directing fluid away from the zone of interest. A sudden spike in pressure could be an indication of "screen-out" or

clogging of the wellbore and nearby fractures with sand. Production logs provide the final answer to the question of hydraulic fracturing effectiveness.

Real-time microseismic monitoring can show concentrations of events along a specific linear feature, such as a fault or well defined joint. Very few events may indicate that the operation is not having the intended effect of causing brittle damage in the reservoir due to insufficient pressure or fluid diversion into highly permeable formations or structures. Few events could also be an indication of aseismic deformation, known as slow slip seismicity, which has been documented in other shale formations in the United States (Zoback, Kohli et al. 2012) and investigated in this study (Sections 2.4 and 3.2 (Zorn, Hammack et al. 2014)). Conversely, a uniform distribution of microseismic events, spreading outward from the stage in the direction of S_{h_max} could be a good sign that fracturing fluid is interacting with a discrete fracture network. However, studies have arrived at mixed conclusions regarding the correlation of microseismicity with hydrocarbon production and the "stimulated reservoir volume" (SRV) in unconventional reservoirs. Wilson, Hart et al. (2015) find good agreement between the density of microseismic energy associated with a hydraulic fracturing stage and the two-year cumulative production from that same stage in the Marcellus Shale. They performed their analysis using the same microseismic data set from Greene County, PA that is studied here. Maxwell (2013) stressed that equating the presence of microseismicity to effective stimulation is misleading and inaccurate. Seismicity can be induced by transferring energy from one point to another via a hydraulic system, with no interaction of the fracturing fluid with the induced fracture. In addition, microseismic events may be induced by infiltration into the formation of only the fluid portion of the sand slurry, resulting in an un-propped fracture. In both of these cases, the stimulation is not "effective" because the fracture is not kept open by sand proppant. Cipolla (2014) and Maxwell

(2013) highlight the fact that unconventional shale reservoirs present unique challenges in the understanding of stimulation. Tight sand reservoirs tend to behave more predictably when hydraulically fractured, with defined and planar fractures emanating away from the well bore. Whereas pre-existing discrete fracture networks in shale reservoirs create a vastly more complex stimulated volume that is difficult to predict.

Lastly, the current environmental and political climate requires oil and gas operators to be able to answer questions about the vertical extent to which fracturing fluid is travelling. Microseismic monitoring in Marcellus has shown that resistant rock layers are present that act as pressure and fluid barriers, and even in the presence of faults the highest vertical extent of fluid migration is still thousands of feet below freshwater aquifers (Figure 6) (Hammack, Harbert et al. 2014).

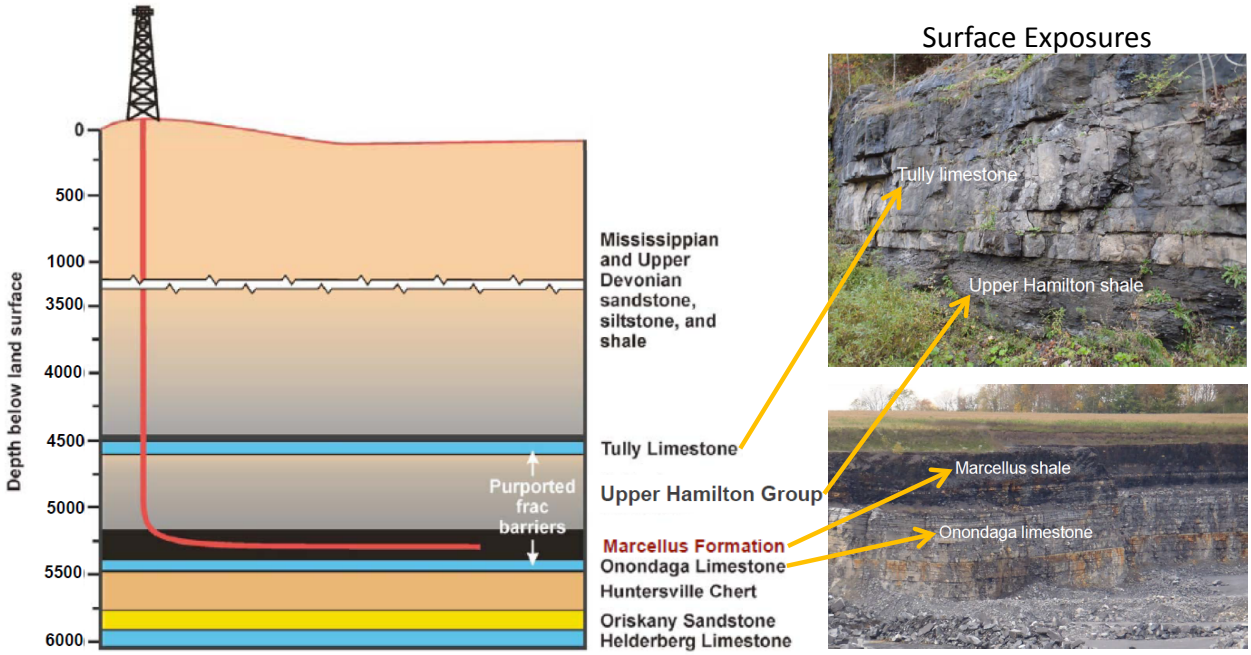

Figure 6 – Schematic geologic section showing horizontal well placement in the Marcellus Shale and surface exposures of key horizons. Modified from Harper and Kostelnik (2011) and Williams (2011).

An instrument setup consisting of two vertical strings of three-component geophones placed near the reservoir elevation is a preferred method of microseismic monitoring, achieving superior elevation control, and adequate x and y location accuracy. Surface and near-surface geophone arrays are another option, offering superior x and y location accuracy and possibly the ability to resolve fault plane solutions. However, vertical accuracy of event locations can suffer (Rutledge, Phillips et al. 1998) (Duncan and Williams-Stroud 2009). Vertical arrays placed at reservoir elevation were employed at both microseismic studies described in this proposal, Greene County and Clearfield County.

Though it is tempting to view the microseismic cloud as a complete picture of the stimulated rock volume, the data is only as good as the instruments deployed to collect it. Microseismic events are typically very small in magnitude (0 to -3.5), and as such are difficult to "hear" under the best conditions. As with any natural earthquake catalog, a microseismic catalog adheres to the Gutenberg-Richter frequency-magnitude distribution described in detail in Section 3.1.1, below (Gutenberg and Richter 1944) and (Gutenberg and Richter 1949). This dictates that there are exponentially more small events than large events and any catalog is controlled by a "magnitude of completion" (Mc) which is imposed by the instrumentation. The apparent increase in the number of small events in the vicinity of the downhole arrays is known as detection bias and it must be taken into account when examining the geometry of the microseismic cloud.

2.3.1 Oak Ridge Study

Throughout the 1960s, research and development of a radioactive waste disposal technique was taking place at the Department of Energy's Oak Ridge National Laboratory (McClain 1971). The technique aimed at utilizing the established practice of hydraulically fracturing rock by injecting

fluid at high pressure (see Section 2.2). In 1966, the first successful injection of cementitious slurry of intermediate-level radioactive waste was completed in the horizontal, very-low permeability Conasauga Shale in Tennessee, creating a laterally extensive, planar lens of hardened waste between the shale laminations. The presence and lateral extent of the waste lens was verified by test borings and surface uplift monitoring by repeated benchmark surveys.

The success of the injection piqued interest in a less invasive method of mapping the extent of waste emplacement, and in November 1967 a single, vertical component seismometer located approximately 5000 feet away was employed to monitor during pumping. As expected, noise dominated the record, but the presence of distinct signal in the form of discrete low frequency events was enough to spur further investigation. In December 1967, a second injection was monitored, this time with improved seismometer sensitivity. Twenty events of higher frequency were recorded, with signal to noise ratios between two and five. Temporally, these events were well correlated with pumping and pumping events such as formation breakdown. Still, hypocentral location of these micro-earthquakes was impossible to achieve with only one monitoring station. Additional experiments were carried out between April 1968 and September 1970, gradually increasing the number and quality of monitoring stations, the frequency range of monitoring, and the sophistication of the signal processing to maximize the signal to noise ratio.

The efficacy of microseismic monitoring of fluid injection and fracture formation was confirmed during the September 1970 tests in which five seismometers were employed to detect microseismic signals with enough redundancy to enable hypocentral location in three dimensions. Eighty-nine events were detected, twenty-nine of which were further analyzed, and eleven of which were determined to be absolutely correlated to fracture propagation in time and space.

2.3.2 Wharton Gas Storage Study

Begun in 1966 at the Pennsylvania State University, in collaboration with the Pipeline Research Council, this study aimed to establish criteria for the safe storage of natural gas in underground reservoirs (Hardy, Jr. et al. 1975). It was determined that safe storage pressure is approximately equal to the lithostatic pressure at the reservoir interval. In order to test this conclusion, field studies were necessary and it was proposed that acoustic monitoring should be tested as a surveillance technique to be implemented during injection. The main accomplishments of this study include the development and testing of a mobile microseismic monitoring facility, the development of equipment such as transducers and the required deployment techniques, computer analysis workflow development, and most importantly, the verification of microseismic monitoring as a viable surveillance technique at storage reservoirs.

2.3.3 Morgantown Study

Following the encouraging results from the Oak Ridge study, the Morgantown Energy Research Center of the U.S. Bureau of Mines undertook a three-phase study of the ability to detect and accurately locate acoustic emissions from hydraulic fracturing in an oil-producing well in Bradford, PA (Shuck 1974).

Phase 1 was conducted in April 1972 and confirmed the source-locating capability of the monitoring system to within 8-10 feet of its true location, by detonating small explosive charges in known, near surface locations, akin to the present-day practice of detecting and locating casing perforation shots as a calibration technique. The monitoring system consisted of twelve doubly-

amplified hydrophones with flat frequency responses of 10-40 Hz. The hydrophones were deployed down eleven existing wells in the field, all located within 900 feet of the injection well.

Phase 2, conducted in July 1973, was a "real-world conditions" test of the monitoring system and took place in a previously fractured well. The aim of this phase was to map the extension of previously created fractures and test the sensitivity of the system when subjected to the noise of pumps, blenders, and the flow of sand-slurry down the well well-bore.

Phase 3, conducted in November 1973, was the final experiment at this location. Following a background noise survey in which the frequency content was analyzed to design cut-offs and filters, a new well was drilled close to the original injection well and the formation was hydraulically fractured. In addition to the seismic monitoring, a full suite of geophysical well logs were obtained, core samples tested, and well pressures monitored.

The results of this comprehensive study include confirming the ability to detect and map hydraulic fractures via seismic methods and concluding that the optimal bandwidth of monitoring equipment should be between 80 and 500 Hz, with appropriate pass filters in place.

2.3.4 El Paso Natural Gas Company Studies

El Paso Natural Gas Company, in conjunction with Sandia National Laboratory and Global Universal Science, performed hydraulic fracturing experiments in the San Juan Basin in New Mexico and the Green River Basin in Wyoming in December 1973 and September 1974, respectively (Power, Schuster et al. 1976). The San Juan experiment took place in the Pictured Cliffs Formation at a depth of ~3,000 feet and hydraulic fractures were generated by injecting ~29,000 gallons of gelled water and 40,000 pounds of sand. The Green River Experiment took

place in the Pinedale Unit at a depth of ~9,000 feet and 270,000 gallons of gas condensate and water emulsion were injected along with 775,000 pounds of sand.

The investigation of fracture formation in the San Juan Basin was accomplished by deploying one 20-5000 Hz hydrophone down an existing borehole, with the intention of detecting a range of low to high frequency signals generated by rock failure. It was found that pumps and other machinery generated a high frequency noise that completely masked any fracture-related signals at the high end of the spectrum; low frequency noise components were also found, but fracture-related signals could be distinguished. p- and s-wave signals were seen despite noise contamination, and researchers concluded that these were generated by tensional failure at the fracture tip during fracture growth. A low frequency component was determined to be fracture-related and likely a product of slow-slip or creep (aseismic) processes at fracture boundaries and intersections. From p- and s-wave arrival time separation, fracture lengths of several hundred feet were calculated, with the understanding that fractures likely extended further out but attenuation by the "earth-filter" would diminish these signals. Additional work completed during the San Juan experiment includes deployment of a single vertical component seismometer and also an array of six 2 Hz vertical geophones at the surface. Neither of these additional instrumentation deployments detected any coherent signal, likely because of the limited bandwidth and sensitivity of the instruments and low signal to noise ratio.

The Green River Basin experiment was a much more rigorous undertaking, employing a three-prong approach to monitoring. A four-arm array of instruments, one mile in each direction, containing 216 vertical seismometers and a single three-component seismometer on each arm, was deployed at the surface. The use of 864 seismometers enabled stacking of the data stream to enhance signal and cancel out random noise. Additionally, seismic and acoustic monitoring

equipment was deployed both downhole and shallowly buried, within 13,000 feet of the injection well, including two seismometer arrays at 300 feet depth, four arrays at 20 feet depth, one array at 11,000 feet, and one hydrophone at 9,000 feet. The third method of monitoring was not seismic in nature, but rather electrical-potential, utilizing the relatively simple but effective approach of using two deep well casings as electrodes. Prior to fracturing, a baseline electrical potential survey was performed. A second survey was performed after fracturing with the intention of delineating the geometry of fluid emplacement by subtracting the baseline survey from the post-fracturing survey to produce a map of fluid-related electrical potential. As this is not a seismic method of fracture delineation, it will not be discussed here in greater detail.

Results of the Green river Basin experiment were promising. Seismic signals consisting of p and s-wave arrivals were detected between 1,000 and 10,000 feet from the injection well, at the depth of injection. Though there was very little alignment of microseismic events to provide information about fracture azimuth, a combination of the three datasets provided a high degree of confidence in fracture length. A moving source was also detected, presumably indicating the presence of a propagating hydraulic fracture.

2.3.5 Geysers Geothermal Study

This study of the utility of microseismic studies to characterize geothermal reservoirs took place between July and September of 1976 (Majer and McEvilly 1979). Eighteen permanent USGS monitoring stations and a temporary array of thirteen seismometers deployed by Lawrence Berkeley Laboratory were used with the primary goal of determining if the presence of an actively producing geothermal reservoir affected the propagation velocities of p-waves. The study was timed to coincide with an unrelated experiment conducted by the USGS in which two

large explosions were detonated to study refracted seismic waves. A velocity model benefits from more data points, and two large events of known location and energy provide additional constraints on the model. Furthermore, the two explosions were exclusively used to develop the baseline velocity model by measuring travel times to stations outside of the known producing field. Velocities within the field were measured by examining travel time anomalies from the explosions and also microseismic events that occurred within the reservoir.

Greater than 300 microseismic events were recorded during the experiment. Key observations from the Geysers study include a high level of shallow (< 0.5 km) microseismic activity in the field that does not define any dominant fault structures and appears to be random in its occurrence. Earthquake source parameters appear to align with the regional fault trend however. Velocity within the producing zone is higher than outside the zone, and the level of attenuation of seismic waves is lower with the producing zone. Pressure, temperature, vapor, and hydrothermal/chemical alteration all play into the anomalous measurements but the extent to which each contributes was not able to be determined from this study. A promising conclusion of this research was the possibility that microseismic studies could be used to delineate geothermal boundaries and also the enthalpic properties of the reservoir.

2.3.6 Fenton Hill Hot Dry Rock Geothermal Study

A hot, dry rock (HDR) geothermal system is one in which there is heat present but no natural fluids, in deep crystalline rock. Although researchers at Los Alamos National Laboratory began to think about the concept in the early 1970s, experimentation at Fenton Hill, approximately 40 miles west of the laboratory, did not take place until 1980 to 1995 (Brown 2009). Microseismic monitoring was used to delineate the boundaries of two HDR systems at depths of 2800 meters

and 3500 meters, and temperatures of 195° C and 235° C, respectively. The reservoirs were created under different injection conditions; the shallower reservoir under lower pressure (~1400 psi) and the deeper reservoir under higher pressure (~3900-4600 psi). The thermal power created from these two reservoirs ranged between three and ten megawatts after development.

Many significant conclusions emerged from these experiments, foremost that HDR is a viable source of geothermal energy. Secondly, in development of HDR resources, it is critical to form the reservoir first, then place the production wells accordingly. Attempting to create the reservoir around the desired production points is difficult and unpredictable. Next, maintaining high reservoir pressure, in this case approximately 2 ½ times the minimum principal stress magnitude, enables your production wells to operate more efficiently due to decreased flow impedance. Also, great differences between were observed between the pressure required to prop open a fracture in the shallow reservoir (~2000 psi) and that required in the deeper reservoir (~5500 psi) even though they were only separated by ~700 meters. Finally, microseismic monitoring is critical in mapping the gross reservoir development and informing the process of siting production wells, but more work is needed to discern the increased effective permeability from unproductive fractures.

2.3.7 MWX (Multi Well Experiment)

The United States government began to focus on the development of low permeability gas plays, what we now know as unconventionals, in the 1960s. They experimented with high explosives and hydraulic fracturing to stimulate production, with disappointing results. The experiments were not providing the necessary data to unlock the secrets behind increasing permeability (Northrop, Myal et al. 1989). The Multi-Well Experiment, so-named because of the three closely

spaced experimental wells, was a product of the Department of Energy that began in 1981 and continued until 1988. The experiment took place in the Mesaverde Formation of the Piceance Basin in Colorado, a sandstone-dominated coastal to marine succession including shale, coal, and mudstone. A variety of testing was performed that brought together a host of disciplines, including geophysical surveying, borehole seismic, geological studies, rock core and well log analysis, in-situ stress analysis, stimulation, fracture analysis, and reservoir analysis.

The microseismic aspect of this experiment aimed at mapping fracture growth in the lateral and vertical directions and the fracture orientation. One hundred sixty events were detected that showed fracture wing lengths of 250 feet and height growth of 120 feet, at an orientation of ~N60°W. A major focus of the microseismic study was to determine workflows for the location of microseismic events using one geophone and two geophones, and to intimately understand the error associated with each.

2.3.8 Hijiori Hot Dry Rock Geothermal Study

At the Hijiori Hot Dry Rock Site in the Yamagata Prefecture, Japan, the natural geothermal energy present in the crust below 1800 m depth, greater than 250˚C, was harnessed by injecting water at high pressure and flow rates in order to fracture the rock formation, essentially creating an artificial geothermal reservoir. The site is located inside the southern rim of the 1.5-2 km wide Hijiori Caldera, within which five deep wells were drilled and used for injection, production, and velocity modeling, and outside of which ten boreholes were advanced for the installation of seismic monitoring equipment (Sasaki and Kaieda 2002). Hundreds of seismic events were induced over the course of four separate injection experiments between 1988 and 1995; two low volume/high flow-rate fracturing experiments and two high volume/low flow-rate

circulation experiments. These events were located and used to determine clustering and alignment of events along pre-existing fractures and also the in-situ stress state of the reservoir rocks. In addition, the rocks exhibited a memory of the last maximum induced stress, all of which will be discussed below.

A fracturing experiment and a circulation experiment were carried out at a depth of approximately 1800 m in 1988 and 1989, respectively, and at a depth of approximately 2175 m in 1992 and 1995, respectively. Sasaki and Kaieda (2002) began by relocating all microseismic events with more than five p-wave arrivals and two s-wave arrivals to ensure a quality dataset, ending up with 792 events. It became immediately apparent that there was a difference in the pattern of event locations between the fracturing and circulation experiments; fracturing resulted in a tight cluster of events along a small planar area and circulation resulted in a diffuse cloud of events away from the injection point. Sasaki and Kaieda (2002) explain that the high pumping rate and pressure and low volume of the fracturing experiment causes the fluids to seek out the most readily available conduit, likely resulting in elastic dilation of the rock. The long duration, high volume, and low pumping rate of the circulation experiment causes pore pressure to diffuse away from the injection point to previously existing discontinuities in the rock. In comparing the event locations to the known E-W geologic structure of the site it is apparent that the fracturing events follow the dominant discontinuities of the caldera and the circulation events are clustered around the dominant discontinuities on the network of smaller fractures.

After accurately locating all of the events, Sasaki and Kaieda (2002) further distilled the dataset by eliminating events with less than eight p-wave arrivals, resulting in a set of 58 events for which high quality focal mechanisms were calculated. Barth, Reinecker et al. (2008) present a good explanation of what a focal mechanism represents and the limitations encountered in

using them to delimit stress field orientation. The classic "beach ball" diagram is composed of four quadrants for a strike slip event and usually three segments for a normal or reverse fault. A well constrained event will be surrounded by p-wave arrivals whose first motion is indicative of either compression or tension. A focal mechanism diagram is constructed by fitting two great circles of a stereonet such that the compressional motions are separated from the tensional motions. The P axis, or pressure axis, bisects the tensional quadrants and represents the direction of maximum shortening, while the T axis, or tensional axis, bisects the compressional quadrants and represents the direction of maximum lengthening (Figure 7 and Figure 40). The B axis, or null axis, lies at the intersection of the P and T axes and is perpendicular to them (Barth, Reinecker et al. 2008). A common practice is to equate the average of a set of P, T, and B axes to σ_1, σ_3, and σ_2, respectively. However, this method only gives an approximation (± 45°) of the principal stress directions because the P, T, and B axes represent the moment tensor, which can be highly variable with a single stress field, and not the stress tensor (Sasaki and Kaieda 2002). Discontinuities in the body of the rock will create variation in the moment tensor of failure from one focal mechanism to another. In addition, a focal mechanism represents two possible fault planes.

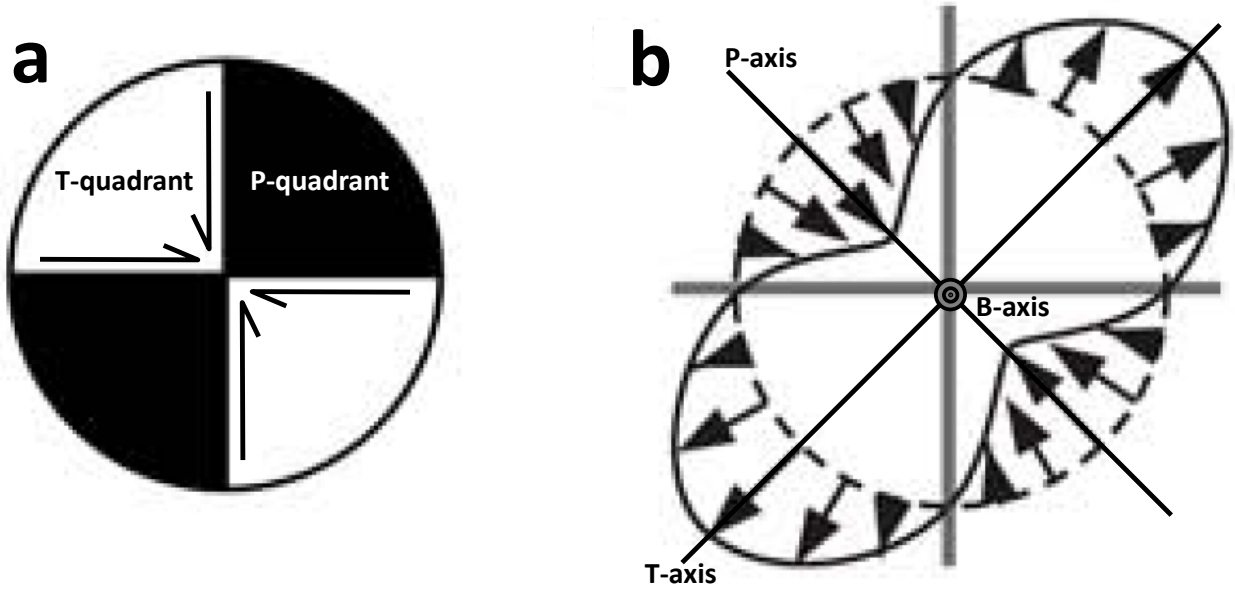

Figure 7 – The P and T quadrants and P, T, and B axes of a strike slip focal mechanism. Modified from Cronin (2010).

In response to these limitations, Sasaki and Kaieda (2002) had to use stress inversion methods (inverting the focal mechanisms) developed by Gephart and Forsyth (1984) in order to study the in situ stress state present in the reservoir. This method attempts to select the correct fault plane from the two nodal planes and determine the principal stress directions that are most consistent with the P, T, and B axes of the focal mechanisms. Essentially, an initial stress model is selected containing σ_1, σ_3, R (stress ratio = $(\sigma_2-\sigma_1)/(\sigma_3-\sigma_1)$), and the slip direction. Comparing this model to all of the focal mechanism's nodal planes, the model in which the least amount of total fault plane rotation is required to bring the observed data into agreement with the model is considered to be the optimal stress tensor orientation (Gephart and Forsyth 1984). Using this method, the researchers were able to determine that the orientation of the best fitting stress model has σ_1 = 4°, 82° (trend, plunge), σ_2 = 270°, 1°, and σ_3 = 180°, 8°, with an average misfit with the data of only 6.8° (Sasaki and Kaieda 2002). This is consistent with other stress

models of the area from literature, and more importantly, it is consistent with the known geologic structure of the site (normal faulting and N-S oriented lengthening).

Similar to an observation by Talwani (2000) of stress memory in the shallow seismogenic crust, Sasaki and Kaieda (2002) observed a similar phenomenon. There had been a previous fracturing experiment in 1986 in which ~1000 m^3 of fluid was injected to ~1800 m depth. During the 1988 fracturing experiment, no microseismic events were recorded for the first six hours, until ~900 m^3 of fluid had been injected. It is hypothesized that the stimulated rock volume dilated aseismically until the previous maximum stress level was reached and surpassed.

2.3.9 KTB Superdeep Borehole Study

Microseismic studies were extensively used at the 9101 meter deep Kontinentale Tiefbohrung (KTB) borehole in Germany in 1994 and again in 2000 (Baisch, Bohnhoff et al. 2002). Forty 3-component surface seismometers and one 3-component downhole sonde were deployed to monitor seismic activity. The primary goal of the experiments was to characterize the in-situ stress state and rheology of the crust at great depth and map structures. In 1994, ~53000 gallons (~1200 bbls) of brine were injected over the course of 48 hours, inducing ~400 detectable microseismic events. Researchers observed that very small pressure perturbations (< 1 MPa) were required to induce brittle failure, leading to the conclusion that the crust is critically stressed at this depth. A second important observation was that no microseismic events were observed below the depth of the borehole, possibly indicating a rheological boundary between the brittle and ductile zones in the upper crust.

In 2000, ~1.06 million gallons (~24000 bbls) of brine were injected over the course of 60 days, inducing 2799 microseismic events, of which 237 were able to be located accurately.

Suspected leaks in the casing caused fluid to be injected at multiple levels in the borehole, rather than only in the bottom uncased section. Several significant observations were made during this study. A few seismic events were detected at depths that surpassed the 1994 injection, leading to a conclusion that while a brittle ductile transition may exist near nine km depth, there are scenarios in which brittle failure may occur. These include local shear stress concentrations and material changes that affect the rheology of the rock. Researchers also observed the Kaiser Effect (Kaiser 1950) in which volumes of rock that produced microseismicity during the 1994 injection were distinctly devoid of any seismic activity during the 2000 injection, presumably due to "de-stressing" the rock, making it less susceptible to failure. This phenomenon was also described by Sasaki and Kaieda (2002) in the previous section (Section 2.3.8), termed "stress memory".

2.3.10 M-Site Project

The Multi-Site Hydraulic Fracture Diagnostic Project (M-Site) took place between 1993 and 1996 and was carried out at the former location of the Multi-Well Experiment, previously described (Warpinski, Branagan et al. 1998). The project was a collaboration between the US Department of Energy and the Gas Research Institute. The site was heavily instrumented, including two downhole microseismic arrays (one five-level and one thirty-level array), a six-level array of inclinometers to measure small deformation related to fracture opening and closing, and wellbores drilled to intersect and "ground-truth" hydraulic fractures.

The microseismic component of the project aimed to refine technology and workflows for mapping hydraulic fracture geometry and test the efficacy of fracture modelling efforts. Key microseismic observations include large discrepancies between the modelled fracture geometry and the microseismically-imaged fracture geometry, greater fracture complexity than expected,

including multiple strands, secondary fracturing, and T-shaped fractures, and differences in the geometry of fractures from one stage to the next, presumably from changes in fluid transport within the reservoir. Different fracturing fluids also result in significantly different fracture geometries due to changes in the viscosity and compressibility.

2.3.11 Cotton Valley Sands Study

In May 1997 a consortia of partners including oil and gas operators, national laboratories, service companies, and others conducted a hydraulic fracture mapping experiment in the tight gas sands of the Carthage Cotton Field of East Texas (Walker 1997). The experimental design follows previous groundbreaking studies such as the M-Site Project. Previous studies showed that it is possible to image hydraulic fractures via the detection of microseismic events along the fractures. However, the Cotton Valley study took place at a grander scale than any study before. Larger well spacing, up to 1,300 feet between the stimulation well and the receiver well, and greater depth to the target zone, approaching 10,000 feet, tested the ability of state-of-the-art technology to perform as intended. The two monitoring wells were heavily instrumented with 48 3-component geophones in each.

Researchers accurately located ~2000 microseismic events, showing that it is possible with a robust array of instrumentation to detect fracture formation at great distances. They concluded that commercially available technology was not yet able to meet the monitoring needs of a large site like this; custom instrumentation setup was necessary. An important finding that still holds true today is that an accurate velocity model is paramount to success in locating far-field events with confidence. In this study, a cross-well velocity profile was acquired for this purpose.

2.4 SLOW SLIP SEISMICITY

Some researchers posit that brittle failure on existing joints is not the only mechanism for stimulation of unconventional shale, nor is it the main contributor to gas production. The radiated microseismic energy added to the theoretical energy required to create a fracture of a specific size still comes up drastically short in accounting for the total amount of energy applied to the system through hydraulic fracturing (Zorn, Hammack et al. 2014). Of course, mechanical losses through heat and friction, and free flow of fluid into high secondary permeability zones can account for some of this imbalance, but the deficit is still large.

Zoback, Kohli et al. (2012) suggest that aseismic slip on pre-existing faults and fractures that are misoriented in the current stress field (i.e. not critically stressed) serves to connect hydraulic fractures that form parallel to S_{h_max} (Figure 8). However, it is difficult to verify the existence of these aseismic tremors without a dedicated monitoring system capable of detecting very low frequency signals. Even with a monitoring system, it is a challenge to pinpoint the location of the events due to the absence of discrete p and s-wave arrivals. We have data from one research-quality seismograph placed at Greene County during hydraulic fracturing. Analysis of these data has shown some indication of the presence of increased power in the low frequency ranges after the start of hydraulic fracturing, but it is difficult to be certain without additional monitoring.

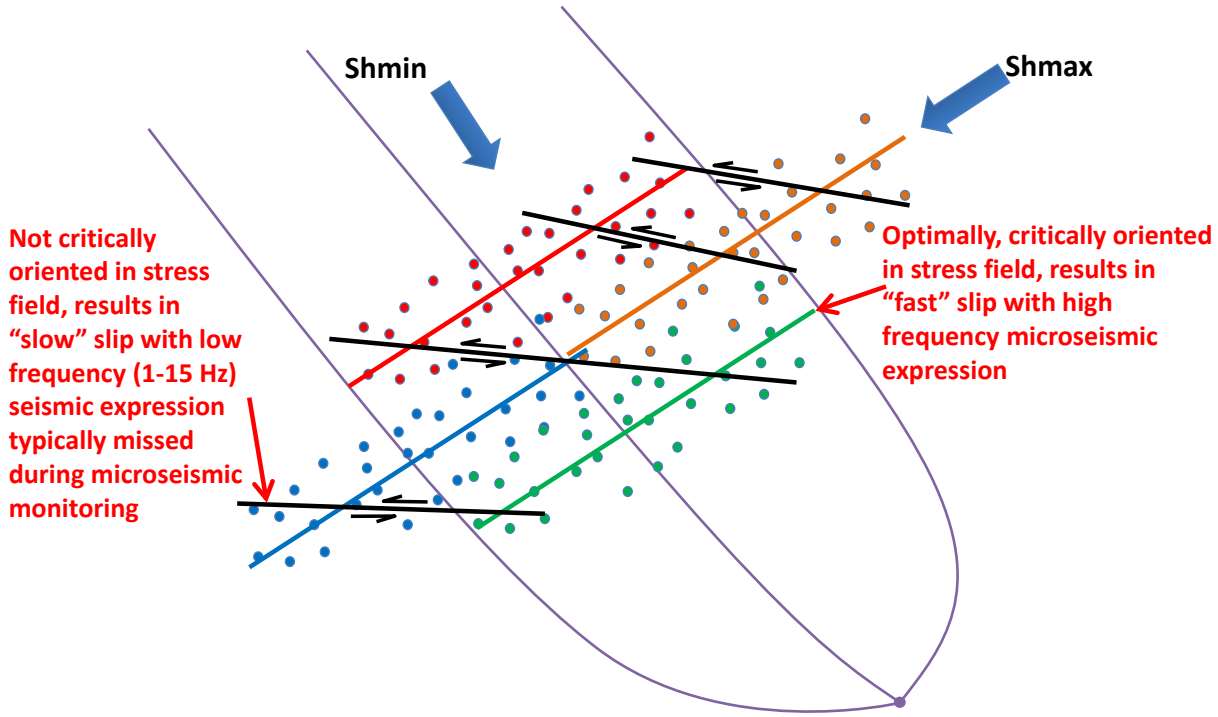

Figure 8 – Schematic diagram of "fast" and "slow" slip along fractures and their position with respect to the principal horizontal stresses. Adapted from Zoback, Kohli et al. (2012)

3.0 MICROSEISMIC CASE STUDIES

3.1 THEORY, DEFINITIONS, AND METHODS

All data for two studies (Greene County and Clearfield County microseismic monitoring) was provided by the Department of Energy's National Energy Technology Laboratory and their industry partners. Default microseismic parameters provided by the contractor (Weatherford and Schlumberger) generally include: time, date, stage number, coordinate, moment magnitude, stress drop, signal to noise ratio, and S-wave/P-wave amplitude ratio of the microseismic event. Additionally, the coordinate of the stage perforations and the temporal pumping pressure, pumping rate, and proppant concentration of each stage are provided. At Greene County, only microseismic and pumping data were provided. At Clearfield County, in addition to a microseismic catalog, two well logs and pre- and post-hydraulic fracturing cross-well seismic velocity sections were provided.

Using this set of data, the first step is to ensure that the pumping information is set to the same relative time scale as the microseismic data, eliminating time and date stamps in favor of an absolute scale in seconds. The entire job is placed onto one timescale, starting at zero, for comparing temporal aspects of all stages in real time. Individual fracturing stages are also broken out separately for more detailed analysis. Once this is complete, additional attributes are

calculated, including: b-value, D-value, hydraulic diffusivity, seismic moment, radiated S, P, and total seismic energy, hydraulic input energy, and fracture formation energy, described below.

3.1.1 Fractal Dimensions

Naturally occurring processes often adhere to power-law distributions. The frequency-magnitude distribution of seismic events has been shown to follow the Gutenberg-Richter relation (Gutenberg and Richter 1949), given by:

$$log_{10}\, N(m \geq M) = a - b * M \text{ (least squares method)} \quad \textbf{Equation 1}$$

or

$$b_{est} = 1 / ln(10) * (M_{avg} - M_c) \text{ (maximum likelihood method)} \quad \textbf{Equation 2}$$

where N(m ≥ M) is the number of events whose magnitude, m, is greater than or equal to M (x-axis value), and b is the absolute value of the slope of the linear portion of the distribution (Figure 9a), the fractal dimension, taken to be an indicator of the dominant stress regime, and thus failure mode of the seismic events (Grob and van der Baan 2011). Traditional interpretation dictates that a b-value < 1 corresponds to a higher proportion of larger events and is thought to be indicative of a compressive stress regime (reverse faulting or fracture closing). A b-value ~1 is thought to be indicative of a shear stress regime (strike-slip faulting). A b-value > 1 corresponds to a higher proportion of smaller events and is thought to be indicative of a tensile stress regime (normal faulting or tensile fracture opening) (Grob and van der Baan, 2012). The interpretation of b-values in the case of microseismic catalogs follows Goertz-Allmann, Gischig et al. (2012), who document that b-value is inversely proportional to the stress differential present at the time of failure. A high b-value would indicate a smaller difference between the maximum and minimum horizontal stresses than a low b-value. M_{avg} is the average magnitude of the catalog of

events considered and M_c is the magnitude of completion of the catalog (Lombardi 2003). The least squares method was applied to the Greene County data and the maximum likelihood method was applied to the Clearfield County data, because Greene County was hand-calculated and Clearfield County utilized a MATLAB-based seismological approach.

The D-value is a fractal dimension which quantifies the spatial distribution (shape of clusters) of the events based upon the separation distance between all unique pairs of events, giving insight into the natural weaknesses in the fractured rock (Figure 10) (Grob and van der Baan 2011), and is defined by the equation:

$$log_{10}\, N(r < R) = a - D * log_{10}\, R \qquad \textbf{Equation 3}$$

where N(r < R) is the number of event pairs whose distance separation, r, is greater than or equal to R, and D is the absolute value of the slope of the linear portion of the distribution (Figure 9b). Following Grob and van der Baan (2012), a D-value = 0 indicates a clustering of events at one point in space; a D-value = 1 indicates a linear clustering of events; a D-value = 2 indicates a planar distribution; and a D-value = 3 indicates a uniform distribution in space (a cloud).

The D-value analysis requires calculation of the distance between all possible unique pairs of events in the seismic catalog (Figure 10). Three dimensional distance, r, between two points, a and b, is calculated using the Euclidian distance equation:

$$r\,(a \rightarrow b) = \sqrt{[(x_a - x_b)^2 + (y_a - y_b)^2 + (z_a - z_b)^2]} \qquad \textbf{Equation 4}$$

where x, y, and z are the coordinates of each point in space. The number of possible unique pairs, P, is given by the following equation:

$$P = (x^2 - x) / 2 \qquad \textbf{Equation 5}$$

where x is the total number of events in the catalog of interest.

The combination of b-value and D-value for an earthquake catalog can allow interpretation of the regional, or in this case, local tectonic setting and rock failure mode (Figure 11).

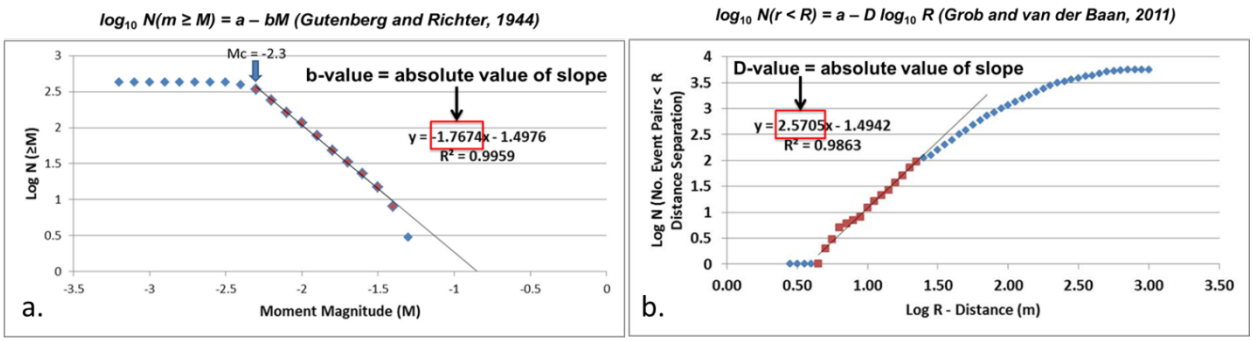

Figure 9 – Typical frequency-magnitude (b-value) and frequency-distance (D-value) distributions from a microseismic dataset in the Marcellus Shale (Zorn, Hammack et al. 2014).

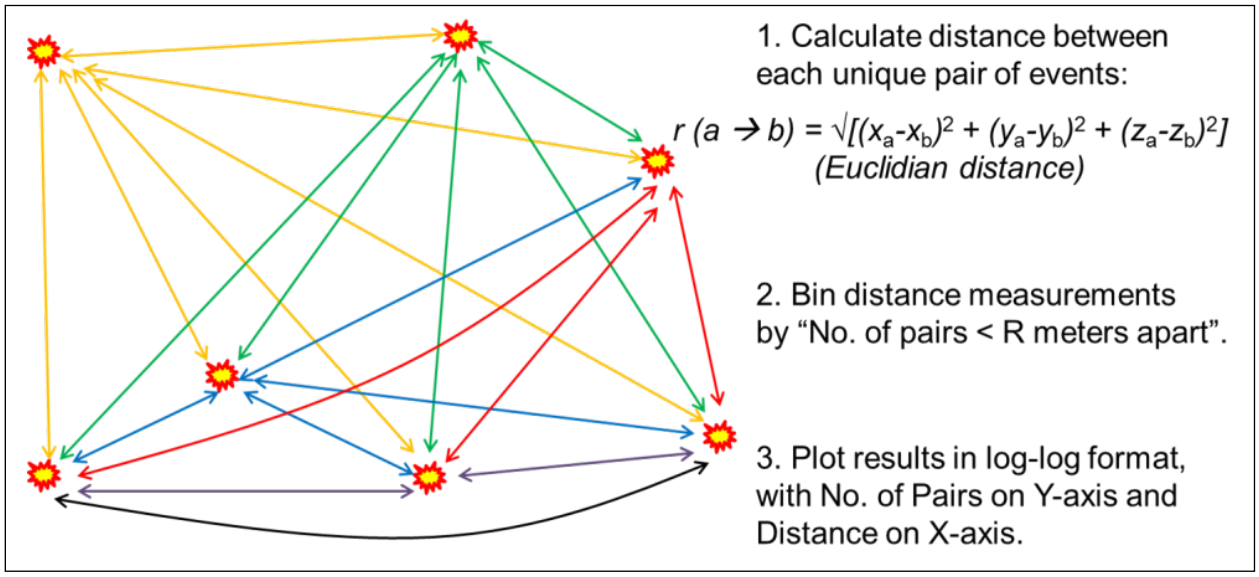

Figure 10 – Graphical representation of D-value calculation (Zorn, Hammack et al. 2014).

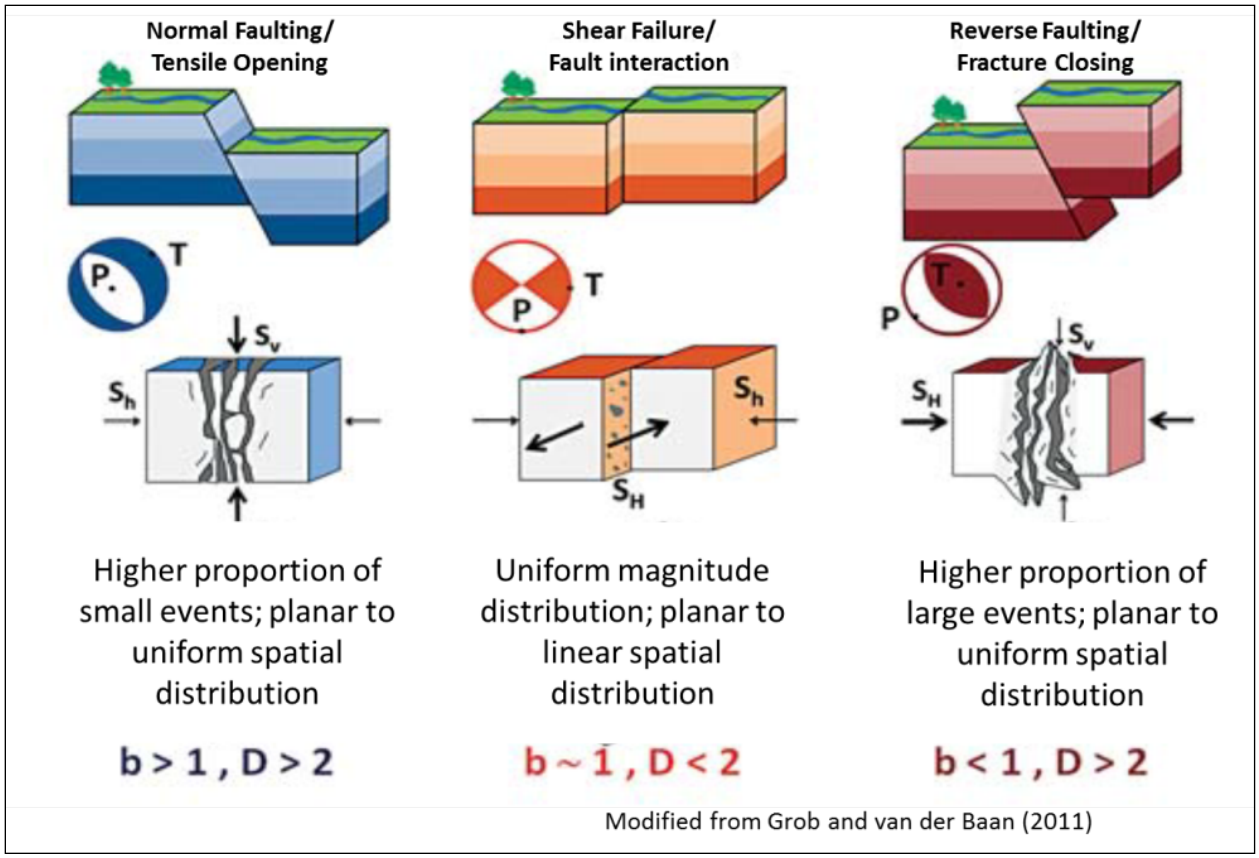

Figure 11 – Tectonic interpretation of b and D-value combinations for a set of seismic events. Modified from Grob and van der Baan (2011).

3.1.1.1 Temporal Fractal Analysis

Both b and D-values can be calculated for the entire stage, resulting in one value for each parameter. In this study, one of the goals was to examine the evolution of b and D through time by sub-setting the dataset into blocks of 200 events (safely above the minimum for a robust fractal analysis of this sort, from Öncel and Wilson (2004)), overlapping by 190 events and moving this window through the stage. The user is able to see sub-stage level changes in the state of stress at failure and the spatial arrangement of events throughout the course of injection. In addition, all pertinent injection activity was recorded to one second resolution, including pumping pressure, slurry rate, and proppant concentration. Plotting this information alongside b,

D, diffusivity, event magnitude, and perforation-to-event distance enables us to observe what, if any, correlation exists between injection parameters at the surface and the microseismic response of the rock mass. The combination of b-value and D-value for an earthquake catalog can allow interpretation of the regional or, in this case, local tectonic setting and rock failure mode.

3.1.1.2 Spatial Fractal Analysis

ZMAP is specialized software developed by the ETHZ (Swiss Federal Institute of Technology – Zurich) for the purpose of analyzing seismic catalogs (Wiemer 2001, Wyss, Wiemer et al. 2001). It enables researchers to quantify seismic risk by calculating recurrence intervals of large earthquakes, fractal dimensions such as the b and D-value in map view, depth, three dimensions, and time, and a host of other statistical and graphical displays of catalog data. We are not concerned with recurrence intervals in the case of microseismic events resulting from hydraulic fracturing due to their man-made nature and close spatio-temporal relationship to injection activities, but fractal dimensions have proven to be most useful in understanding the state of stress at failure of these events and characterizing their interaction with existing geologic structure.

3.1.2 Hydraulic Diffusivity

The microseismic "front", i.e. the distance between the injection source and leading edge of the seismic cloud as a function of time, is controlled by the hydraulic diffusivity of the rock mass. Hydraulic diffusivity can be directly linked to rock permeability if the compressibility and viscosity of the reservoir fluid, reservoir porosity, fluid leak-off coefficient, ambient reservoir pressure, injection pressure, injection rate, and fracture height are known or can be reasonably

estimated (Grechka, Mazumdar et al. 2010). Rothert and Shapiro (2003) describe the triggering front as the boundary between the rock mass experiencing reduced effective stress as a result of increased pore-pressure from injection and the region of baseline effective stress in the un-stimulated rock mass. The back front is the distance between the trailing edge of the pressure front and the injection point as a function of time, measured post shut-in (Figure 12b). It should be noted that Shapiro and others (Shapiro 2015, Hummel and Shapiro 2016) developed this concept of microseismic-front based diffusivity to evaluate geothermal stimulations which are completed by injecting fluid at pressures below the minimum principal stress magnitude. Hence it is reasonable to presume the dominant transport mechanism is diffusion, where the triggering front distance is linearly related to time. Hydraulic fracturing stimulation is completed at pressures exceeding the minimum principal stress in order to overcome the forces keeping fractures closed. In a hydraulic fracture modelling space, the triggering front distance is not linearly related to time and the hydraulic fracture propagation becomes pressure-dependent (as opposed to diffusion-dependent). However, in our study, we found that the linear equations shown below calculate a triggering and back-front that adequately fit the microseismic cloud.

Shapiro, Rothert et al. (2002) define the distance-time relationship of the triggering front by the equation:

$$r_t(t) = \sqrt{(4 * \pi * D_{tf} * t)} \qquad \textbf{Equation 6}$$

where r is the distance from the perforated section of the casing to the event, D_{tf} is the triggering front scalar hydraulic diffusivity, and t is the time elapsed between the start of fluid injection and the microseismic event.

The back front is given by the equation:

$$r_b(t) = \sqrt{(2 * d * D_{bf} * t * [(t / t_s)-1] * ln [t / (t-t_s)])} \qquad \textbf{Equation 7}$$

where r is distance from the perforated section of the casing to the event, d is the dimensionality of the pressure diffusion model (1, 2, or 3 dimensional), D_{bf} is the back front scalar hydraulic diffusivity, t is the time elapsed between the start of fluid injection and the microseismic event, and t_s is the shut-in time.

We have rearranged the above equations to calculate D_{tf} directly for each event and D_{bf} for events occurring after shut-in, enabling us to contour D within the cloud of events on the r-t plot (Figure 12a). In this way, a best-fit triggering front and back front is visualized quickly, requiring no previous knowledge of the diffusivity of the rock mass.

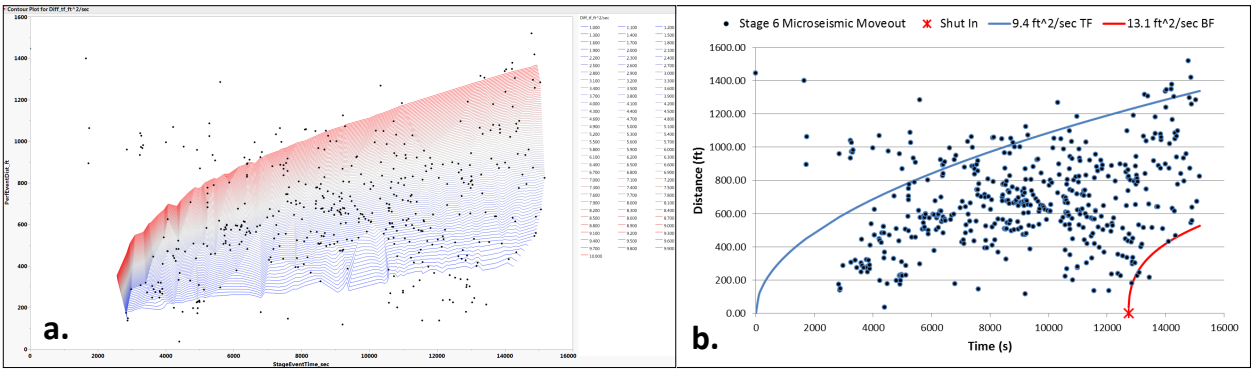

Figure 12 – a) r-t plot from Clearfield – Stage 6 showing microseismic events contoured by the triggering front diffusivity value. With this method, it is straightforward to visualize the best-fit contour in the cloud. b) The triggering and back-front picked using the contour method shown in (a.)

3.1.3 Microseismic and Fracture Formation Energy

Kanamori (1977) described the radiated seismic energy (E_{out}, in joules) and seismic moment (M_o, in N-m) of an earthquake as a function of the moment magnitude, Mw, with the following equations:

$$E_{out} = 10^{(1.5 * Mw + 4.8)}$$ **Equation 8**

$$M_o = 10^{(1.5 * Mw + 9)}$$ **Equation 9**

The calculation of fracture formation energy (energy required to create a fracture) follows Boroumand and Eaton (2012). The microseismic cloud can be used to estimate the area of the fracture created during a single stage. The cloud can be treated as one or multiple fractures, depending upon the resolution of the data. D-value analysis can give some quantitative insight into the spatial arrangement of the microseismicity.

$$E_f = P_d * A_f * w * 1.356$$ **Equation 10**

where w = width of the fracture. E_f = energy (joules) required to create a fracture of area A_f (ft^2). P_d = average down-hole pressure (treatment pressure at the perforation) in lb/ft^2. This information can be obtained from the operator or calculated from surface pressure relationships. Boroumand and Eaton (2012) report that a width of 0.016 – 0.082 feet is typical of a fracture that is wide enough to accept proppant. In this study, we use the conservative case of a single fracture, 0.016 feet wide.

The calculation of fluid energy input (E_{in}, in Joules), following Boroumand and Eaton (2012), requires knowledge of the pumping rate (R, in ft^3/min), pumping pressure at the surface (P, in lb/ft^2), and the pumping duration (t, in minutes). Use average values of pumping rate and pumping pressure for the entire pumping duration.

$$E_{in} = R * P * t * 1.356$$ **Equation 11**

The calculation of seismic energy, fracture formation energy, and fluid energy input can help us to understand the energy balance of hydraulic fracturing. Figure 12 shows the calculated energy values for all stages of a single well at Greene County and the percentage of injected energy accounted for by microseismic radiation and theoretical fracture formation energy. Not

accounting for losses to friction and other sources, over 75% of the input energy is not expressed as a microseismic event or a generated fracture, giving rise to the notion that there are aseismic deformation mechanisms at work (Boroumand and Eaton 2012, Zoback, Kohli et al. 2012).

3.1.4 Microseismic Cloud Analysis

The microseismic cloud offers us the first insight into the behavior of the subsurface during hydraulic fracturing. Microseismic events will largely propagate in the direction of maximum horizontal stress ($S_{h\text{-}max}$) if there is a stress differential (i.e., σ1-vertical > σ2-horizontal > σ3-horizontal), due to the minimum resistance to fracture opening in the direction of minimum horizontal stress. As a result, the microseismic cloud can provide a fairly accurate estimate of the $S_{h\text{-}max}$ orientation.

The presence of faults and open fractures can affect the placement of fracturing fluid into the formation. A well-established system of pre-existing fractures will tend to control the overall pattern of microseismicity as these fractures serve as lower-resistance pathways for fluid flow, though new fractures may be formed that connect pre-existing structures to each other. More dominant structures such as faults can direct large amounts of hydraulic energy out of the zone of interest, resulting in a less effective fracturing operation. In addition, faults can act as boundaries to fluid and pressure, preventing the uniform placement of fracturing fluid and proppant in the reservoir. As such, faults tend to be avoided by constraining a horizontal well within the boundaries of a fault block or arranging the stages and perforations to straddle a fault.

The Clearfield County dataset provided the opportunity to calculate a directional distribution of events on a stage-by-stage basis using GIS, to constrain the direction of maximum horizontal stress and also changes to this direction over the length of the lateral well. The Greene

County dataset, due to its single vertical monitoring array, allowed for azimuthal energy analysis to constrain the dominant microseismic focal plane orientation.

In addition to providing $S_{h\text{-}max}$ orientation, the microseismic cloud can be treated as a vertical or lateral distribution of microseismic properties (magnitude, event count) that are correlated with rock mechanical properties (elastic moduli, Poisson's ratio, brittleness). The Clearfield dataset contained both a vertical and lateral well log which were compared to the cloud and analyzed in a cross-plot space.

3.1.4.1 Vertical Variation of Rock Properties and Microseismicity

Accumulated seismic energy, stress drop, and event count in each fracturing stage can be normalized to a 100% scale and binned by elevation. Viewed along with the event magnitude vs. elevation, this examination of the data gives insight beyond a total quantity and allows us to see the vertical distribution of microseismic activity and how it evolves through the entire job. If well logs are available, they can be related to vertical microseismic data distributions through direct side-by-side comparison or three-axis cross-plots. Well logs offer direct readings of rock properties such as gamma emission, sonic velocity, density, porosity, and elastic constants (Young's, bulk, and shear modulus, and Poisson's ratio).

In order to directly compare properties of the microseismic catalog such as event magnitude and event count to the geophysical well logs, the microseismic cloud was sampled using a five foot vertical window that was advanced through the cloud at the same interval and elevation as the well logs. The moment magnitude of events within the window at each sampling point was averaged to create a moment magnitude "log". The number of events within the moving window at each sampling point was also used to create an event count "log". The benefit of matching the sampling interval and elevation of the geophysical logs to the microseismic logs

is gaining the ability to compare data in a three-axis cross plot space, e.g. Young's modulus versus Poisson's ratio colored by moment magnitude.

Following are definitions and equations for seismic energy and stress drop. Microseismic event magnitude is reported as Mw (moment magnitude). Kanamori (1977) showed that:

$$log_{10}(E_{out}) = 1.5 * Mw + 4.8 \quad \textbf{Equation 12}$$

rearranged, gives:

$$E_{out} = 10^{(1.5 * Mw + 4.8)} \quad \textbf{Equation 13}$$

where E_{out} is the total energy output, or radiated energy (s + p-wave energy, or $E_s + E_p$) of the microseismic event in joules and Mw is the moment magnitude of the microseismic event.

Stress drop, or the stress release on a fracture resulting from a change in the state of stress at the source location (Urbancic, Maxwell et al. 2002), was described in detail by Aki (1967) and Brune (1970) and is calculated by the following equations:

$$r = (2.34 * V_s) / (2 * f_o) \quad \textbf{Equation 14}$$

and

$$\Delta\sigma = (7 * M_o) / (16 * r^3) \quad \textbf{Equation 15}$$

where r is the source radius (which must be calculated first), V_s is the shear wave velocity of the fractured media, f_o is the corner frequency of the shear wave frequency spectrum (Figure 13), M_o is the seismic moment, and $\Delta\sigma$ is the stress drop (Mooney 1989).

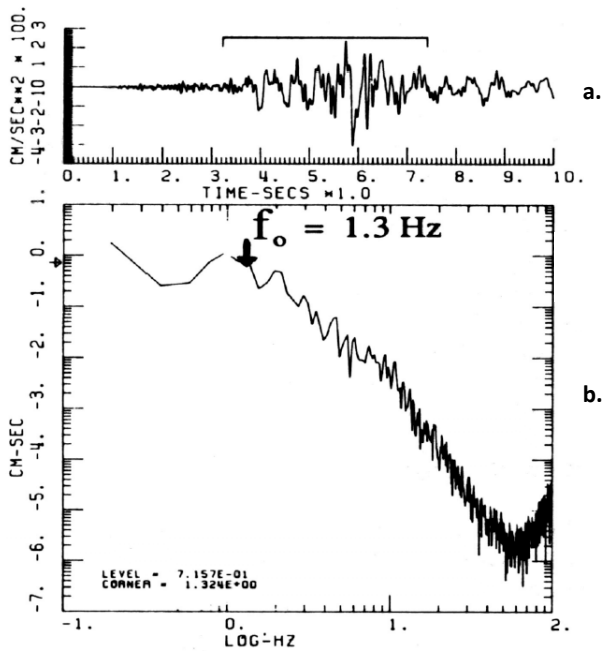

Figure 13 – Seismogram (a.) and corresponding frequency spectrum (b.) of a microearthquake. Modified from Mooney (1989).

The energy release of a seismic event is related to the magnitude by Equation 13, above, and for an increase in magnitude of 1.0, there is a corresponding exponential increase in energy release of 31.6 times. For example, a magnitude 1.0 event releases ~ 2E6 Joules of energy; a magnitude 2.0 event releases ~ 63E6 Joules; and a magnitude 3.0 event releases ~ 1995E6 Joules. Simply comparing the cumulative seismic energy release of hydraulic fracturing stages as a measure of effective stimulation can be misleading as a few large events can release the same energy as numerous small events. Viewing the average magnitude and event count alongside the energy release will provide information about the energy distribution of microseismic events and show that this distribution is not constant throughout the vertical extent of the stimulated rock volume.

Sedimentary sequences such as those within the Appalachian Basin comprise sandstone, shale, limestone, and other lithologies with differing geomechanical properties and even different

states of stress. For example, in comparing shale with an overlying limestone, the shale generally will have a lower density, lower sonic velocity, lower elastic modulus, higher Poisson's ratio and higher porosity than the limestone, and be less prone to fracturing in a brittle manner. In addition, the shale could be under a lower overall state of stress due to its ability to deform and redistribute stresses more efficiently than the limestone. Although the stronger limestone may serve as a barrier to fluid flow and deformation, failures that do occur will be of a different character than those within the shale. Pre-existing faults and fracture networks can also serve to focus or distribute hydraulic energy, respectively.

The robust stress drop measurement is complimentary to seismic energy and event count in that it can add information about the state of stress of the rock upon failure and whether new fractures are being created or existing fractures are being stimulated. Urbancic, Maxwell et al. (2002) compare the stress drop in cases of failure on existing open fractures and failure in un-fractured rock or on tight existing fractures. Microseismic events are generated on pre-existing open fractures simply by increasing the pore pressure, thereby reducing the resisting normal stress. As the fracture is already at equilibrium with any driving (shear) stresses present, this decrease in resisting stress will cause re-equilibration (a microseismic event) and a minimal amount of stress release (stress drop). A tightly closed, healed fracture or an un-fractured rock-mass will behave differently in response to hydraulic fracturing due to the higher yield strength and the larger buildup of driving stresses. In an open fracture, only the normal stress (σ_3 or S_h min) must be overcome in order to cause a microseismic event, whereas intact rock presents the additional challenges of overcoming the strength of the rock itself (shear, compressive, and tensile) or frictional coefficients of the tightly closed fractures. This results in a greater overall stress release upon formation of the fracture.

3.1.4.2 Lateral Variation of Marcellus Properties and Microseismicity

Evaluating the absolute quantity of microseismic events, seismic energy, and stress drop on a stage by stage basis (Figure 14) can be useful for evaluating the effectiveness of the stimulation as the job progresses. The amount of apparent work done on the rock mass in the form of brittle microseismic failure can vary from stage to stage and is controlled by the presence or absence of pre-existing fractures and faults, the geomechanical properties and stress state of the rock, the pumping schedule, equipment sensitivity, and other less well-understood reasons. If event count and energy is treated as a proxy for deformation or stimulation then we can begin to quantify the effectiveness of each stage and deduce reasons for the variation such as open fluid pathways that prevent sufficient pore pressure increase or lateral stress variations that concentrate fracture initiation to only a few perforations. Of course, other data are necessary for a more complete understanding such as high resolution pumping data and geomechanical well logs.

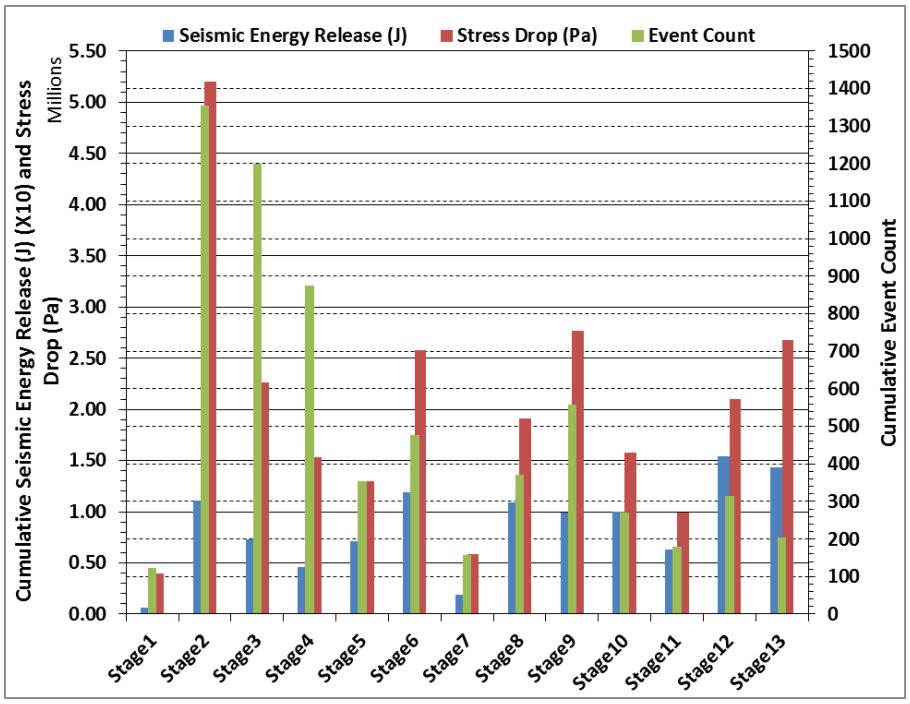

Figure 14 – Cumulative energy release, stress drop, and event count per stage at Clearfield.

A vertical well log crossing stratigraphic boundaries is a useful tool for estimating rock properties to compare with vertically changing microseismic parameters such as magnitude, energy, stress drop, and event count, as described in the section above. However, this vertical log only presents a small window of observation into the surrounding rock mass. A lateral well log residing wholly within one stratigraphic unit, in this case the Lower Marcellus Shale, offers thousands of linear feet of observation and can shed light on the complex geomechanical changes within an unconventional reservoir.

In much the same way that the vertical well logs were compared to the vertical distribution of microseismic data by employing a "moving window average" of microseismic values at the same sampling interval as the logs, the relationships between the lateral well logs and microseismic data were analyzed. The difference between the two workflows arises from the fact that the lateral well log represents properties of only the Lower Marcellus Shale; as such the comparison is only valid for microseismic data within the Lower Marcellus Shale. In order to accommodate this condition, microseismic values were sampled using an inclusive modified sphere moved along the well at the same sampling interval as the well logs. For example, a sphere of 100-foot-radius centered on a point along the well will include all data within 100 feet of the well in all directions. Where the sphere crosses the stratigraphic boundaries of the Lower Marcellus it is truncated to exclude outlying data. A 100-foot-radius sphere was sufficient to adequately sample the microseismic properties of the shale, avoid over-averaging too large a volume, and remain representative of the in-situ rock properties characterized by the well logs. An exercise was performed in which the microseismicity was sampled with 20, 40, 60, 80, and 100-foot-radius spheres, as a sensitivity analysis, to verify that the relative distribution of microseismic properties remained similar at these different radii (Figure 15).

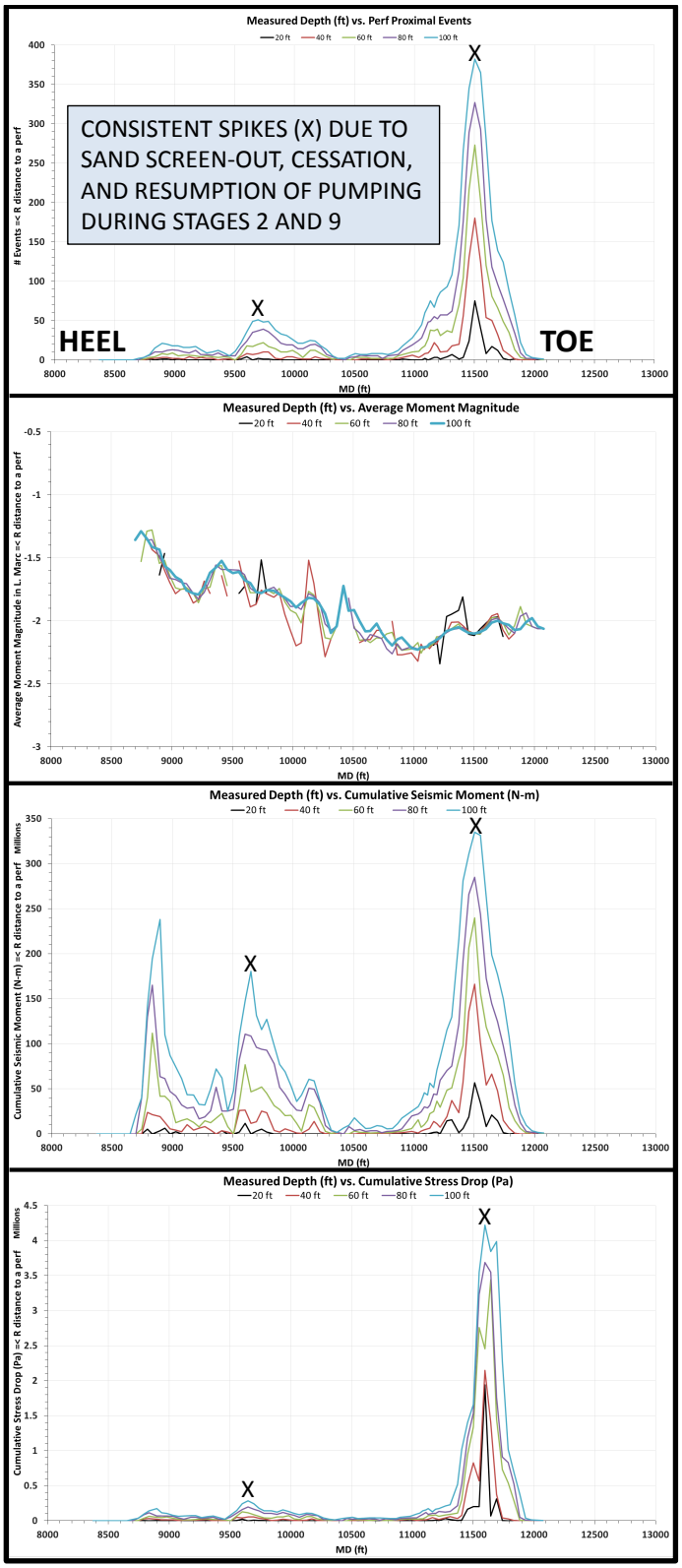

Figure 15 – Results of distance sensitivity analysis verify that event count, stress drop, moment magnitude, and energy release remain relatively consistent along the lateral well bore out to 100 feet radial distance.

3.2 GREENE COUNTY MICROSEISMIC STUDY – SPE MANUSCRIPT

SPE-168647-MS

Time Dependent b and D-values, Scalar Hydraulic Diffusivity, and Seismic Energy From Microseismic Analysis in the Marcellus Shale: Connection to Pumping Behavior During Hydraulic Fracturing

Erich V. Zorn*, SPE, University of Pittsburgh, NETL-Regional University Alliance (RUA); Richard Hammack, US DOE-NETL; William Harbert, SPE, University of Pittsburgh, NETL-RUA

3.2.1 Introduction

The most accessible product of microseismic monitoring during hydraulic fracturing is the 3-dimensional seismic cloud around the wellbore. To realize the benefit of microseismic monitoring, we must quantify the data seismologically, spatially, and spatio-temporally, and compare this with pumping data and energy input/output to/from the system. Our goal is to quantify meaningful correlations between the fractal dimensions b (frequency-magnitude; <1 = compression, 1 = shear, >1 = tension) and D (spatial clustering; 0 = point, 1 = line, 2 = plane, 3 = cloud), calculated from microseismic data collected in the Marcellus Shale of Southwestern Pennsylvania. Limitations are related to the sensitivity and geometry of the acquisition system, which affects microseism coordinates (and any calculated distances), magnitudes, signal/noise ratios, and energy arrivals.

We illustrate the evolution of b and D as a function of time through four stages, with between 328 and 1048 events per stage. In addition we compute the hydraulic diffusivity triggering front for each stage using time-distance plots and diffusivity contouring, the cumulative seismic energy and the s and p-wave energy components for each of the five stages. Plotting b, D, and diffusivity values as well as pumping pressure, slurry rate, proppant concentration, and seismic energy release against time will shed light on the complex down-hole interactions between fluid and rock that create and propagate fractures. In all stages, we see correlation between the b and D-values, but it is not consistently positive or negative throughout any stage. Changes in the correlation are accompanied by a change in pumping pressure, rate, and the frequency of microseismic events. An intriguing observation is a correlation between abrupt increases in total s-wave energy and decreasing b-value.

In addition, we introduce the concept of slow slip seismicity during hydraulic fracturing in the Marcellus Shale and its importance to the reservoir stimulation process. A preliminary analysis of data collected by a 2 Hz, three-component seismometer at the surface indicates the presence of this phenomenon and creates an opportunity to extend this research into the Appalachian Basin.

3.2.2 Project Site Background

In mid-2012, six horizontal wells in Southwestern Pennsylvania were drilled and hydraulically fractured in the Marcellus Shale over 56 stages, using a "zipper-frac" configuration. Microseismic monitoring was completed by deploying eight geophones down two existing vertically oriented deep wells, but only one well at a time was used; first the three western laterals were monitored and then the three eastern laterals. Moreover, a 2 Hz, three-component

seismometer was placed at the surface within the extent of the laterals to passively monitor throughout the fracturing process. A total of 10,288 microseismic events were recorded at the geophones over the course of treatment, ranging between moment magnitude M -3.15 and M -0.56. This study will focus on four of these stages, with between 328 and 1048 events/stage (Figure 16). The green arrow points to the north, and notice that the microseismic clouds are elongated in a northeast-southwest orientation.

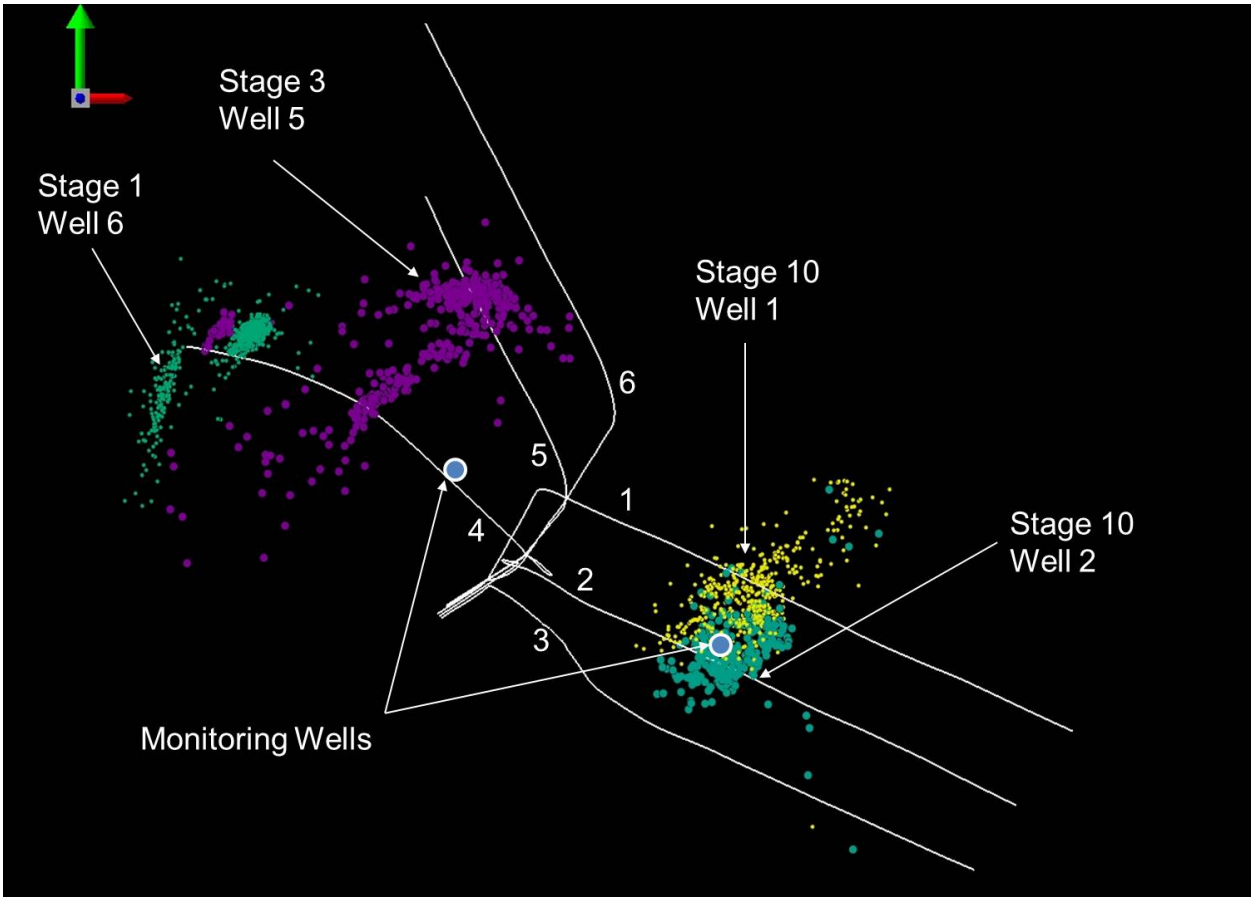

Figure 16 – Map view of six laterals, numbered 1-6, monitoring well locations, and the microseismic events associated with the four stages analyzed in this study. Green arrow points to the north.

3.2.3 Theory and Definitions

3.2.3.1 Fractal Properties of Microseismics

Naturally occurring processes frequently adhere to power-law distributions, specifically, the frequency-magnitude distribution of seismic events has been shown to follow the Gutenberg-Richter relation (Gutenberg and Richter 1944), given by:

$$log_{10} N(m \geq M) = a - b * M \quad \textbf{Equation 16}$$

where $N(m \geq M)$ is the number of events whose magnitude, m, is greater than or equal to M, and b is the absolute value of the slope of the linear portion of the distribution, taken to be an indicator of the dominant stress regime, and thus failure mode of the seismic events (Grob and van der Baan 2011). A b-value < 1 indicates a higher proportion of larger events and is thought to be indicative of a compressive stress regime (reverse faulting or fracture closing). A b-value ~1 is thought to be indicative of a shear stress regime (strike-slip faulting). A b-value > 1 indicates a higher proportion of smaller events and is thought to be indicative of a tensile stress regime (normal faulting or tensile fracture opening) (Grob and van der Baan 2012).

Another property of seismicity that has been shown to follow a power-law distribution is the D-value, a spatial distribution analysis that quantifies the shape and clustering of seismic event clouds, giving insight into the natural weaknesses in the fractured rock (Grob and van der Baan 2011). This relationship is given by:

$$log_{10} N(r < R) = a - D * log_{10} R \quad \textbf{Equation 17}$$

where $N(r < R)$ is the number of unique event pairs whose separation distance, r, is less than R, and D is the slope of the linear portion of the distribution. Following Grob and van der Baan (2012), a D-value = 0 indicates a clustering of events at one point in space; a D-value = 1

indicates a linear clustering of events; a D-value = 2 indicates a planar distribution; and a D-value = 3 indicates a uniform distribution in space (a cloud).

3.2.3.2 Hydraulic Diffusivity

Moving beyond the statistical b and D-value analyses, we will examine the concept of apparent hydraulic diffusivity, derived from mapping the microseismic "front", i.e. the distance between the injection source and outer envelope of the seismic cloud as a function of time. Rothert and Shapiro (2003) describe this front as the boundary between the rock mass experiencing reduced effective stress as a result of increased pore-pressure from injection and the region of baseline effective stress in the un-stimulated rock mass.

Large microseismic datasets from hydraulic fracturing operations offer the opportunity to measure this important rock parameter, which can be directly linked to rock permeability if the compressibility and viscosity of the reservoir fluid, reservoir porosity, fluid leak-off coefficient, ambient reservoir pressure, injection pressure, injection rate, and fracture height are known or can be reasonably estimated (Grechka, Mazumdar et al. 2010). Diffusivity is defined as the ratio of hydraulic conductivity to storativity of a medium, and can be graphically represented by a best-fit parabola upper-bounding the majority of seismic events on an r-t plot, where r is the distance between the event and the injection source or perforated section, and t is the time since the start of injection. This parabola and the one defined by the spatio-temporal distribution of post-injection events have been termed the Triggering Front and Back Front, respectively, and have been investigated by a small group of researchers over the last ~15 years (Shapiro, Huenges et al. 1997, Shapiro, Rothert et al. 2002, Grechka, Mazumdar et al. 2010, Hummel and Shapiro 2012, Angus and Verdon 2013). Shapiro, Rothert et al. (2002) define the distance-time relationship of the triggering front by the equation:

$$r_t(t) = \sqrt{(4 * \pi * D * t)} \quad \textbf{Equation 18}$$

where r is distance from the perforated section of the casing to the event, D is the triggering front diffusivity, and t is the time elapsed between the start of fluid injection and the microseismic event. The back front is given by the equation:

$$r_b(t) = \sqrt{(2 * d * D * t * [(t / t_s)-1] * \ln [t / (t-t_s)])} \quad \textbf{Equation 19}$$

where r is distance from the perforated section of the casing to the event, d is the dimensionality of the pressure diffusion model (1, 2, or 3 dimensional), D is the back front diffusivity, t is the time elapsed between the start of fluid injection and the microseismic event, and t_s is the shut-in time. It should be noted that in order to calculate the diffusivity back front, there must be post shut-in microseismic events recorded. In this study, we were only able to calculate a preliminary diffusivity back front value for Stage 3 of Well 5 (Stage 5_3).

3.2.3.3 Energy Calculation and Insight into Energy Balance

The calculation of seismic energy output is valuable in two ways; it can be correlated to changes in the b and D-value curves and it can be compared to hydraulic energy input and fracture formation energy to shed light on the efficiency (or lack thereof) of hydraulic fracturing (Boroumand and Eaton 2012). Our study will confirm that seismic energy output in the form of microseisms is approximately 7 orders of magnitude less than the energy put into the system in the form of fracturing fluid (10^3 – 10^5 Joules as compared to 10^{11} Joules, respectively) and fracture energy is one order of magnitude smaller than injection energy. These energy losses are presumably a result of viscous fluid flow into discontinuities and friction between the fluid and the well casing. We also have to acknowledge that not all microseismic events were detected, and examination of a frequency-magnitude distribution will reveal the magnitude of completion of the seismic catalog. In addition to these sources of energy loss, we propose that slow slip

seismic events, which are not registered as traditional microseisms during microseismic monitoring, could account for a significant portion of this "lost" energy. This deformation of the rock results in no brittle failure but is seen as an important stimulation mechanism in shale gas reservoirs and is recognized by long period, long duration seismic signals in the records of surface seismometers (Brown, Tryon et al. 2005, Zoback, Kohli et al. 2012).

3.2.4 Methods

3.2.4.1 Fractal Dimensions

The b-value is based only upon the frequency of event magnitudes in a seismic catalog, so a simple binning function can be used to calculate the number of events whose magnitude is greater than or equal to the bin value. In other words, if the smallest event is magnitude -3.1, then the -3.1 bin will contain all events in the catalog, and larger bin values will contain successively smaller numbers of events until the maximum magnitude is reached. A plot of the $\log_{10}$ value of the number of events in the bin on the ordinate, versus the corresponding bin value on the abscissa is the source of the b-value of the catalog of events.

The D-value analysis requires calculation of the distance between all possible unique pairs of events in the seismic catalog. Three dimensional distance, *r*, between two points, *a* and *b*, is calculated using the Euclidian distance equation:

$$r\,(a \rightarrow b) = \sqrt{[(x_a-x_b)^2 + (y_a-y_b)^2 + (z_a-z_b)^2]} \qquad \textbf{Equation 20}$$

where *x*, *y*, and *z* are the coordinates of each point in space. The number of possible unique pairs, *P*, is given by the following equation:

$$P = (x^2-x) / 2 \qquad \textbf{Equation 21}$$

where x is the total number of events in the catalog of interest. Next, a binning function is executed which calculates the number of pairs, N, whose separation distance, r, is less than the bin value, R. The $\log_{10}$ of the number of pairs in each bin, N, is plotted on the ordinate, versus the $\log_{10}$ of the corresponding bin distance value, R, on the abscissa; this curve is the source of the D-value of the event cloud.

Both b and D-values can be calculated for the entire stage, resulting in one value for each parameter (Figure 17**;** Figure 18). In this study, our goal was to study the evolution of b and D through time by sub-setting the dataset into blocks of 100 events (the minimum for a robust fractal analysis of this sort, from Öncel and Wilson (2004)), overlapping by 70 to 80 events and moving this window through the stage. In this way we are able to see sub-stage level changes in the mechanism of failure and the spatial arrangement of events throughout the course of injection. In addition, all pertinent injection activity was recorded to one second resolution, including pumping pressure, slurry rate, and proppant concentration. Plotting this information alongside b, D, diffusivity, event magnitude, source-event distance, and seismic energy enables us to observe what, if any, correlation exists between injection parameters at the surface and the microseismic response of the rock mass.

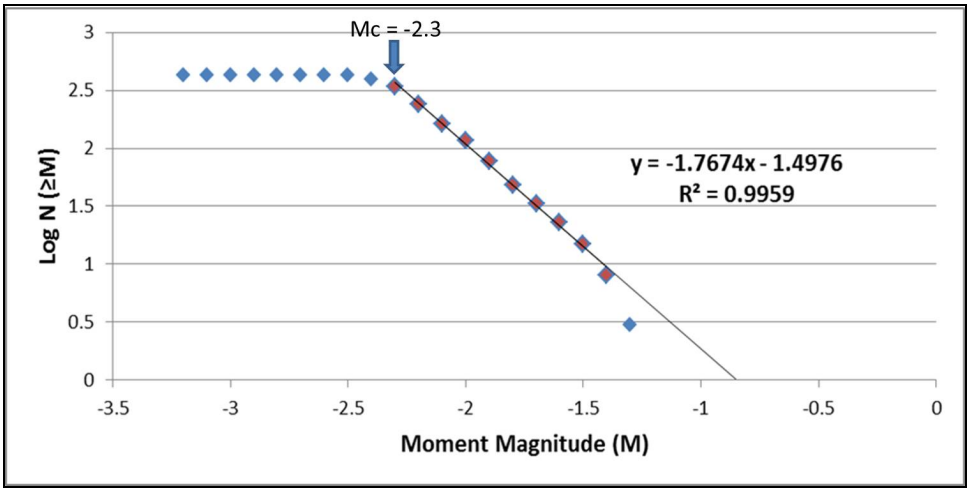

Figure 17 – Example frequency-magnitude plot for the calculation of b-value. The b-value is the absolute value of the slope of the best-fit line within the complete seismic catalog. Magnitude of completion is -2.3.

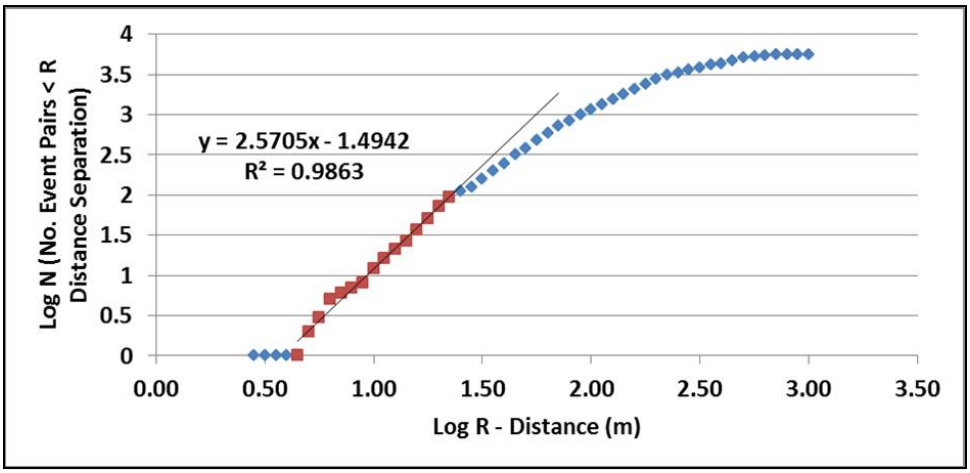

Figure 18 – Example frequency-distance separation plot for the calculation of D-value. The D-value is the slope of the best-fit line through the data "below" the first major inflection point.

3.2.4.2 Hydraulic Diffusivity

The apparent scalar hydraulic diffusivity (*D*) estimate is derived by plotting the seismic events on an r-t plot. First, the distance between the event and the point of injection must be calculated using Equation 20. Shapiro, Rothert et al. (2002) first estimate the diffusivity of the rock mass

and then calculate *r* in Equation 18 and Equation 19 by inputting values for *t*, repeating until a best-fit curve is achieved. We have rearranged Equation 18 and Equation 19 to calculate *D* directly for each event, enabling us to contour *D* within the cloud of events on the r-t plot. In this way, a best-fit triggering front and back front is visualized quickly, requiring no previous knowledge of the diffusivity of the rock mass (Figure 19).

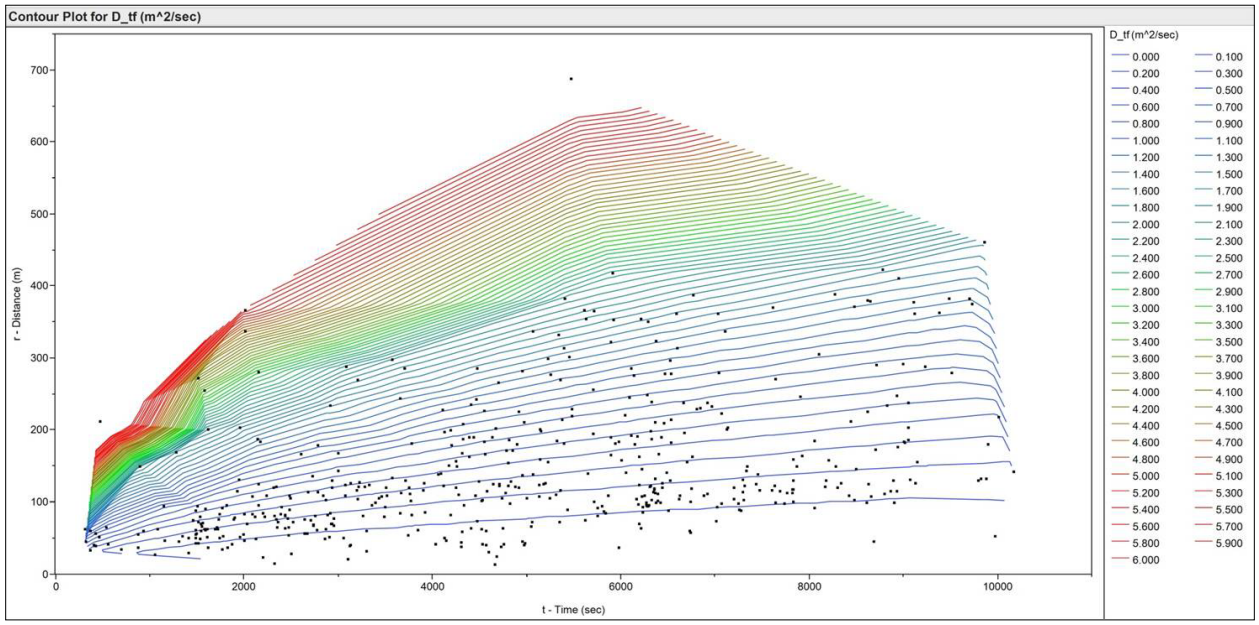

Figure 19 – Example plot showing microseismic events contoured by the triggering front diffusivity value. With this method, it is straightforward to visualize the contour which serves as the best-fit envelope of the cloud.

3.2.4.3 Energy Calculations

Microseismic event magnitude is reported as Mw (moment magnitude). Kanamori (1977) showed that:

$$log_{10}(E_{out}) = 1.5 * M_w + 4.8 \qquad \textbf{Equation 22}$$

We can rearrange to give:

$$E_{out} = 10^{(1.5 * Mw + 4.8)} \quad \textbf{Equation 23}$$

where E_{out} is the total energy output, or radiated energy (s + p-wave energy, or $E_s + E_p$) of the microseismic event in joules and *Mw* is the moment magnitude of the microseismic event. Add energy values of all microseismic events to give cumulative seismic energy released during the stage. If the Es/Ep ratio is known, then:

$$E_s = (E_{out} / [(E_s / E_p)+1]) * (E_s / E_p) \quad \textbf{Equation 24}$$

and,

$$E_p = E_{out} - E_s \quad \textbf{Equation 25}$$

The calculation of fluid energy input (E_{in}) following Boroumand and Eaton (2012) requires knowledge of the pumping rate (R), pumping pressure at the surface (P), and the pumping duration (t) and is simplified by converting all units to feet, pounds, and minutes to give energy in joules, so:

1 bbl (blue-barrel) = 42 gal → 1 gal = 0.134 ft^3

Psi (lb/in^2) should be converted to psf (lb/ft^2), so: 1 ft^2 = 144 in^2

$$E_{in}\ (ft\text{-}lb) = R\ (ft^3/min) * P\ (lb/ft^2) * t\ (min) \quad \textbf{Equation 26}$$

Finally, convert ft-lb to joules by: 1 ft-lb = 1.356 joules and use average values of pumping rate and pumping pressure for entire pumping duration.

The calculation of fracture energy (energy required to create a fracture) follows Boroumand and Eaton (2012). The microseismic cloud can be used to estimate the area of the fracture created during a single stage. The cloud can be treated as one or multiple fractures, depending upon the resolution of the data. D-value analysis can give some quantitative insight into the spatial arrangement of the microseismicity.

$$E_f = P_d * A_f * w * 1.356 \qquad \textbf{Equation 27}$$

where w = width of the fracture, E_f = energy (joules) required to create a fracture of area A_f (ft^2). P_d = average down-hole pressure (treatment pressure at the perforation) in lb/ft^2. This information can be obtained from the operator or calculated from surface pressure relationships. Boroumand and Eaton (2012) report that a width of 5-25 mm (0.016 – 0.082 feet) is typical of a fracture that is wide enough to accept proppant. In this study, we use the conservative case of a single fracture, 0.016 feet wide, and apply it to all stages in Well No. 1, discussed later.

3.2.5 Results and Discussion

3.2.5.1 Well 1, Stage 10

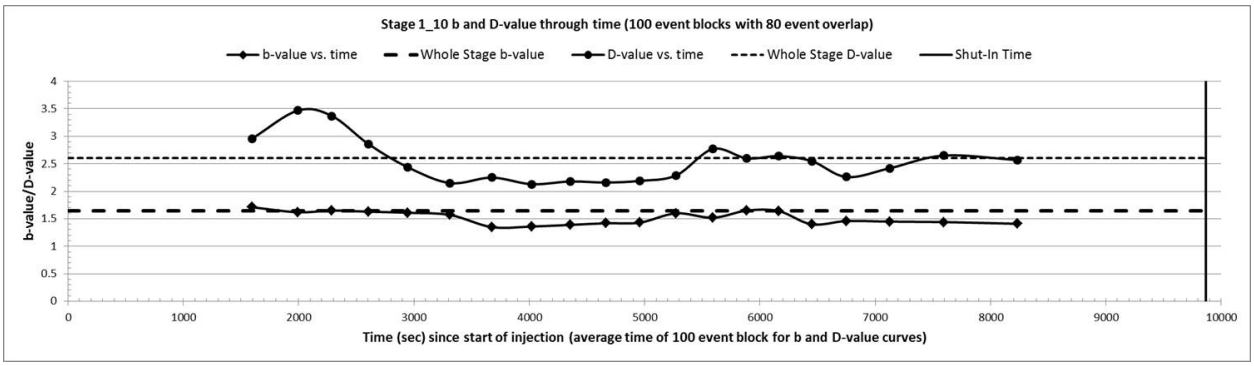

Figure 20 – Evolution of Stage 1_10 b and D-values through time

The b and D-values for Stage 1_10 as a whole, 1.65 and 2.60 respectively (Figure 20), and the microseismic spatial distribution indicate dominant tensile failure and a stress regime in which σ_1 is vertical, σ_2 (S_{h_max}) is horizontal and oriented roughly northeast-southwest (from Figure 16), and σ_3 (S_{h_min}) is horizontal and oriented roughly northwest-southeast. Microseismic events are distributed between a planar orientation and spatial uniformity, perhaps on a series of parallel

planes or fractures (Grob and van der Baan 2012). This is a good indicator of effective hydraulic fracturing and relatively uniform stimulation of the rock mass.

However, the evolution of the b and D-values throughout the stage (Figure 20) indicate that changes are taking place in both values, ranging from b = 1.35 to 1.71 and D = 2.13 to 3.47. Observations include an overall similarity between the shape b and D-value curves, in which D-value highs correspond with b-value highs and vice-versa. Figure 21 shows two distinct perturbations in the pumping pressure and pumping rate at approximately 4700 and 6500 seconds, accompanied by changes in both b and D-value (bold arrow markers on Figure 21). At 4700 seconds, a sharp, temporary decrease in both rate and pressure is accompanied by an increase in b and D from oblique shear and planar microseismic activity to levels more indicative of uniformly distributed tensile failure. At approximately 6500 seconds, the b-value and D-value both decrease to 1.4 and 2.25 respectively, then rebound slightly. These apparent correlations between changes in fractal properties of the microseisms and pumping pressure and rate perturbations reveal quantitatively that the extent of rock mass stimulation is continuously changing throughout hydraulic fracturing.

The diffusivity triggering front seen in Figure 20 represents the 1.9 m^2/sec contour line within the event cloud on an r-t plot (Figure 19). It is a best-fit upper bound of the event move-out from the injection point, below which lie ~97% of the events induced during this stage. The fourteen events that lie above the triggering front, and more specifically the five events that occur greater than 200 meters away from the injection point in the first 2000 seconds of injection, are outliers. They are interpreted to represent events triggered by pressurization of fluids within pre-existing natural fractures or previously opened hydraulic fractures.

As stated earlier, a b-value of 1 is indicative of shear failure at the seismic event locations. Figure 22 shows a correlation between increased total shear wave energy (E_s) radiated by the microseismic events and a corresponding decrease in b-value between ~3500 and 5000 seconds and again between ~6100 and 7700 seconds (between arrows A-A' and B-B' respectively). Though the b-value only falls as low as 1.35, the correlation is worth noting as supporting evidence for the validity of the b-value analysis even at very small magnitudes and in induced seismicity swarms.

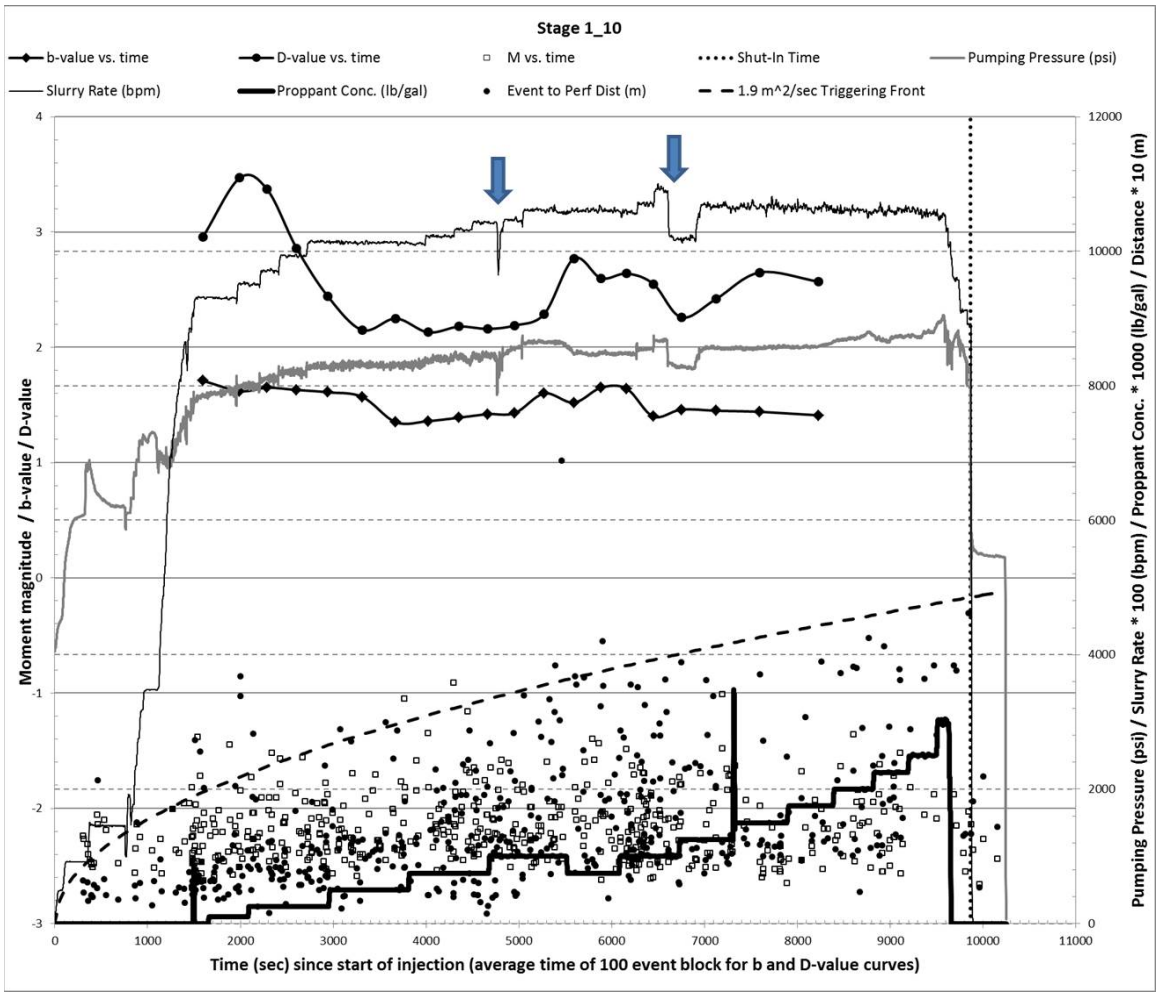

Figure 21 – Plot of Stage 1_10 b and D-values, pumping pressure, pumping rate, proppant concentration, event magnitude, event distance from perforation, and the 1.9 m^2/sec triggering front curve versus time.

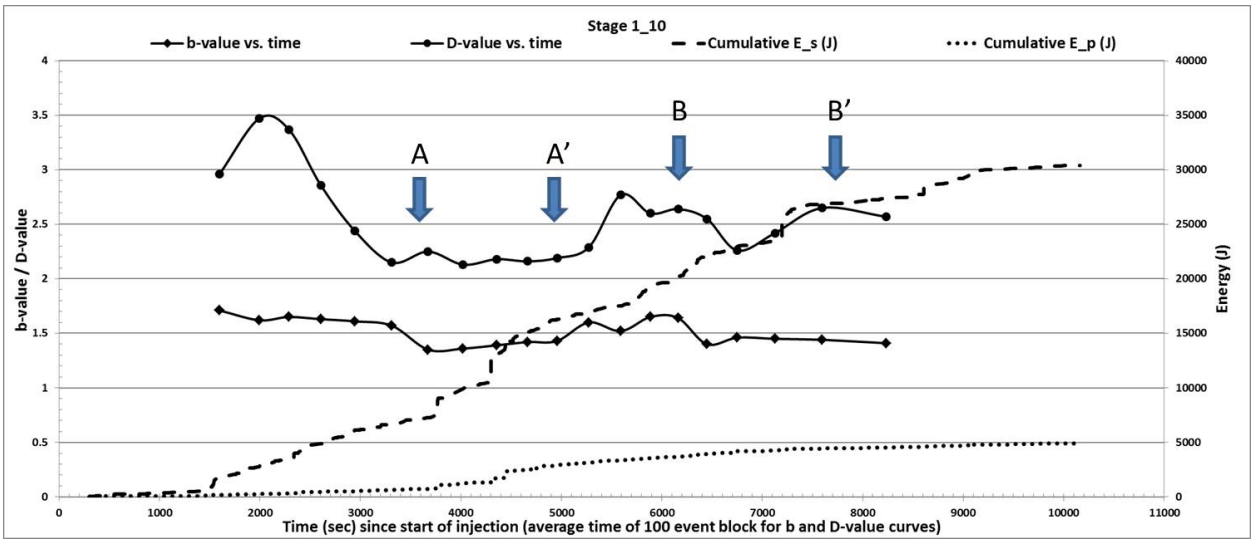

Figure 22 – Plot of Stage 1_10 b and D-values and cumulative s and p-wave energy versus time.

3.2.5.2 Well 2, Stage 10

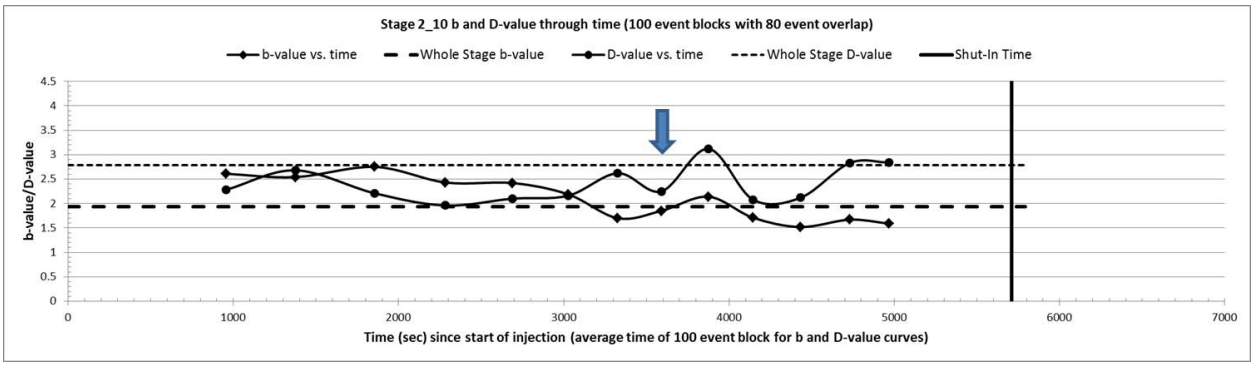

Figure 23 – Evolution of Stage 2_10 b and D-values through time.

The b and D-values for Stage 2_10 as a whole, 1.94 and 2.78 respectively (Figure 23), and the microseismic spatial distribution (Figure 16) indicate dominant tensile failure and a stress regime in which σ_1 is vertical, σ_2 (S_{h_max}) is horizontal and oriented roughly northeast-southwest (from Figure 16), and σ_3 (S_{h_min}) is horizontal and oriented roughly northwest-southeast. Overall, microseismic events are uniformly spatially distributed based upon the D-value.

The evolution of the b and D-values throughout the stage (Figure 23) shows a roughly negative correlation between b and D until ~3600 seconds (arrow on Figure 23). After t = 3600 seconds, the correlation is positive until the end of the stage. It is compelling to note that at ~1700 seconds, there is a decrease in pumping pressure of approximately 400 psi (Figure 24). Over the next 1300 seconds (~22 minutes), the pumping rate is increased stepwise from ~90 bpm to ~97 bpm in order to maintain this lower pressure (A-A' on Figure 24). Coincident with these adjustments in the pumping rate is a gradual decrease in the D-value from 2.6 to 2, indicating a shift in the spatial arrangement of microseisms from uniform to planar. For the remainder of the stage, after the pressure and rate have been stabilized, the D-value varies between 2 and 3 and the b-value varies between 1.5 and 2 (Figure 24). Taken as a whole, it can be inferred that in the first half of the stage, one or two planar features were stimulated and the second half of the stage stimulated smaller hydraulic fractures branching off of the main planes.

The diffusivity triggering front seen in Figure 24 represents the 1.5 m^2/sec contour line within the event cloud on an r-t plot (Figure 19). The 24 events that lie above the triggering front are interpreted to represent events triggered by pressurization of fluids within pre-existing natural fractures or previously opened hydraulic fractures.

Similar to Stage 1_10, Figure 25 shows a correlation between an increase in the total shear wave energy emitted by the microseismic events during Stage 2_10 and a corresponding decrease in b-value after ~3000 seconds into the injection (arrow on Figure 25).

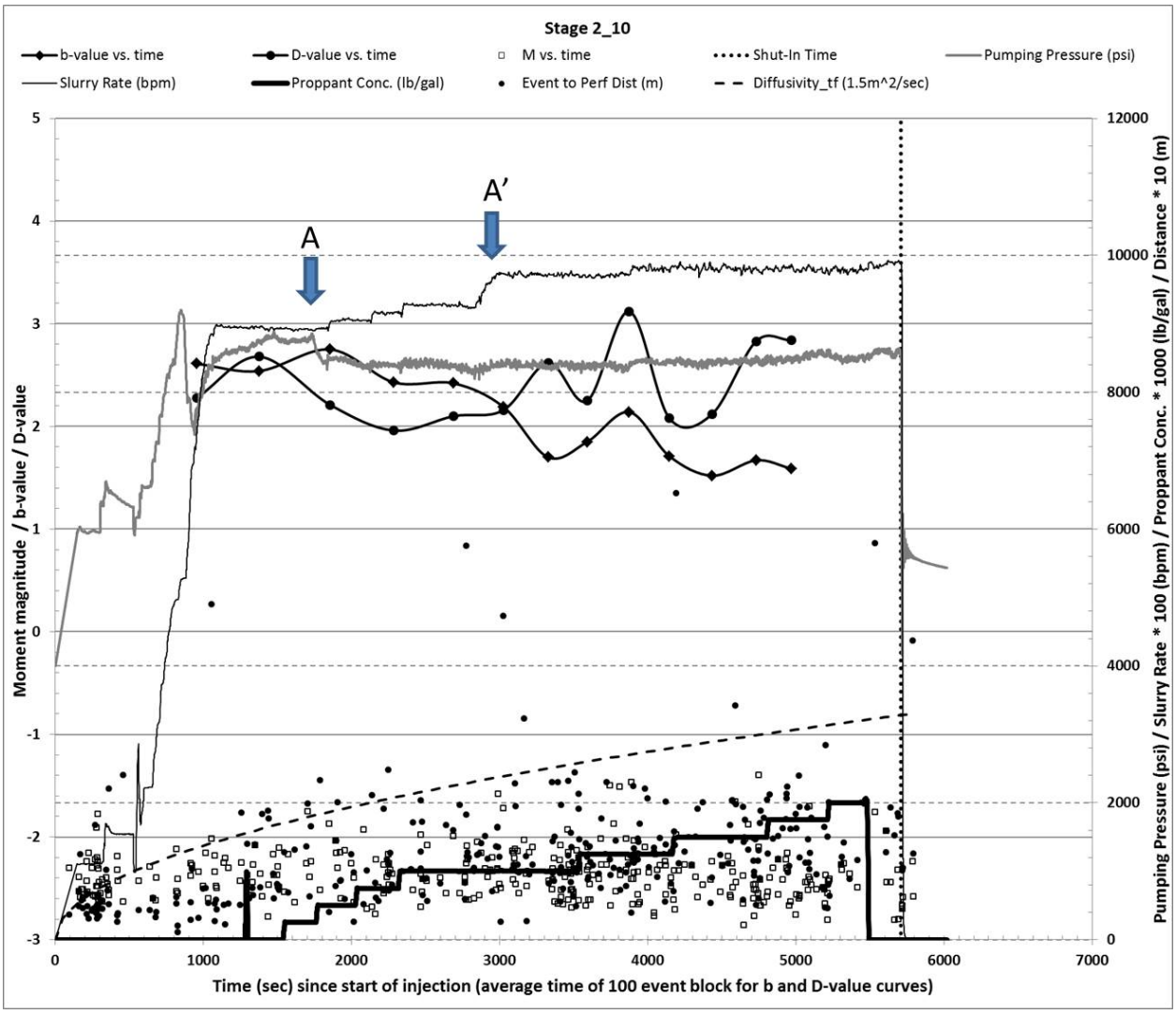

Figure 24 – Plot of Stage 2_10 b and D-values, pumping pressure, pumping rate, proppant concentration, event magnitude, event distance from perforation, and the 1.5 m^2/sec triggering front curve versus time.

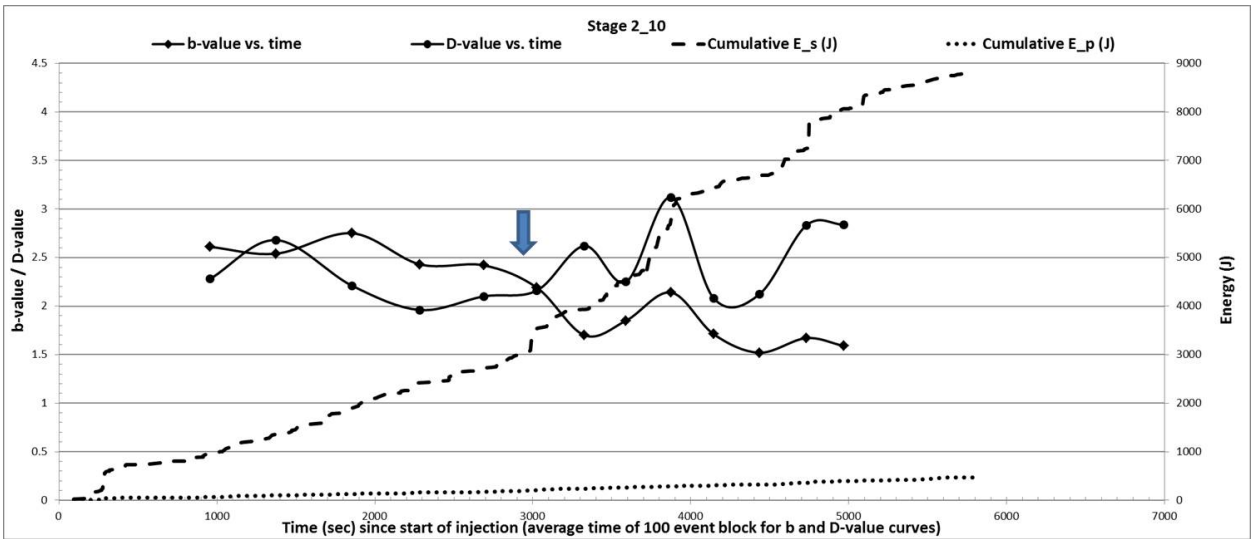

Figure 25 – Plot of Stage 2_10 b and D-values and cumulative s and p-wave energy versus time.

3.2.5.3 Well 5, Stage 3

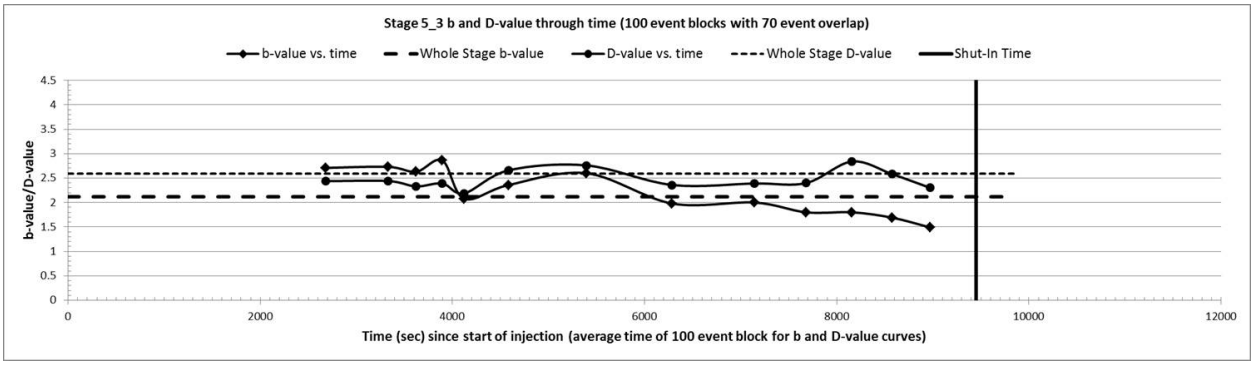

Figure 26 – Evolution of Stage 5_3 b and D-values through time.

The b and D-values for Stage 5_3, 2.12 and 2.59 respectively (Figure 26), indicate overall tensile failure along hydraulic fractures and a stress regime in which σ1 is vertical, σ2 (S_{h_max}) is horizontal and oriented roughly northeast-southwest (from Figure 16), and σ3 (S_{h_min}) is horizontal and oriented roughly northwest-southeast. Microseismic events are generally spatially uniform, with a strong planar component, and the cloud is aligned in the direction of S_{h_max}.

The evolution of the b and D-values throughout the stage (Figure 26) shows remarkable similarity between the curves and positive correlation between b and D throughout the stage. Figure 27 shows that there are numerous small perturbations in the pumping pressure and rate throughout the stage which are difficult to correlate with the b and D-value changes. Starting at ~4000 seconds, the pumping pressure begins to decrease, from approximately 8700 psi to 8000 psi at ~ 6000 seconds (A-A' on Figure 27), at which point the pumping rate is increased stepwise in order to raise the pressure. It is not until the pumping rate has been increased by ~10 bpm (15% increase) that the pressure returns to previous consistent levels. Figure 16 and Figure 27 show two distinct groupings of microseismic events, which could explain the erratic pumping behavior; one group is clustered within a 150 meter radius around the well bore perforation and the second group is more linear in nature and extends between 280 and 840 meters to the southwest of the perforation (encircled clusters in Figure 27). From Figure 27 we can see that this second, linear group begins to more fully develop between 280 and 500 meters distance after ~6000 seconds, which could explain the gradual decrease in b-value to 1.5 during this time period. However, the continued occurrence of spatially uniform, tensile microseisms close to the well bore keeps the b and D-values from wholly reflecting the fluid interaction with this far-reaching discontinuity.

The diffusivity triggering front seen in Figure 27 represents the 2.3 m^2/sec contour line within the event cloud on an r-t plot. This stage offered the opportunity to attempt to model the diffusivity back front as well, due to the presence of a few post shut-in events. Though one would expect the back front diffusivity to be higher than the triggering front, due to the fact that the formation has been fractured and propped, resulting in faster flow of the post shut-in pressure perturbation away from the injection point, the diffusivity back front value of 51 m^2/sec seems to

be abnormally high, and this is likely due to the low number of events used to constrain it. For a more convincing back front value, a higher number of post shut-in events for a longer duration are needed. The 72 events that lie above the triggering front (16% of the total number of recorded events) are interpreted to represent events triggered by pressurization of fluids within pre-existing natural fractures or previously opened hydraulic fractures.

Figure 28 and Figure 29 show an exciting correlation between radiated s-wave energy and b-value. In Figure 28, we can see that the slope of the cumulative s-wave energy curve increases dramatically, accompanied by decreasing b-value, as expected (marked by arrow on Figure 28). However, unlike Stages 1_10 and 2_10 in which we could not link the source of increased s-wave energy with any particular structure, Figure 29 shows that the microseisms with the highest Es/Ep energy ratios follow the diffusivity triggering front after 5000 seconds (encircled cluster on Figure 29). This is the same cluster described above which represents a propagating linear feature between 280 and 500 meters distance from the well bore.

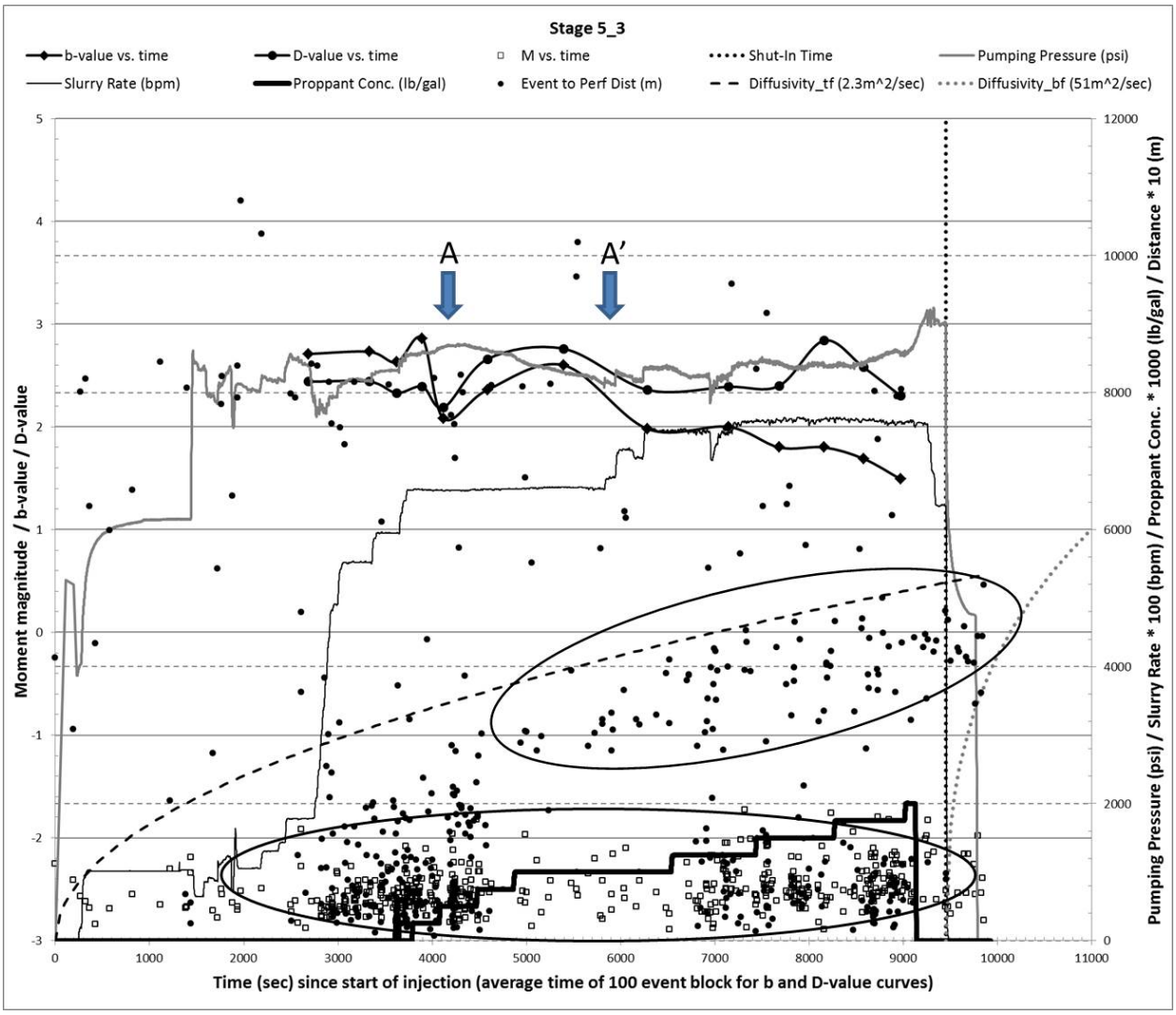

Figure 27 – Plot of Stage 5_3 b and D-values, pumping pressure, pumping rate, proppant concentration, event magnitude, event distance from perforation, the 2.3 m^2/sec triggering front, and the 51 m^2/sec back front curve versus time.

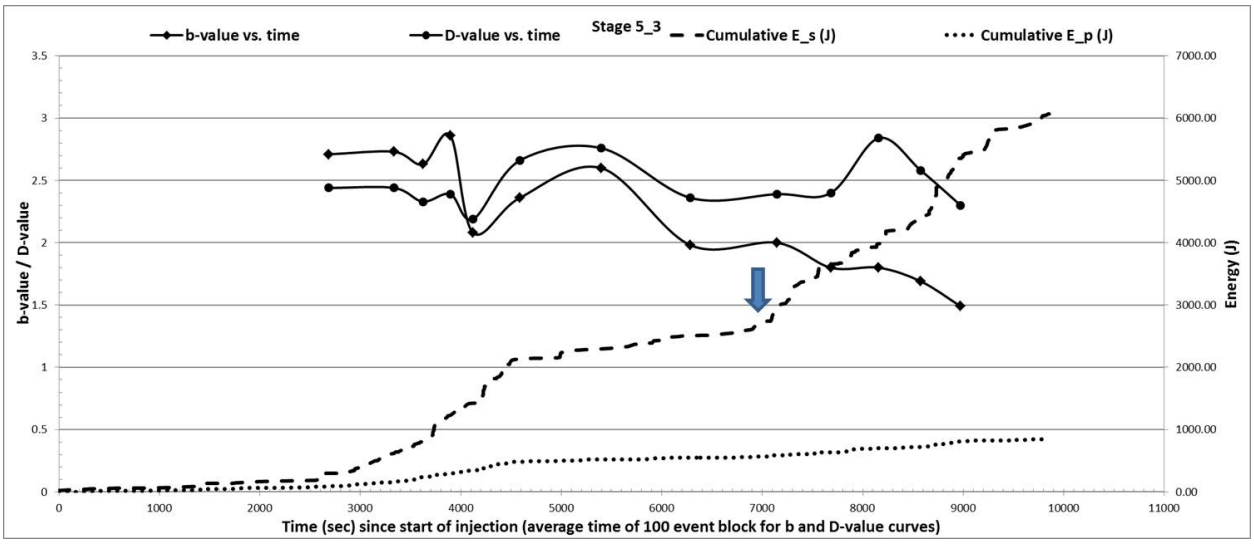

Figure 28 – Plot of Stage 5_3 b and D-values and cumulative s and p-wave energy versus time.

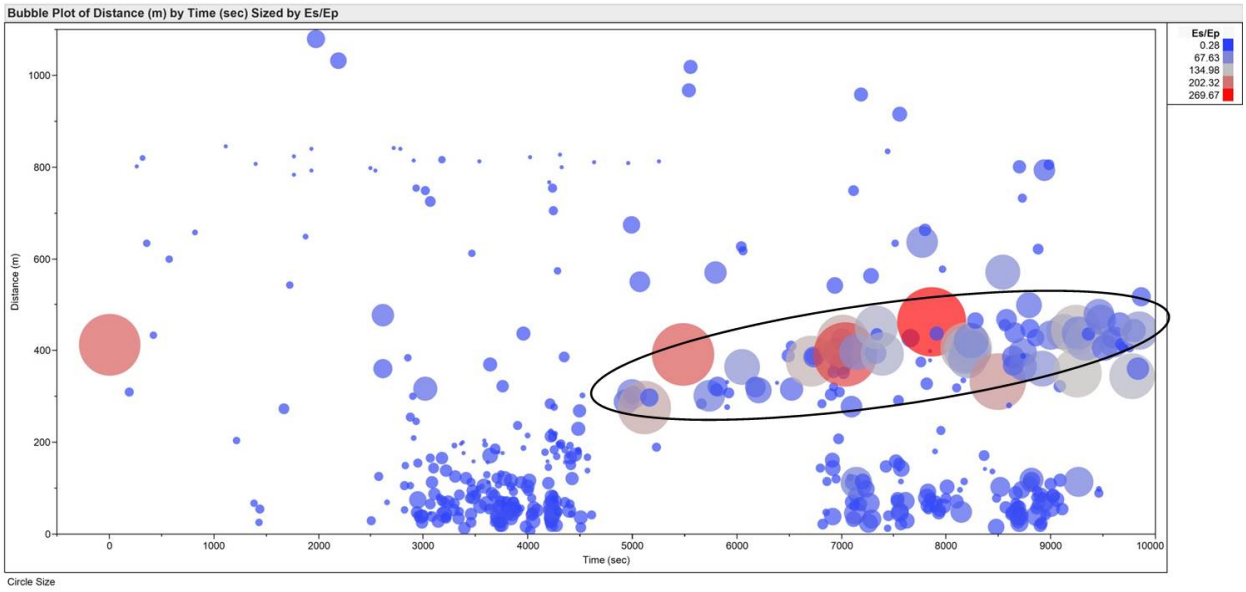

Figure 29 – Stage 5_3 event-to-perforation distance versus time, colored/sized by Es/Ep: blue = small (0.28), red = large (269.67). Note the concentration of larger Es/Ep values from 280 to 500 meters distance.

3.2.5.4 Well 6, Stage 1

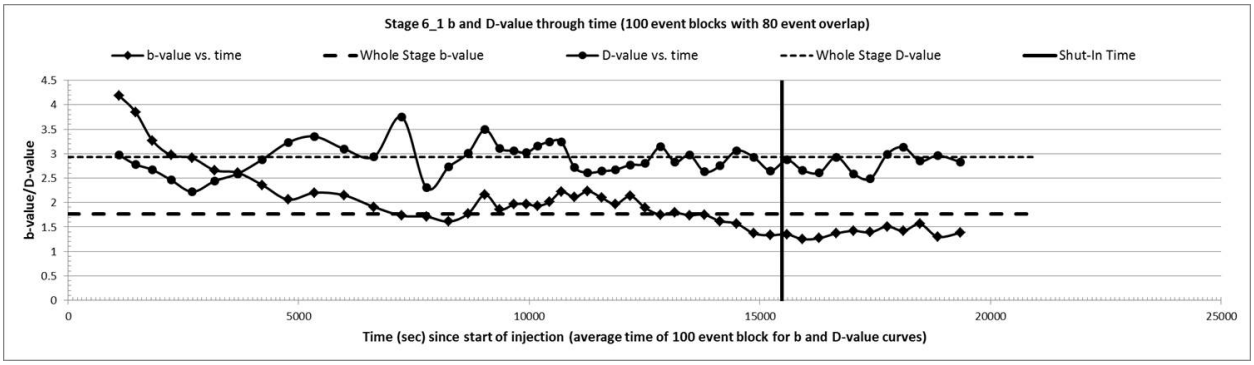

Figure 30 – Evolution of Stage 5_3 b and D-values through time.

The b and D-values for Stage 6_1, 1.77 and 2.93 respectively (Figure 30), indicate a dominant tensile failure mechanism and a stress regime in which σ1 is vertical, σ2 (S_{h_max}) is horizontal and oriented roughly northeast-southwest (from Figure 16), and σ3 (S_{h_min}) is horizontal and oriented roughly northwest-southeast.

Stage 6_1 was unique among all 56 fracturing stages for four reasons: **1)** During this stage, no events were recorded closer than approximately 830 meters from the perforation, and the majority of events are greater than 950 meters from the perforation (Figure 16). Events began occurring at this distance within two minutes of the start of injection and continued after shut-in for an unknown period of time; the microseismic contractor stopped listening after ~5000 seconds post shut-in, at which point the event frequency showed no indications of slowing down (Figure 31). Though this "blank" spot in the microseismic cloud is due in part to being outside of the effective listening distance of the monitoring well, a simple calculation of fracture propagation velocity, 950 meters in 120 seconds, gives a velocity of 7.9 meters/second, over 150 times the normal hydraulic fracture propagation velocity of 0.05 meters/second (Dohmen, Zhang

et al. 2013). We postulate that a pressure connection was established through an existing fault or well defined fracture system that was below the resolution of the seismic survey and that the stimulated rock mass was fractured with natural formation fluid and not fracturing fluid. **2)** Looking back to the three previously described stages, we see that radiated s-wave energy dominates those stages as a whole, radiating approximately 8 to 9 times as much s-wave energy as p-wave energy. Stage 6_1, on the other hand, is dominated by p-wave energy, radiating 3.5 times more p-wave energy than s-wave energy (Figure 32). **3)** All events occurred outside of the Marcellus zone of interest, approximately 400 meters above Well 4. **4)** There are two distinct groupings of events; one group comprises a vertical "column" of events and the other group is more linear in nature to the WSW of the column. These two groups possess different characteristics in terms of moment magnitude and seismic energy emissions (Es/Ep ratio) (Figure 33; Figure 34).

The two groups mentioned above are also easily distinguished on Figure 16; the coherent vertical column of events is to the east of the elongated linear cloud. It is apparent from Figure 33 and Figure 34 that the two groups of events possess different seismological properties. The vertical column contains the majority of the larger magnitude events, but these events have exclusively very low Es/Ep ratios approaching zero. The linear group on the other hand, contains small magnitude events of higher Es/Ep ratio. We conclude that the event column is a product of fluid interaction with a network of closely spaced fractures, resulting in pure tensile opening, and the linear group is a product of fluid interaction with a well-defined planar-linear structure, resulting in pore pressure increase, effective stress decrease, and incremental shear or oblique slip failures.

The evolution of the b and D-values throughout the stage (Figure 30) shows little correlation between b and D-value curves. Figure 31 shows that workers had difficulty maintaining consistent pumping pressure; with each stepwise increase in pumping rate, the pressure increased momentarily, but gradually bled off in to the formation. This happened repeatedly for the entire stage. The b and D-values change rapidly and it is unclear if there is any relation between their changing values and the pumping parameters. However, it is safe to assume that the overall b and D-values represent composite values from the two families of microseisms and that the rapid variations in the values with time indicate more or less interaction with one family or the other throughout the stage.

We are unable to calculate a meaningful diffusivity triggering front for Stage 6_1 due to the extreme distance between the injection point and the event cloud.

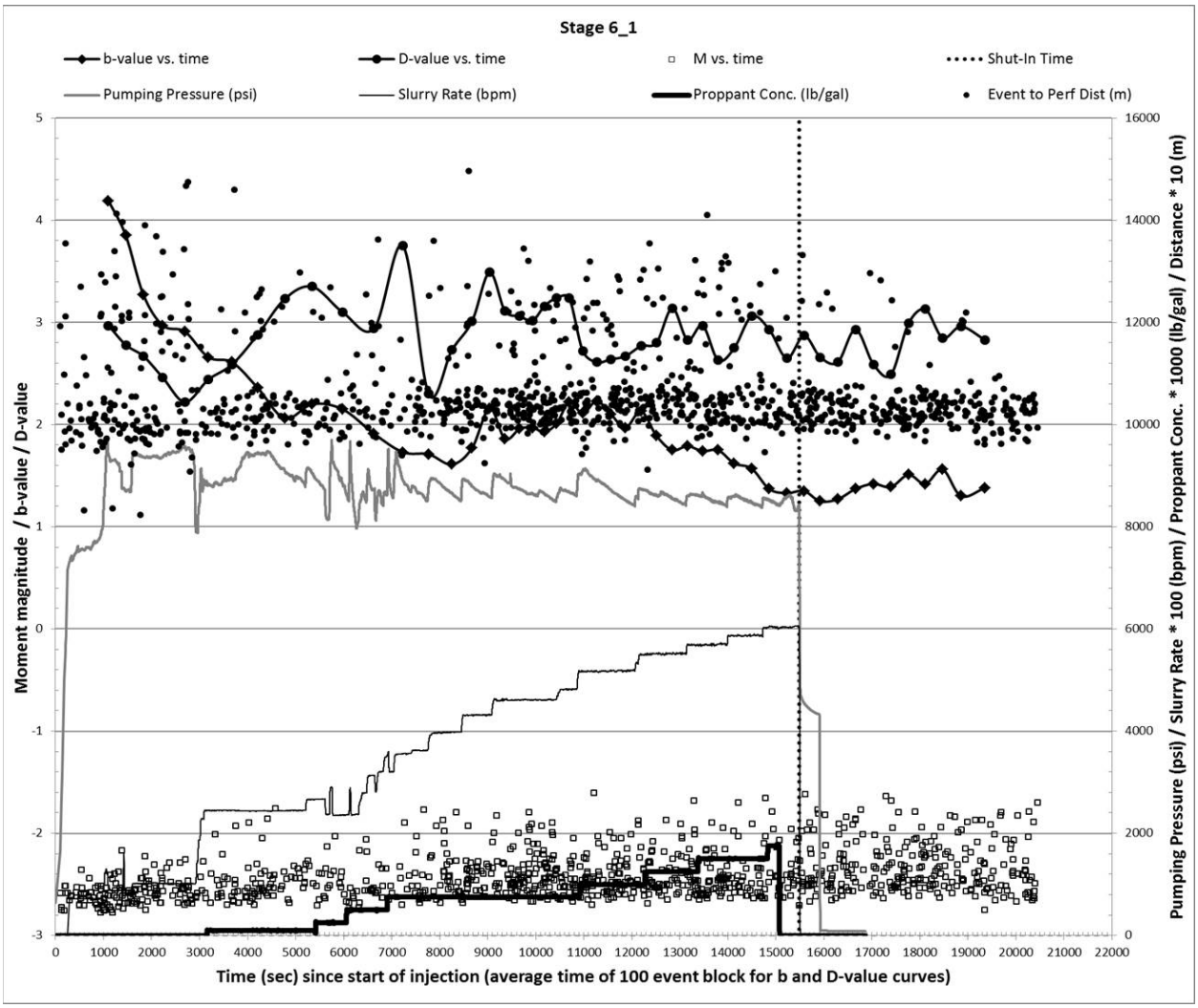

Figure 31 – Plot of Stage 6_1 b and D-values, pumping pressure, pumping rate, proppant concentration, event magnitude, and event distance from perforation versus time.

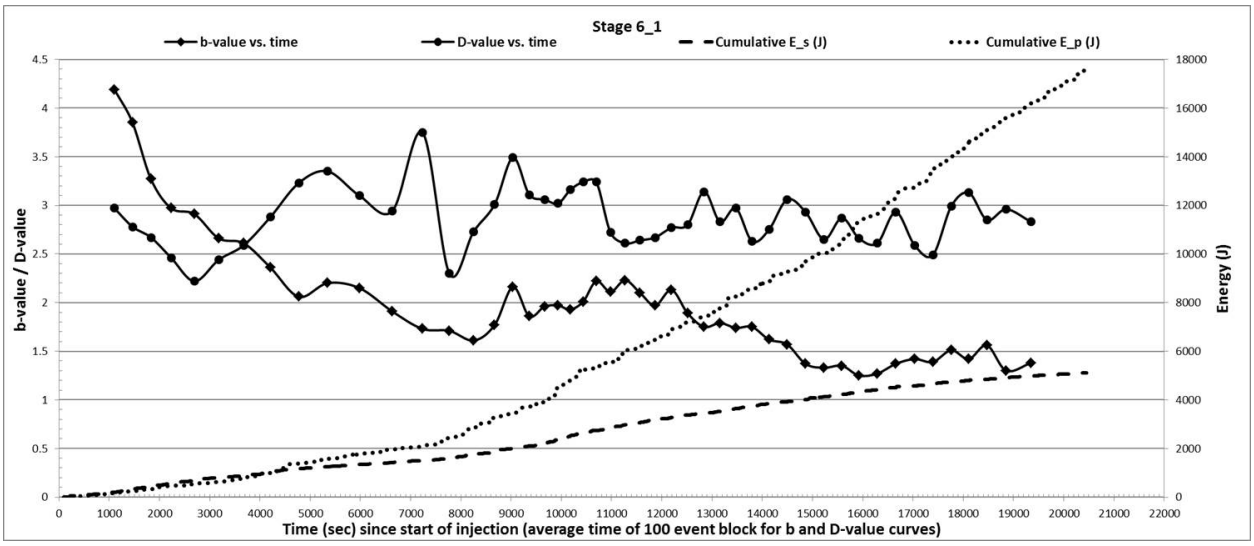

Figure 32 – Plot of Stage 6_1 b and D-values and cumulative s and p-wave energy versus time.

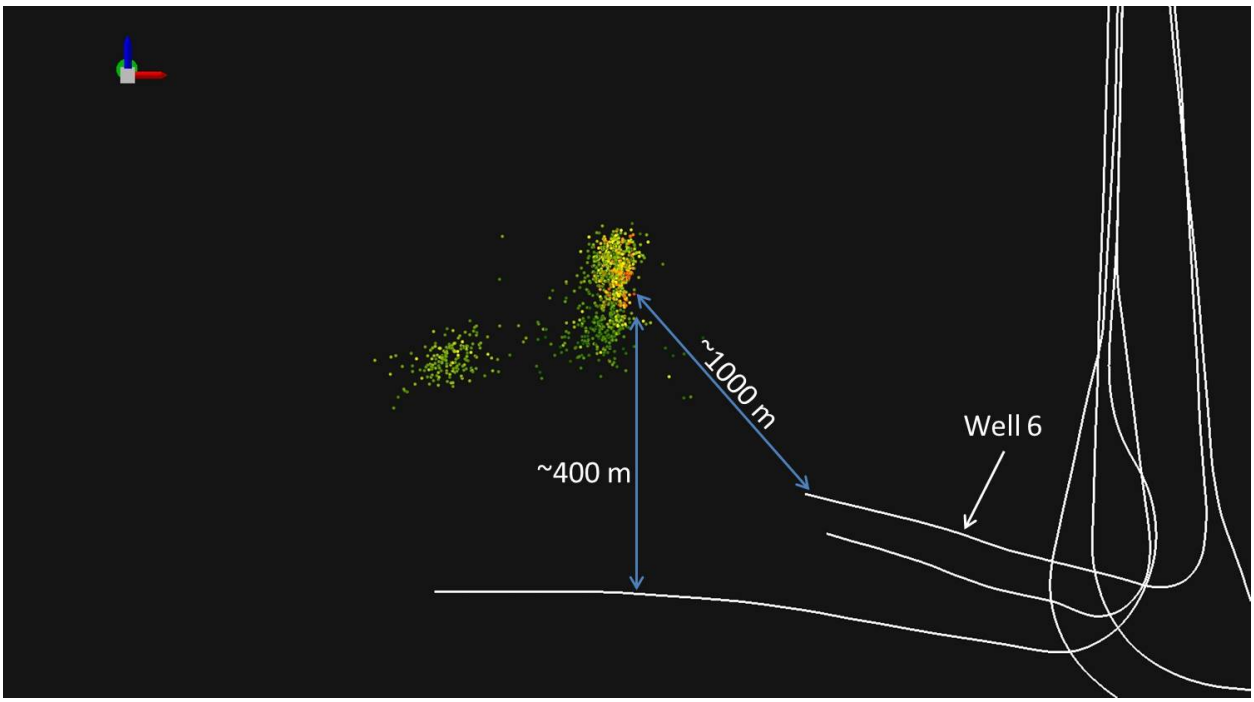

Figure 33 – Side view of Stage 6_1 events colored by Mw: green = small (-2.78), red = large (-1.61). Note concentration of larger events in the vertical cloud located ~ 1000 meters to the SSW of Well 6 and approximately 400 meters above Well 4.

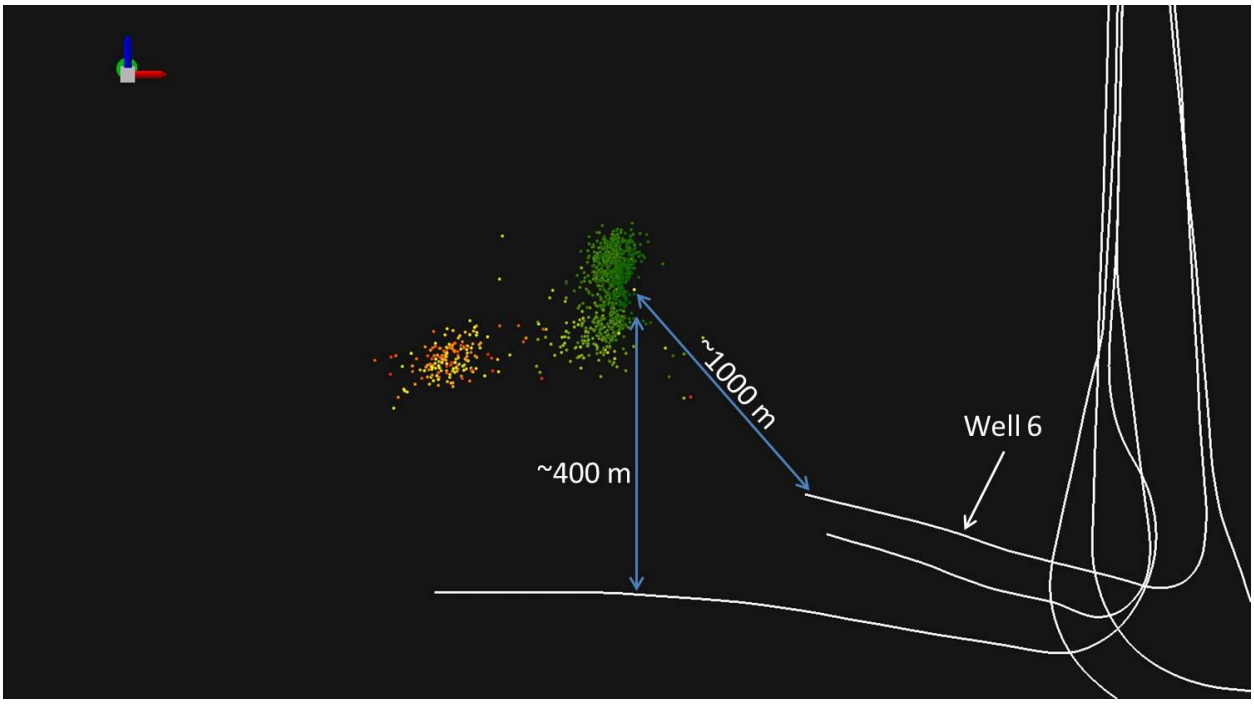

Figure 34 – Side view of Stage 6_1 events colored by Es/Ep value: green = small (0.02), red = large (17.99). Note concentration of smaller values in the vertical cloud located ~ 1000 meters to the SSW of Well 6 and approximately 400 meters above Well 4.

3.2.5.5 Energy Calculations and Introduction to Slow Slip Seismicity

As described in the Methods section of this study, the radiated energy of microseismic events can be calculated using well-established equations (Kanamori 1977). Though the seismic catalog is incomplete at very small magnitudes, Boroumand and Eaton (2012) showed that accounting for this missing energy using the frequency-magnitude distribution (Figure 17) adds a negligible amount of energy to the total. This radiated energy total is only useful if compared to the injection energy (energy input) and the fracture energy, which is easily calculated if detailed injection pressure, rate, and time are known and a reasonable estimate of fracture area can be attained. Boroumand and Eaton (2012) showed that the percentage of injection energy returned in the form of radiated seismic energy is very small, approximately 0.05%, and the percentage

returned in the form of fracture formation energy ranges from 12 to 41% (average of 22.5%). We have verified these findings for all stages of Well No. 1 (Table 4). Though the percentage of radiated seismic energy is 4 orders of magnitude smaller than documented in Boroumand and Eaton (2012), fracture energy accounts for approximately 10 to 28% of the total input energy, with an average of 22.5%.

Table 4 – Summary of energy values and relationships for Stages 1 through 14 of Well 1.

Well #	Stage	Injection Energy (J)	Radiated Energy (J)	Fracture Energy (J)	% Radiated Energy	% Fracture Energy
1	1	1.08E+11	8.23E+02	1.80E+10	7.6E-07	16.7
1	2	1.67E+11	2.87E+03	1.74E+10	1.7E-06	10.4
1	3	1.77E+11	1.17E+04	4.69E+10	6.6E-06	26.5
1	4	1.69E+11	5.39E+03	3.75E+10	3.2E-06	22.2
1	5	1.61E+11	2.75E+03	3.41E+10	1.7E-06	21.2
1	6	1.62E+11	1.49E+04	3.41E+10	9.2E-06	21.1
1	7	1.64E+11	9.47E+03	4.55E+10	5.8E-06	27.7
1	8	1.57E+11	1.03E+04	3.44E+10	6.5E-06	21.8
1	9	1.51E+11	1.13E+04	3.63E+10	7.5E-06	24.1
1	10	1.58E+11	3.53E+04	3.98E+10	2.2E-05	25.2
1	11	1.55E+11	2.16E+04	3.40E+10	1.4E-05	22.0
1	12	1.61E+11	1.44E+04	4.18E+10	9.0E-06	26.0
1	13	1.51E+11	1.27E+04	4.18E+10	8.4E-06	27.7
1	14	1.78E+11	1.11E+04	3.92E+10	6.2E-06	22.0

Although this analysis of the energy components of hydraulic fracturing is interesting and offers some insight into the efficiency of the operation, it begs the question: What is happening to 78% of the energy put into the system? Brown, Tryon et al. (2005) and Zoback, Kohli et al. (2012) studied what is known as slow slip seismicity, or long period, long duration (LPLD), low frequency (0.1 to 5 Hz, from Brown, Tryon et al. (2005); 1 to 15 Hz, from Zoback, Kohli et al. (2012)) seismic signals that are not typically recorded during microseismic monitoring of hydraulic fracturing. Figure 35 shows seismograms and their running frequency spectra (spectrograms) for natural fluid flow through the subsurface and a volcanic tremor in Costa Rica, which are good analogs for induced hydraulic fracture formation. Zoback, Kohli et al. (2012)

put forth the idea that slow slip seismicity (as opposed to fast slip brittle failure) will occur on faults and fractures that are not oriented optimally within the present day stress field, i.e. not parallel to the S_{h_max} direction, during hydraulic fracturing of shale reservoirs. The reason for this is that the discontinuities are not critically stressed as they would be if they were optimally oriented, so slip along these faults will only occur as fast as increased pore pressure can dissipate along them. Zoback, Kohli et al. (2012) contend that slow slip seismicity is not only pervasive during stimulation of shale reservoirs such as the Marcellus and Barnett, but it is the dominant mechanism of deformation. This would explain the apparent disconnect between microseismicity and gas production in recent studies (Moos, Vassilellis et al. 2011, Vermylen and Zoback 2011), which show more production than would be expected from microseismically mapped fractures alone. Zoback, Kohli et al. (2012) assert that slow slip deformation creates a network of dense permeable fractures that branch off of the main induced hydraulic fractures.

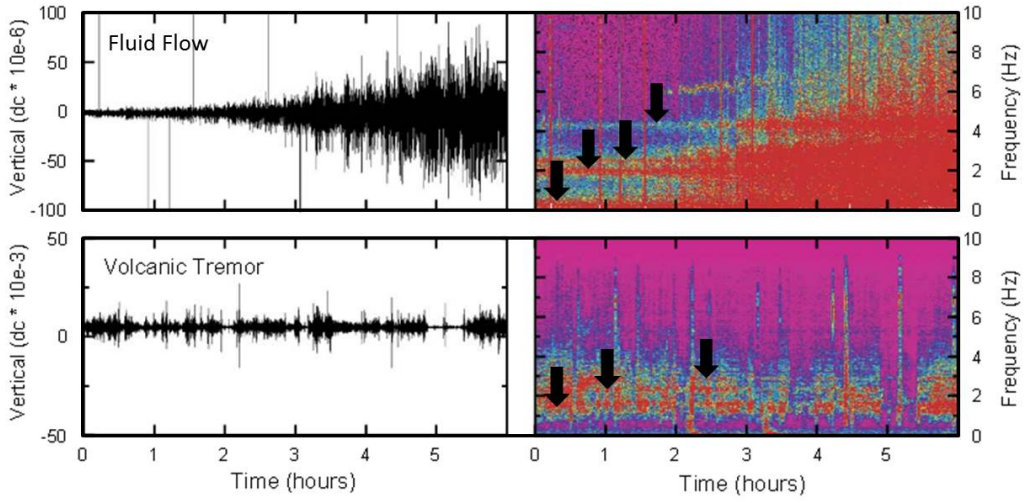

Figure 35 – Modified from Brown, Tryon et al. (2005). Seismograms and spectrograms during fluid flow measurements and a volcanic tremor at Arenal in Costa Rica. As power increases, the spectra reddens. The arrows indicate increased power across the entire timeframe at < 1, 2, 2.5, and 4.5 Hz during fluid flow in the subsurface, and at 1.5, 2, and 3 Hz during volcanic tremor.

We have begun a preliminary analysis of seismic signals acquired by one 3-component, research quality seismometer with a corner frequency of 2 Hz (Figure 36). The instrument was buried in a shallow pit in the vicinity of this well pad and left to passively monitor for a five month time window inclusive of all hydraulic fracturing operations. We isolated a seismogram recorded before the commencement of fracturing on the site (Figure 37) for comparison to one recorded during the first stage (Figure 38; Figure 39) and have found evidence for LPLD seismic activity. Additionally, we were able to pinpoint the onset of LPLD activity during this stage.

Figure 36 – Portable 3-component seismometer used at the site.

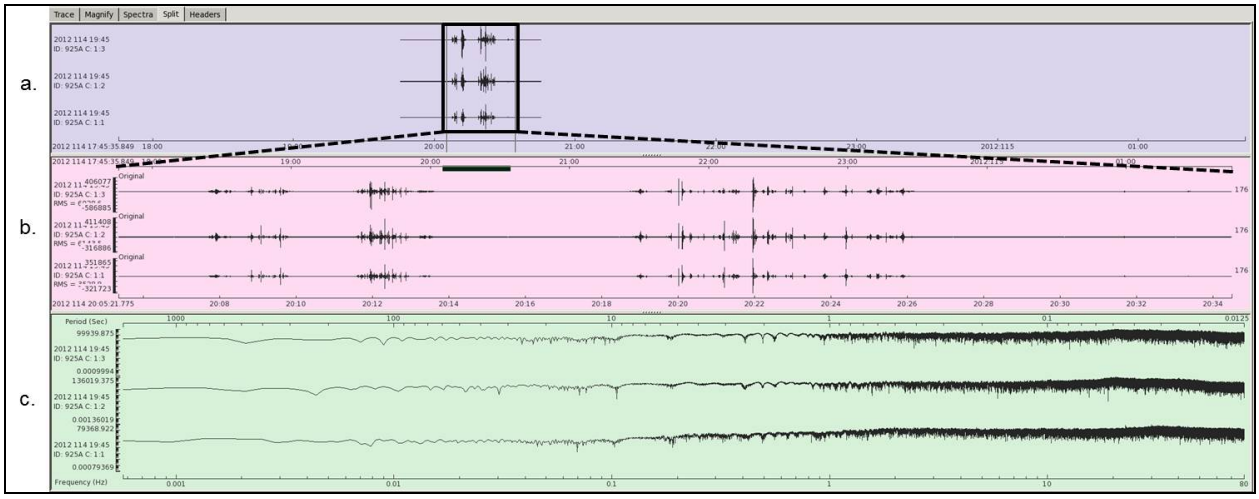

Figure 37 – Seismogram (a) and detail (b) from this study site for a ½ hour time period on the day prior to the initiation of any hydraulic fracturing operations. (c) shows the frequency spectrum of the seismogram.

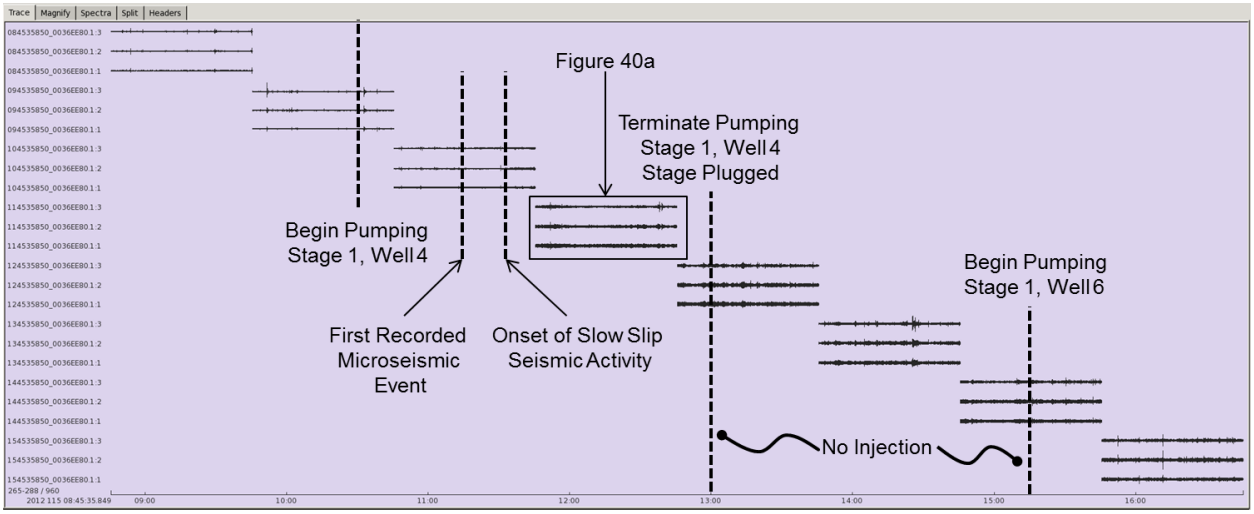

Figure 38 – Seismograms for an eight-hour time period on the first day of hydraulic fracturing operations, inclusive of Stage 1 of Well 4 and the beginning of Stage 1 of Well 6. What appear to be seismic tremors appear on the seismograms approximately one hour into pumping of Stage 1 of Well 4 and continue through the record.

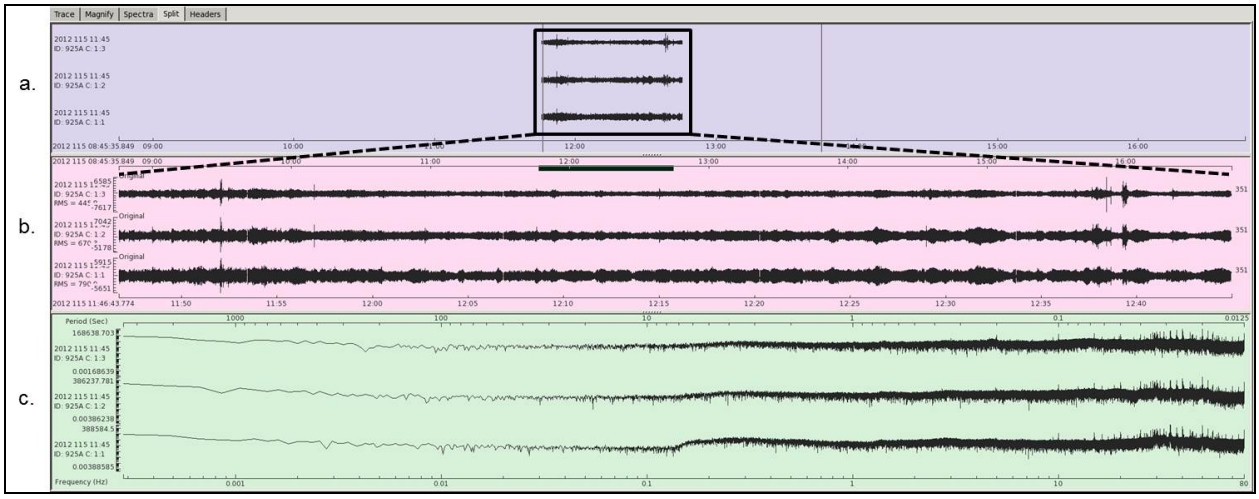

Figure 39 – Seismogram (a) and detail (b) from this study site for a one-hour time period during injection into Stage 1 of Well 4. Notice the more sustained signal through time in (b) when compared to Figure 37b. (c) shows the frequency spectrum of the seismogram; notice the increased power in the 0.01 to 10 Hz range when compared to Figure 37c.

3.2.6 Conclusions

As we have shown, much insight can be gained from performing intra-stage level b and D-value analysis by comparing to pumping data, seismic energy, and time-distance cross-plots. One must utilize attributes such as Es/Ep and moment magnitude. The front-end data organization can be time consuming but the lessons-learned can be valuable, arriving at more informed conclusions about not only stimulated volume and fracture complexity, but also geomechanical behavior of the rock mass, interaction with existing geological structures, changes in failure mechanism, and fracturing efficiency. Rather than study erratic pumping pressure and rate curves and only speculate as to "what happened down there", we can start to explain with evidence.

3.2.7 Acknowledgements

This ongoing research is funded through the US DOE – National Energy Technology Laboratory, Regional University Alliance, in collaboration with the Department of Geology and Planetary Science and Swanson School of Engineering at the University of Pittsburgh, Pennsylvania.

3.2.8 Additional Discussion/Work for Greene County Microseismic Study

3.2.8.1 Estimation of Maximum Horizontal Stress Orientation

Additional analysis includes an examination of the S to P wave energy ratio of microseismic events as a function of the azimuth of the travelling wave, known as the "poor man's focal mechanism", and its application to the understanding of lateral stress orientations (Rutledge, Downie et al. 2013). Normally, a single earthquake is viewed from multiple azimuths (seismometers) to determine the orientation of the nodal planes, based upon the first motion of the P-wave arrival (Figure 40). Receiving the waves at monitoring stations surrounding the event allows the quadrants of the "beach ball" diagram to be populated and delineated with first motions. Often a microseismic monitoring program consists of a single downhole receiver array, essentially a single seismometer. In this case, the microseismic event is only being "seen" from one azimuth, but if the assumption is made that the distribution and properties of a microseismic cloud of *n* events are heavily influenced by the regional stresses present, one may treat the cloud as a single event seen at *n* stations (and *n* azimuths).

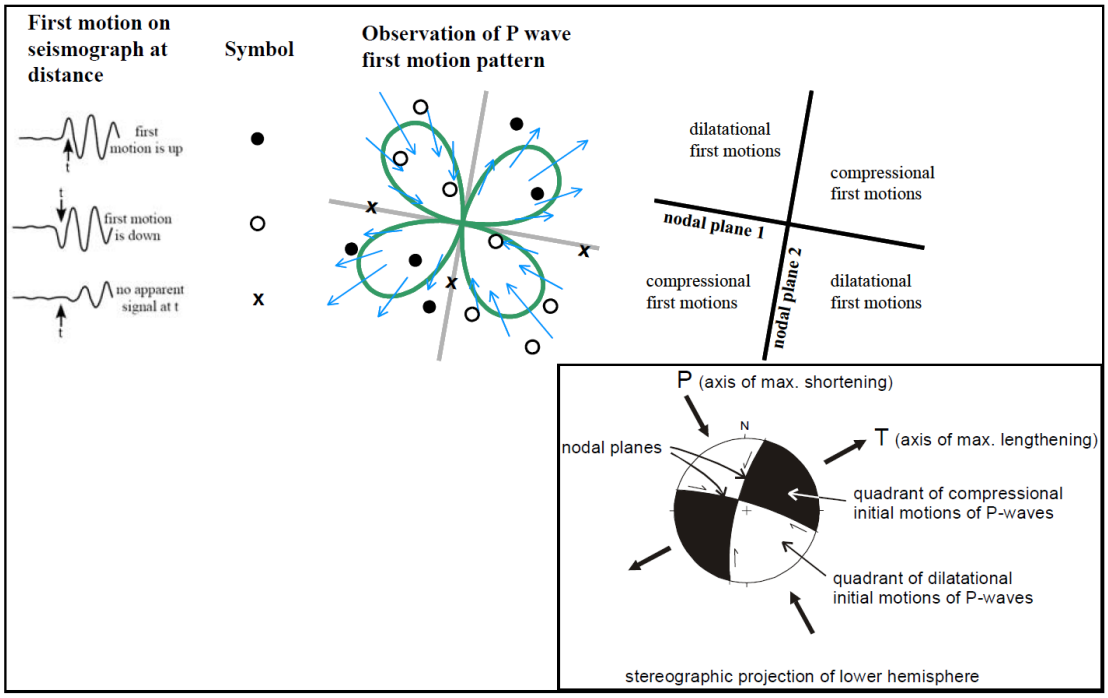

Figure 40 – The elements of a fault plane solution. Modified from Barth, Reinecker et al. (2008)

The energy characteristics of the arriving wave will change based upon the source (microseismic event) to receiver (monitoring well) azimuth. Figure 41 is a schematic illustration of a microseismic cloud around a single downhole receiver array. Both P and S waves will propagate from shearing at the tips of hydraulically induced fractures. While P waves will radiate outward along the P and T axes (Figure 40) (bisecting the nodal planes), S waves will largely be restricted to the azimuth of the focal plane (fracture plane) of the microseismic event. Fractures tend to propagate in the direction of S_{h_max} (Figure 4); hence a source to receiver azimuth close to the orientation of S_{h_max} (Figure 41, azimuth 220°) will contain a higher shear wave content and higher S/P ratio than all other compass directions (azimuth 139°).

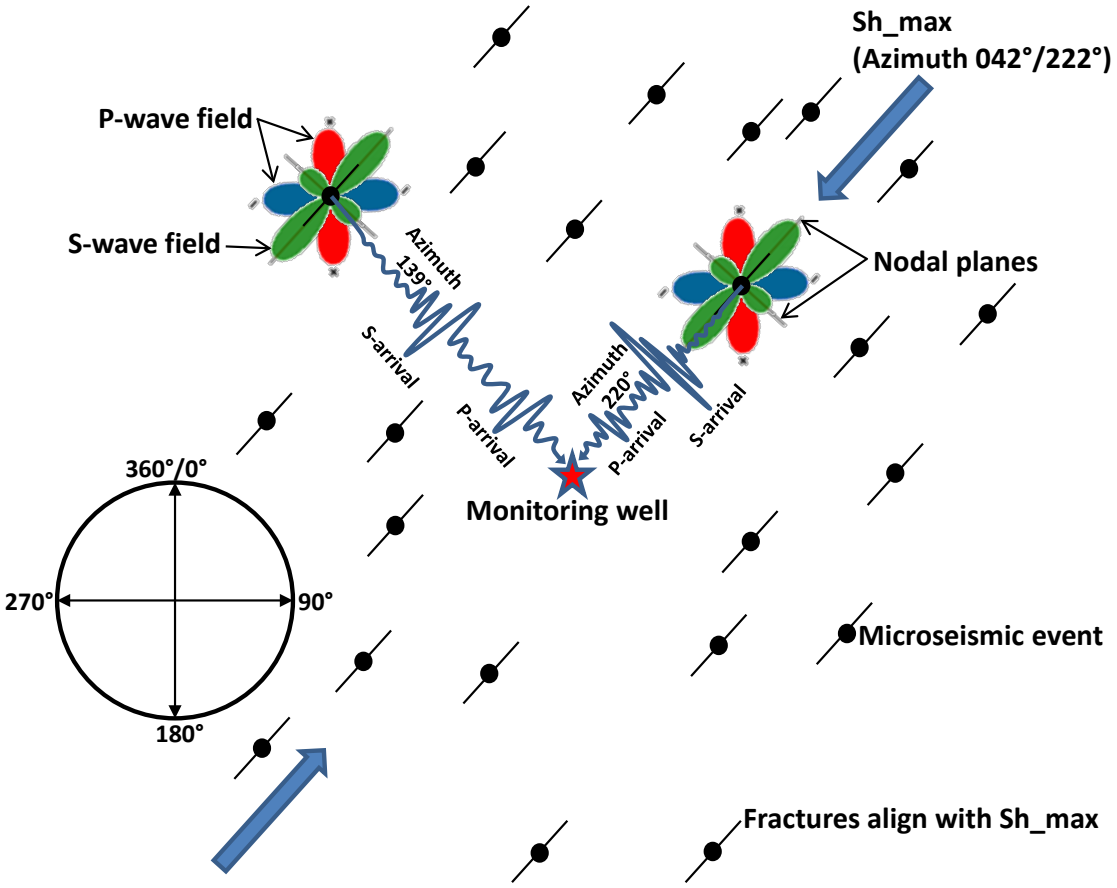

Figure 41 – Schematic diagram of p and s-waves arriving at a monitoring well from different azimuths.

Figure 42 represents the azimuthal analysis of S to P wave energy ratio from the Greene County microseismic catalog. There are two nodal planes for every fault plane solution; one is the actual fault plane and the other is the auxiliary plane, normal to the fault plane. Despite scatter in the data, it is apparent that there is differentiation in the S to P wave energy ratio as a function of azimuth. An estimate of the distribution of Log Es/Ep is illustrated with a black line on Figure 42, and a running average of four degree blocks of azimuth is illustrated with an orange line. The point scatter seen on Figure 42 is likely due to the presence of focal plane orientations (fracture surfaces) that have been generated at larger angles to the S_{h_max} direction. This could be a product of smaller fractures connecting larger ones. As the differential stress

(S_{h_max} - S_{h_min}) becomes larger in a given geologic setting, this scatter would decrease as fracture formation is forced into alignment with S_{h_max}. Studies in the Barnett Shale in Texas (Rutledge, Downie et al. 2013), where microseismicity tends to form long, thin clouds aligned with S_{h_max}, illustrate the increased effectiveness of this analysis when differential stress is high.

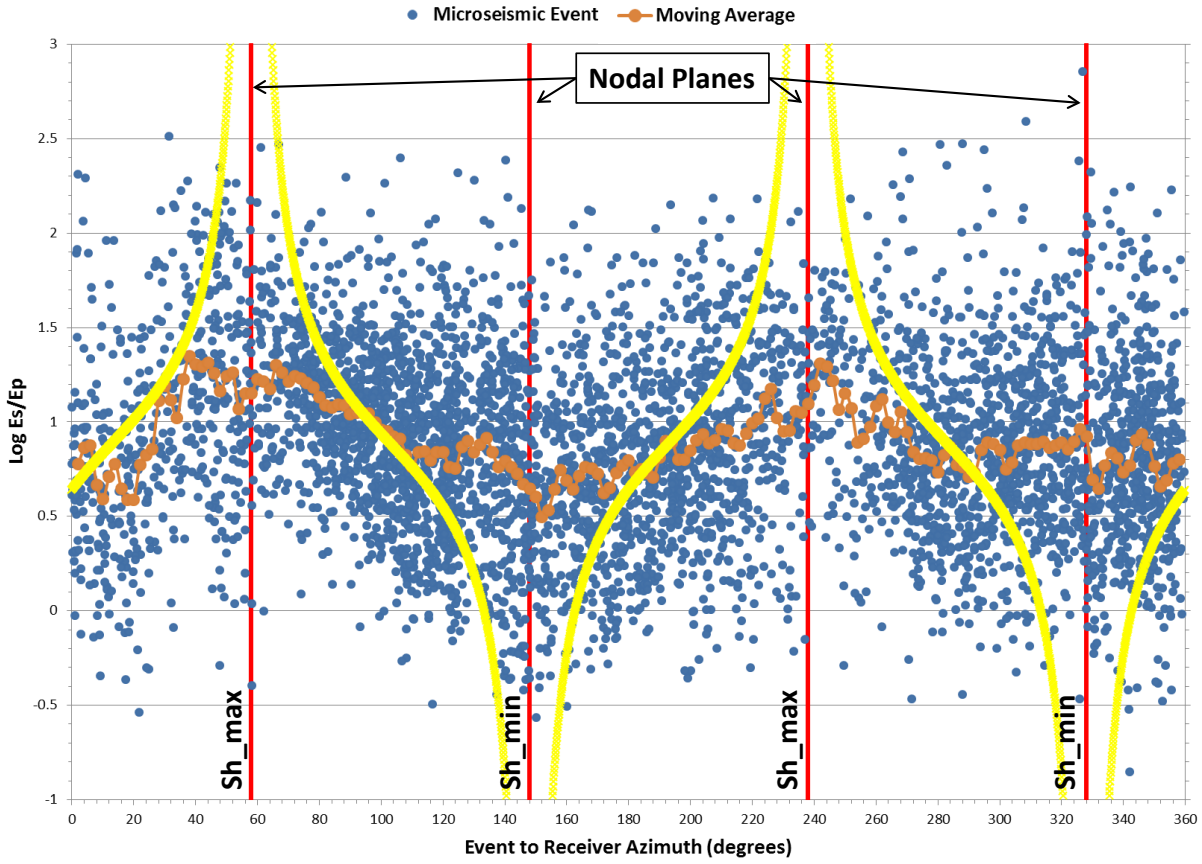

Figure 42 – s/p-wave energy ratio versus the azimuth from the event to the receiver. Inferred nodal planes are shown in red and data can be compared to the ideal, theoretical distribution shown in yellow.

3.2.8.2 Expanded Discussion of Slow Slip / LPLD Seismicity

In 3.2.5.5 above, slow slip or long period-long duration seismicity was introduced and a preliminary analysis of data from a single 2 Hz seismometer installed on the surface was reviewed. Additional analyses to support these preliminary results includes a more detailed look

at the imbalance between the injection energy and the sum of microseismic and theoretical fracture formation energy, as well as a comparison of pre- and syn-frac frequency spectra of the arriving signal.

Figure 43 is a graphical representation of Table 4, illustrating the consistent shortfall in fracture formation and radiated energy when compared to the total energy put into the system hydraulically. An average of 22.5% of the injection energy over 14 stages can be accounted for by calculating the amount of energy required to generate the fracture defined by the microseismic cloud, and adding the radiated microseismic energy to this figure. It is possible that energy is being lost to such things as friction, tortuous fluid flow near to the well-bore, and through-flow of fluid into existing fractures and natural conduits. However, it has been proposed by Zoback, Kohli et al. (2012) that aseismic deformation during hydraulic fracturing could account for much of this missing energy, and in fact, represents a fundamentally important stimulation mechanism in organic shale.

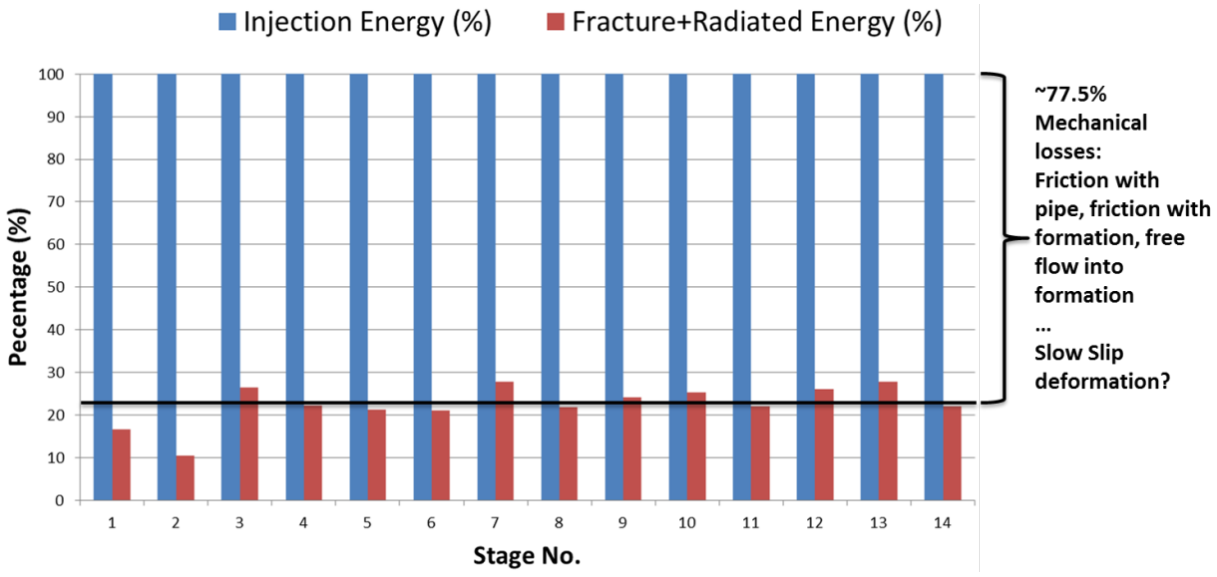

Figure 43 – Injected energy (normalized to 100%) compared to the energy of fracture formation and microseismic energy shows that > 75% of the hydraulic energy is unaccounted-for by brittle fracturing.

Approximately 36 days elapsed between the completion of hydraulic fracturing at Wells 4, 5, and 6, and the commencement of hydraulic fracturing at Wells 1, 2, and 3. This is fortunate in that it provides two opportunities to compare the low frequency acoustic emissions from relatively "quiet" site conditions with those from a state of active hydraulic fracturing. Stage 1 of Well 4 was the first stage to be hydraulically fractured of all six wells. Stage 1 of Well 1 was fractured first at the remaining three wells. Figure 44 shows the frequency spectra from ten hours prior to and ten hours after the start of injection at Well 1; the early spectra (black) are overlain on the later (red). The underlying spectra on Figure 44 show a slight increase in power in the 3 Hz range within the first hour of injection. This increase in power spreads out to between 1 and 20 Hz over the next ten hours, continuing through short (1-2 hour) periods of downtime between stages. The third hour of injection at Well 1 has been enlarged to show the detail in the frequency spectrum (Figure 45). There is a one order of magnitude increase in the power between 3 and 11 Hz, with discrete peaks at 3, 4 and 11 Hz.

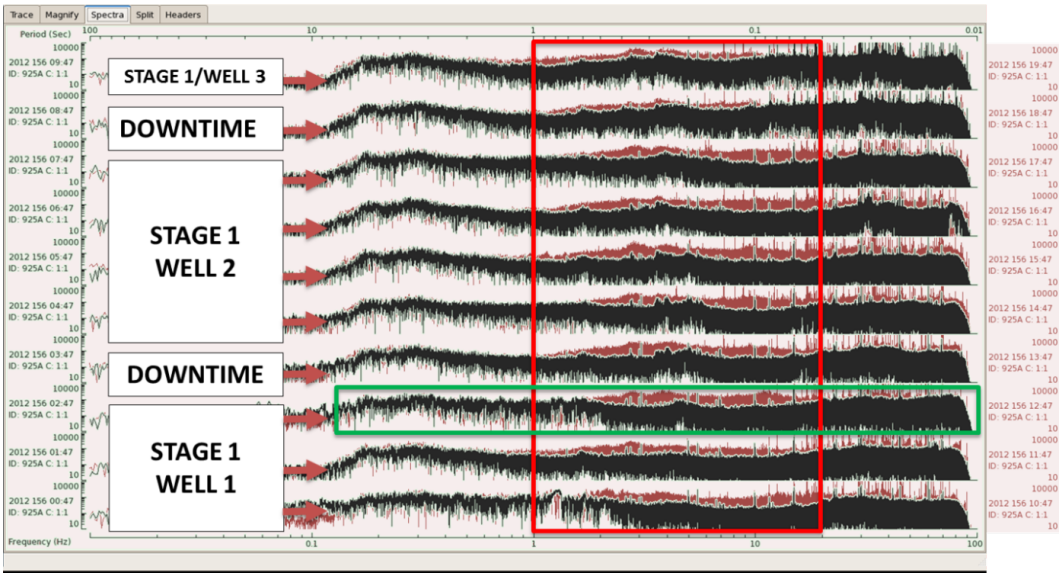

Figure 44 – Frequency spectra from ten hours prior to and after the start of fracturing at Well 1, in one hour increments. Syn-frac spectra are shown in red, with pre-frac spectra in black, overlain on top.

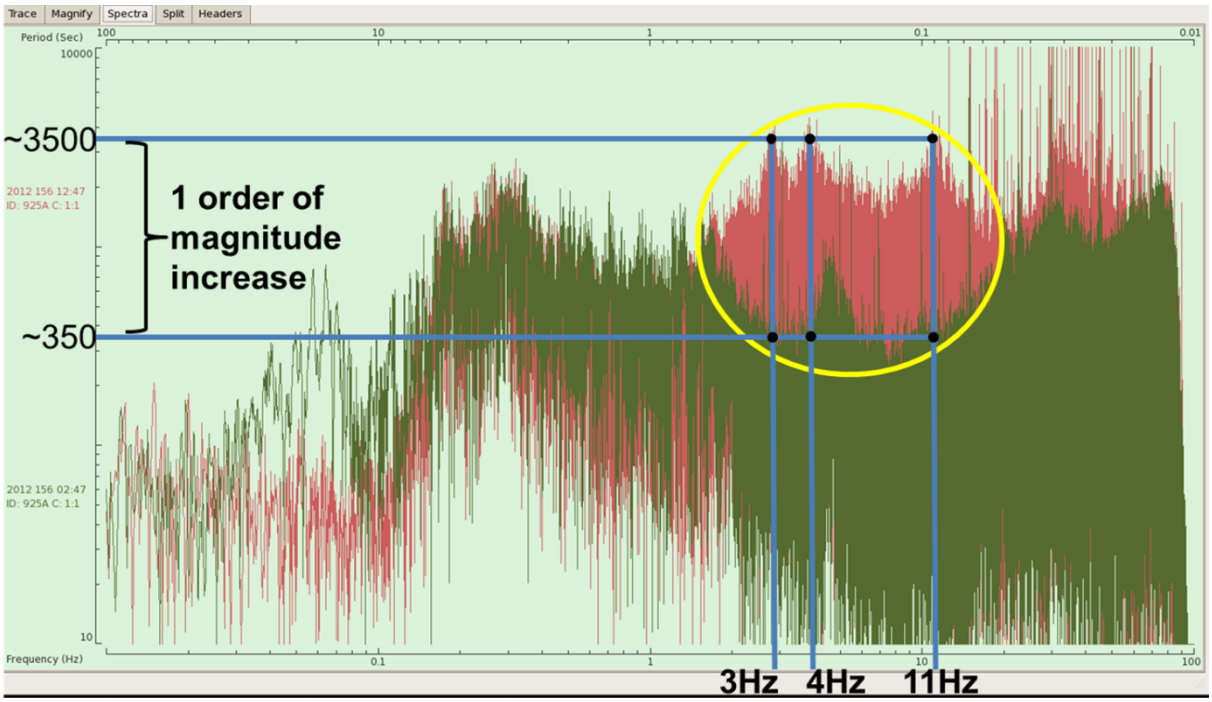

Figure 45 – Spectrum from the third hour of fracturing in red overlain by the spectrum from eight hours prior to fracturing.

A more detailed spectral analysis was completed by examining the 20 hour time-windows around the start and finish of hydraulic fracturing in each set of wells. The previous figures have illustrated that there is an increase in power in the low frequencies after the start of fluid injection, but is there any order to this change? Is the increase gradual or abrupt? Does the inverse observation hold true for the time period surrounding the termination of hydraulic fracturing?

Figure 46 shows the ten hours before and after the start of fracturing at Well 4 on April 24, 2012. The pre-frac time period can be thought of as the active site baseline because there would have been activity related to preparations for fracturing but no actual fluid injection taking place. There is no apparent order to the spectra in time, such as an increase in power spectral density (PSD) leading up to Stage 1, which makes sense. The ten hours following the

commencement of fluid injection tells a different story however. Overall, the PSD has increased above 3 Hz, but the more compelling observation is the gradual increase in PSD starting at hour zero. The spectrum from each subsequent hour shows higher power between 3 and 20 Hz than the previous. Figure 47 makes the comparison between the pre- and syn-frac time periods easier to interpret. In addition, note the peaks in spectral density during fracturing at ~4, 7, 8, 9, and 10 Hz that were not present in the active site baseline. This is very similar to the peaks seen in Figure 45.

The ten hours before and after the termination of injection in the last stage of the first three wells is not as well ordered. However, the trend of decreasing PSD after the well has been shut-in is observable. After shut-in, one might expect the amount of aseismic tremor to decrease gradually as fluid pressures equilibrate. In reality, that is not the case (Figure 48), but overall, the PSD is lower post shut-in than during fracturing (Figure 49).

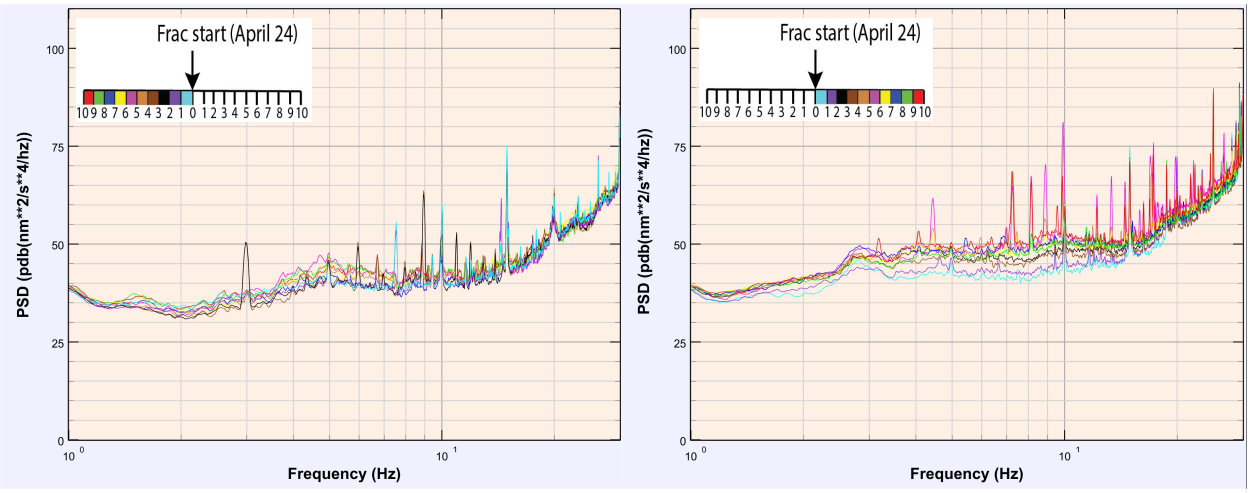

Figure 46 – Hourly frequency spectra for 10 hours before and 10 hours after injection began at Well 4.

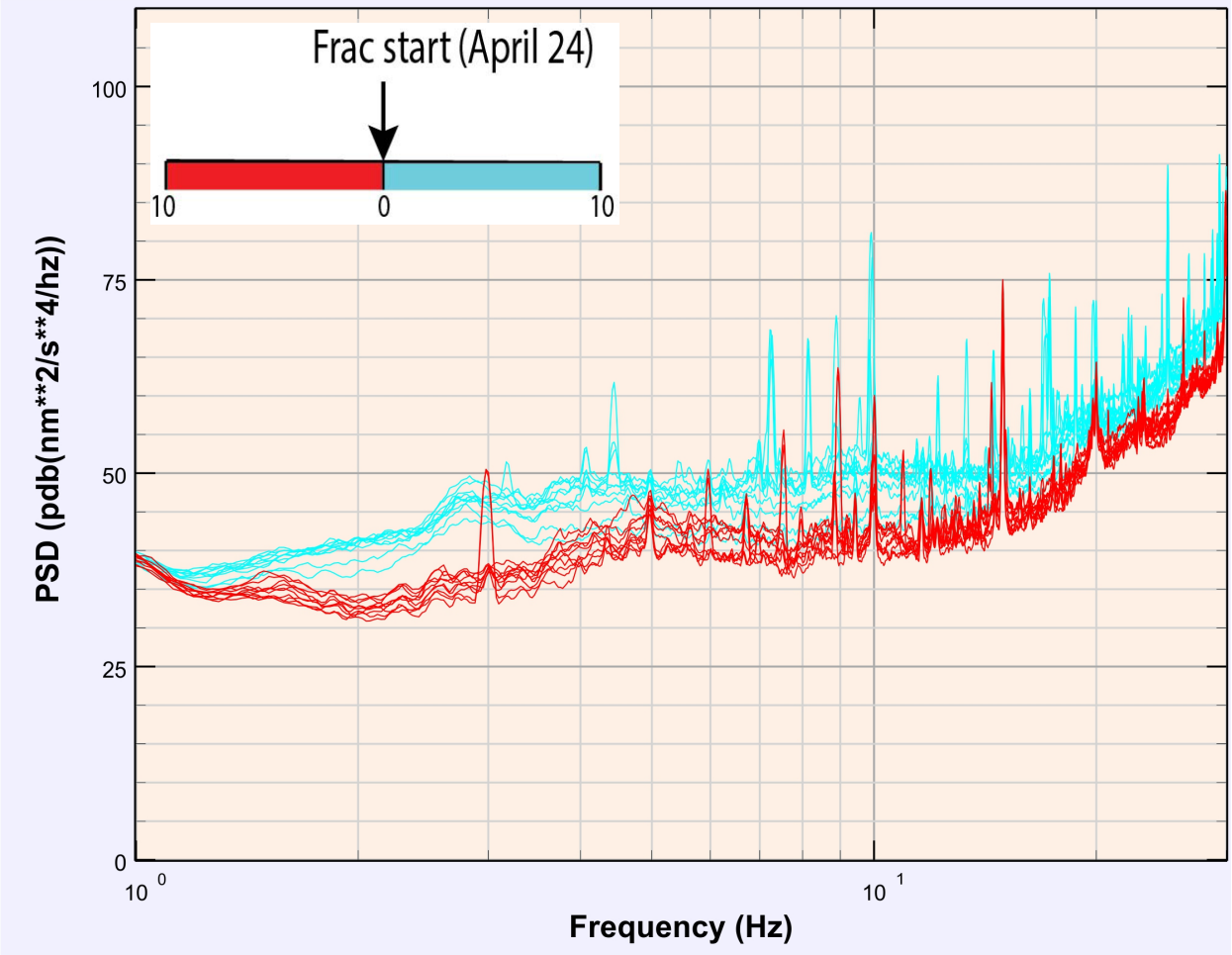

Figure 47 – Comparison of the pre- and syn-frac spectra at Well 4. Pre-frac in red and syn-frac in blue.

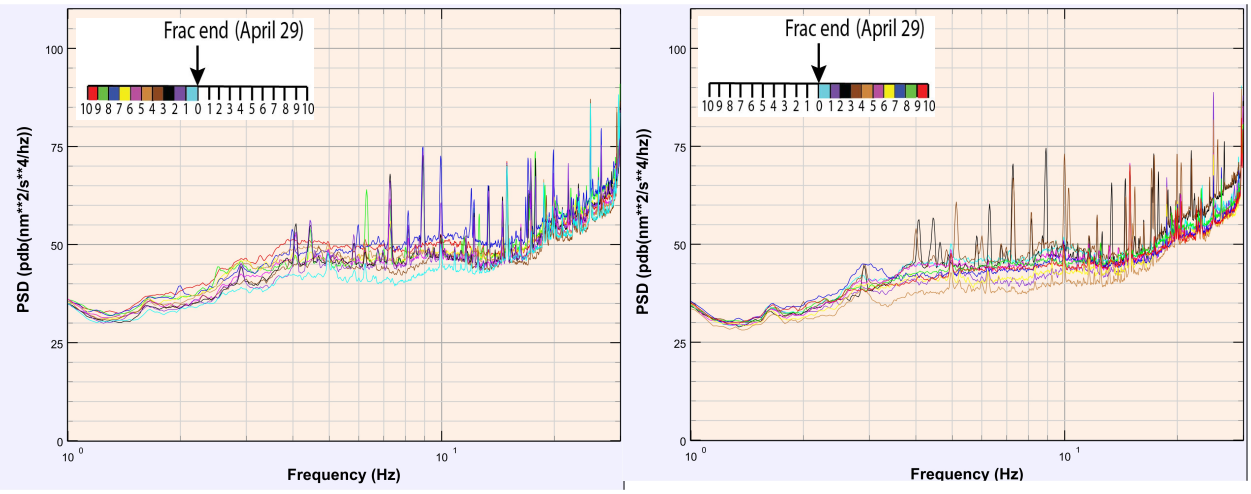

Figure 48 – Hourly frequency spectra for 10 hours before and 10 hours after final shut-in at Well 4.

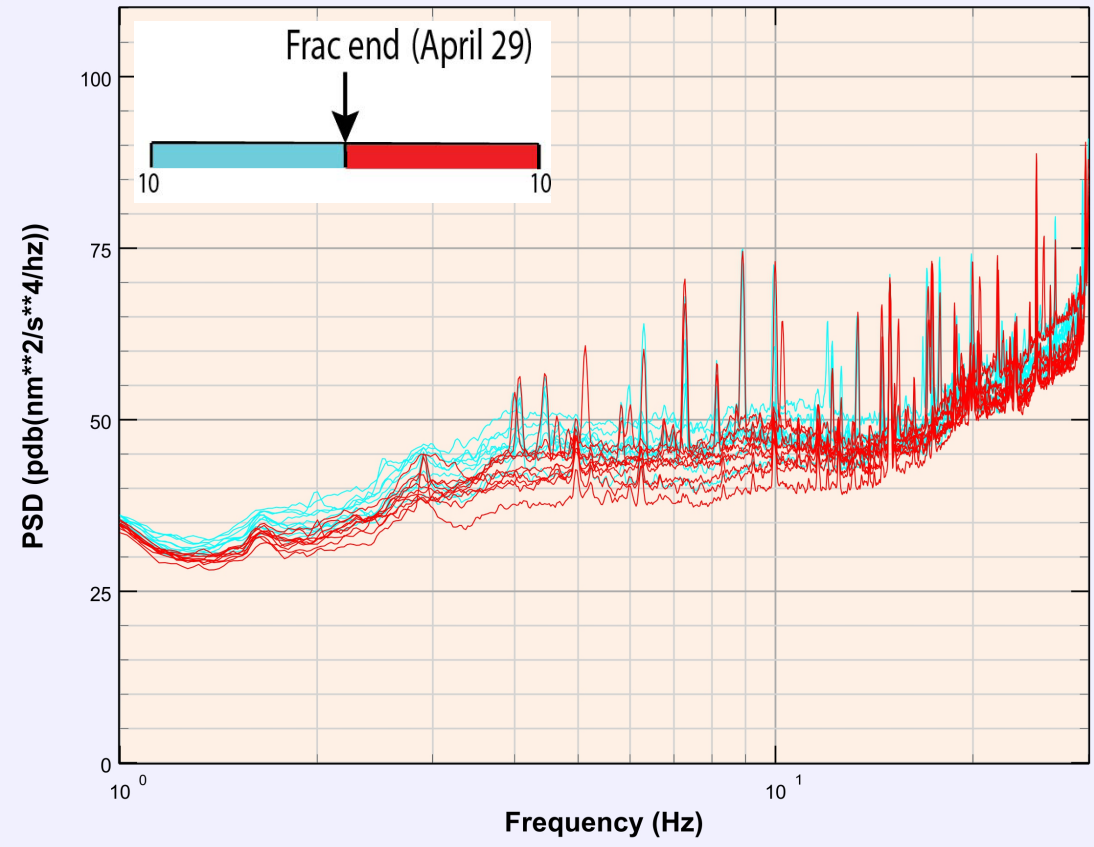

Figure 49 – Comparison of the syn- and post-frac spectra at Well 4. Syn-frac in blue and post-frac in red.

Approximately 36 days after the final stage of Well 4, the first stage of Well 1 was fractured on June 4, 2012. Similar to the commencement of fracturing on April 24th, PSD in the low frequencies increases overall from pre-to syn-frac, and PSD gradually increases from hour zero to hour ten after injection starts (Figure 50). Distinct peaks in PSD that were not present in the active baseline are observed at ~4, 7, 8, 9, and 10 Hz.

The 20-hour time window around the termination of fracturing on June 11th is difficult to interpret. The average PSD from post shut-in appears to be about the same or higher than the PSD during fluid injection (Figure 52 and Figure 53). The peaks in PSD at 4, 5, 9, and 10 Hz appear to have been muted after injection is terminated, but there is still considerable power in the low frequencies overall.

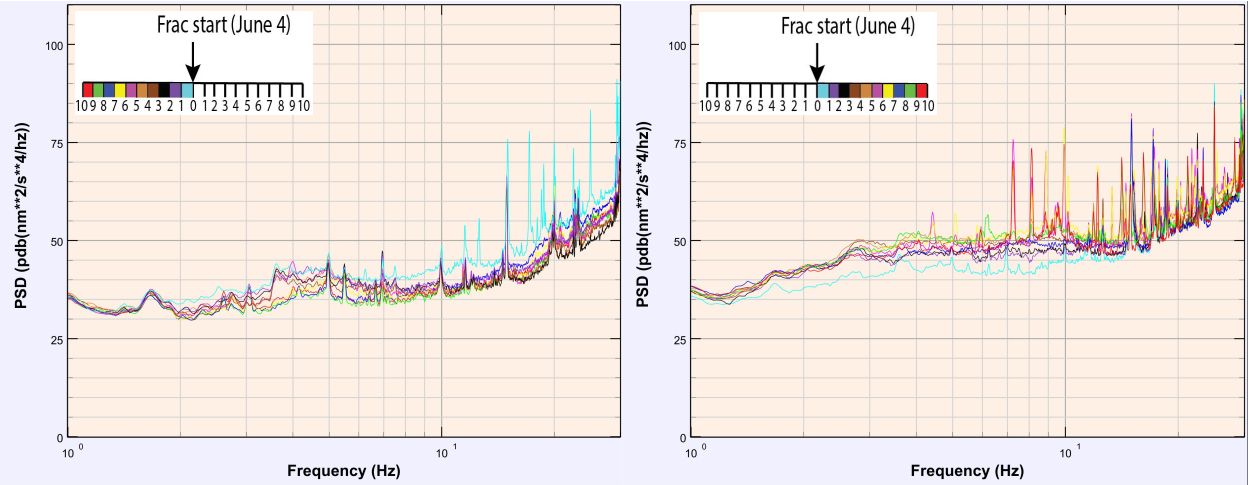

Figure 50 – Hourly frequency spectra for 10 hours before and 10 hours after injection began at Well 1.

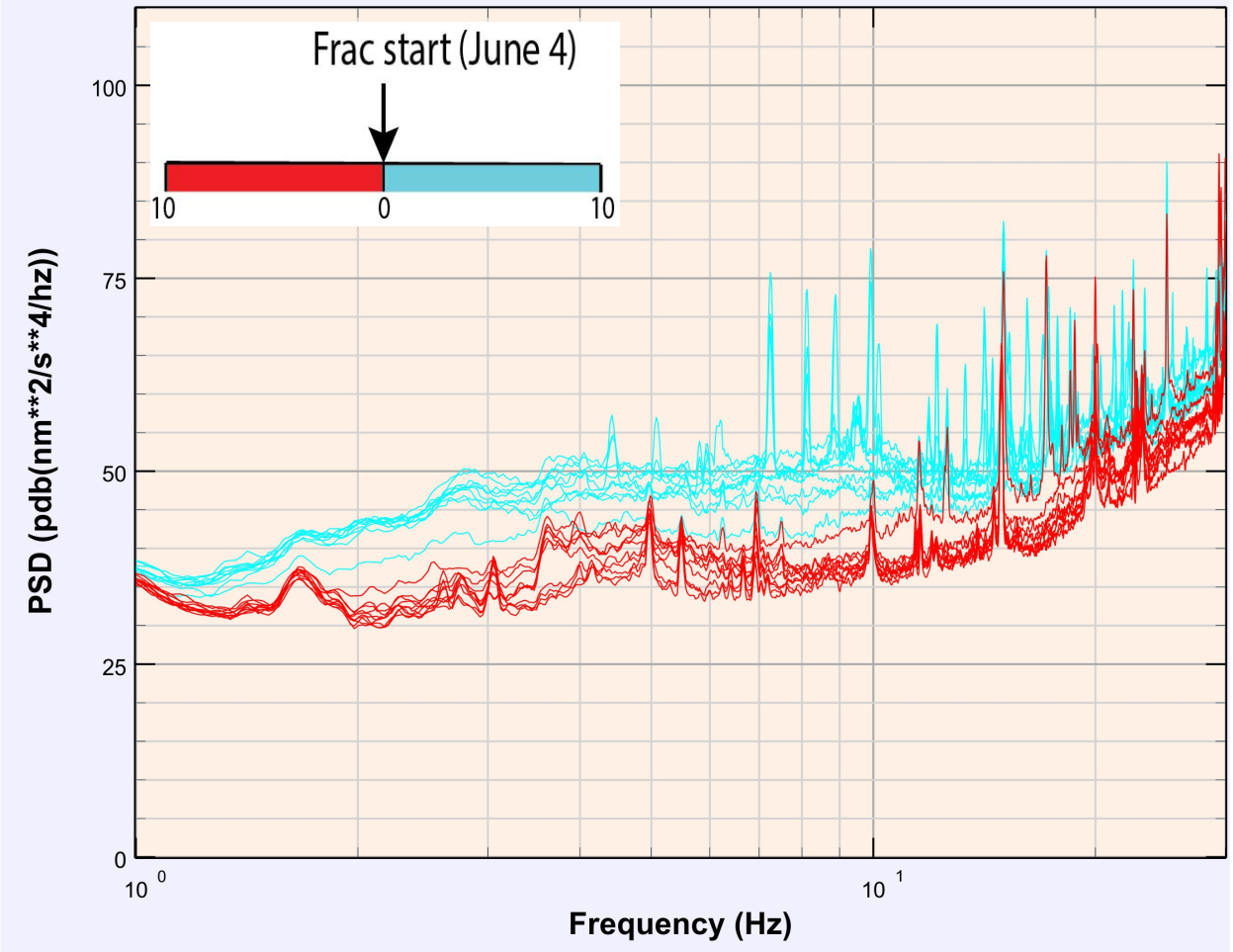

Figure 51 – Comparison of the pre- and syn-frac spectra at Well 1. Pre-frac in red and syn-frac in blue.

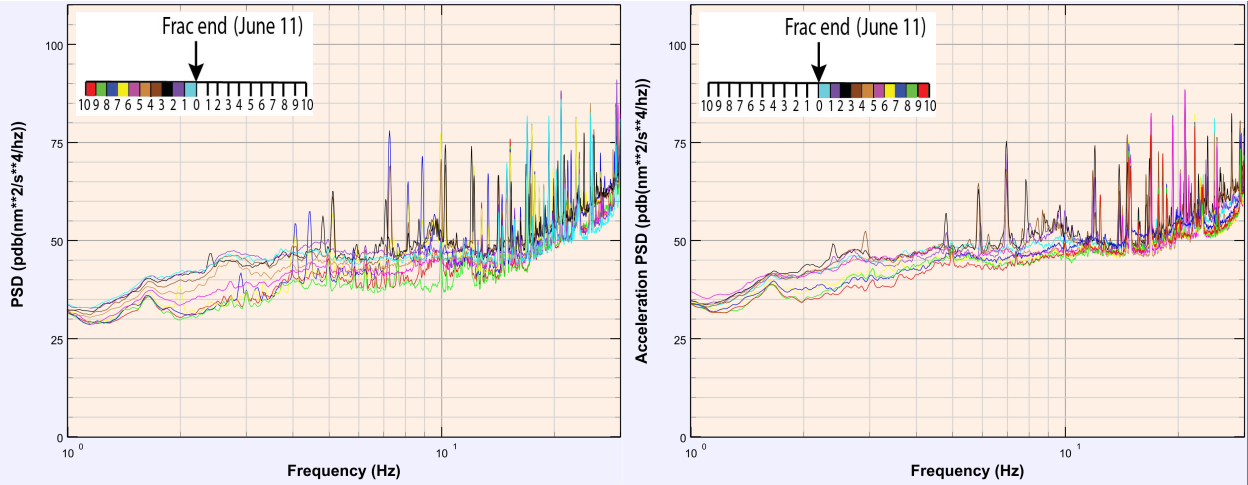

Figure 52 – Hourly frequency spectra for 10 hours before and 10 hours after final shut-in at Well 1.

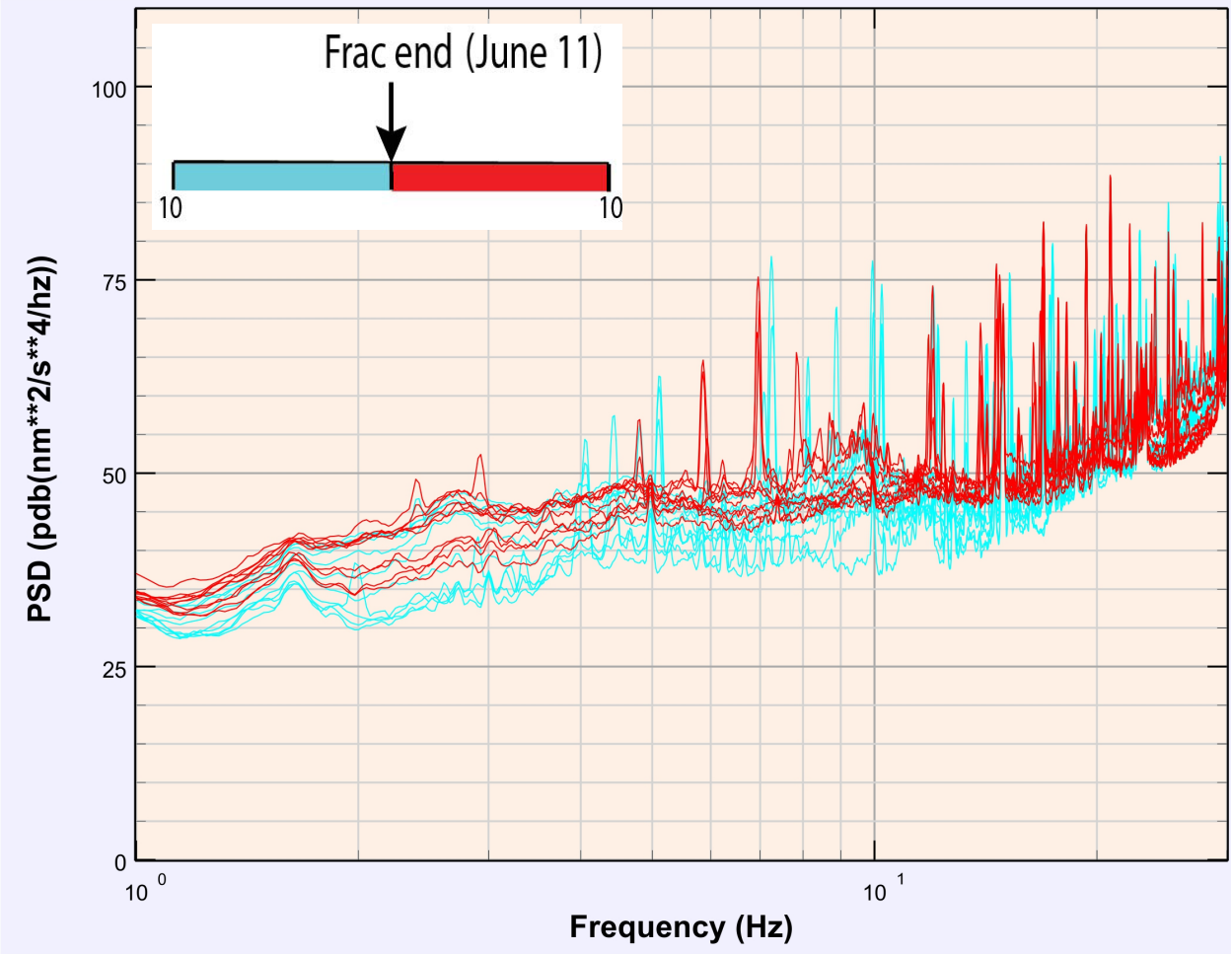

Figure 53 – Comparison of the syn- and post-frac spectra at Well 1. Syn-frac in blue and post-frac in red.

It has been shown that spectral analysis of broadband seismic signals can be informative and that there is absolutely an increase in the power of the signal in the very low frequency (VLF) ranges during and after fluid injection (for some time). There are a few sources of uncertainty in this study. Only one instrument was available for monitoring. Having more than one data stream for comparison of signals can be invaluable to the quality control of picked events. Secondly, there are obviously sources of noise on a well-pad that can contaminate the signal such as pumps and motors. The ten hours post-shut-in on both sets of wells show high PSD in the VLF early on that decreases gradually. Presumably, there is vastly less pump and motor noise during this time, which supports the interpretation here. However, without a detailed schedule of operations on the well-pad, there is uncertainty about noise sources. Lastly, the post-shut-in analysis may require longer time periods, such as 15 or even 20 hours. A decrease in PSD is observed during the ten hours post-shut-in, but perhaps a longer time period may show a complete return to baseline acoustic conditions.

3.3 CLEARFIELD COUNTY MICROSEISMIC STUDY

3.3.1 Introduction and Project Site Background

In mid-2013, one horizontal well in Clearfield County, North-Central Pennsylvania was drilled and hydraulically fractured in the Marcellus Shale over 13 stages. Microseismic monitoring was completed by Schlumberger, deploying two 12-level Versatile Seismic Imager (VSI) arrays down two existing vertical deep wells, simultaneously monitoring in both wells during fracturing (Figure 55a). Sensor spacing was 100 feet. This three-axis, single sensor seismic hardware/software combination features 24-bit analog to digital output, sensitivity of > 0.5 V/g +/- 5%, a natural frequency of 25 Hz with flat response from 3 to 200 Hz (Figure 54), dynamic Range of 105 dB at 36 dB gain, distortion < -90 dB, and variable sampling rate of 1, 2, or 4 milliseconds.

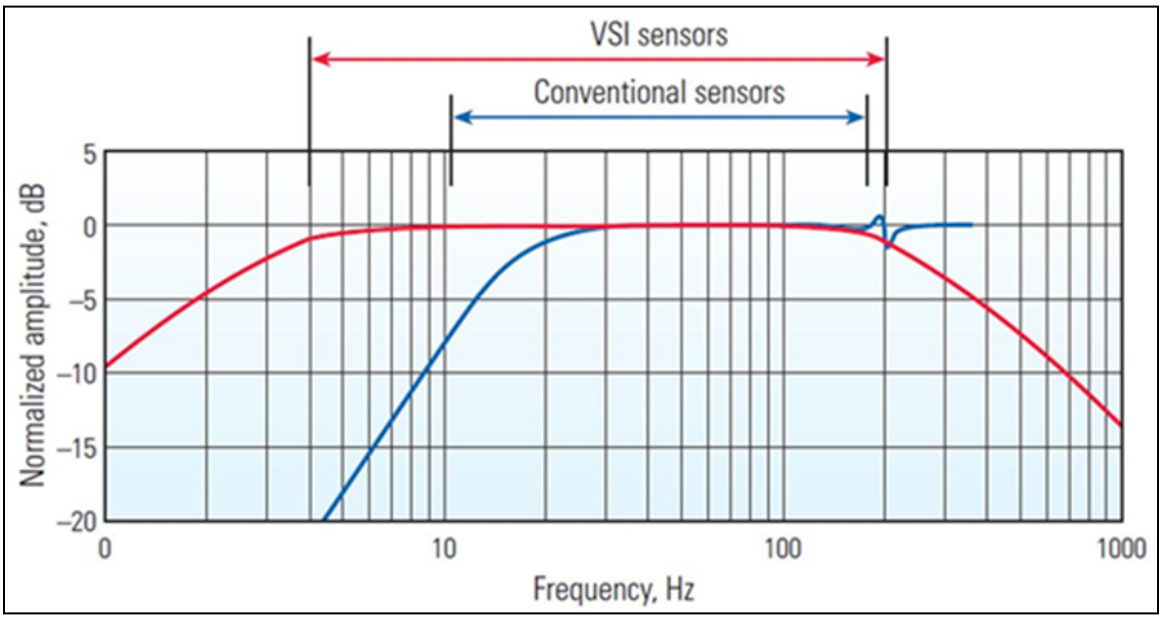

Figure 54 – Response of VSI sensors (red), showing flat response from 3 to 200 Hz, compared to conventional sensors. Modified from Arroyo, Breton et al. (2003).

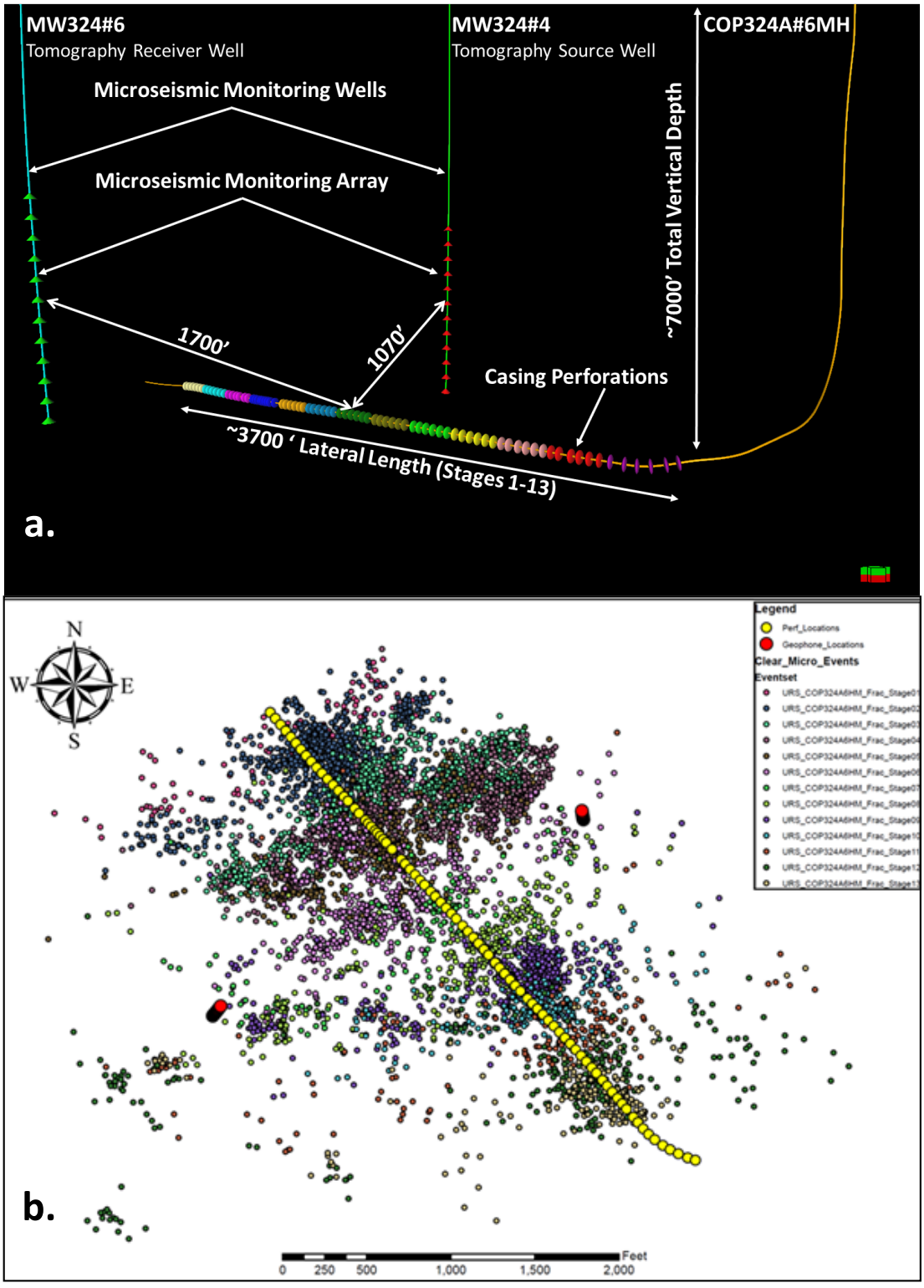

Figure 55 – a) Production and monitoring well geometry. b) Map view of lateral well, perforation locations, monitoring well locations, and the microseismic events associated with all stages in this study.

A total of 6,435 microseismic events were recorded at the geophones over the course of treatment (Figure 55b), ranging between moment magnitude M -3.26 and M -0.15, with a mean value of M -2.08. Additionally, cross-well tomography was acquired, utilizing the two monitoring wells as source and receiver, before and after hydraulic fracturing to measure changes in compressional and shear wave velocity in the volume of rock above the treatment/production well. The cross-well survey was also completed by Schlumberger with a 20 level array of geophones deployed down one of the vertical wells and a seismic source deployed down the other vertical well. The tomographic cross section is roughly perpendicular to the direction of the horizontal production well.

Two well logs were acquired: a standard suite including gamma ray, porosity, and sonic in one of the vertical monitoring wells, and a geomechanical suite including density, stress, horizontal and vertical elastic moduli and sonic velocity, Young's modulus, Poisson's ratio, and closure pressure in the lateral well, for its full length.

In Section 3.3.4, this study will focus on eight stages, with between 314 and 1354 events/stage, for a temporal fractal (b and D-value) analysis, similar to the Greene County Study previously described. Pumping pressure, rate, and proppant concentration, along with event magnitude, and diffusivity are incorporated in an effort to observe the interaction of hydraulic inputs and microseismic production.

In Section 3.3.5, an evaluation of energy, stress drop, microseismic event count, and average event magnitude as a function of elevation (i.e. stratigraphy) shows that there is a heterogeneous distribution of microseismic activity vertically. The geomechanical properties of the rock such as Poisson's ratio and Young's modulus, the presence of faults or open fracture systems, and the stress state of the rock at failure can cause this heterogeneity. Applying a

similar analysis, in Section 3.3.6, to the Lower Marcellus Shale sampled along the lateral well yields the insight that even within a single stratigraphic unit there is considerable geomechanical heterogeneity that controls the expression of microseismicity within that unit.

A critical shortcoming in the analysis of microseismic datasets is often that evidence for certain phenomenon, such as the presence of faults or the formation of fractures, is treated as stand-alone when it is more prudent to integrate with additional data to gain an understanding of local discontinuities, structural boundaries, and local stress field changes. Section 3.3.7 will integrate seismic attributes, microseismic cloud analysis, moment density maps, temporal and spatial b-values, and a cross-well p and s-wave tomography profile to characterize a previously unmapped discontinuity, likely an extension of an existing seismically mapped fault.

3.3.2 Overview of Rock and Fracture Mechanics

The objectives of Section 3.3 require an introduction to and high level discussion of rock and fracture mechanics. What is the physical definition of Poisson's ratio (PR) and Young's modulus (YM)? What causes a fracture to form? Once formed, how does the failure propagate through the rock?

Young's modulus and Poisson's ratio quantify how the rock strains (deforms) in response to stress. PR (Equation 31) is unitless and equal to the negative ratio of vertical strain (Equation 28) to lateral strain (Equation 30); more simply, if a material is compressed vertically, how much does it bulge outward laterally (Figure 56)? YM of elasticity (Equation 29) is simply the ratio of vertical stress (σ_{zz} in Figure 56) to vertical strain (Equation 28) (resultant units of stress); how difficult is it to strain the rock? The crossplot space of PR vs. YM (Figure 57) is informative in that it provides a relative measure of brittleness and density (Rickman, Mullen et al. 2008). In

this study, its primary function is to qualify the brittleness of a material, so data will generally follow the "brittleness vector" with deviations from this vector along the "density vector" with changes in density.

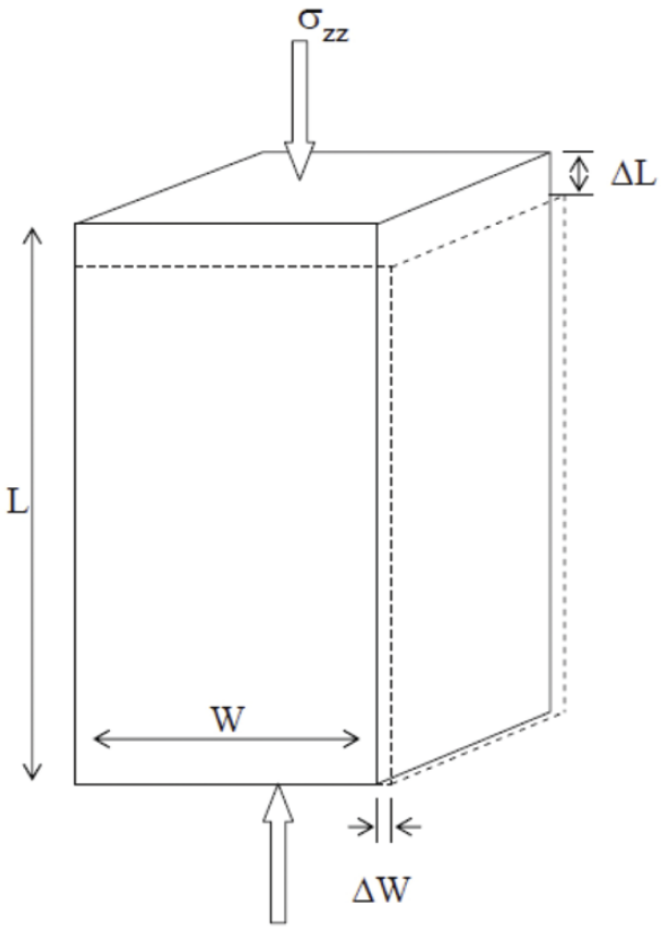

Figure 56 – The physical meaning of Young's modulus and Poisson's ratio. Modified from Wikel (2011)

$$\varepsilon_{zz} = \Delta L / L \qquad \textbf{Equation 28}$$

$$E = \sigma_{zz} / \varepsilon_{zz} \qquad \textbf{Equation 29}$$

$$\varepsilon_{yy} = \Delta W / W \qquad \textbf{Equation 30}$$

$$\nu = - \varepsilon_{zz} / \varepsilon_{yy} \qquad \textbf{Equation 31}$$

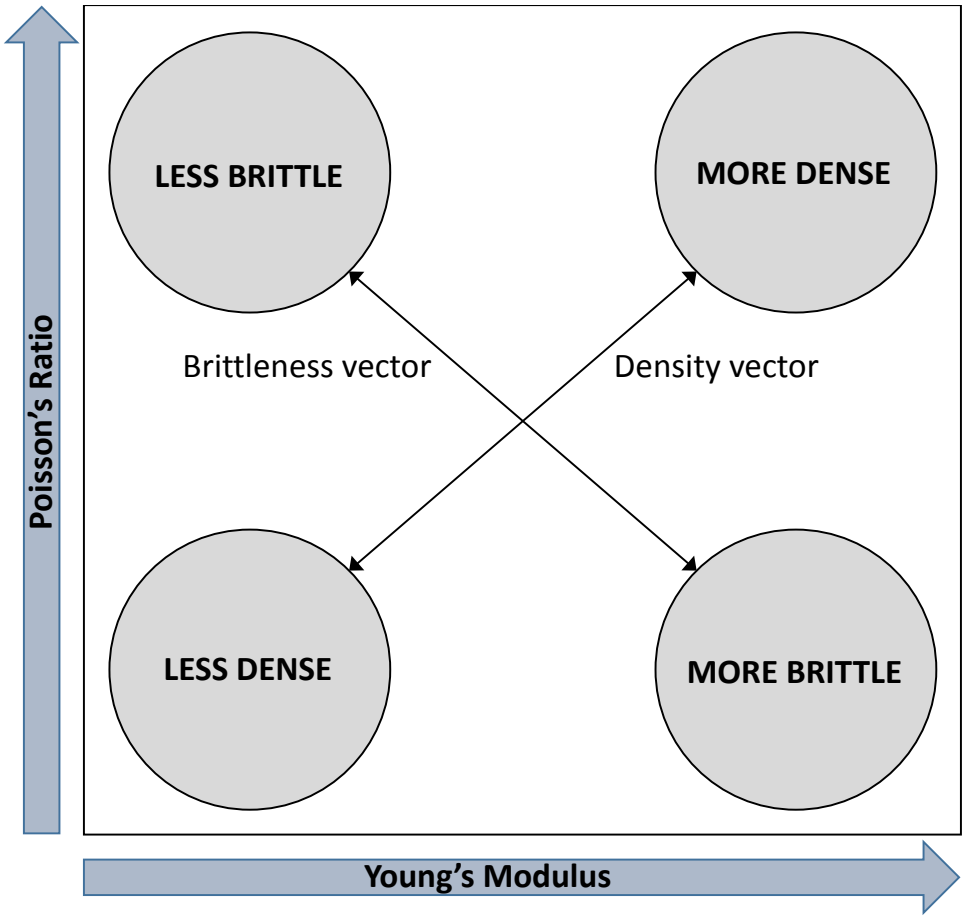

Figure 57 – A PR versus YM cross-plot provides information about brittleness and density.

Table 5 shows laboratory-calculated values of PR for various natural and synthetic materials, including ranges of values for common rocks. The end members of PR represent "strong but elastic or plastic" at the high end (0.5 – rubber) and "strong but brittle" at the low end (0.1 – diamond). The engineering definition for "brittle" is the tendency to fracture without straining under stress. A brittle material loses all of its strength at the point of the fracture. The middle values are occupied by the Earth-forming rocks and minerals. PR varies between 0.12 as an average minimum and 0.32 as an average maximum for naturally forming rocks. Shale spans the range of 0.05 to 0.32 and limestone: 0.1 to 0.33. A site specific vertical PR log in the zone of interest, including ~600 feet of interbedded shale and limestone, ranges from 0.18 to 0.28. The

lateral PR log, located wholly within the Lower Marcellus Shale, contains values ranging between 0.09 and 0.29. We use the term "brittle" on a relative scale of "more" or "less" due to the assumption that rock will not deform appreciably in this geologic setting, under the application of hydraulic fracturing stresses.

Table 5 – Poisson's ratios of natural and man-made materials. Modified from Gercek (2007)

Material	Poisson's ratio
Cork	~0
Diamond	
(natural)	0.10–0.29
(synthetic)	0.20
Concrete	
(28-day old)	0.10–0.21
(high performance)	0.13–0.16
Glass	
(quartz)	0.167
(obsidian)	0.185
(soda)	0.23
(borosilicate)	0.25
Sulfur	0.20–0.34
Porcelain	0.208
Tungsten carbide (WC)	0.222
Cast iron	
(gray)	0.26
(nodular)	0.28
Steel	
(mild)	0.27–0.30
(high strength)	0.30
Shotcrete	0.25–0.29
Human dentine (dry)	0.29
Perspex	0.311
Ice (at 257 K)	0.324
Aluminum 2024	0.33
Brass (70 Cu/30 Zn)	0.35
Lucite	0.358
PVC (hard)	0.378
Phosphor bronze (5% Sn)	0.38
Epoxy resin	0.38–0.40
Teflon	0.399
Nylon	0.40
Rubber	~0.50

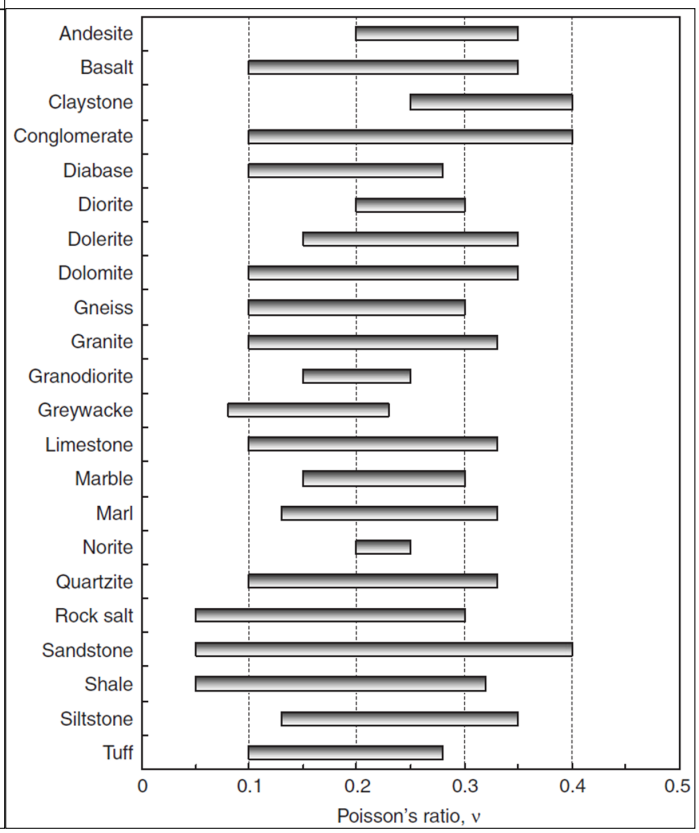

Expanding upon the basic PR-YM crossplot and its brittleness and density vectors, Goodway, Chen et al. (1997) introduced the Mu·Rho (shear rigidity x density) versus Lambda·Rho (incompressibility x density) cross plot (LMR) and its brittleness, lithology, and porosity vectors (Goodway 2009) as a more useful tool for the oil and gas industry (Figure 58). The general equations for MR and LR used in this study are acoustic impedance-based:

$$\mu\rho(MR) = SI^2 \qquad \textbf{Equation 32}$$

$$SI\ (shear\ impedance) = V_s\ (s\text{-}wave\ velocity) * \rho\ (density) \qquad \textbf{Equation 33}$$

$$\lambda\rho\ (LR) = AI^2 - 2 * SI^2 \qquad \textbf{Equation 34}$$

$$AI\ (compressional\ impedance) = V_p\ (p\text{-}wave\ velocity) * \rho\ (density) \qquad \textbf{Equation 35}$$

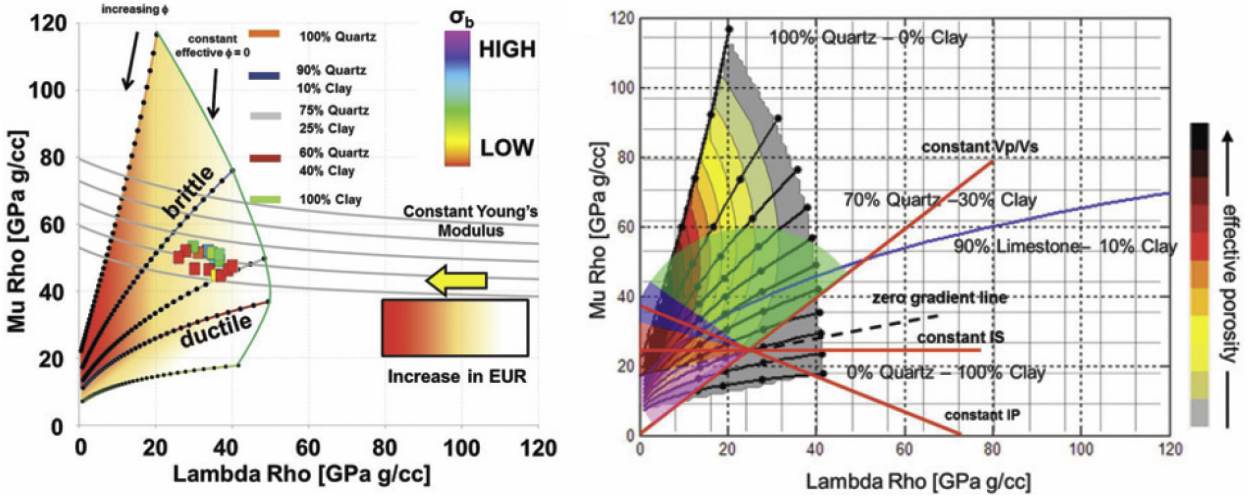

Figure 58 – The various property vectors of the MR-LR cross-plot, including brittleness, hydrocarbon recovery, Young's modulus, porosity, lithology, and impedance. Modified from Goodway, Monk et al. (2012)

Fractures form naturally in the Earth due to changing stress states (lithostatic, hydrostatic, tectonic) and the migration of fluids during processes such as catagenesis (hydrocarbon maturation). During hydraulic fracturing, pore pressure is perturbed to the point that either new fractures are formed, or more likely, existing fractures are stimulated. Mohr circles are typically used to illustrate the process of transitioning a rock from a stable stress state in which existing fractures in any orientation will not fail, to a critical stress state in which fractures existing at the

critical angle to the maximum stress direction are likely to fail, to an unstable stress state in which fractures at a wider range of azimuths are likely to fail (Figure 59). The transition is accomplished by increasing the pore pressure in the rock, thereby decreasing the effective pressure keeping the fractures from failing. In the case of hydraulic fracturing, failure is induced through the injection of fluid at sufficient pressure and rate to surpass the Mohr-Coulomb failure criteria. The failure envelope defined in Figure 59 is a function of the internal friction angle of the rock and also its inherent cohesion. Friction in rock is the mechanical resistance to movement due to surface asperities; cohesion is developed by cementing grains together. Cohesion is also responsible for the presence of tensile strength in rock. This is evident in the fact that the addition of cohesion pushes the end portion of the failure envelope into the negative compressive stress regime (i.e. tensile stress).

When fluid is injected, the differential stress (maximum horizontal stress – minimum horizontal stress) does not change because the pore pressure is subtracted from the confining pressure equally in all directions. The result is simply a translation of the Mohr circle to the left, toward the failure envelope. Once failure is induced, stress drop (see Section 3.1.4.1 for definition) causes a decrease in the differential stress, returning the rock to a stable stress configuration (Figure 60). It should be noted that there are, in fact, three principal earth stresses; two horizontal and one vertical. This example has neglected the vertical component, which would be denoted as $\sigma 1$ (the largest of the three stresses), because the dominant fracture orientation in this geologic setting is near-vertical. A near-vertical plane of failure minimizes the vertical component of the stress tensor, and the horizontal components become most important.

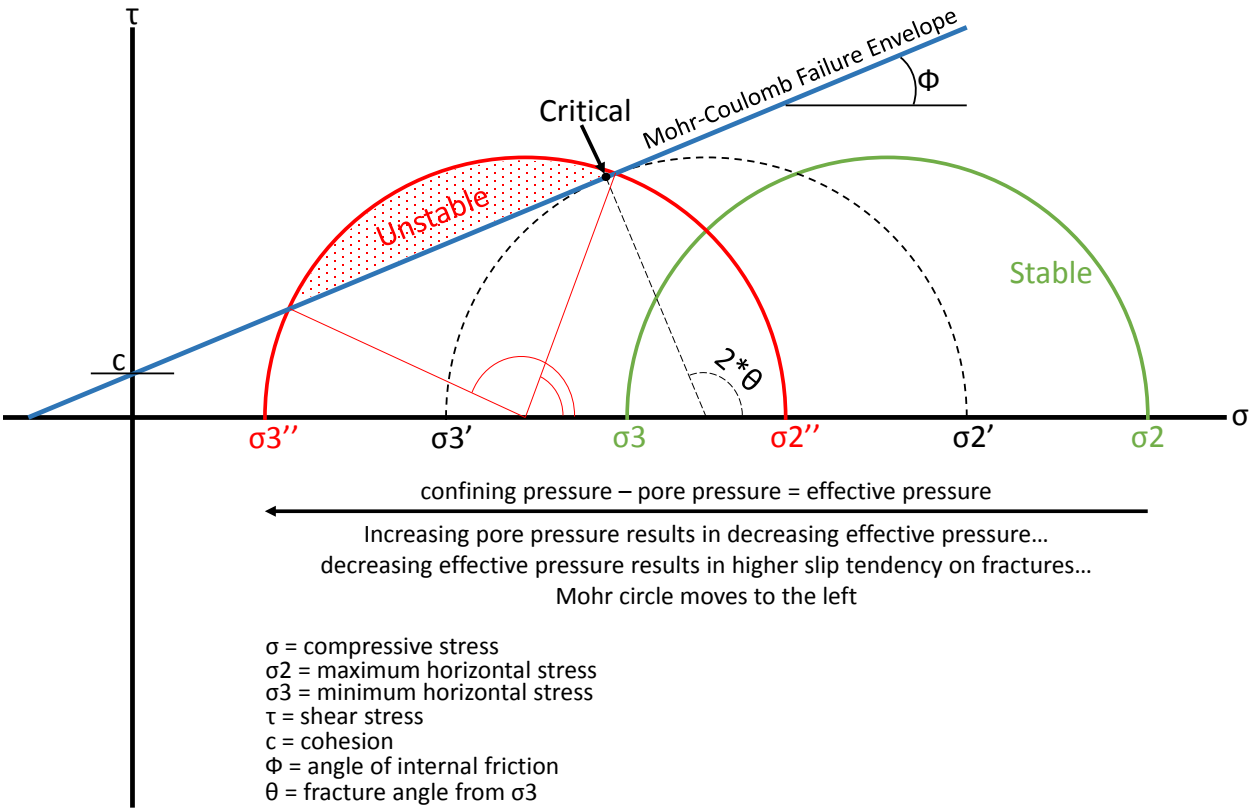

Figure 59 – Stable, critical, and unstable states of stress on a pre-existing fracture with respect to the Mohr-Coulomb failure envelope.

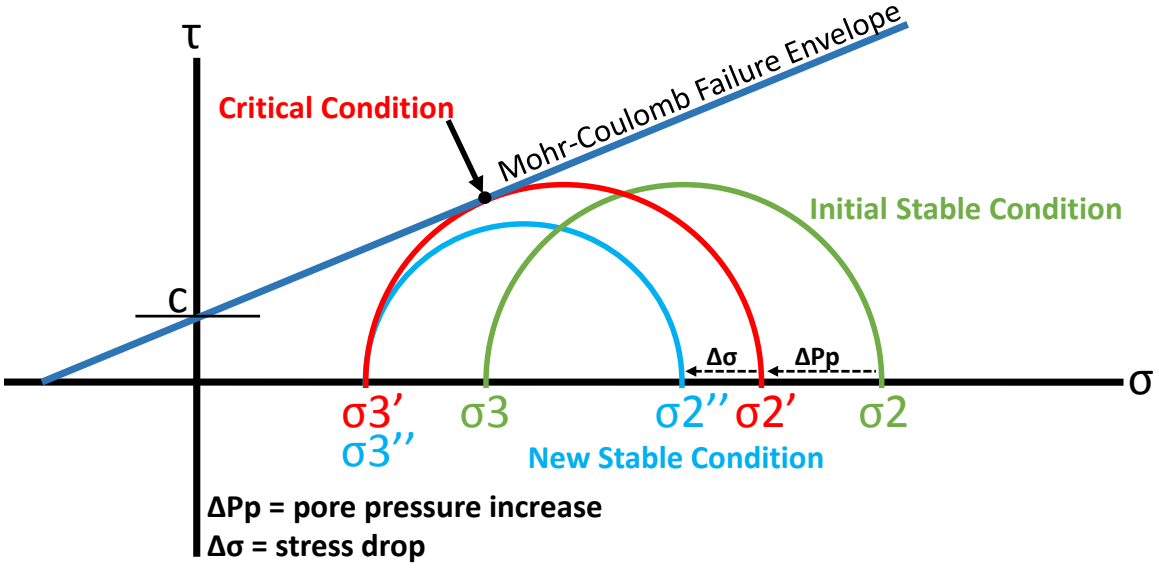

Figure 60 – The evolution of failure on a fracture: stability→pore pressure increase→failure→stress drop→stability. After Goertz-Allmann, Gischig et al. (2012).

There are multiple types of failure that can happen along a fracture. Figure 61 illustrates the different types that may be encountered during hydraulic fracturing and their associated location on a Mohr diagram. A fracture can fail from tensile opening, sliding and tearing (pure shear), or some combination of tensile and shear failure (mixed mode). Around a propagating fracture, the stresses are constantly evolving as the fracture develops (Figure 62). Mode I failure is most likely at the distal fracture tip (Warpinski 2013) where tensile stresses are most concentrated, and Mode III or some mixed mode failure will occur to either side of the tip. The fracture left in the wake of the propagating tip will experience very little additional deformation aside from aperture increase, as the surrounding rock is being put into compression, effectively strengthening the medium. Within the "compressive zone" fracturing fluid is "leaking off" from the main fracture into existing micro-fractures, causing additional damage to the rock. Recall the discussion in Section 3.1.2 about hydraulic diffusivity. Microseismic events occurring in the "tensile zone" and the "shear zone" likely correspond to the triggering front while microseismicity with the "compressive zone" likely occupies the space behind the triggering front. The back front would correspond to the progressive collapse of the "compressive zone" as the pore pressure in the fracture dissipates upon well shut-in.

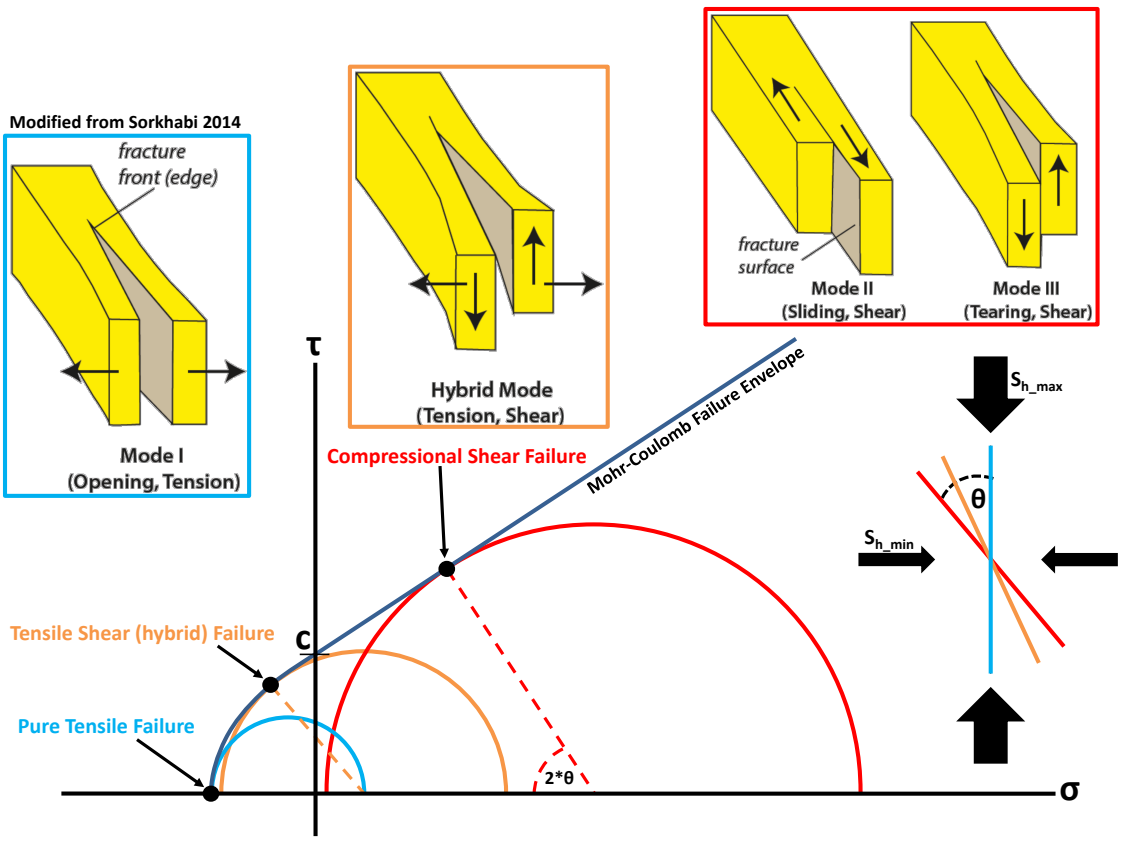

Figure 61 – Failure mechanisms, their location on a Mohr diagram, and the relative angular relationship between the failure plane and the principal horizontal stresses. Modified from Sorkhabi (2014).

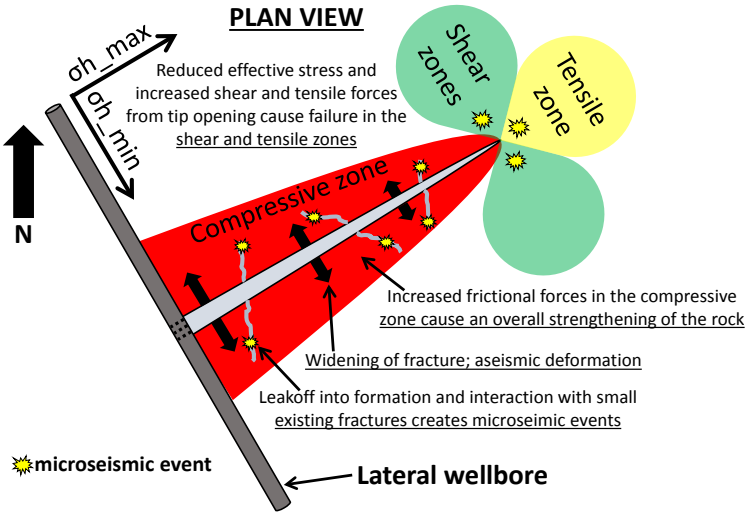

Figure 62 – Schematic diagram of the stress zones around a propagating hydraulic fracture. After Warpinski (2013).

3.3.3 Characteristics of the Microseismic Catalog

A striking characteristic of the Clearfield microseismic catalog is the distinct vertical separation into two groups of events; one centered at -5,220 feet EL (Lower Marcellus target zone) and one at -4,700 feet EL (below the Tully Limestone, within the Upper Hamilton Group's Moscow Shale and Ludlowville Shale members) (Figure 63a). Plots such as Figure 63a can be used to easily identify out-of-zone event concentration that may indicate stimulation of existing faults or fracture sets. Magnitude versus count plots provide multiple pieces of information, namely the distribution of magnitudes, maximum event magnitude, and the absolute detection limit of the receiver array (Figure 63b). In nature, the number of seismic events increases exponentially with decreasing magnitude (Gutenberg and Richter 1944), but the ability to instrumentally detect seismicity decreases with decreasing magnitude. Figure 64a and Figure 64b illustrate that total fracture length (laterally away from the wellbore) ranges between 1,600 feet and 2,100 feet with longer fracture lengths to the SW, and height growth reaches 650 feet upward and 200 feet downward.

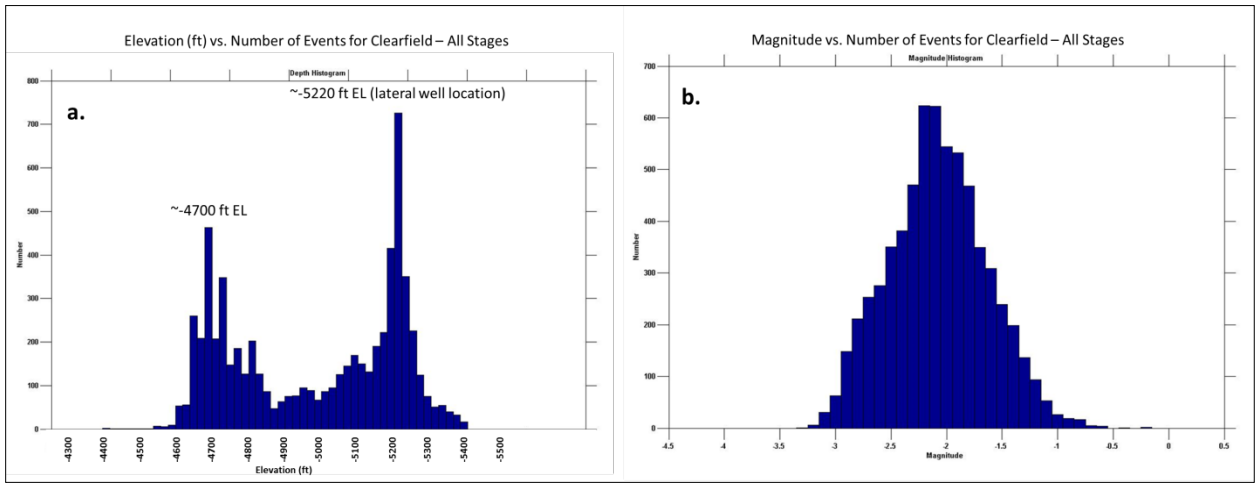

Figure 63 – Basic plots of event elevation versus count (a) and event magnitude versus count (b).

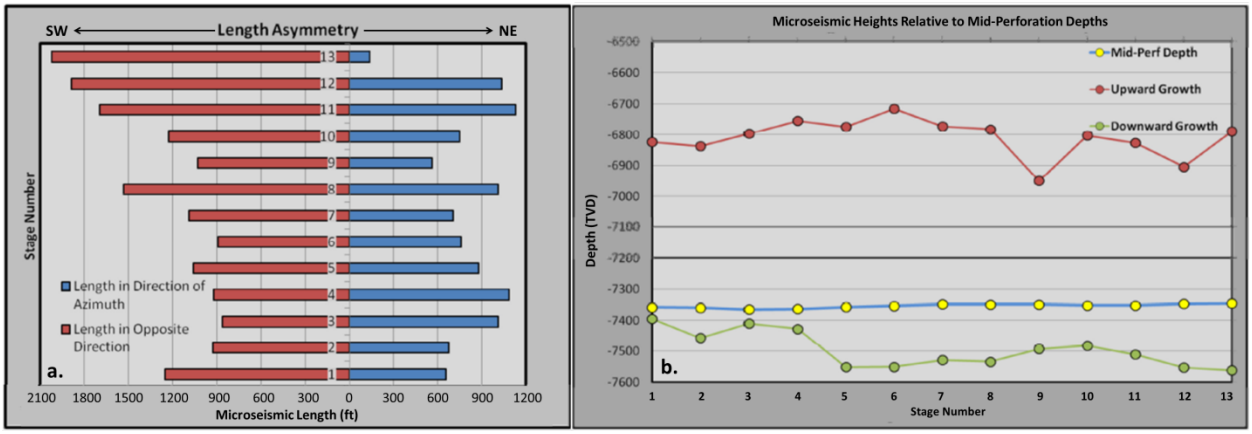

Figure 64 – Lateral and vertical microseismic growth for each stage. Modified from Schlumberger (2013).

Figure 65 and Figure 66 show that as the job moves forward in time through the stages, both the average magnitude and the moveout distance (distance between microseismic events and the stage perforations) gradually increases. Magnitude increases from -2.40 in the first few stages to -1.54 in the last stage. The maximum moveout distance of the microseismic cloud increases from approximately 1,500 feet during Stage 1 to approximately 3,600 feet during Stage 12. If the elevation of the microseismic events is viewed against cumulative time for all stages it becomes evident that microseismic activity is not homogeneously distributed across stratigraphy in time or space in any stage. Stages 3 through 6 contain high concentrations of microseismic events in the Moscow and Ludlowville Shale members of the Upper Hamilton Group, with distinct clustering of events around thin limestone beds. Only stages 2, 3, 4, and 9 contain high concentrations of microseismic activity in the Lower Marcellus target zone.

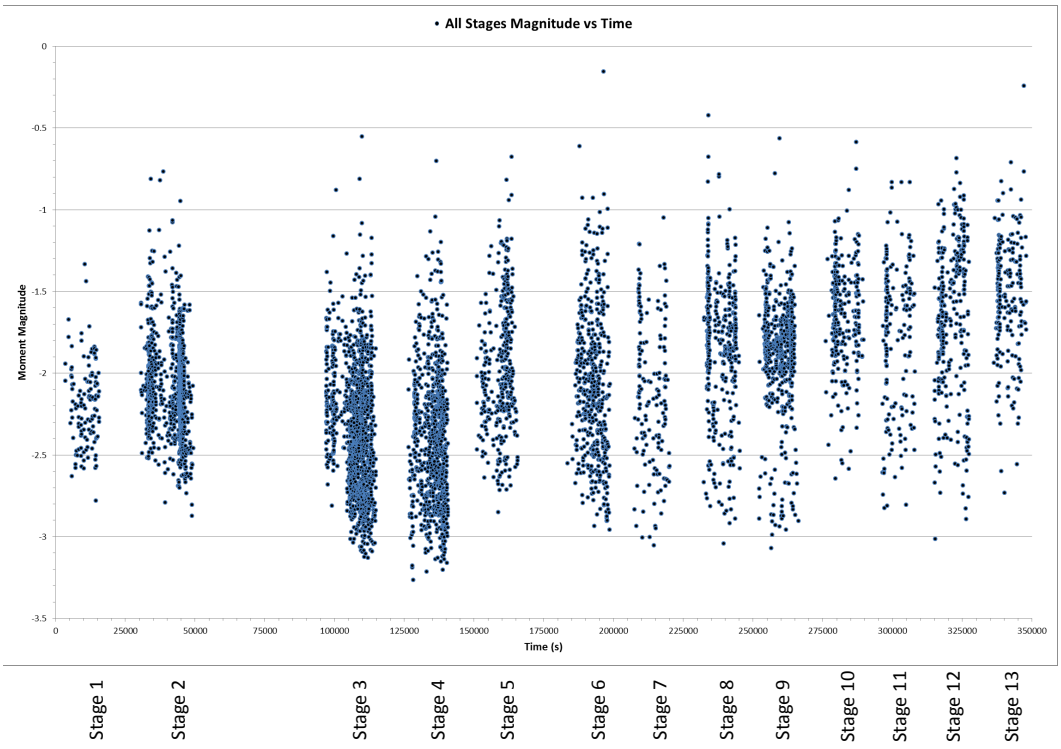

Figure 65 – Event moment magnitude versus time. Discrete stages become apparent.

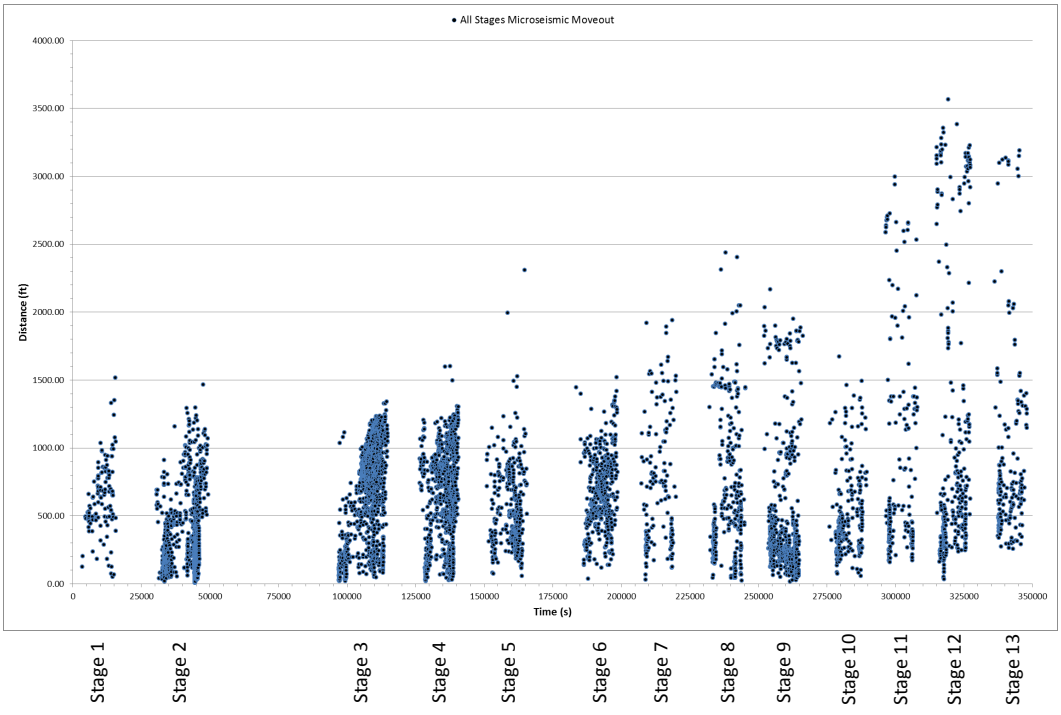

Figure 66 – Injection point to event distance versus time since start of injection.

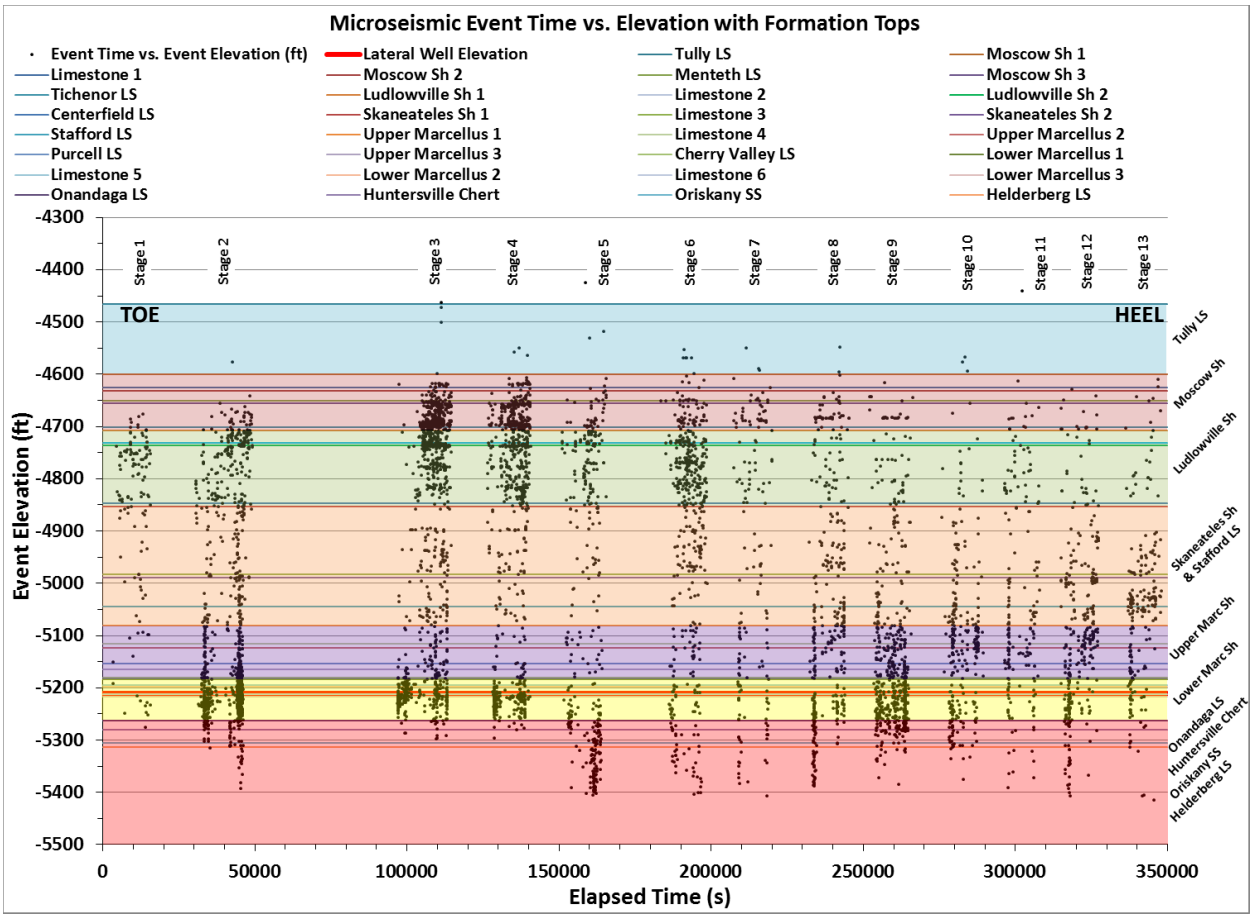

Figure 67 – Event elevation versus time since the start of injection, with geologic column. Detailed stratigraphy from USGS (1993).

An important aspect of microseismic data that is often overlooked is the inherent limitation related to array geometry and sensitivity. In this case there are two vertical wells with twelve broadband (3-200 Hz) geophones in each, at the depth of the stimulation, monitoring simultaneously. As the distance from the geophone array increases, the minimum magnitude that can be detected also increases, known as detection bias (Figure 68). The sloping line illustrates the distance-magnitude relationship; at a given distance along the abscissa the seismic catalog is complete above this line and incomplete below the line. For example, at a detection distance of ≤ 2,000 feet, the seismic catalog is complete above a magnitude of -2.3. One must keep in mind

when interpreting the microseismic cloud that detection of smaller events diminishes away from the array. To remove this bias during large scale structure interpretation, the user should employ a detection distance versus magnitude plot to implement an appropriate lower magnitude cutoff that still represents the majority of the data points but removes the small magnitude event clustering close to the array. However, the user should keep in mind that close to the monitoring array, small events may help to partially define geologic structures and this information should not be discarded. Figure 69 illustrates the change in the microseismic detail as a function of event magnitude. The top left scenario includes all events > -3.1 M (essentially the entire catalog). The 500 foot radius circles in this case represent the area of the map in which the user can have confidence in the completeness of the catalog above this very small magnitude. As smaller events are removed from the catalog, the confidence radius becomes larger. At a radius of 2,000 feet, most of the area of interest is contained within the circles; however the map now contains no microseismic events smaller than -2.31 M. The overall shape and extent of the microseismic cloud is similar between the top left and bottom right scenarios, but the level of detail, especially in close proximity to the monitoring arrays, has been softened by removing the smaller magnitude events.

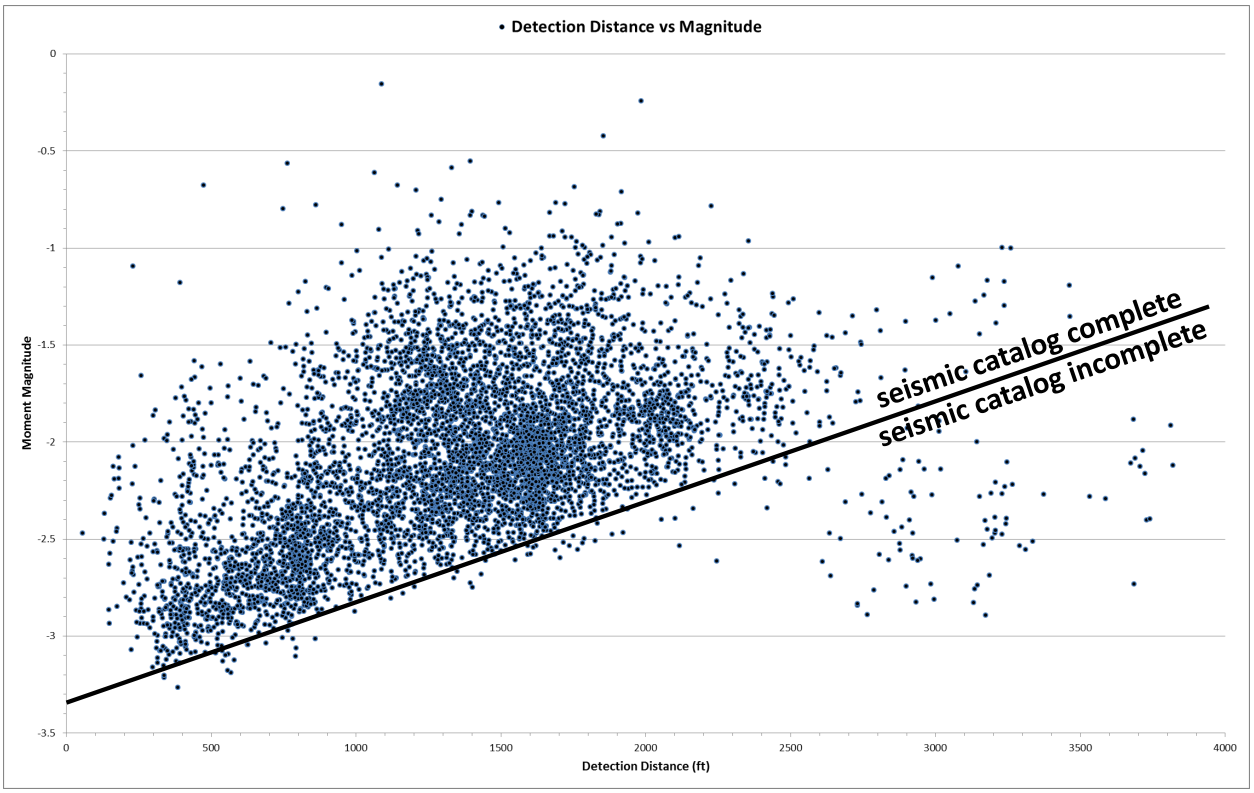

Figure 68 – Moment magnitude versus the distance from the event to the receiver string. This plot provides information about the completeness of the microseismic catalog at a given distance from the receiver.

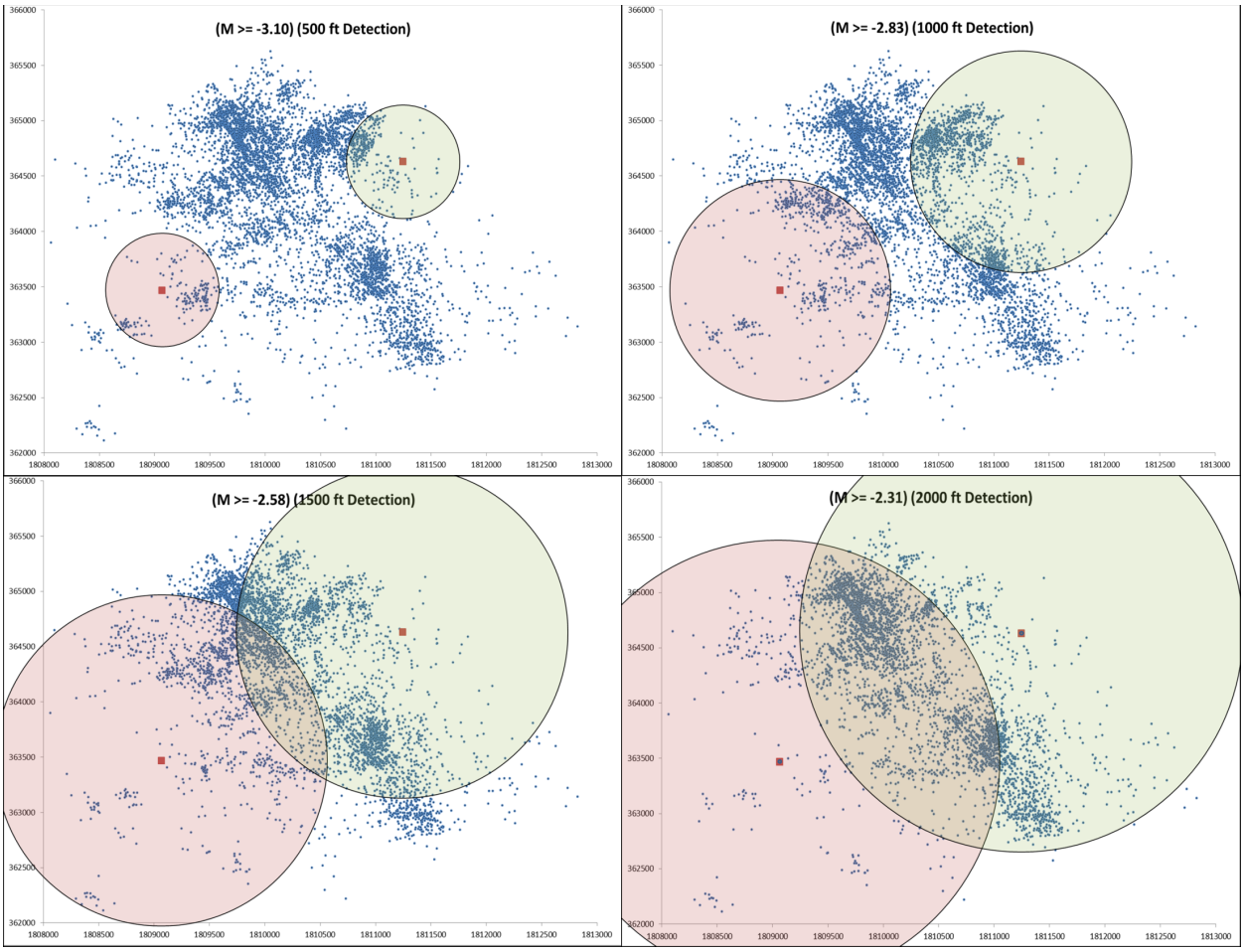

Figure 69 – Graphical representation of detection bias. At < 500 feet distance from the receiver, the microseismic catalog is complete for all events ≥ M-3.10. At 2,000 feet distance, the catalog is complete only for events ≥ M-2.31.

The signal to noise ratio (SNR) of the detected events should be scrutinized to ensure that confidence in the magnitude, s-wave/p-wave amplitude ratio, and event location is high. This dataset has been filtered to remove all but the most confidently detected and located events (Figure 70a; Figure 70b). However, even after a 38% reduction in the event count, it is evident that the overall relative distribution of events and shape of the microseismic cloud has not been altered significantly as a result of the filtering process.

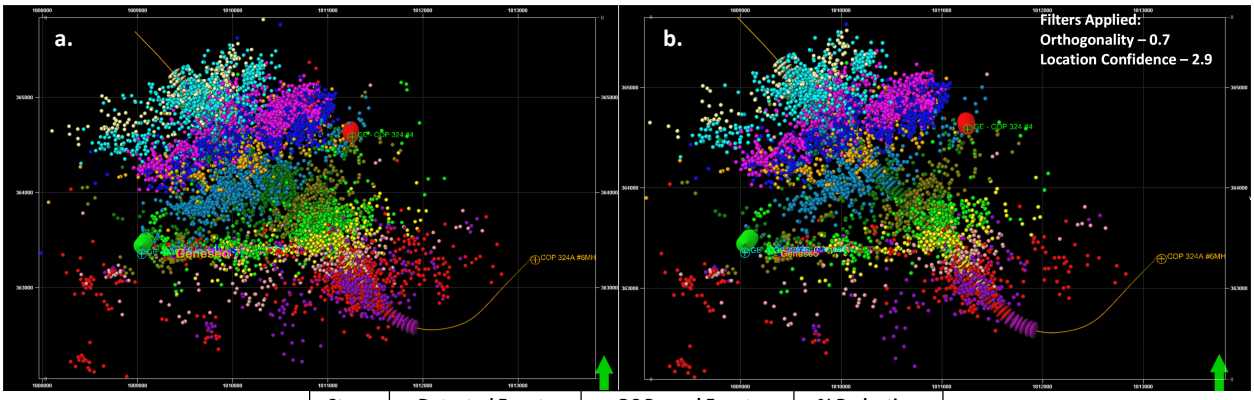

Stage	Detected Events	QC Passed Events	% Reduction
1	201	124	38
2	1697	1354	20
3	1446	1199	17
4	1139	874	23
5	475	354	25
6	1006	478	52
7	463	158	66
8	510	370	27
9	1684	557	67
10	421	270	36
11	299	179	40
12	618	314	49
13	376	204	46
Total	10335	6435	38

Figure 70 – Spatial distribution of microseismicity, pre- and post-QC/filtering process.

The SNR should absolutely be > 1 and preferably > 2.5. Figure 71 and Figure 72 show that ~90% of the events have a location SNR ≥ 2.5, 100% > 2.0, and ~90% have a detection SNR ≥ 2.0. Figure 73 shows an example of the differences in microseismic waveform quality that can be present in the catalog, with a high quality seismogram and a low quality seismogram from two different events. On the high quality seismogram, the P and S wave arrivals are distinct, the arrival time difference can be accurately measured (allowing accurate X and Y location), and there is strong similarity in the parabolic moveout between the two monitoring arrays (allowing accurate Z location). The low quality seismogram lacks well defined P and S wave arrivals.

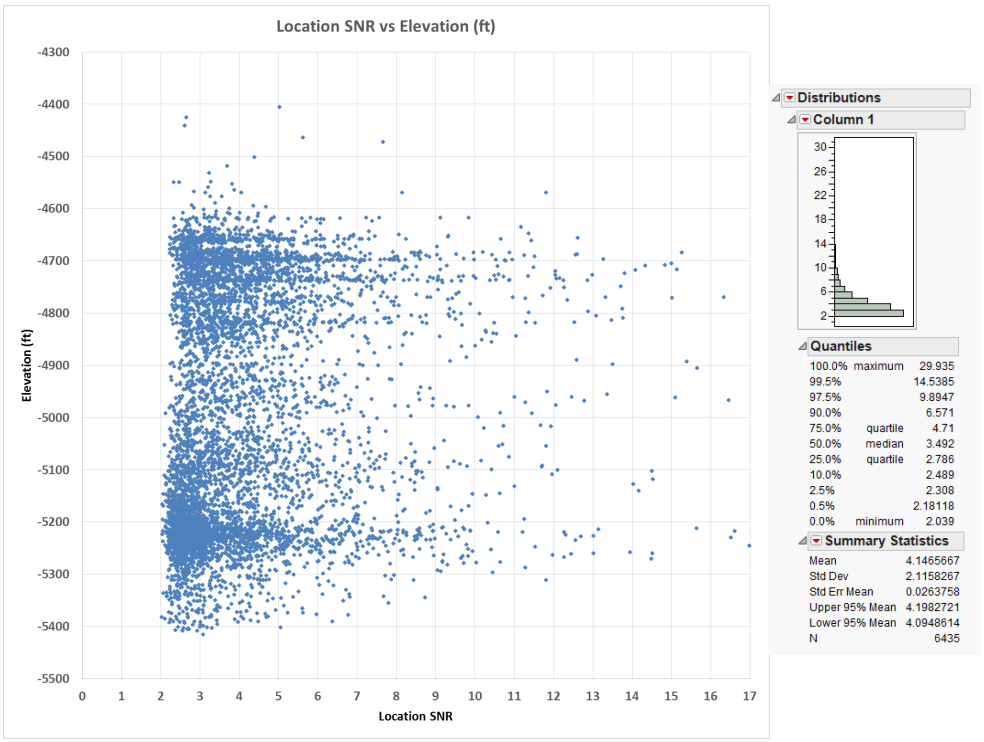

Figure 71 – Event elevation versus the location signal to noise ratio.

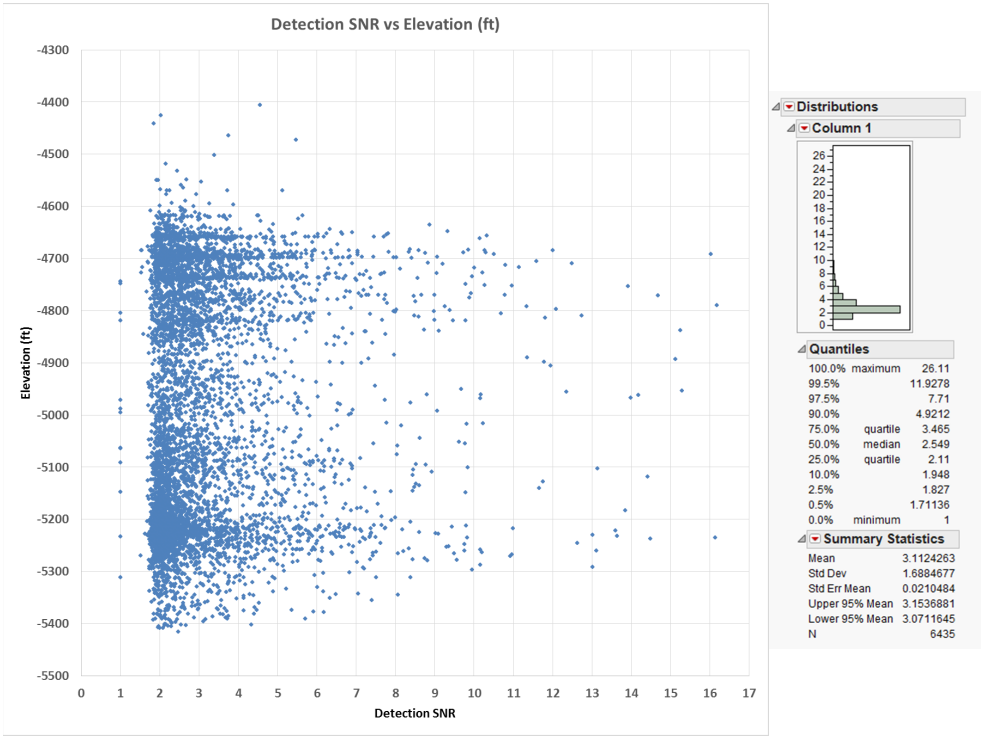

Figure 72 – Event elevation versus the detection signal to noise ratio.

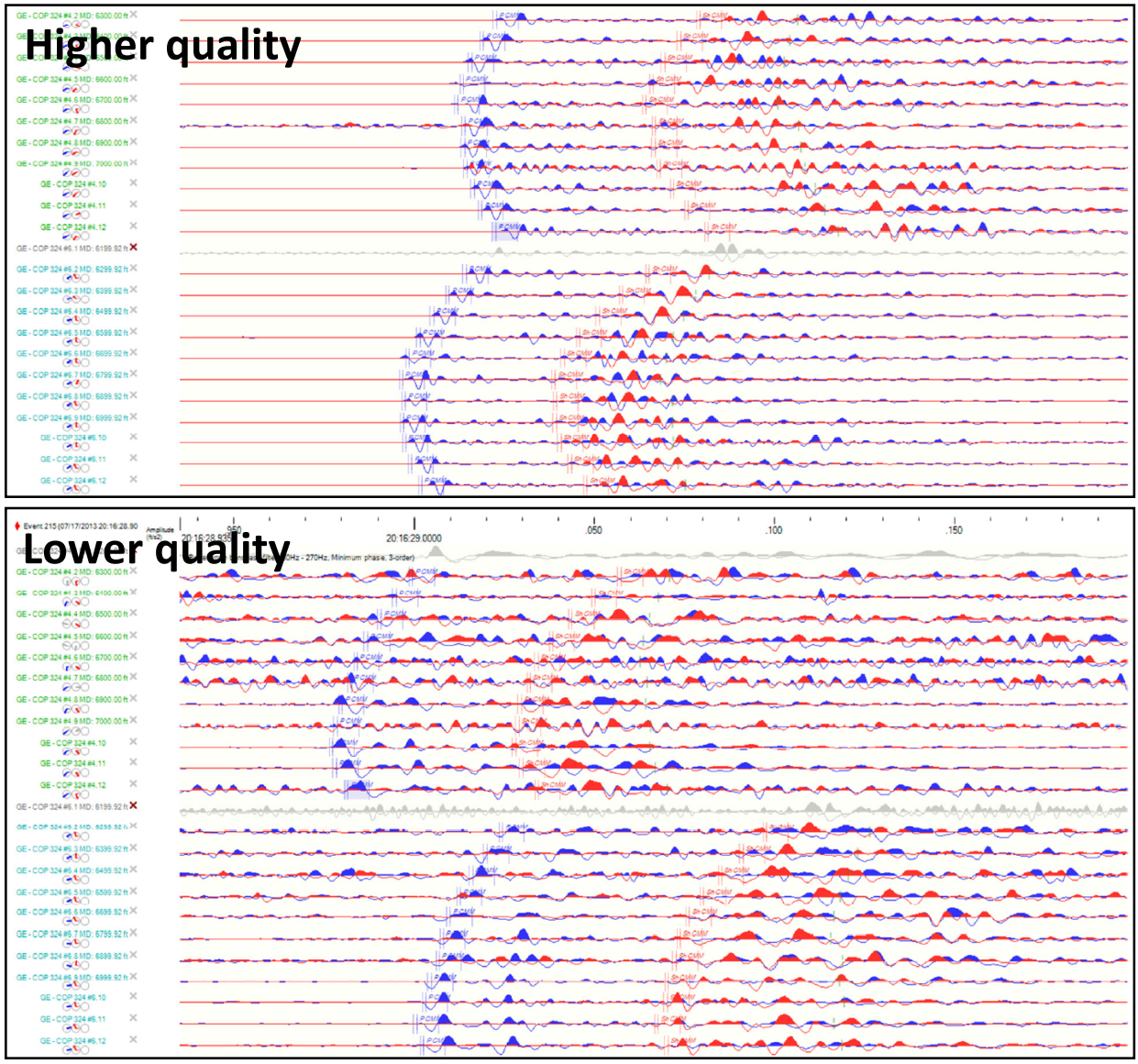

Figure 73 – Examples of high and low quality seismograms from a microseismic event.

The display of location uncertainty to the end user is accomplished in this particular dataset through the use of uncertainty ellipsoids (Figure 74), the three axes of which define the three principal dimensions of maximum, medium, and minimum uncertainty, the eigenvectors and eigenvalues.

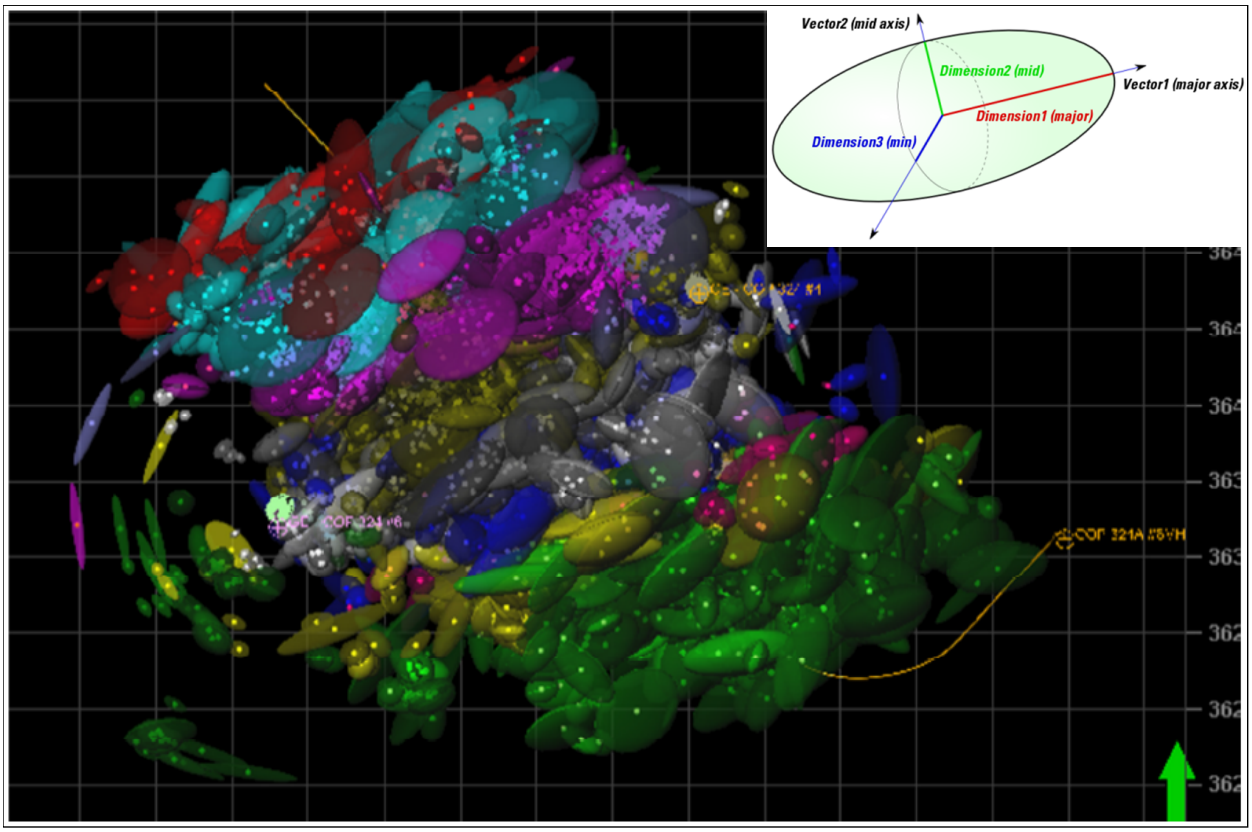

Figure 74 – The eigenvector/value method of reporting location uncertainty on three independent axes.

3.3.4 Temporal and Spatial Analysis of Hydraulic Fracturing Stages

As seen in the previous Section 3.2 - GREENE COUNTY MICROSEISMIC STUDY – SPE MANUSCRIPT, a similar approach has been applied to the calculation and comparison of b- and D-values to the temporal and spatial location of microseismic events and also the pumping information such as pressure, rate, and proppant concentration. The b- and D-values were calculated using the program ZMAP (see Section 3.1.1.2 – Spatial Fractal Analysis). The analysis of Clearfield data focuses on eight stages that yielded a sufficient number of events to allow a robust analysis.

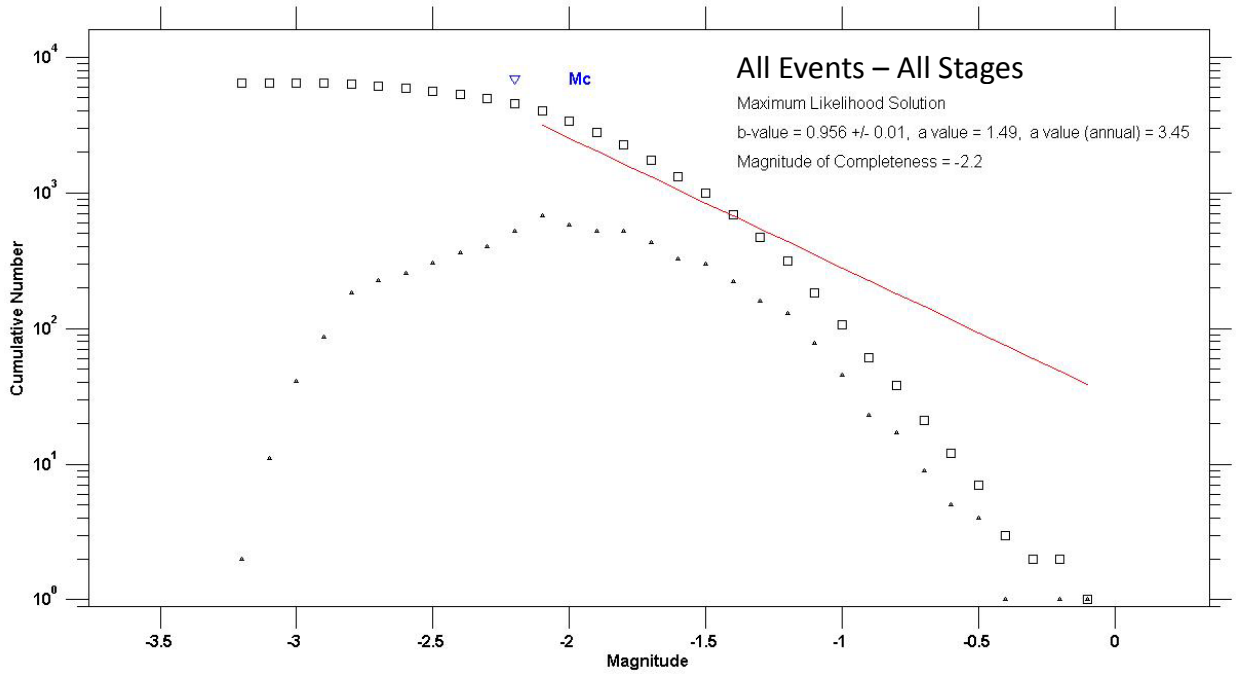

Figure 75 – The frequency-magnitude distribution and overall b-value for the entire microseismic catalog.

A single b-value calculation for the entire catalog (Figure 75) yields a value of ~ 1. However, there is stage and sub-stage level variation in b-value that suggests heterogeneity in the stress state and geomechanical properties of the rock as the hydraulic fracture network is developed. Figure 76 and Figure 77 represent the b-value calculated for each stage and by advancing an event selection window forward in time, respectively. Both figures show an overall lower b-value (< 1) in the middle stages of the well. Section 3.1.1 discusses the interpretation of b-values in the case of microseismic catalogs, stating that low b-values represent failure in a state of higher overall differential stress, such as at the boundary of two fault blocks. Figure 77 also includes the temporal D-value for comparison to the b-value. This b- to D-value comparison follows previous studies by Grob and van der Baan (2011). Similar to their findings, we show here a poor correlation between b and D during development of the fracture network, indicated by high b-values signifying a large proportion of small events. However, microseismicity from

stages 5, 6, and 7 results in relatively focused b- and D-values, compared to other stages. During these three stages, D-values plot between ~1.5 and ~2.0 and b-values plot between ~0.8 and ~1.3. This observation of planar D-values (D=2) and fault related b-values (b=1) also agrees with the findings of Grob and van der Baan (2011). During the time period in their microseismic dataset when they suspect the presence of fault interaction, they see this relationship between b and D. During the time period of the Clearfield microseismic dataset when fault interaction is suspected, this relationship is observed. This observation will be discussed in greater detail in Section 3.3.7 as one identifying characteristic of a possible fault crossing the stimulated rock volume.

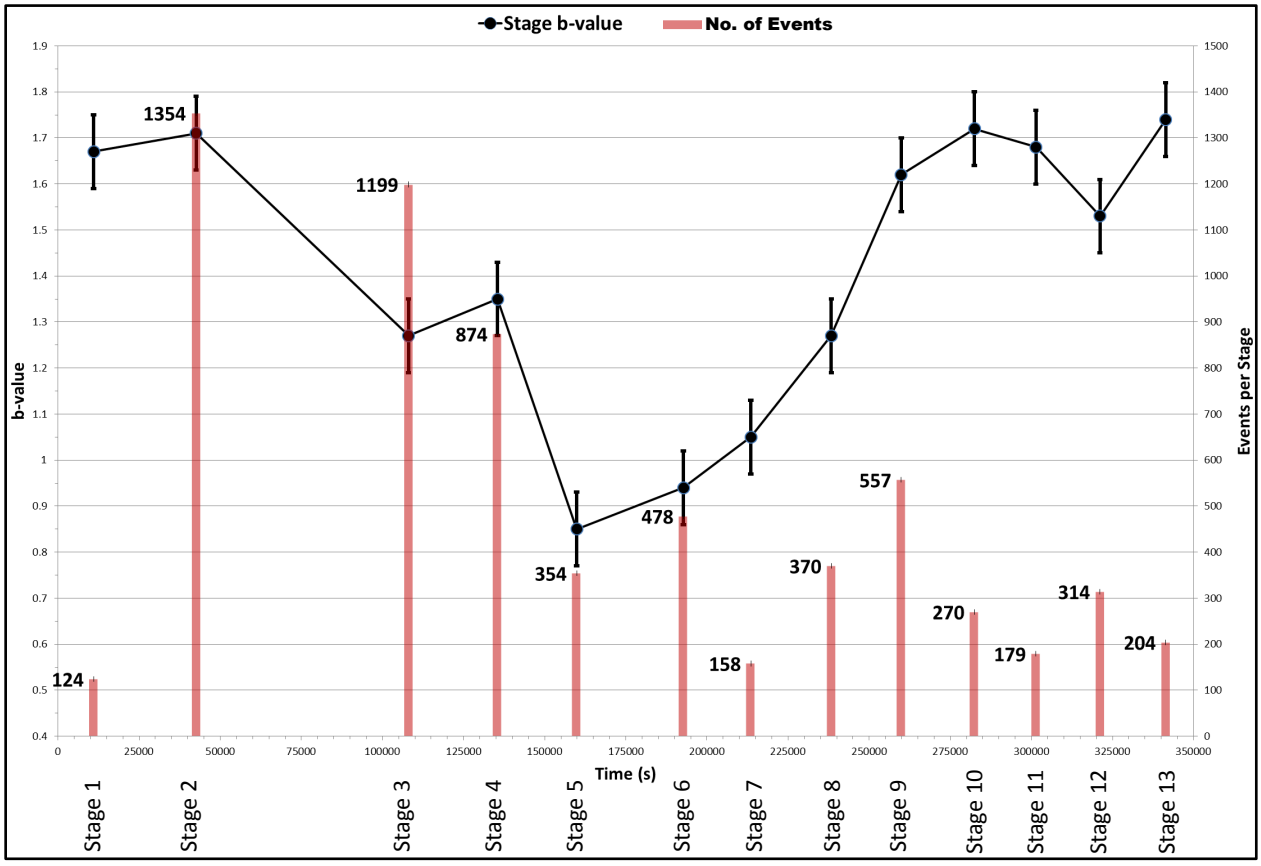

Figure 76 – Stage-by-stage b-values along with the total numbe of events in each stage.

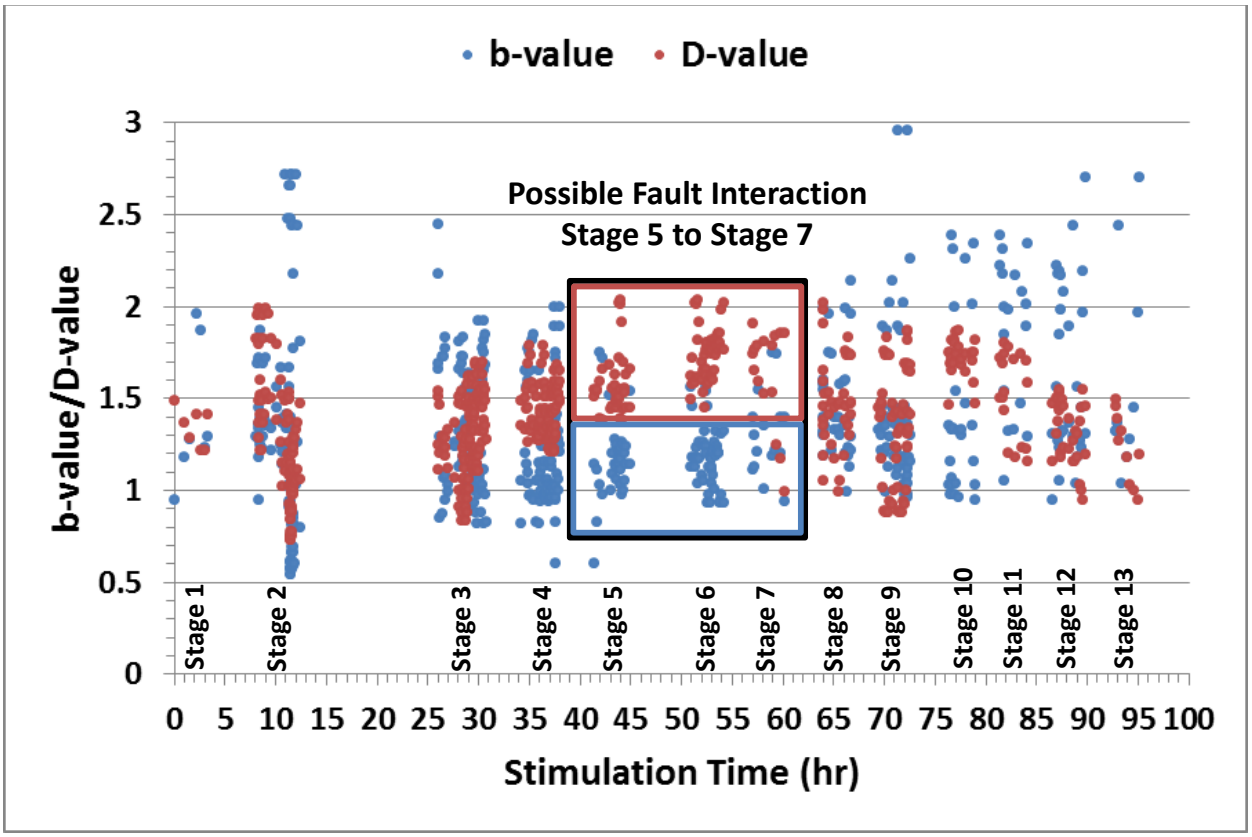

Figure 77 – Temporal b- and D value for all events from all stages at Clearfield. Calculation is made for a 200 event window moving forward in time, overlapping by 180 events.

Eight out of thirteen total stages contained greater than 300 microseismic events, allowing for better fractal and spatial analysis of these stages. The following pages contain description and discussion of the spatial, temporal, fractal, and hydraulic properties of each of these eight stages. This familiarity will benefit the reader in later sections.

3.3.4.1 Stage 2

After a relatively non-productive (microseismically) first stage, with only 124 verified events (Figure 76), Stage 2 was much more active; the most active stage of the entire well. Figure 78 shows the top (a) and side (b) views of the microseismic cloud associated with Stage 2. The

events are colored by relative time since the start of fluid injection; red is early in the stage and dark blue is late. The early events occurring ~400 feet above the well are likely attributed to the previous stage, occurring post-shut-in, but the recording process includes them in Stage 2. Recall the earlier discussion in Section 3.1.2; the pressure front radiates outward from the injection point, known as the Triggering Front (Rothert and Shapiro 2003). Microseismic events beyond the triggering front in space can be attributed to the previous stage, or they are the result of stress and pressure transfer. Figure 63a shows that there are two distinct concentrations of microseismic events vertically, at -4,700 feet and -5,220 feet elevation, within the entire catalog. It is evident that this spatial distribution is reflected in Stage 2 (Figure 78b).

There is limited lateral growth in the direction of S_{h_max}, and growth is mostly vertical and concentrated around the well perforation. The single b-value for the stage equals 1.71, but the b-value time series tells a slightly different story (Figure 79a and Figure 79b). Figure 80 shows the b-value time series, along with the D-value, pumping data, moment magnitude, source-event distance, and diffusivity time series. The stage is characterized by concentrations of events in the first 60 minutes and the last 30 minutes of pumping, with a dearth of events in the 2½ hours between. Observe in Figure 78 that, aside from the few events very early on (likely associated with the previous stage), microseismicity initiates at the perforation and propagates away from the wellbore. After the prolonged period of relative inactivity, the operator abruptly stops the flow of fluid and proppant into the wellbore, and then restarts the flow (sans proppant). This reinitiates microseismicity close to the wellbore, creating a cloud of ~800 events, or about 60% of the total recorded microseismicity for Stage 2 over a time span of ~30 minutes. The onset of this concentrated microseismicity coincides with an increase in the b-value from ~1.25 to ~2.0

(Figure 80, dark red curve). The dense cloud exists in a volume of rock which had been previously fractured, and is presumably in a state of lower differential stress.

The D-value time series in Figure 80 indicates that as the microseismic cloud evolves its spatial arrangement changes from planar to linear and then events begin to cluster near a point source when activity is reinitiated near to the wellbore.

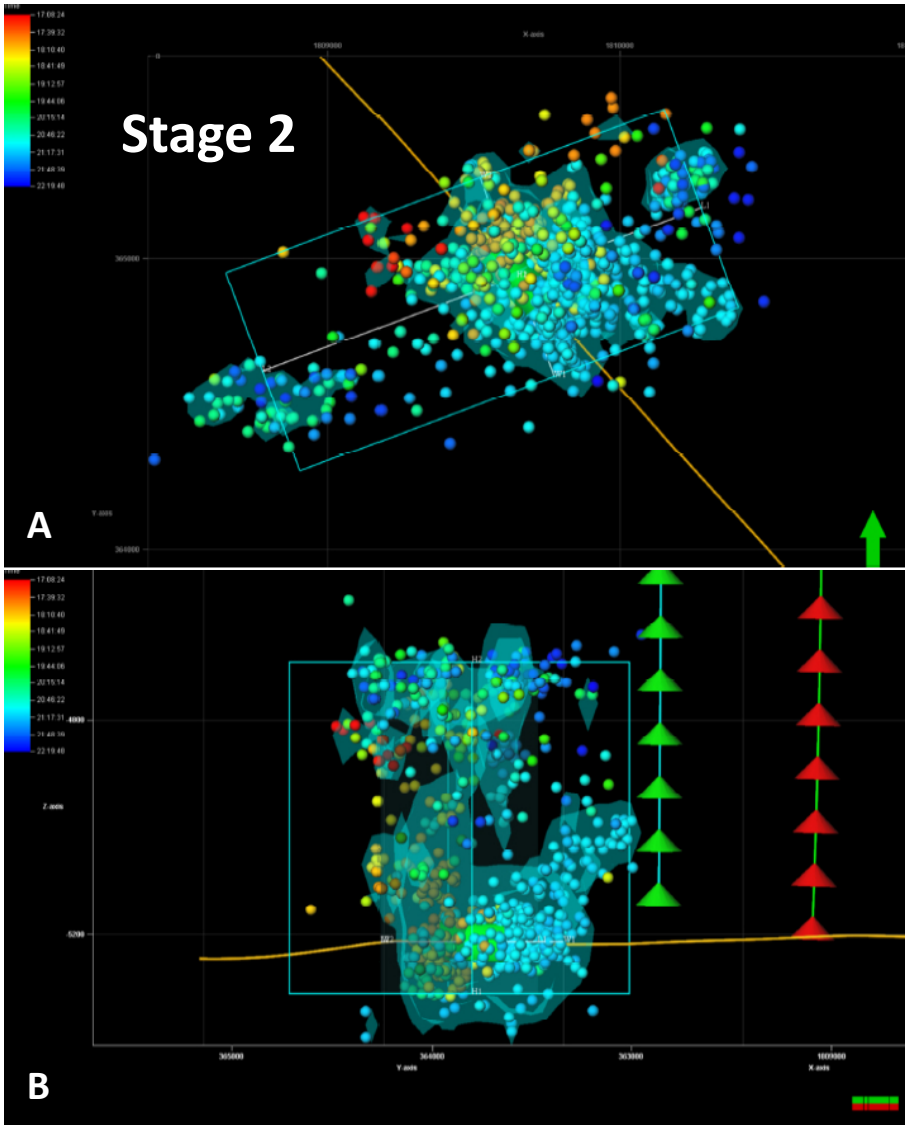

Figure 78 – (a) Map view of microseismic events during Clearfield Stage 2. (b) Side view of microseismicity during Stage 2, view looking northeast. Events colored by time of occurrence: red = early, blue = late.

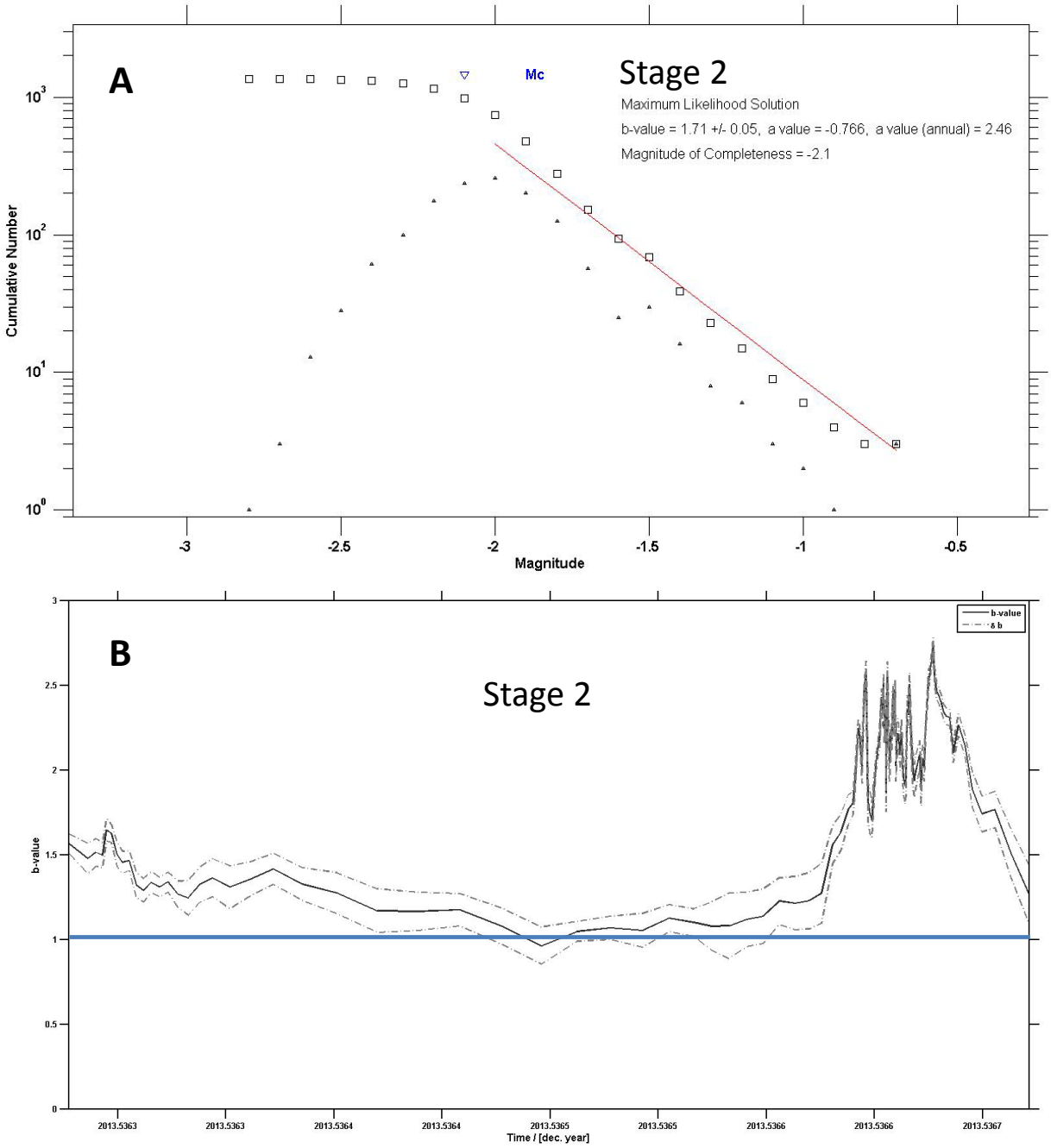

Figure 79 – (a) Overall b-value of Clearfield Stage 2 = 1.71. Magnitude of completion = -2.1. (b) b-value time series for Stage 2. Dotted lines represent error bounds.

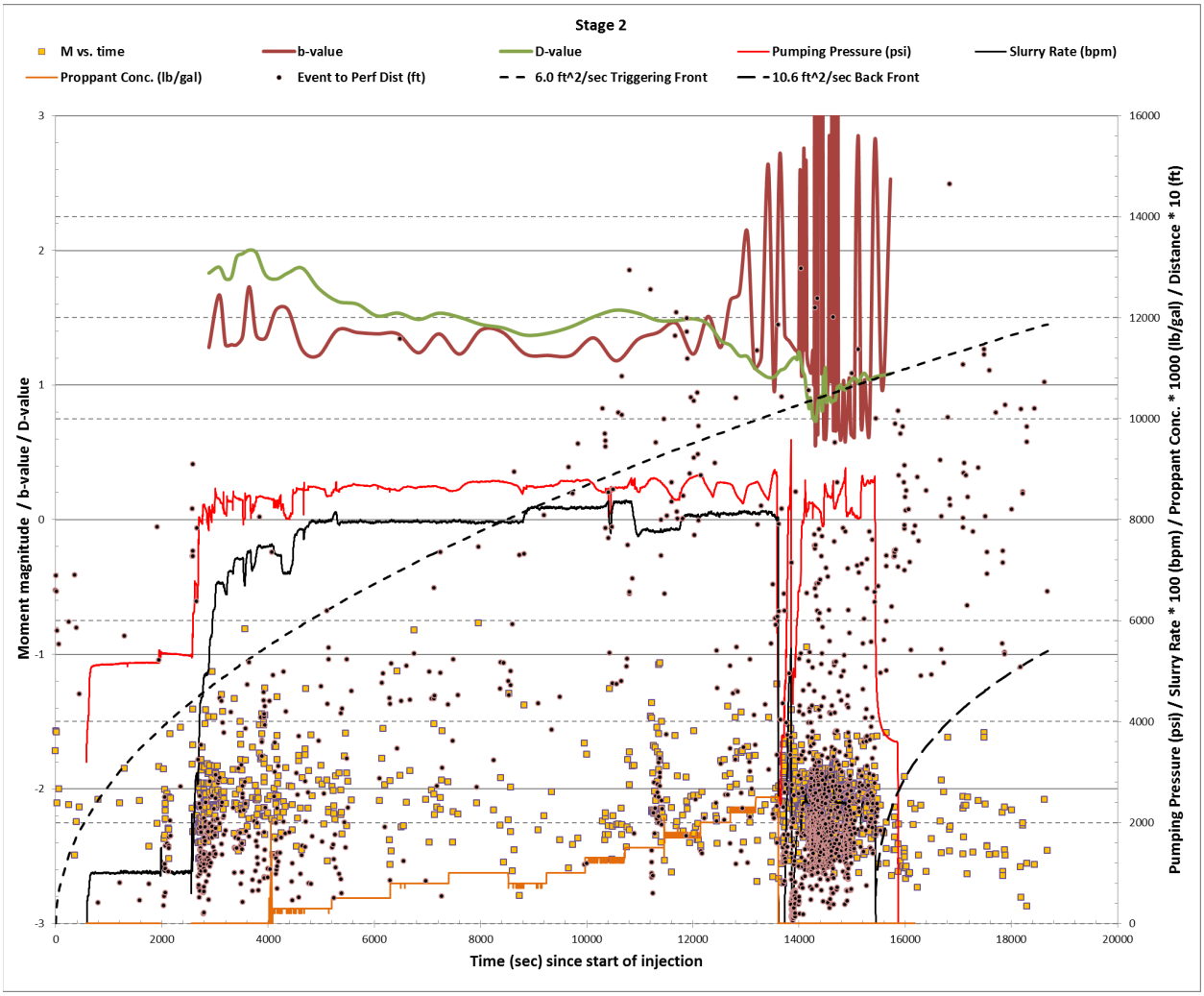

Figure 80 – Pumping pressure, rate, and proppant concentration, diffusivity triggering front and back front, event magnitude, perforation to event distance, b-value, and D-value versus time for Clearfield Stage 2.

3.3.4.2 Stage 3

Stage 3 created the second most number of recorded microseismic events, at 1199. The events form a well-defined elongated cloud with a long axis aligned with S_{h_max} (Figure 81a). As expected, microseismicity originates at the well perforation and radiates away from the well as fractures propagate outward and vertical growth is mostly upward (Figure 81b). The cloud is split into two distinct groups, vertically, as was seen in Stage 2. A small number of events are

observed close to the wellbore late in the stage (Figure 81b, blue events and Figure 83, ~16,100 seconds). This is significant because it represents a distinct back-front (discussed in Section 3.2.3.2) (Rothert and Shapiro 2003). As the pumping of fluid commences at the beginning of the stage a pressure front moves away from the injection point, triggering microseismic events (the triggering front). When pumping is ceased, known as "shut in", a second pressure front moves away from the injection point, with relatively high pore pressure in front of it and lower pressure behind it (the back front).

Stage 3 has an overall b-value of 1.27 but varies between ~1.3 and 0.8 (Figure 82; Figure 83). The b-value gradually decreases throughout the stage as the microseismic cloud reaches farther from the injection point. The lowest b-values occur in the second half of the injection, when the great majority of events are occurring between 600 and 1,200 feet from the perforation. A small increase in the b-value is observed at around 16,000 seconds, as a back front forms in response to well shut in. The variation in D-value is unremarkable, ranging between ~0.8 and ~1.7, indicating a linear to planar arrangement of sequential events.

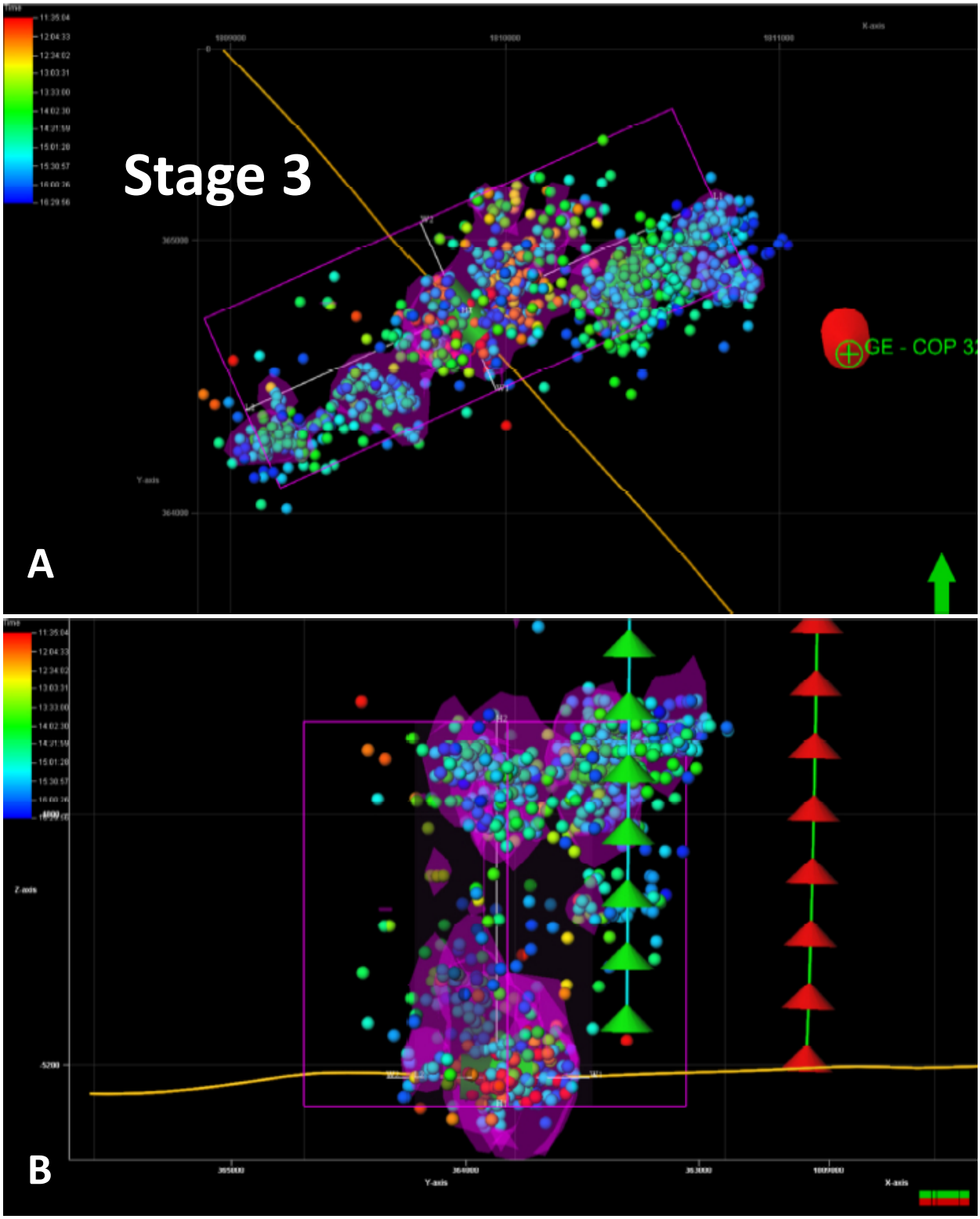

Figure 81 – (a) Map view of microseismic events during Clearfield Stage 3. (b) Side view of microseismicity during Stage 3, view looking northeast. Events colored by time of occurrence: red = early, blue = late.

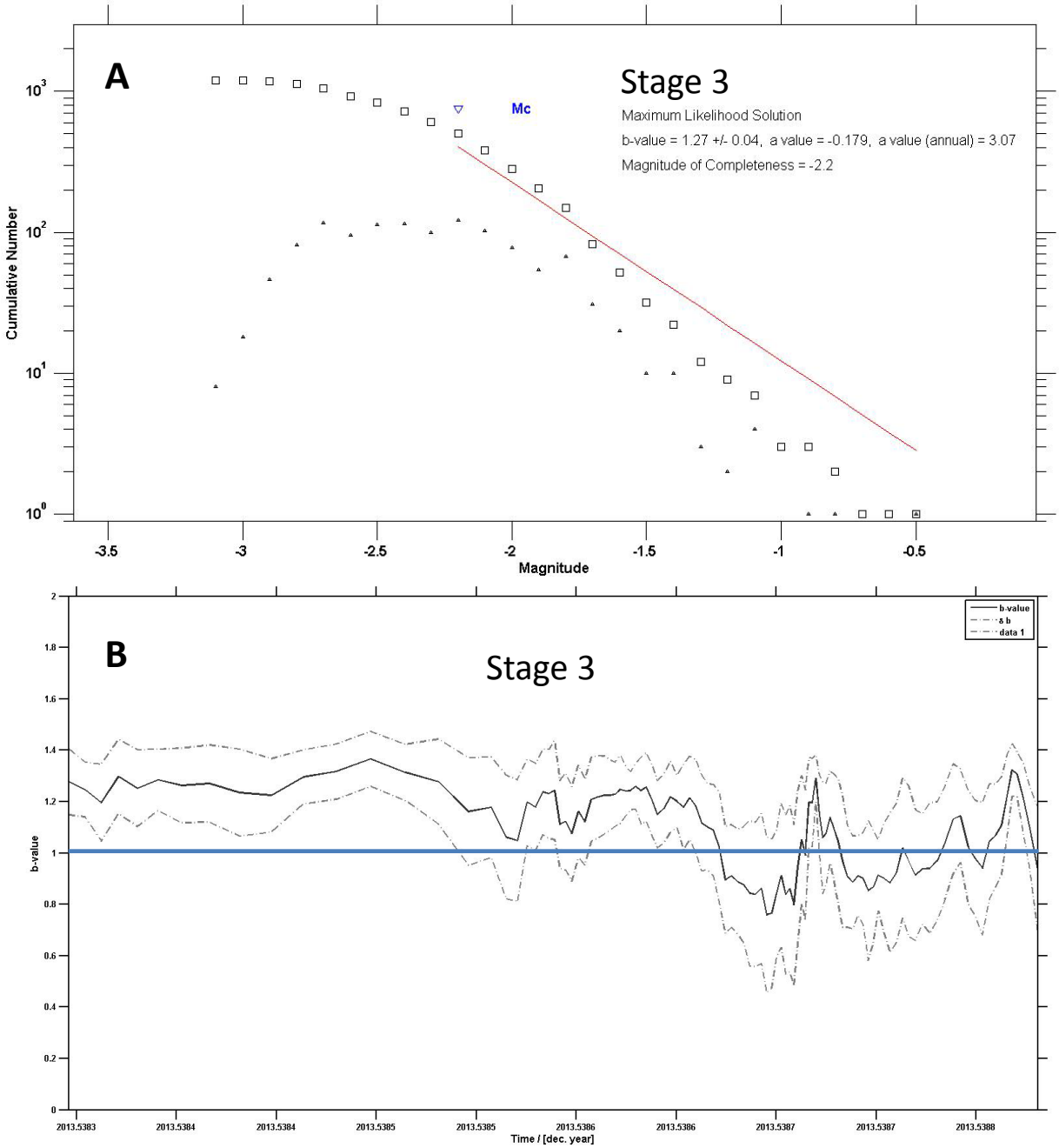

Figure 82 – (a) Overall b-value of Clearfield Stage 3 = 1.27. Magnitude of completion = -2.2. (b) b-value time series for Stage 3. Dotted lines represent error bounds.

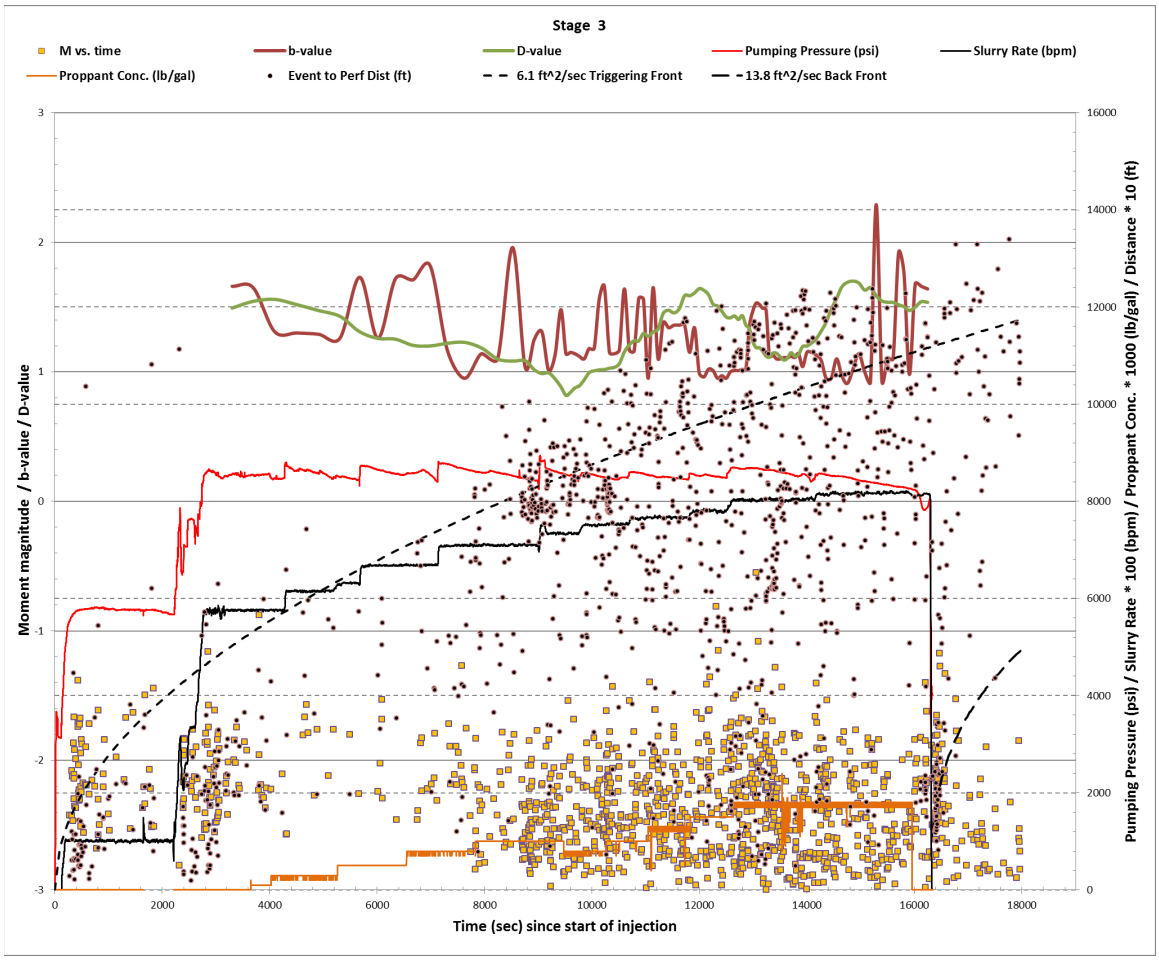

Figure 83 – Pumping pressure, rate, and proppant concentration, diffusivity triggering front and back front, event magnitude, perforation to event distance, b-value, and D-value versus time for Clearfield Stage 3.

3.3.4.3 Stage 4

874 microseismic events were recorded during Stage 4, which forms a well-defined elongated cloud that is similar in extent and character to Stage 3 (Figure 84). The events that occur in the first ~2000 seconds of the injection, far beyond the triggering front, are certainly remnant events from Stage 3; they happen before pressure is fully developed in the well and also occur in the same spatial location as the final events from Stage 3 (Figure 84; Figure 86).

The overall b-value for Stage 4 is 1.35 and the time-series varies between ~0.8 and ~1.8 (Figure 85). The early events from Stage 4 are very small magnitude events, mostly between -3.0

and -2.5, causing an increased b-value in the beginning of the stage (Figure 85b). The remainder of the stage is relatively well behaved, with most of the events constrained between the triggering front and the back front (Figure 86). The b-value shows a slight increase toward the end of the stage; again, related to the lower magnitude back front microseismic events taking place in the previously fractured rock. The D-value time-series varies between 1.2 and 1.8 for the duration of the stage, firmly in the planar-linear spatial configuration.

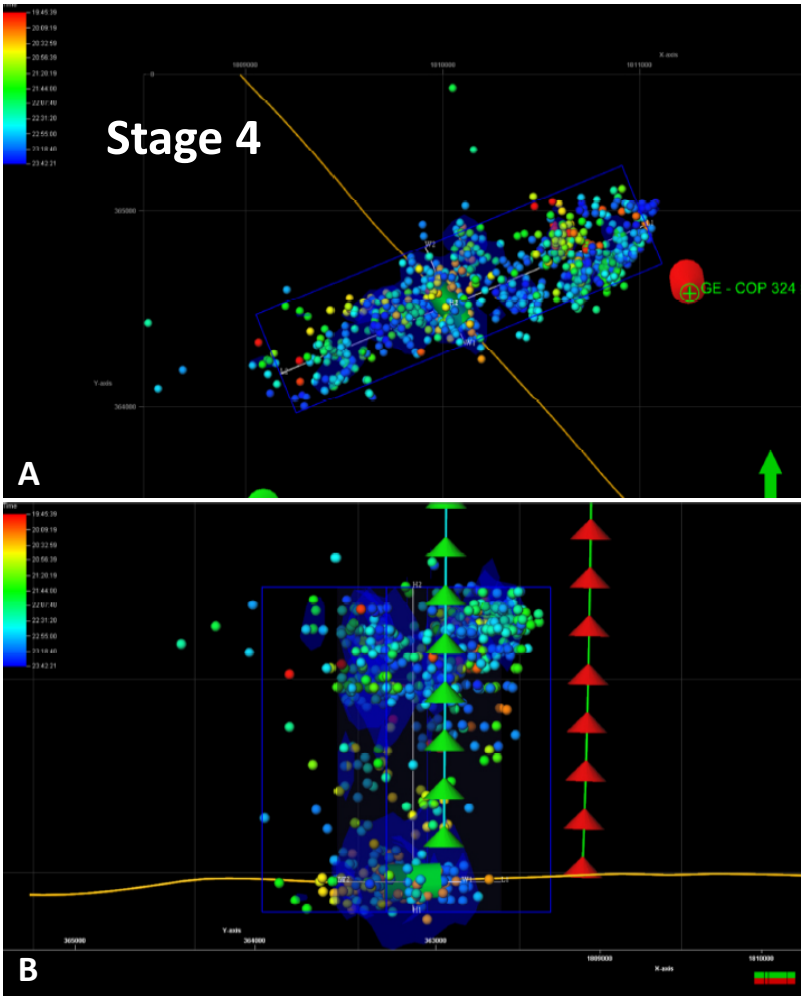

Figure 84 – (a) Map view of microseismic events during Clearfield Stage 4. (b) Side view of microseismicity during Stage 4, view looking northeast. Events colored by time of occurrence: red = early, blue = late.

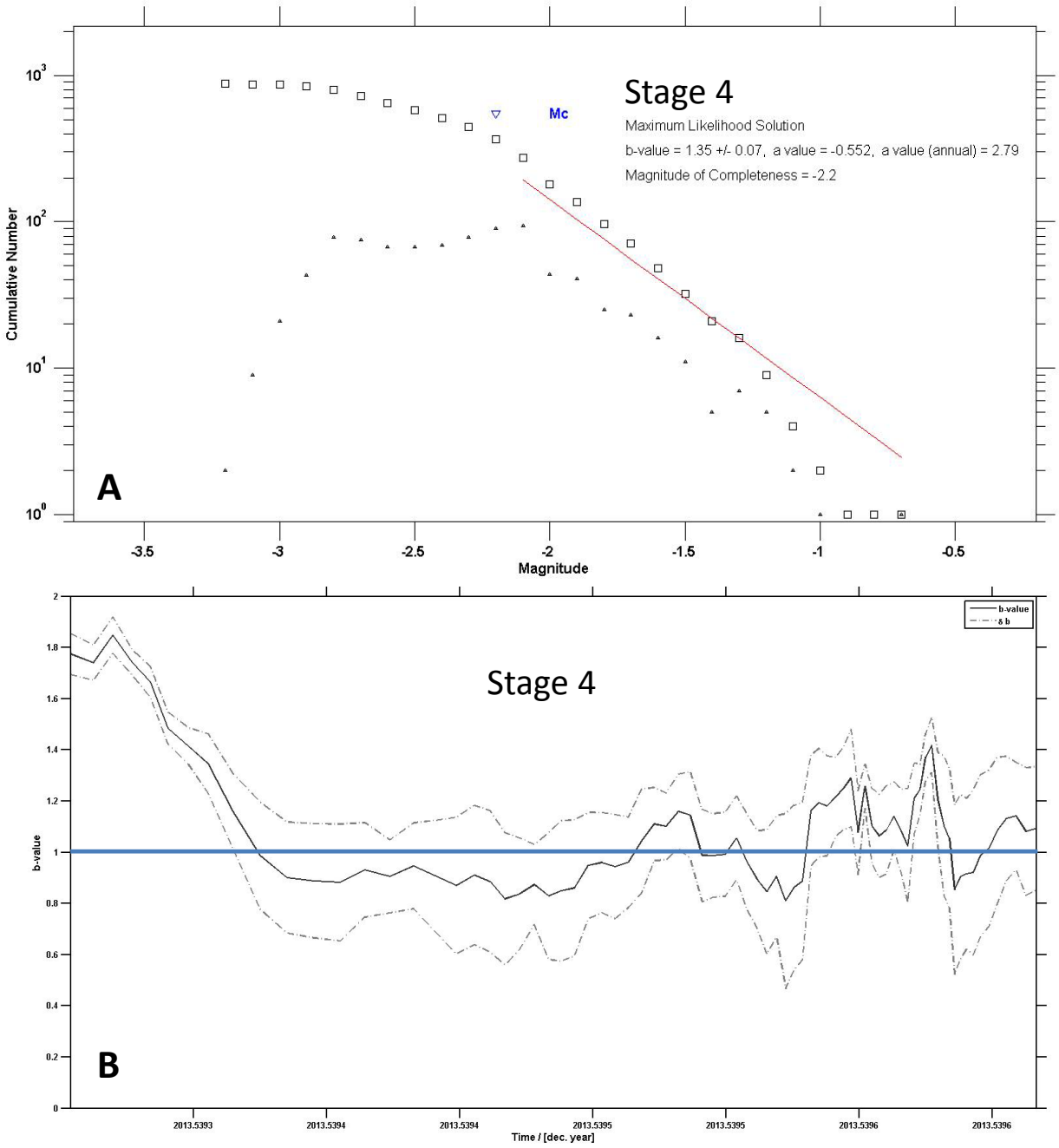

Figure 85 – (a) Overall b-value of Clearfield Stage 4 = 1.35. Magnitude of completion = -2.2. (b) b-value time series for Stage 4. Dotted lines represent error bounds.

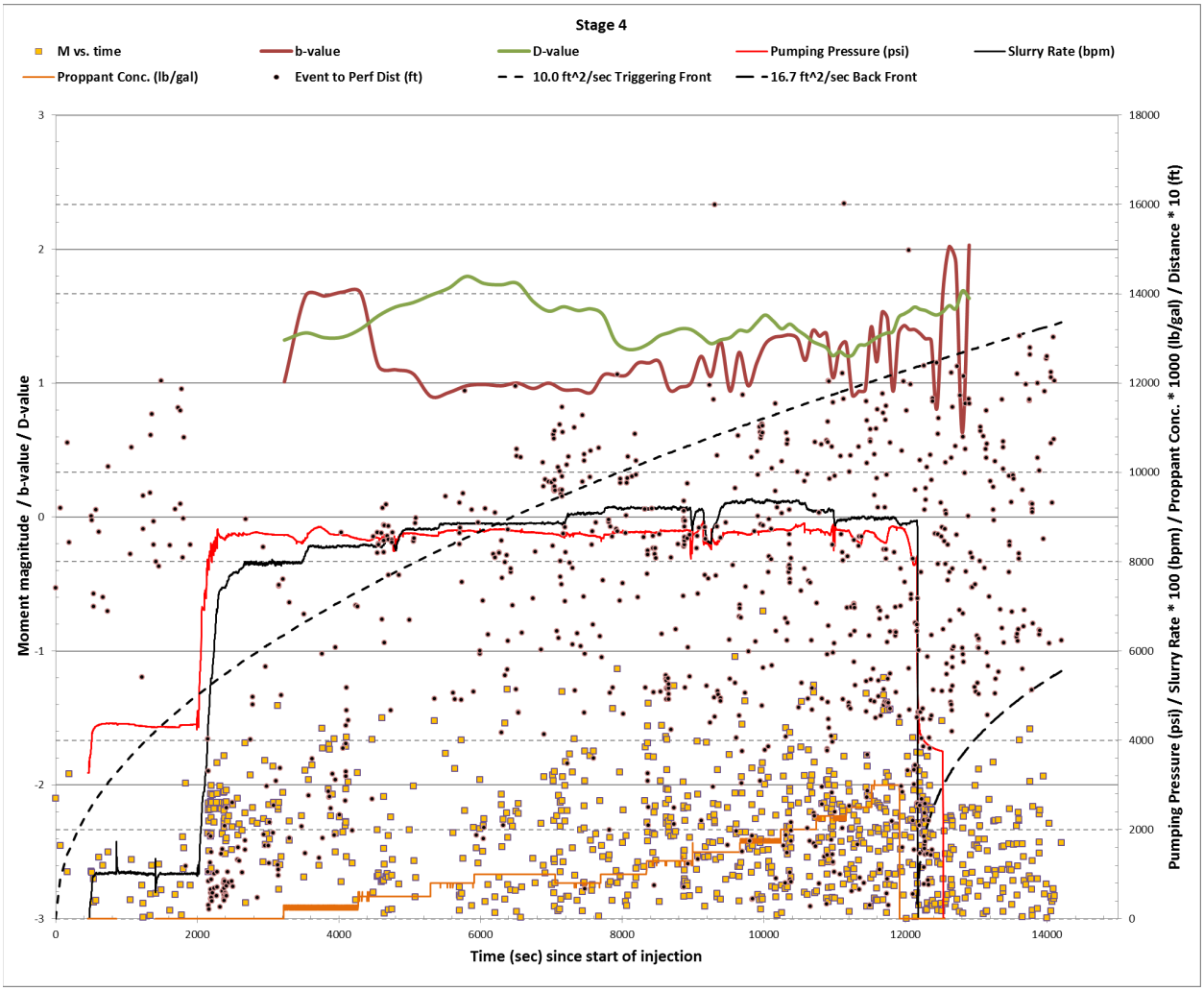

Figure 86 – Pumping pressure, rate, and proppant concentration, diffusivity triggering front and back front, event magnitude, perforation to event distance, b-value, and D-value versus time for Clearfield Stage 4.

3.3.4.4 Stage 5

354 microseismic events were recorded during Stage 5, forming a poorly-defined, elongated cloud that still delineates two clusters of events vertically (Figure 87). Overall, Stage 5 was fairly uneventful, with low event density in the first half of the stage (< ~7000 seconds pump time) but an increase in the second half. There is no obvious reason for this, though it may be caused by reaching a critical proppant concentration in the fracturing fluid, which appears to be ~1 pound/gallon (Figure 89).

The overall b-value for Stage 5 is 0.85, the lowest of all stages. The time-series varies between ~0.8 and ~1.4 (Figure 88). As mentioned before, a low b-value is indicative of failure under a higher state of stress, resulting in larger magnitudes, but lower event count. The spatial arrangement of events does not indicate any unusual behavior such as tight clustering along a plane. Additionally, the pumping pressure and rate is relatively flat and well behaved (Figure 89), not indicative of fluid loss into a fault. The low b-value and low event count are the only initial indicators of fault interaction.

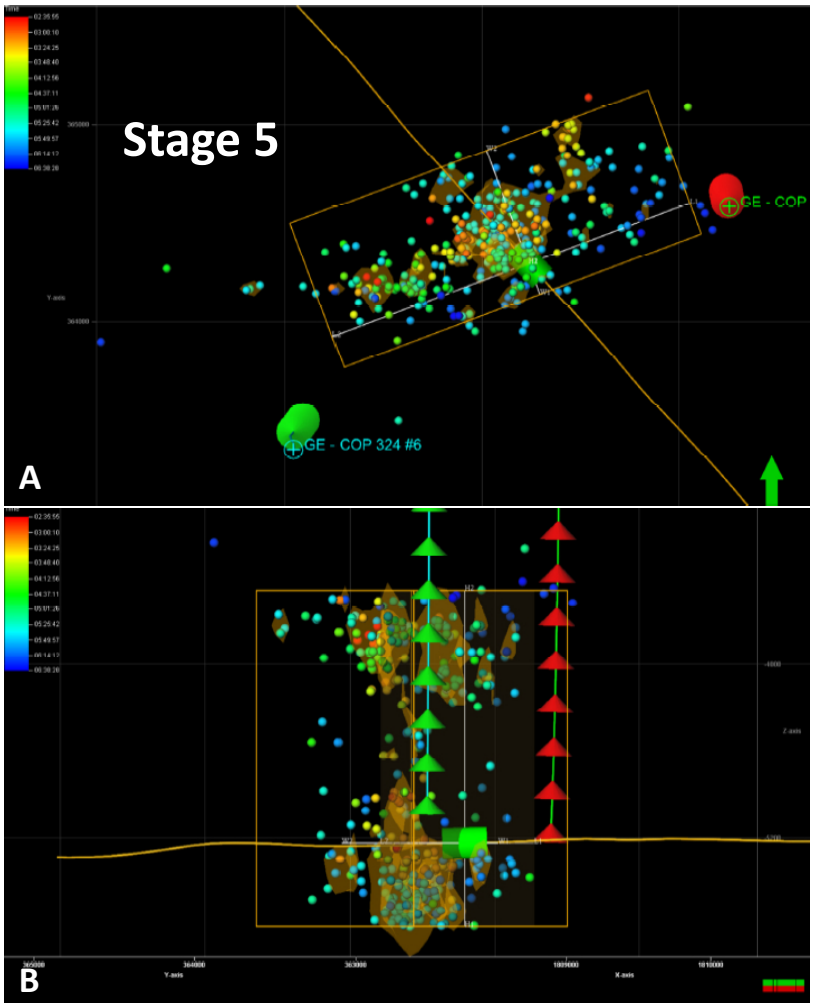

Figure 87 – (a) Map view of microseismic events during Clearfield Stage 5. (b) Side view of microseismicity during Stage 5, view looking northeast. Events colored by time of occurrence: red = early, blue = late.

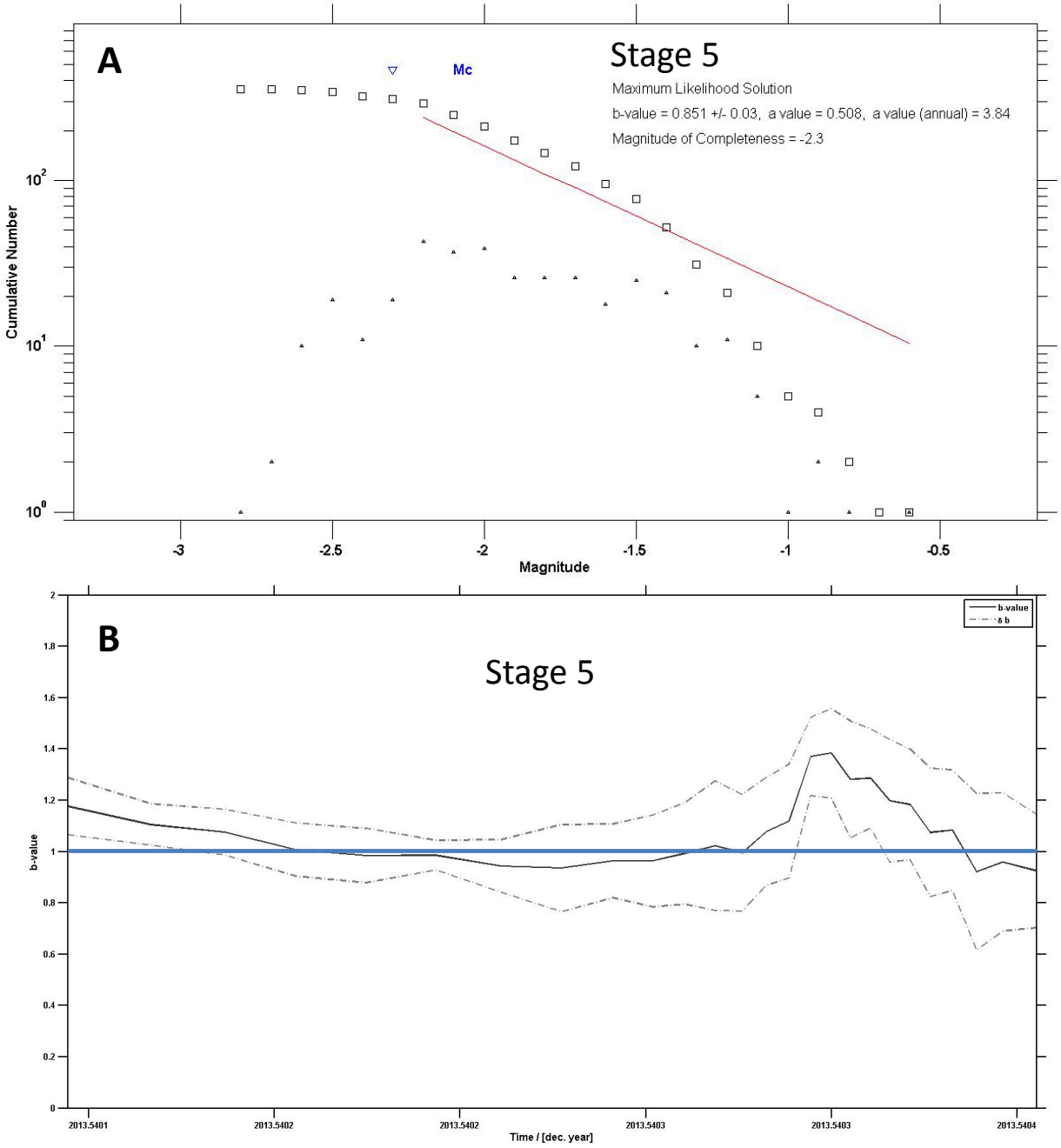

Figure 88 – (a) Overall b-value of Clearfield Stage 5 = 0.85. Magnitude of completion = -2.3. (b) b-value time series for Stage 5. Dotted lines represent error bounds.

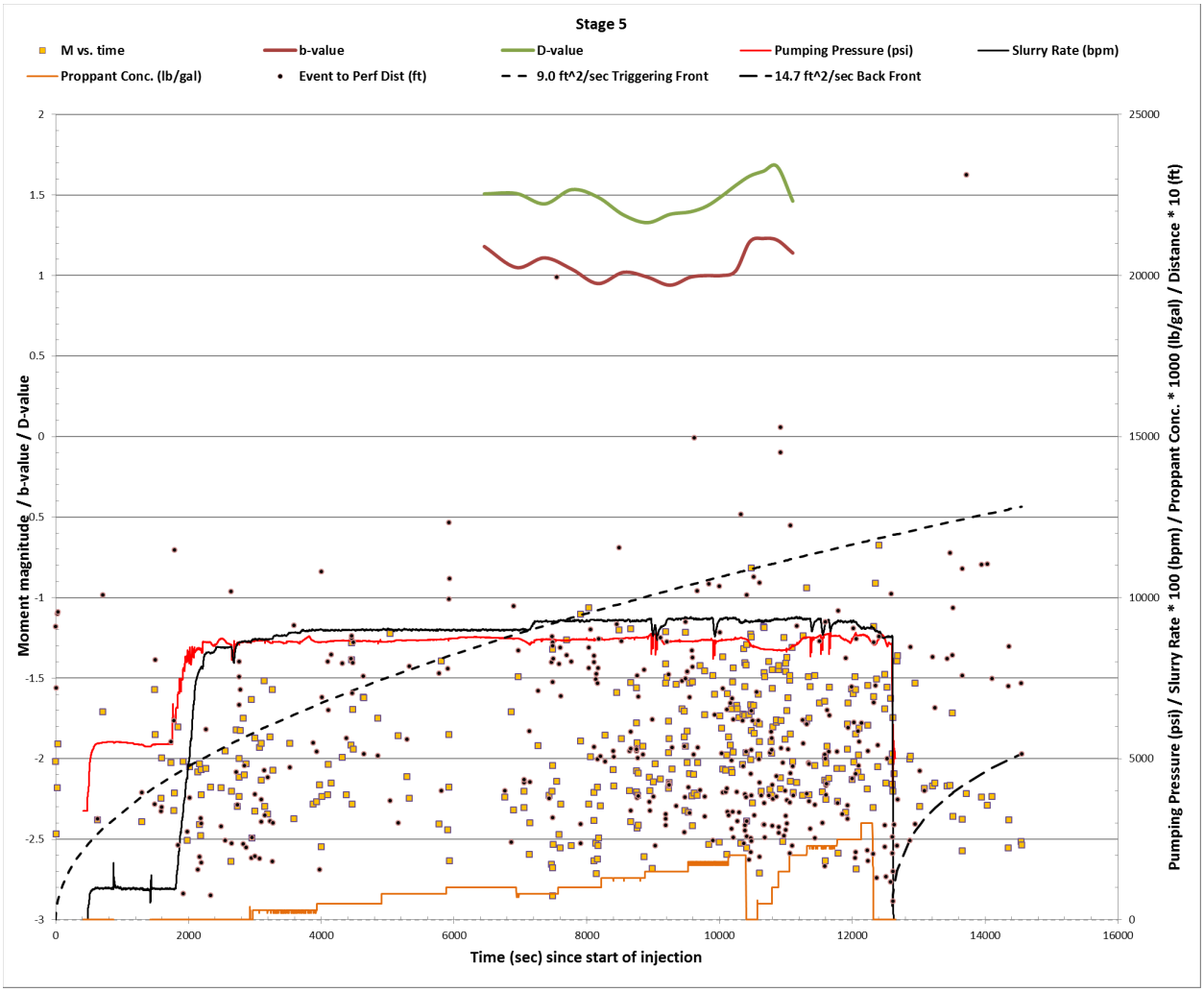

Figure 89 – Pumping pressure, rate, and proppant concentration, diffusivity triggering front and back front, event magnitude, perforation to event distance, b-value, and D-value versus time for Clearfield Stage 5.

3.3.4.5 Stage 6

478 microseismic events were recorded during Stage 6. The events form an elongated cloud aligned east-northeast with some out-of-plane activity occurring to the northwest (Figure 90). The out-of-plane events occur in a previously stimulated volume of rock and may be related to the proposed fault mentioned in the Stage 5 description. The pumping pressure is fairly constant at ~8700 psi throughout the stage, but the pumping rate increases consistently, to almost 110 barrels per minute (Figure 92).

The overall b-value for the stage is 0.94, but the time series varies between ~0.7 and ~1.4 (Figure 91). This is the second lowest average b-value of the entire well, after the previous stage. There is a distinctly lower event density on the northeast side of the lateral well than on the southwest side (Figure 90a). This will be discussed in Section 3.3.7 as an identifying characteristic of an unmapped fault crossing the well bore

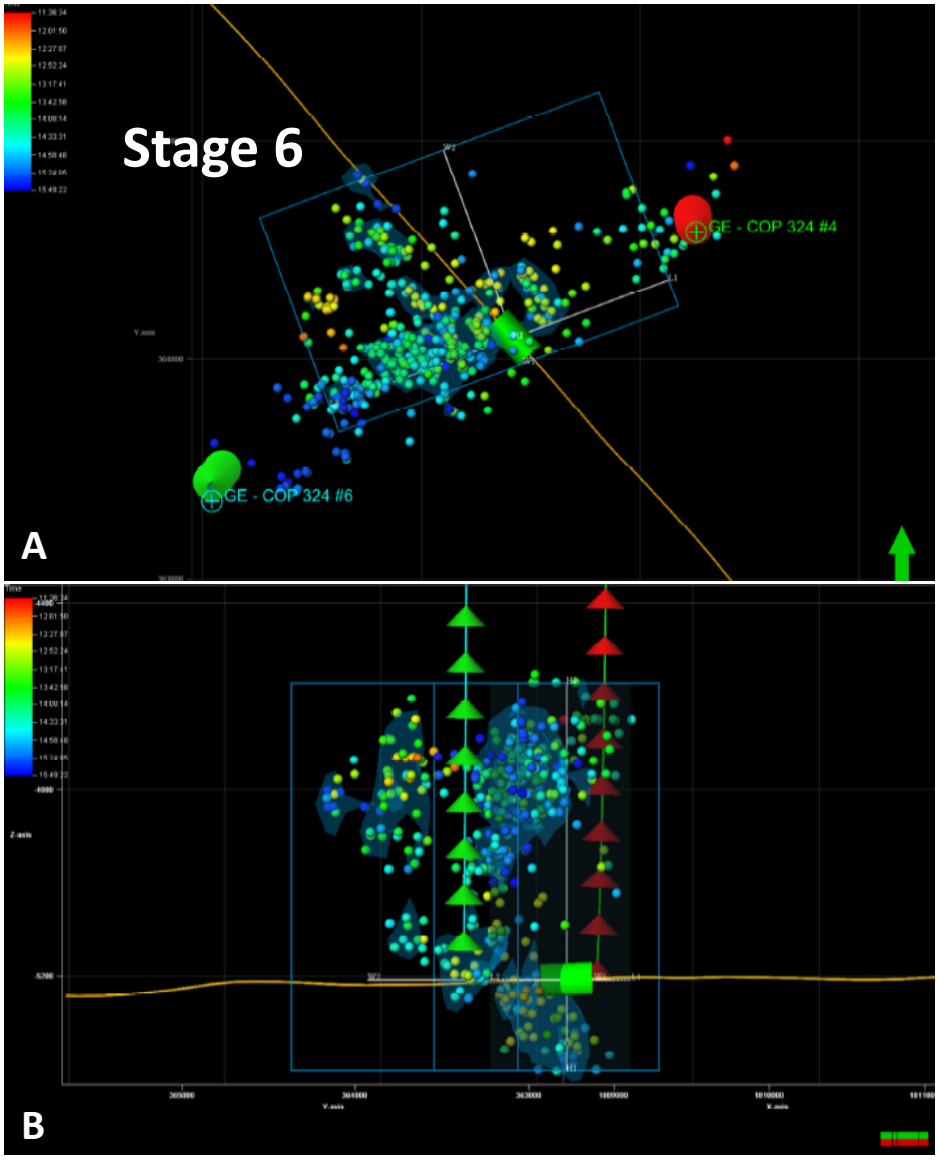

Figure 90 – (a) Map view of microseismic events during Clearfield Stage 6. (b) Side view of microseismicity during Stage 6, view looking northeast. Events colored by time of occurrence: red = early, blue = late.

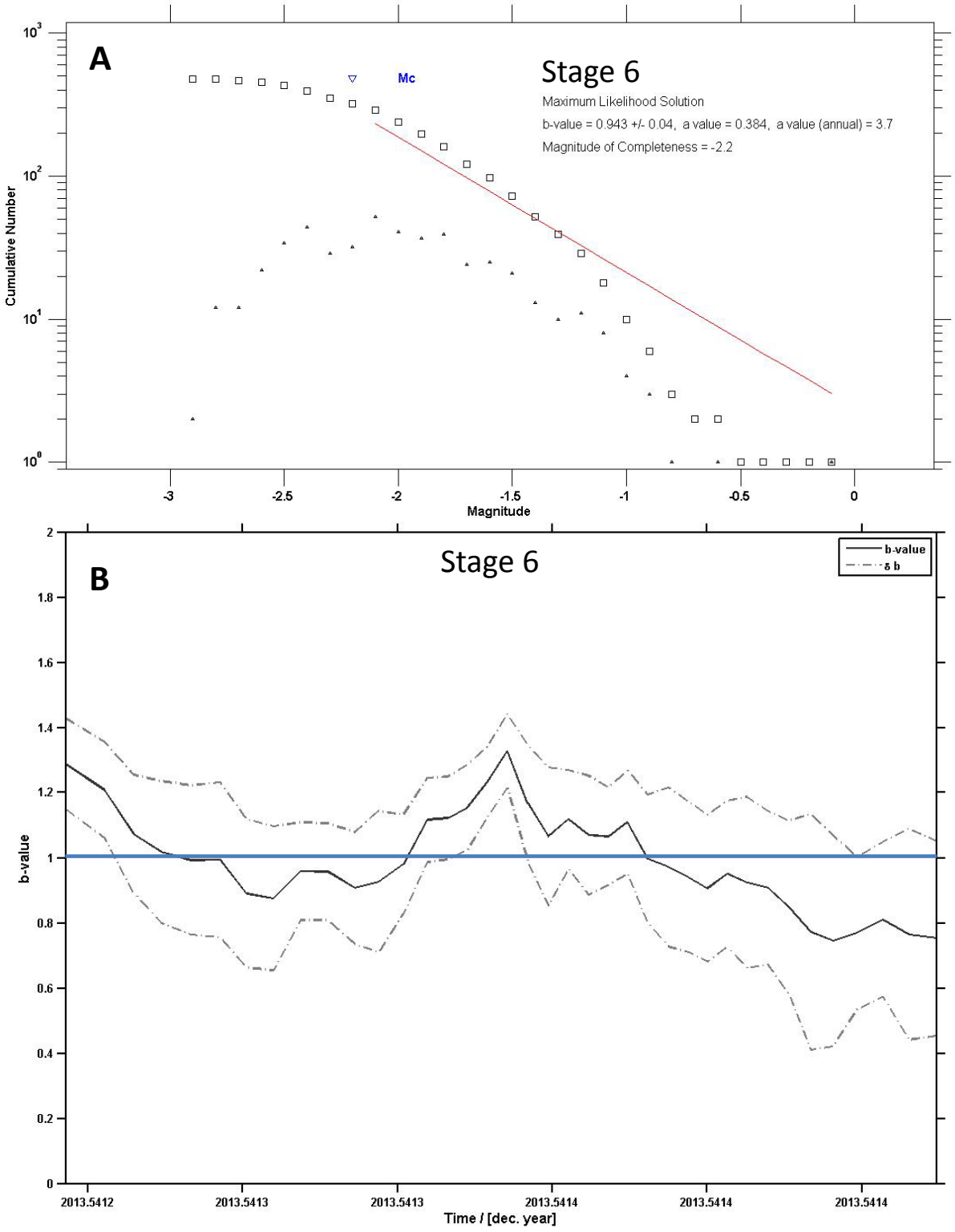

Figure 91 – (a) Overall b-value of Clearfield Stage 6 = 0.94. Magnitude of completion = -2.2. (b) b-value time series for Stage 6. Dotted lines represent error bounds.

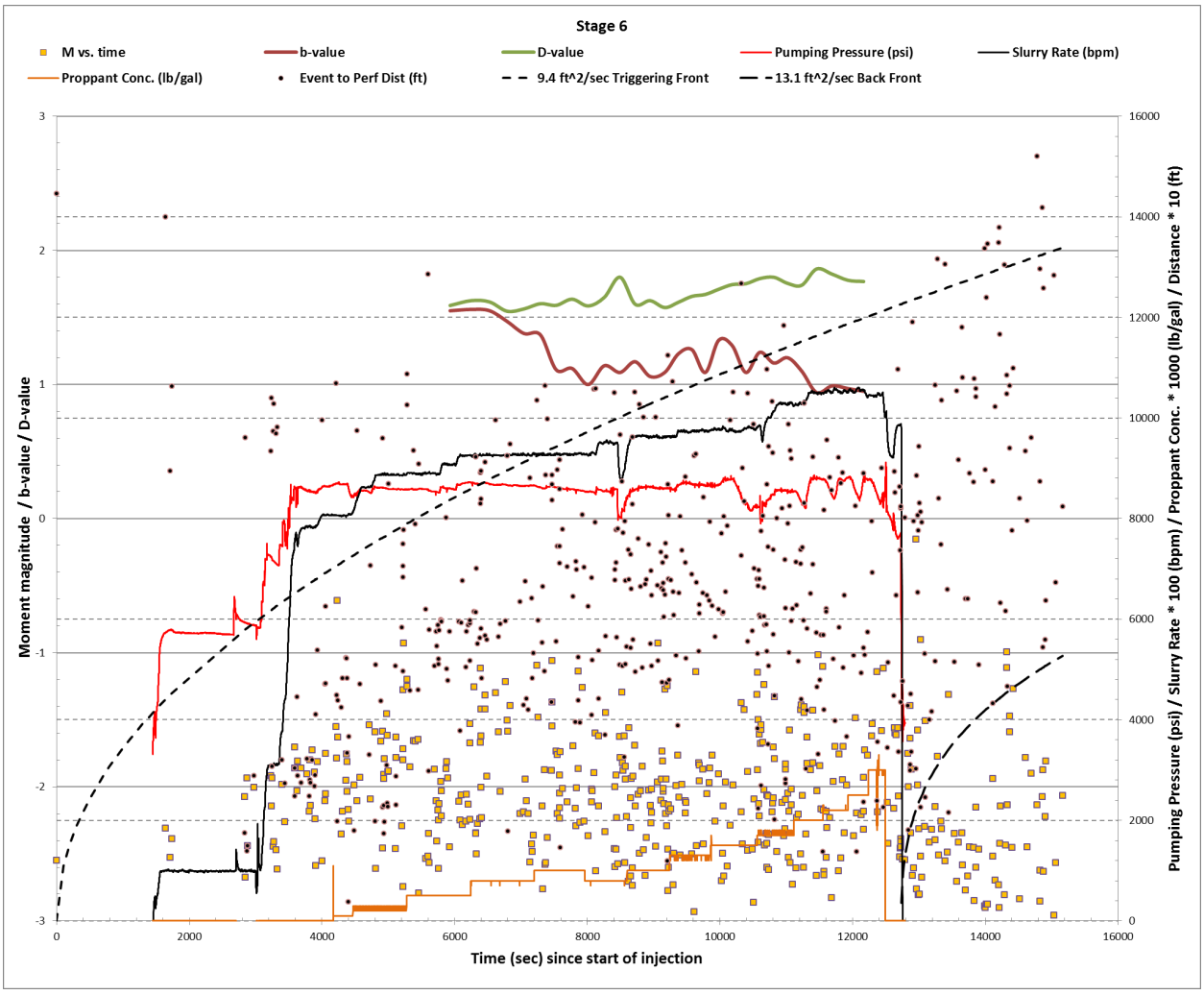

Figure 92 – Pumping pressure, rate, and proppant concentration, diffusivity triggering front and back front, event magnitude, perforation to event distance, b-value, and D-value versus time for Clearfield Stage 6.

3.3.4.6 Stage 8

370 microseismic events were recorded during Stage 8. Even though the event count is relatively low, there are a few interesting observations to be made. All stages before Stage 8 have shown a distinct separation into two groups of events: one near to the well bore and one approximately 600-800 feet above. There is still upward growth in Stage 8, but the concentration of events above the well bore is much lower (Figure 93). Secondly, almost all of the events occur in the first 2,000 seconds (~30 minutes) of pumping (Figure 95). There is a distinct cutoff in

microseismicity near to the well bore at approximately 30 minutes, and for the next ~2.5 hours events are sparse and mostly occur in the overlying shales of the Hamilton Group. Lastly, the effect of the diffusivity back-front is shown in Figure 95. Microseismicity is re-initiated close to the well bore after the well is shut in. A pressure front radiates from the injection point, with higher pressure in front and lower pressure behind.

The overall b-value for Stage 8 is 1.27 and the time series varies between ~1.1 and ~1.7 (Figure 94). The lowest b-values occur at the beginning the stage, when out of zone microseismicity can be observed along a linear feature west of the stage perforations.

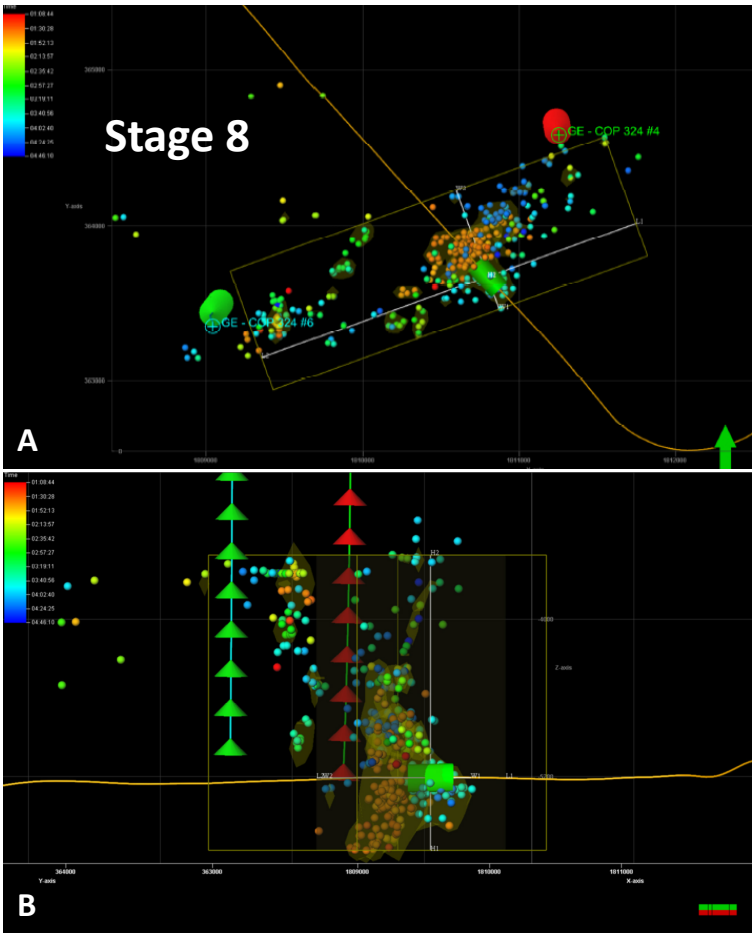

Figure 93 – (a) Map view of microseismic events during Clearfield Stage 8. (b) Side view of microseismicity during Stage 8, view looking northeast. Events colored by time of occurrence: red = early, blue = late.

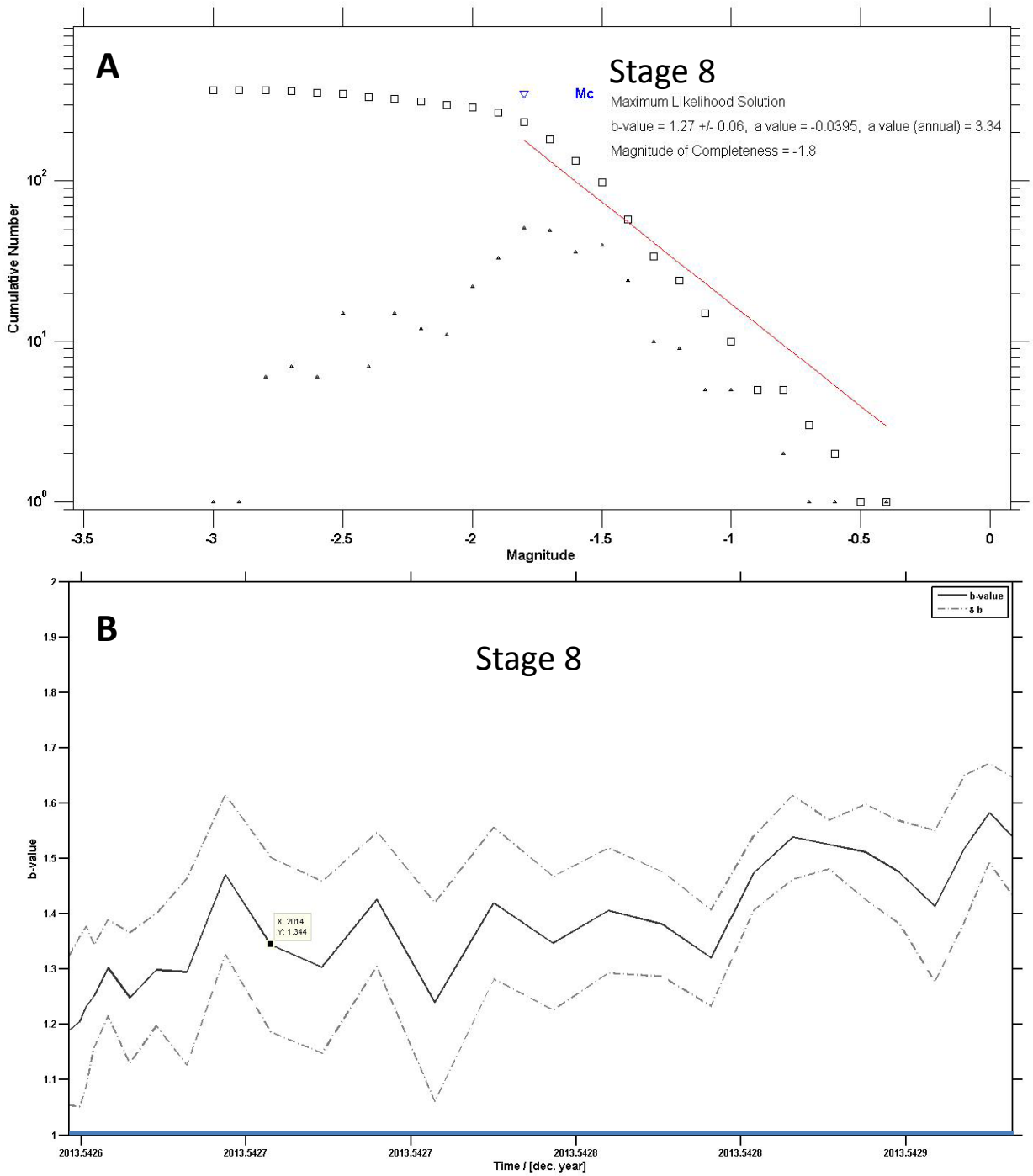

Figure 94 – (a) Overall b-value of Clearfield Stage 8 = 1.27. Magnitude of completion = -1.8. (b) b-value time series for Stage 8. Dotted lines represent error bounds.

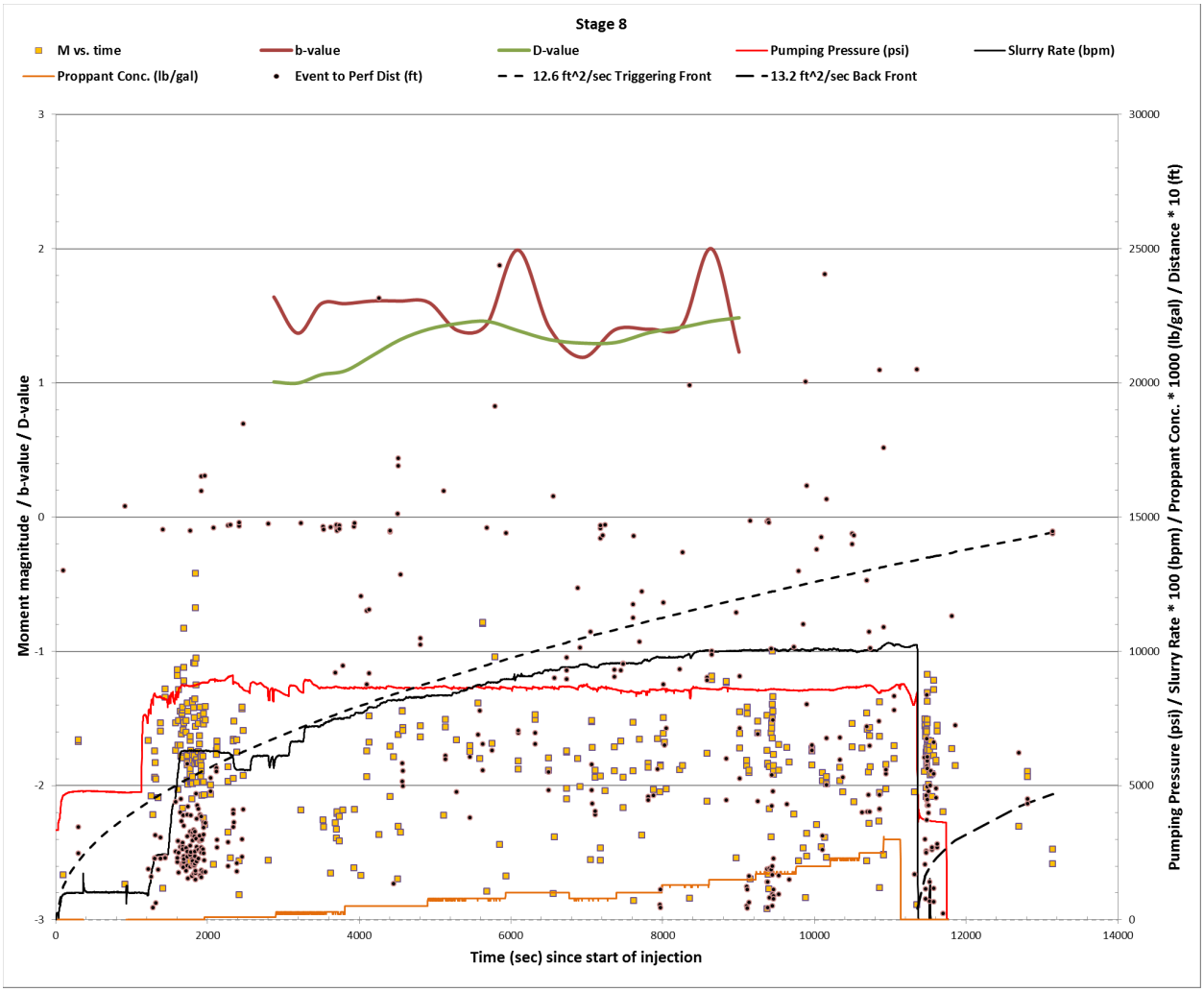

Figure 95 – Pumping pressure, rate, and proppant concentration, diffusivity triggering front and back front, event magnitude, perforation to event distance, b-value, and D-value versus time for Clearfield Stage 8.

3.3.4.7 Stage 9

557 microseismic events were recorded during Stage 9. Similar to Stage 8, Stage 9 contains even less vertical growth, and most microseismicity is confined to within 300 feet above or below the well (Figure 96). Events that occur in the far field, very early in the injection (Figure 96a and Figure 98) are likely a continuation of microseismicity from previous stages. Temporally, microseismicity is well distributed, with the exception of the final ~2000 seconds (30 minutes) of pumping. Similar to Stage 2, the operator cut the flow rate and proppant concentration to zero,

and cut the pressure by half. Upon restarting fluid injection and specifically when reintroducing proppant to the fracturing fluid, a dense cloud of microseismicity formed around the well bore. As a side note, based upon the observation of this phenomenon in two out of two stages where large perturbations to the pressure front were introduced intentionally, this may be a technique worth investigating to "corral" microseismicity back to the formation of interest.

The overall b-value for Stage 9 is 1.62 and the time series varies between ~1.5 and ~2.3 (Figure 97). According to these values, microseismicity in this stage is mainly small magnitude events associated with discrete fracture formation, and not fault interaction.

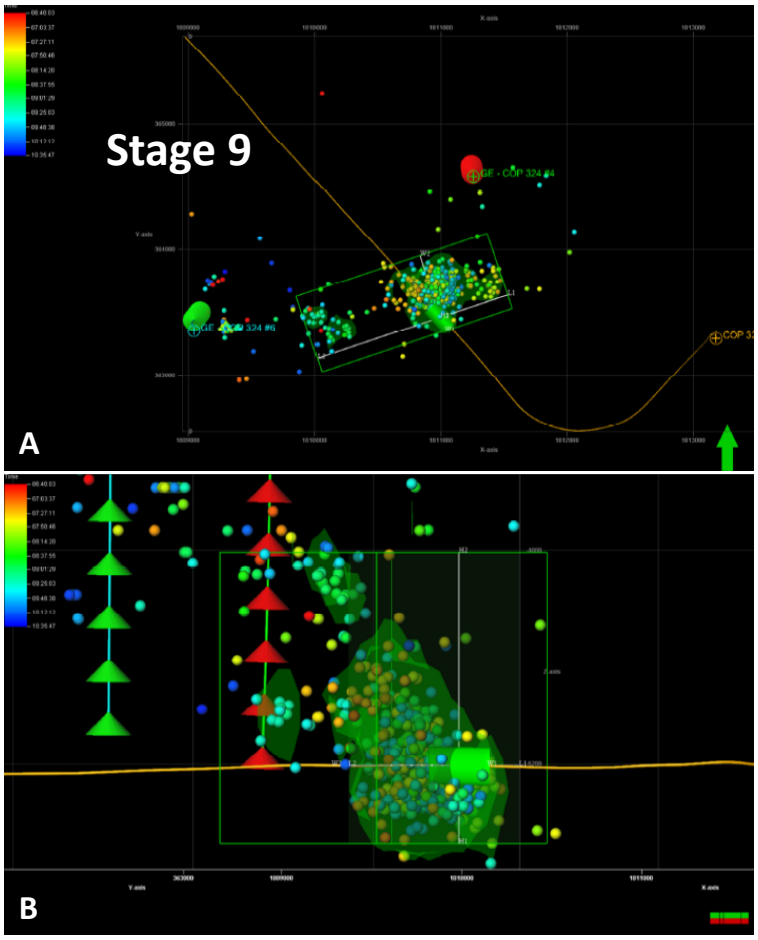

Figure 96 – (a) Map view of microseismic events during Clearfield Stage 9. (b) Side view of microseismicity during Stage 9, view looking northeast. Events colored by time of occurrence: red = early, blue = late.

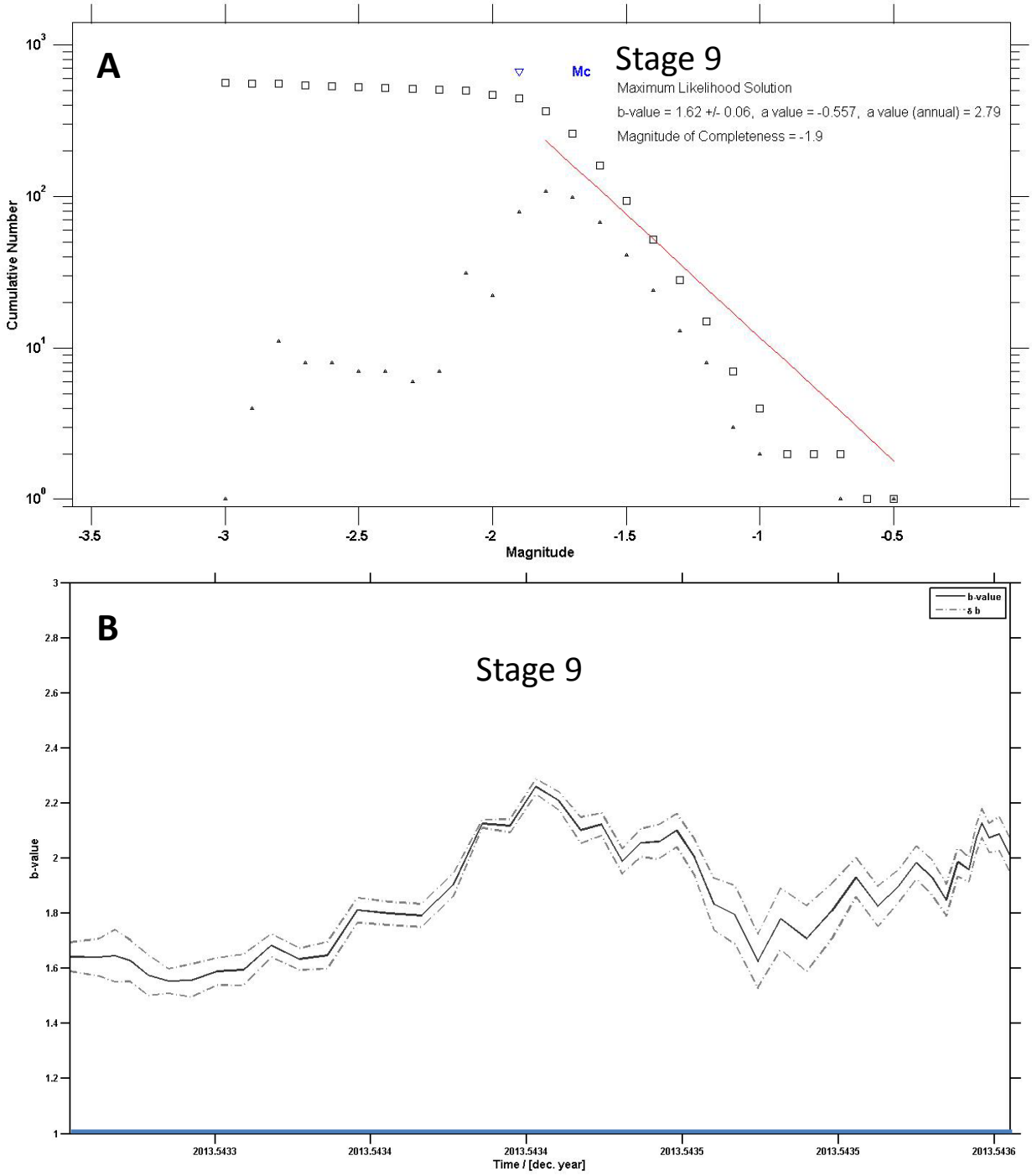

Figure 97 – (a) Overall b-value of Clearfield Stage 9 = 1.62. Magnitude of completion = -1.9. (b) b-value time series for Stage 9. Dotted lines represent error bounds.

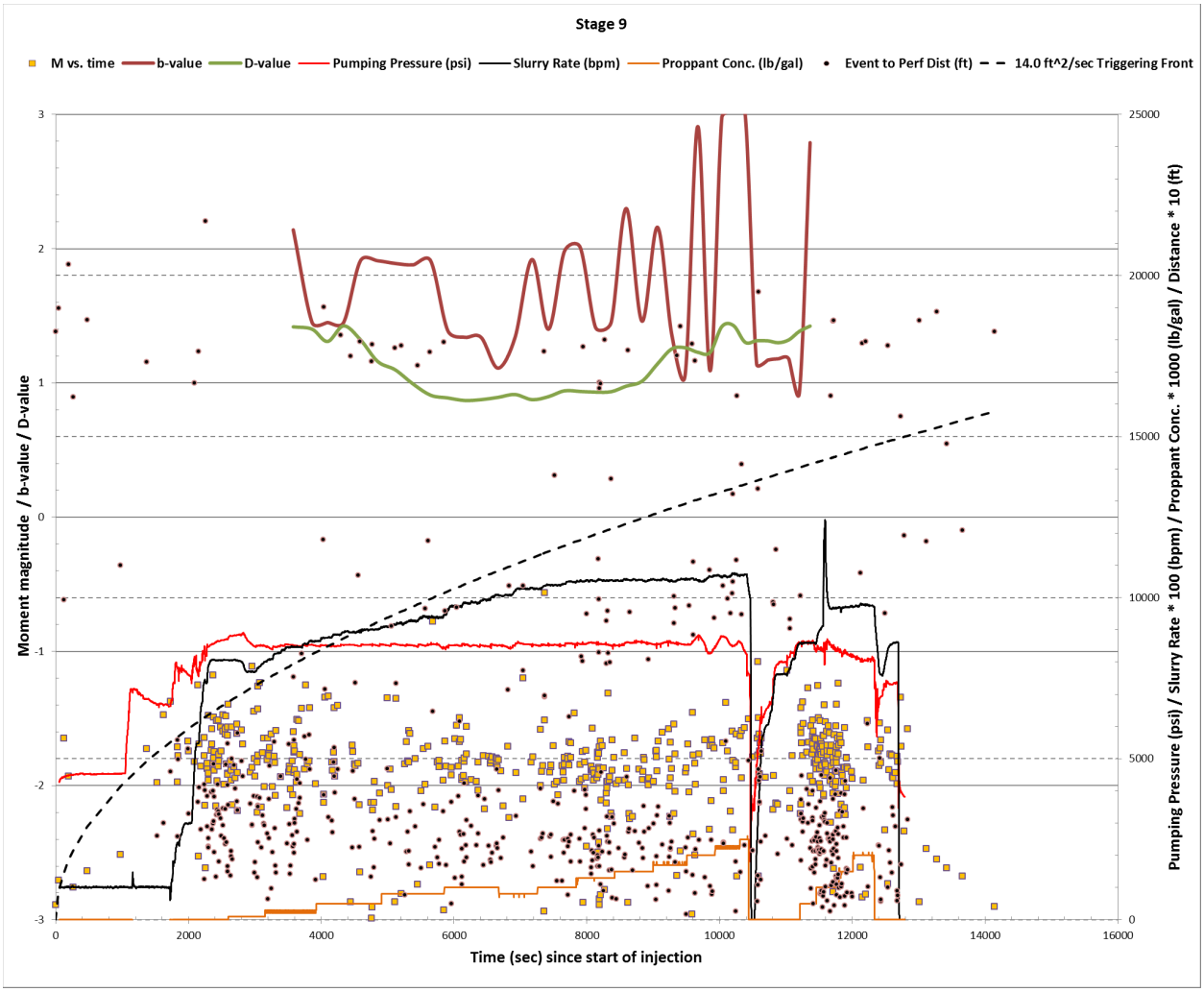

Figure 98 – Pumping pressure, rate, and proppant concentration, diffusivity triggering front and back front, event magnitude, perforation to event distance, b-value, and D-value versus time for Clearfield Stage 9.

3.3.4.8 Stage 12

314 microseismic events were recorded during Stage 12, the majority of which are located within 300 feet, vertically, of the well bore (Figure 99). This is the second lowest amount of upward or downward height growth, behind Stage 9. Additionally, a large portion is out-of-zone, in the Upper Marcellus Shale (Figure 67). This stage is mainly characterized by a small concentration of events at the beginning of the stage and a concentration at the end of the stage, after well shut-in. The middle portion of the pumping cycle is sparsely populated with microseismicity (Figure

101). Notice a small number of events in Figure 99, far to the north and west of the injection point that occur at the beginning of pumping and after the well has been shut-in. This is likely the result of previous stages establishing more direct fluid pathways to the far-field.

The overall b-value for Stage 12 is 1.53 and the time series varies between ~1.1 and ~1.7, giving little indication of any fault interaction (Figure 100).

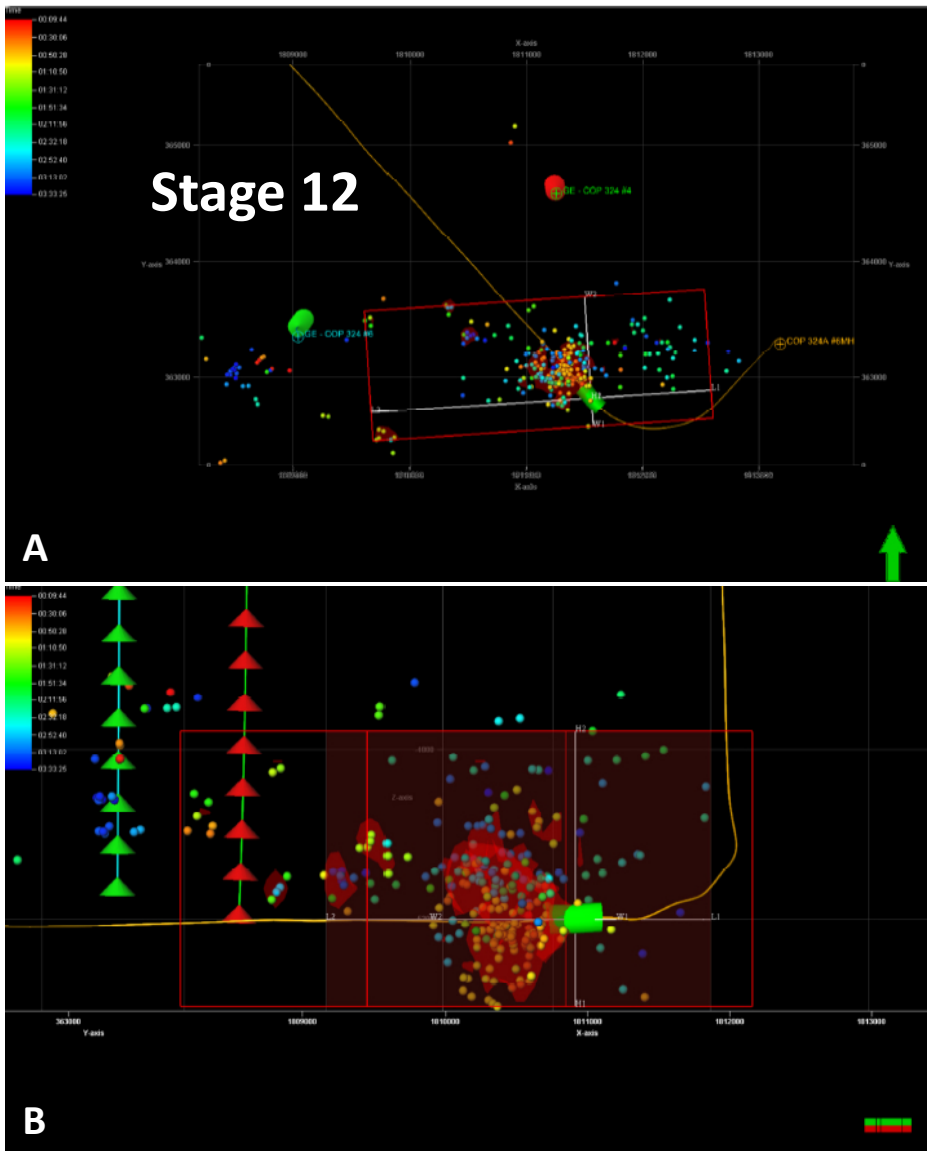

Figure 99 – (a) Map view of microseismic events during Clearfield Stage 12. (b) Side view of microseismicity during Stage 12, view looking northeast. Events colored by time of occurrence: red = early, blue = late.

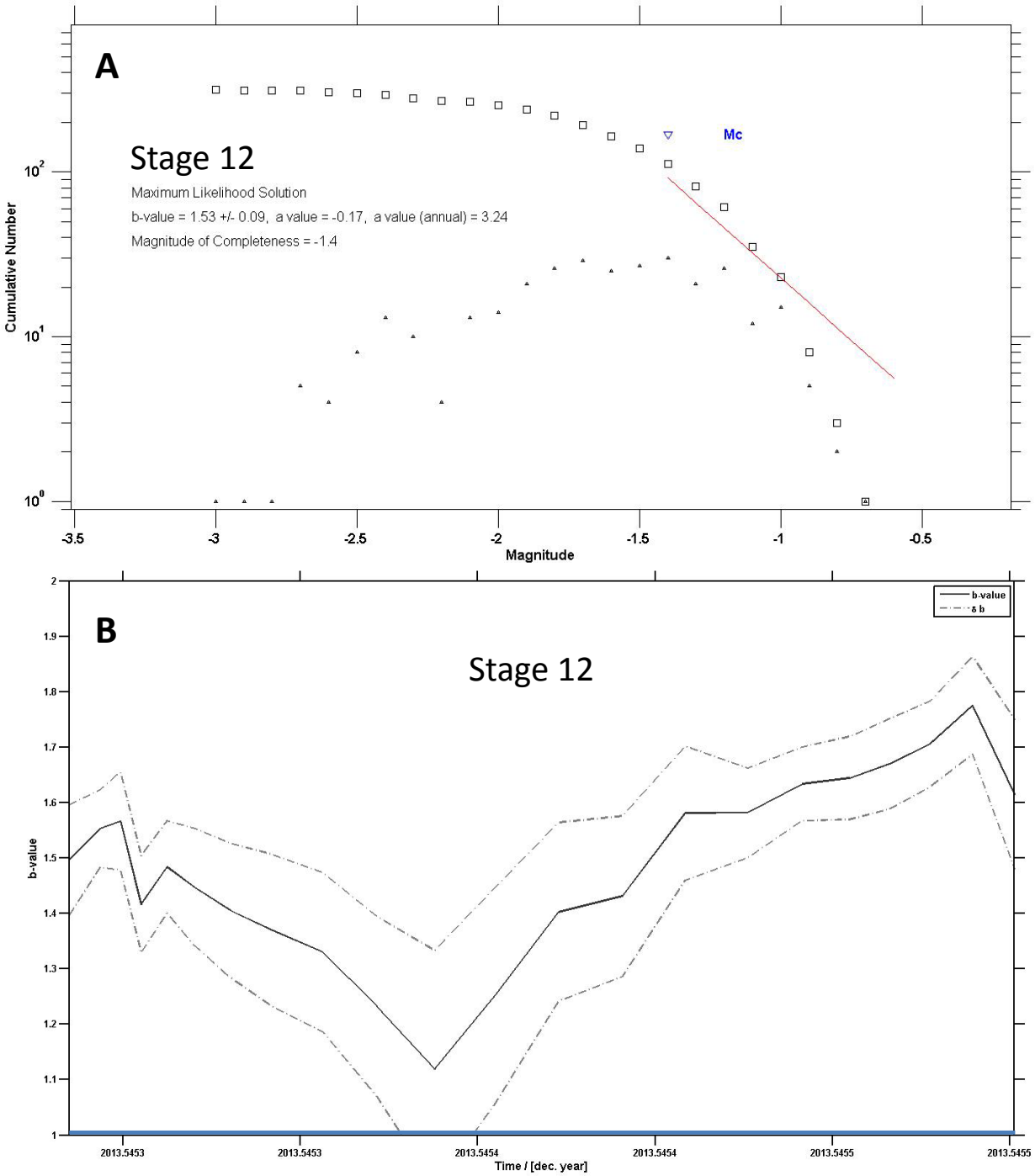

Figure 100 – (a) Overall b-value of Clearfield Stage 12 = 1.53. Magnitude of completion = -1.4. (b) b-value time series for Stage 12. Dotted lines represent error bounds.

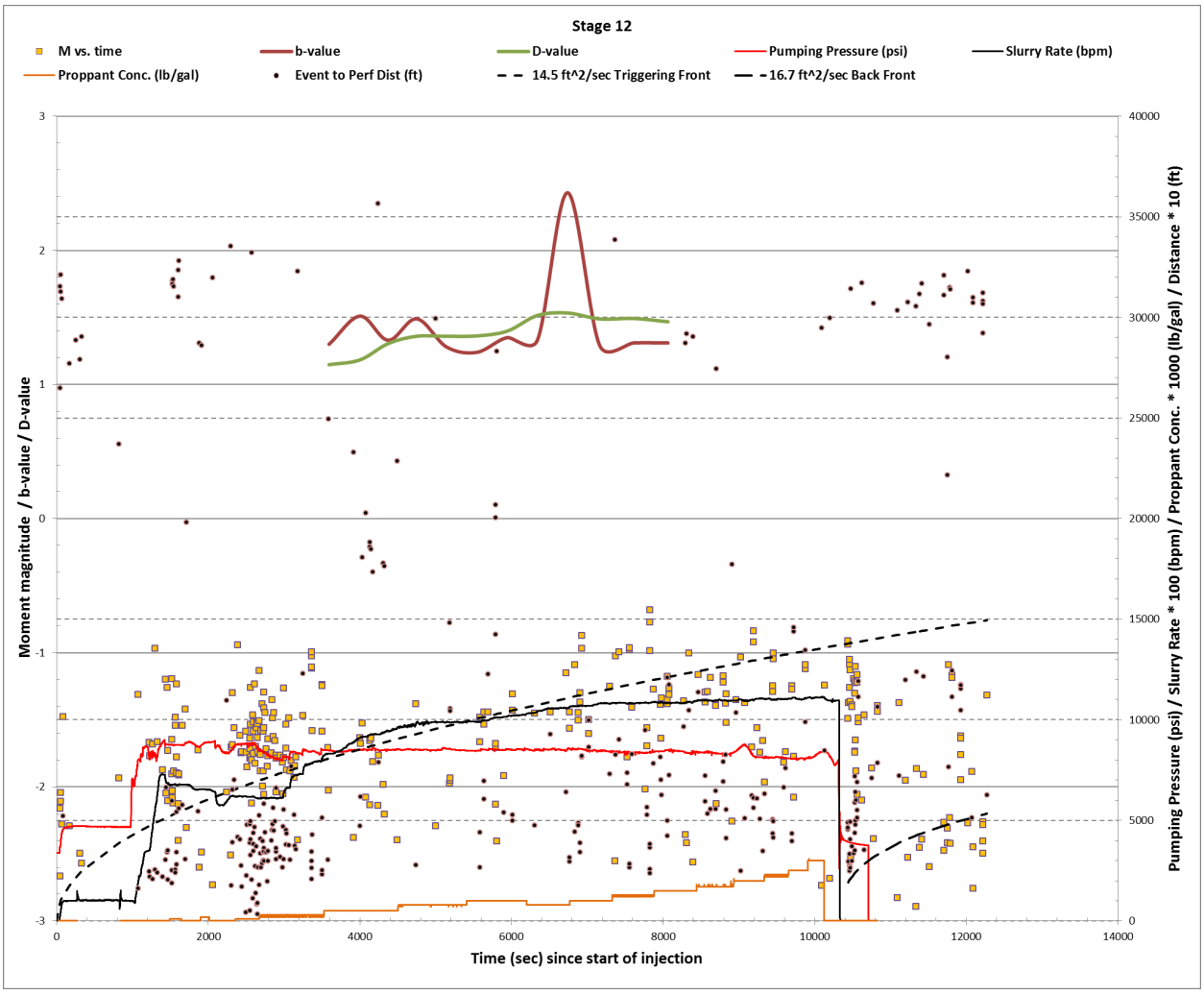

Figure 101 – Pumping pressure, rate, and proppant concentration, diffusivity triggering front and back front, event magnitude, perforation to event distance, b-value, and D-value versus time for Clearfield Stage 12.

3.3.5 Vertical Microseismicity Distribution

Introduced in Section 3.1.4.1, there is much insight to be gained by examining the spatial variability in microseismicity, especially in a geologically complex environment such as the Appalachian Basin. The presence of thinly bedded shale with interbedded sandstone and limestone, interspersed with faults and fractures all serves to create a homogeneous medium in

which to hydraulically fracture. It is proposed in this section that a major factor which controls the expression of microseismicity is the geomechanical character of the stimulated rock layer.

In the development of unconventional resources like the Marcellus Shale, where natural gas is trapped within porosity, direct stimulation of the source/reservoir layer through hydraulic fracturing is critical to the recovery of hydrocarbons. Microseismic monitoring provides direct evidence of fracture formation by detecting the resulting seismic events. However, not all of the hydraulic energy that is transferred downhole is applied to the task of creating fractures in the zone of interest. Much of this energy is lost to heat, friction, and aseismic deformation (discussed in Sections 3.2.5.5 and 3.2.8.2. Furthermore, the majority of microseismicity occurs outside of the zone of interest. Figure 102, Figure 103, and Figure 104 illustrate the vertical event count, microseismic energy, and stress drop (See Section 3.1.4.1) distributions for all fracturing stages and each stage individually. All totals are normalized to 100%; for exact totals, see Figure 14. Only 26.5% of the total number of events for all stages occurred within the Lower Marcellus target zone, with the percentage ranging from 6.5% (Stage 1) to 59.7% (Stage 2). 16.2% of the total seismic energy was constrained to the Lower Marcellus, with a range between 2.7% (Stage 6) and 42.6% (Stage 2). 34.8% of the total stress drop occurred in the Lower Marcellus, with a range between 4.5% (Stage 5) and 75.3% (Stage 2). Figure 105 shows that microseismicity is distributed over a vertical range of ~1,000 feet. The microseismic cloud gradually transitions from a two-part cloud in the first six stages (one concentration of events around the Marcellus and one approximately 600 feet above in the upper Hamilton Group) to a single diffuse cloud in the last seven stages, mostly concentrated in the lower Hamilton Group (Skaneateles Shale/Upper Marcellus/Lower Marcellus).

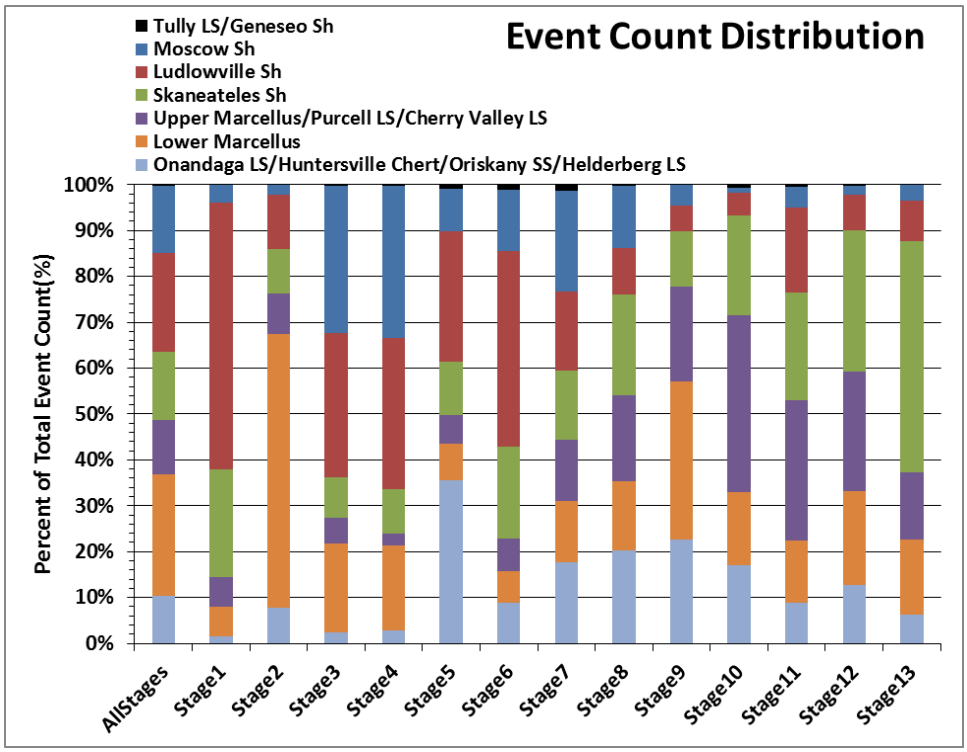

Figure 102 – Event count (% of total) versus Stage #, colored by geologic formation/member.

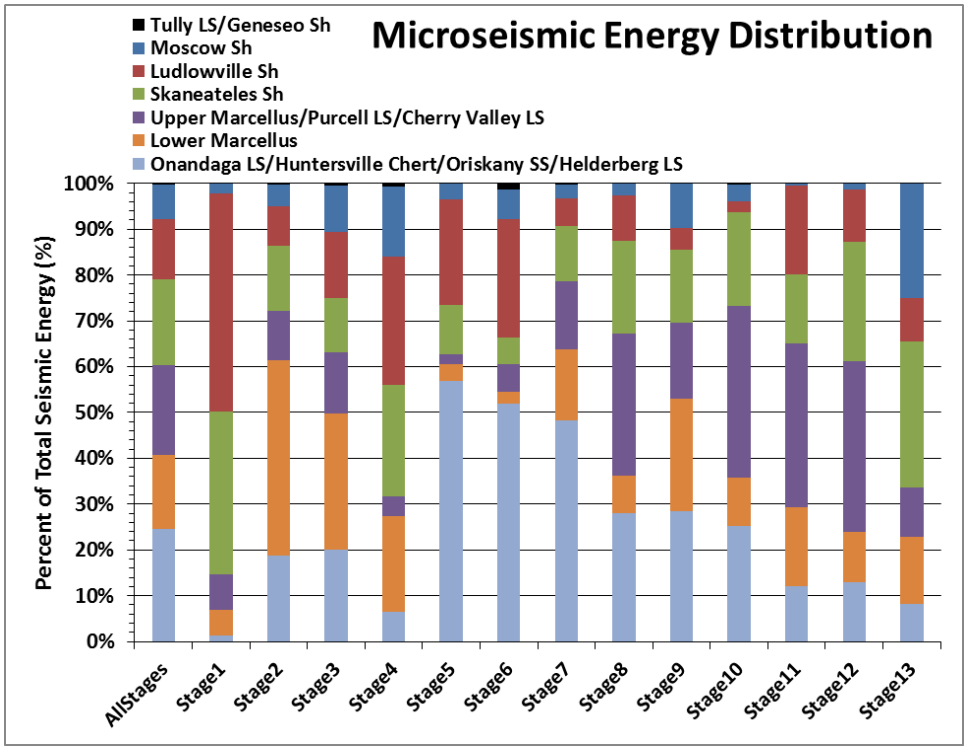

Figure 103 – Radiated seismic energy (% of total) versus Stage #, colored by geologic formation/member.

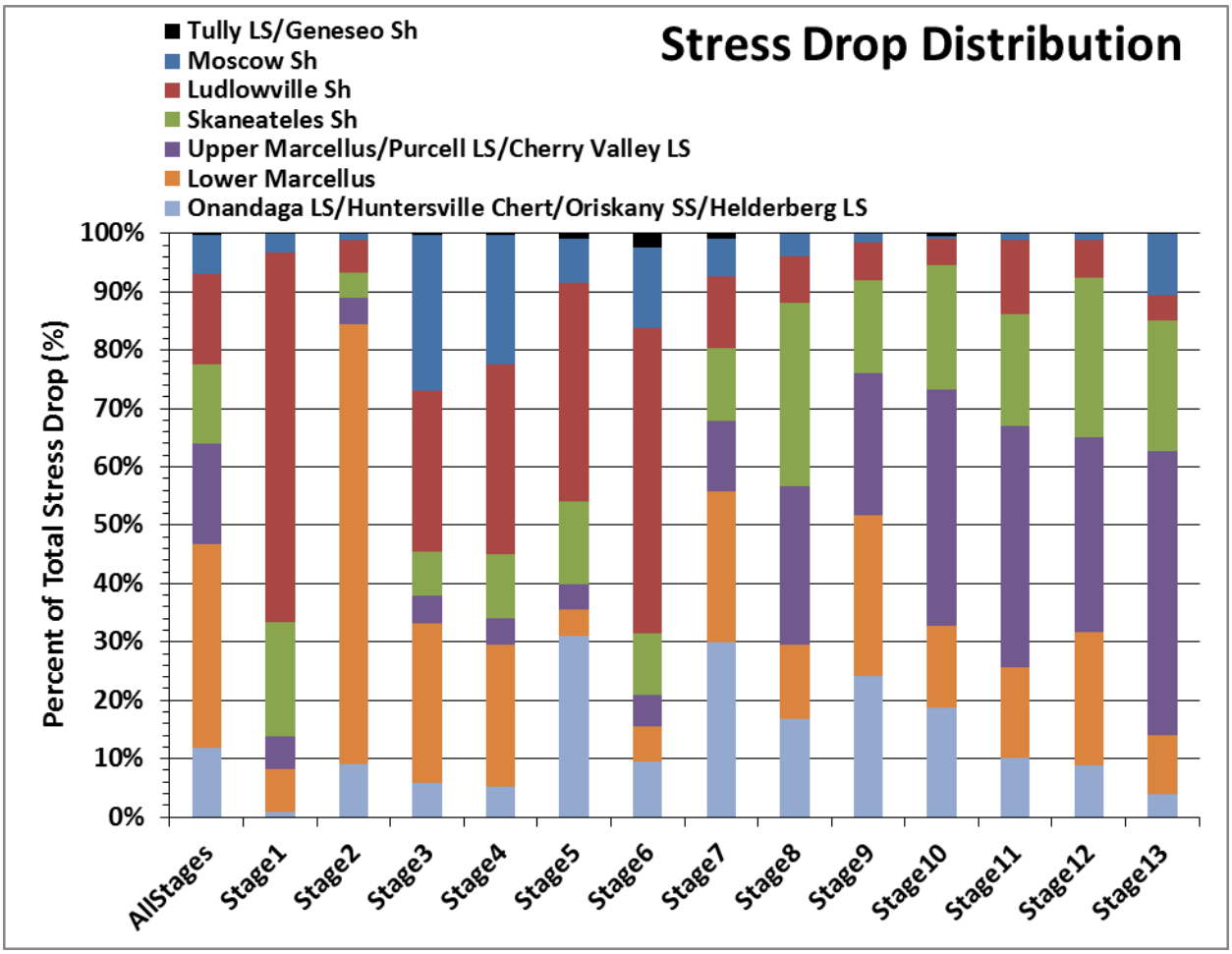

Figure 104 – Seismogenic stress drop (% of total) versus Stage #, colored by geologic formation/member.

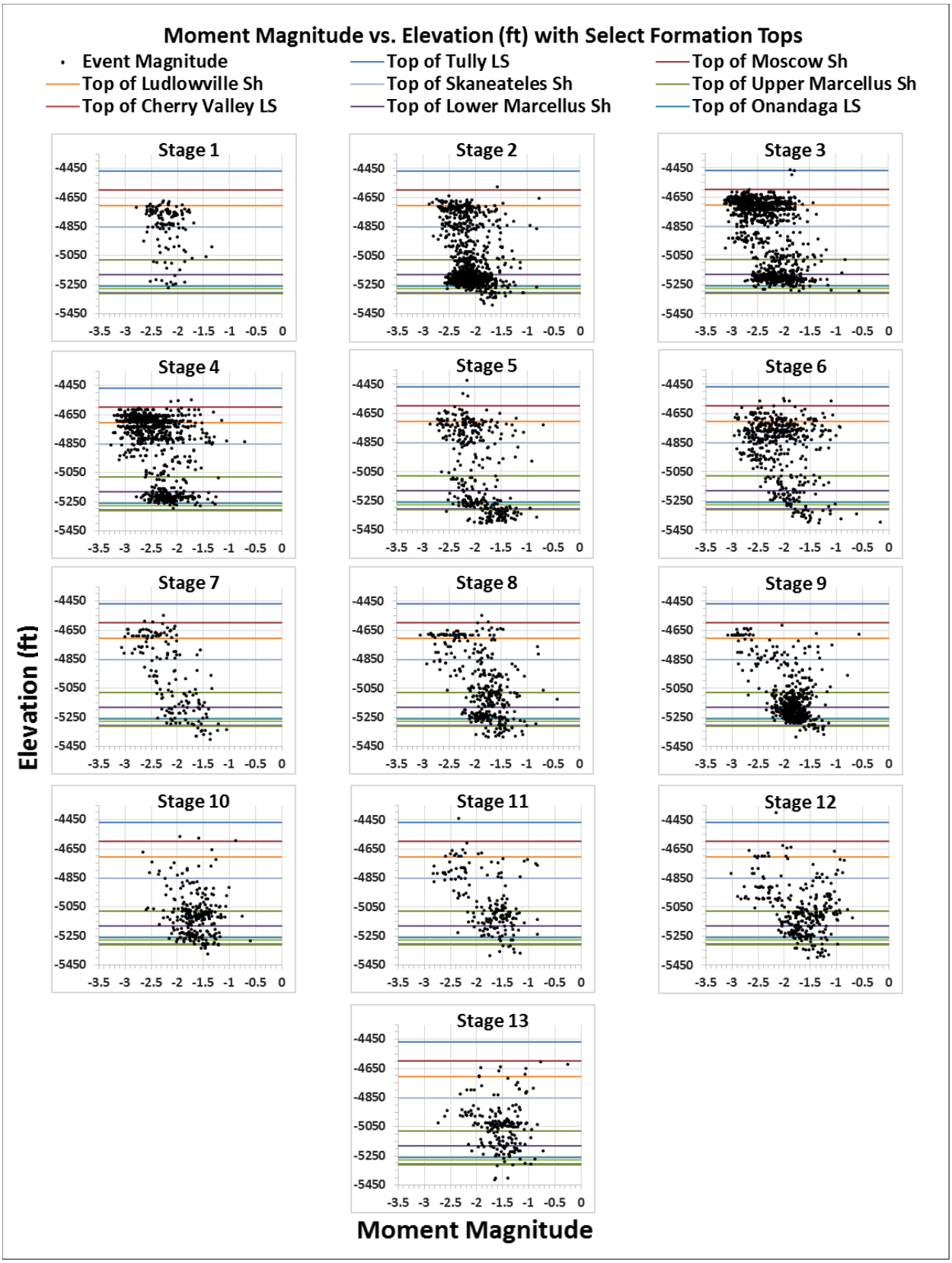

Figure 105 – Elevation (ft) versus moment magnitude for each stage separately, with select formation tops.

The inefficiency described above should be accounted for when using microseismic data as a measure of stimulation. A too simplistic approach in which high microseismic "production" should correspond to high hydrocarbon production can lead to overestimates of production. However, from a research perspective the distribution of microseismicity over a vertical span that includes five distinct shale units and at least fourteen limestone units presents the opportunity to examine the relationship between rock mechanical properties and microseismic characteristics.

Using the methods described in Section 3.1.4.1, pseudo "logs" of microseismic attributes, specifically moment magnitude and event count, were generated for comparison to traditional geophysical well logs (Figure 106; Figure 107). A vertical b-value distribution was generated in ZMAP (Section 3.1.1.2).

There is apparent control over microseismic magnitudes by the geologic formations, i.e. the rock mechanical properties (Figure 106). Above the Hamilton Group, within and above the Tully Limestone, there is a sparse zone of higher magnitude events averaging approximately -2.0. Within the Hamilton Group's Moscow Shale, Ludlowville Shale, and Skaneateles Shale Members, above the Upper Marcellus, the average magnitude ranges from -2.6 to -1.75, increasing at a fairly constant rate with increasing depth. There is a zone of -1.75 magnitude events constrained within the Upper Marcellus. Within the sequence of the Purcell/Cherry Valley Limestone, Lower Marcellus, Onondaga Limestone, and Huntersville Chert the average magnitude varies with increasing depth, starting at -1.8, decreasing to -2.05 in the center of the Lower Marcellus, then increasing again to -1.7 at the bottom of the chert. Below the top of the Oriskany Sandstone and extending approximately 100 feet into the Helderberg Limestone, the average event magnitude is -1.5.

The evaluation of b-values in a one-dimensional (elevation) space can simplify and highlight overall vertically-controlled trends in the data (Figure 107). A distinct separation into two groups of b-values is observed. In the Hamilton Formation, above the Upper Marcellus, between EL -4400 and EL -5020, b-values range from ~0.7 to ~1.4, centered at a value of ~1.0. Below EL -5020, b-values range from ~0.85 to ~2.5, averaging ~1.5. A possible cause for this abrupt transition from low to high b-values is a change in the stress state of the rock across this boundary, from high differential stress to low differential stress, relatively. The relationship between Young's modulus and Poisson's ratio changes somewhat at this transition. Figure 107 shows that above the transition (7,120 feet MD or -5,020 feet EL), there is a slight negative correlation between these two parameters. Below the transition, the correlation becomes positive. Figure 108 is a correlation diagram for various well log and microseismic parameters; it is evident that the overall correlation is only slightly positive (~0.2). Analysis above and below the transition provides more insight.

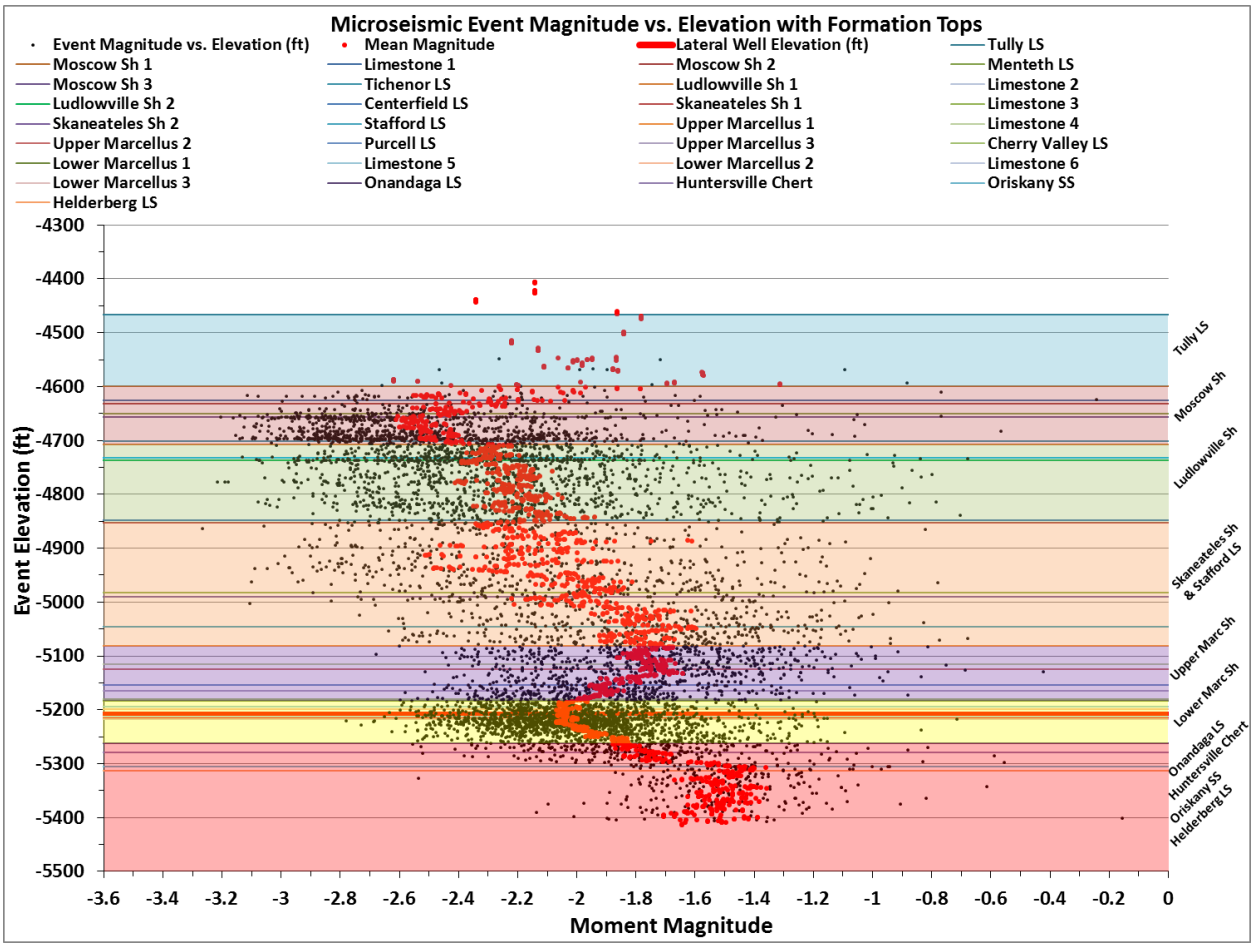

Figure 106 – Elevation (feet) versus moment magnitude for the entire microseismic catalog, with detailed formation and member tops. Red dots are average values of moment magnitude for a 5-foot thick sampling window, moved vertically though the microseismic cloud. Detailed Stratigraphy from USGS (1993).

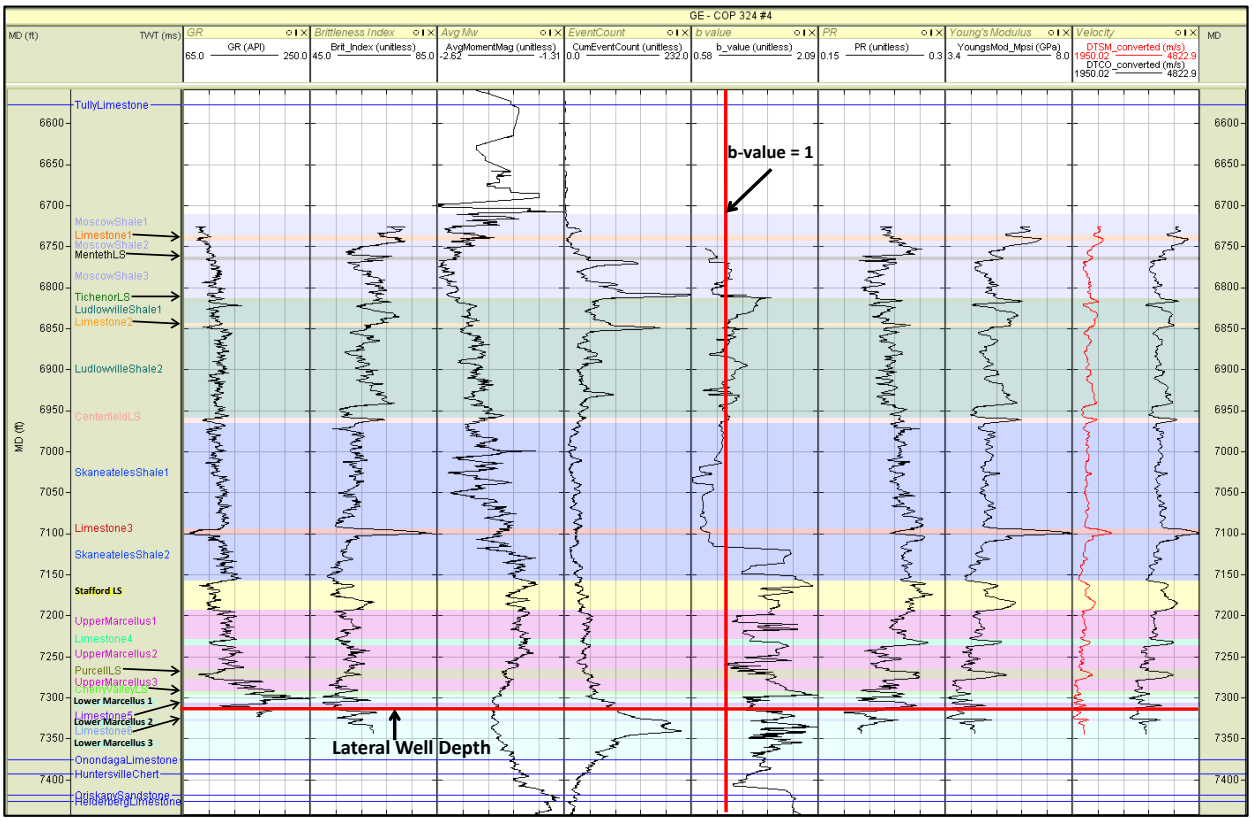

Figure 107 – Vertical geophysical well logs and microseismic pseudo-logs at Clearfield County.

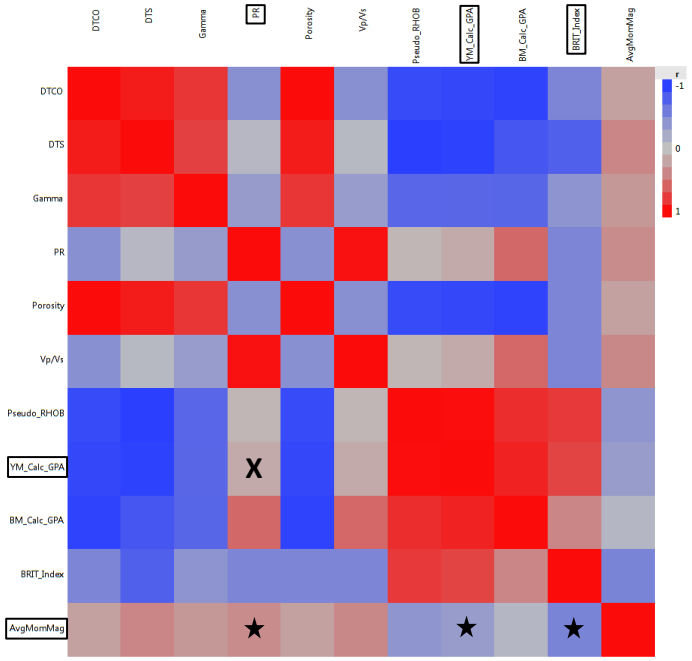

Figure 108 – Correlation diagram for geophysical and microseismic logs. Relationships of interest marked.

Cross plot analysis of the vertical geophysical well logs and microseismic pseudo-logs (Figure 109 to Figure 117) shows a distinct distribution of microseismic event magnitudes in a Young's Modulus (YM)-Poisson's Ratio (PR) cross plot space, and also separation of different shale and different limestone units resulting from varying geomechanical properties. Event magnitudes tend to be larger in the high PR/low YM area of the cross plot corresponding to a less brittle rock, and vice-versa. A cross plot of PR and YM separately, versus event magnitude reveals that both mechanical properties exert control over the magnitude, but it is difficult to definitively identify the more dominant property with just one study. Lastly, high PR tends to result in a low number of microseismic events, and the number of events increases rapidly as PR decreases.

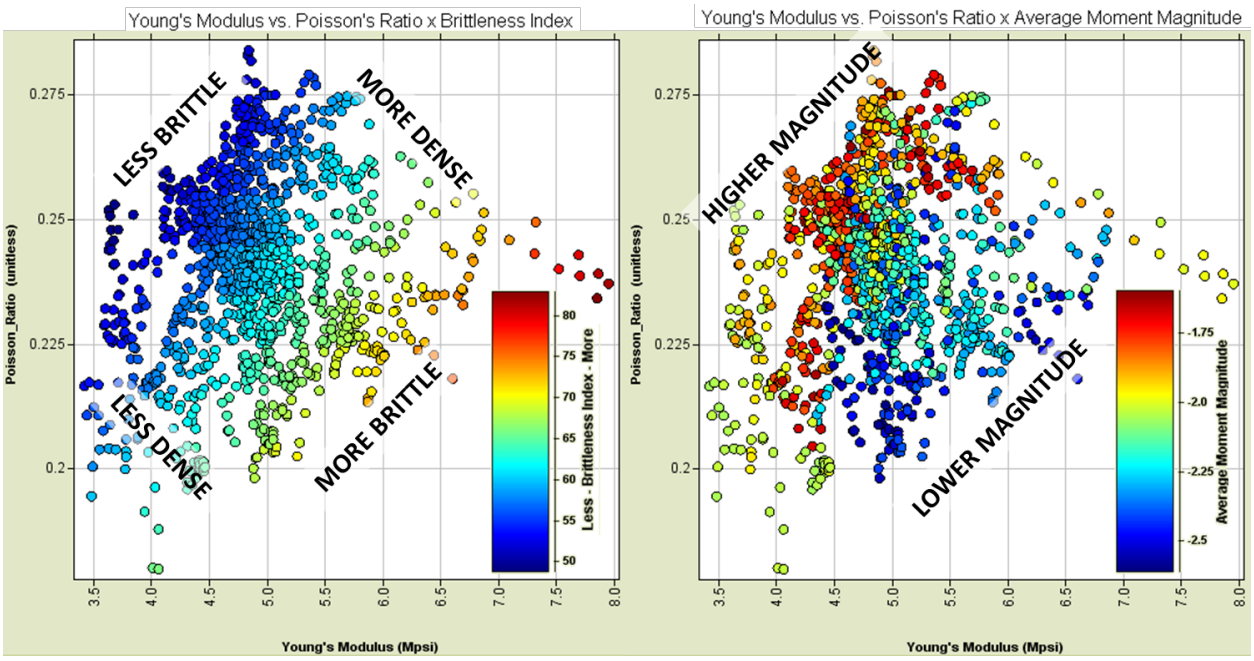

Figure 109 – PR versus YM colored by brittleness and moment magnitude for all rock types.

Brittleness is an attribute calculated using YM and PR to quantify the readiness of a material to fracture when strained. A brittle material will fracture without absorbing much energy and without deforming significantly. A non-brittle (plastic) material will absorb more energy and deform before fracturing. Brittleness is calculated using the following equation:

$$Brittleness = ((YM-1) / 7 + (PR-0.4) / (-0.25)) * 50 \quad \textbf{Equation 36}$$

after Rickman, Mullen et al. (2008). The smooth brittleness gradient on a PR-YM crossplot (Figure 109) is due to the fact that brittleness is a function of only YM and PR. Replacing brittleness with average moment magnitude as the third (colored) dimension on the PR-YM crossplot highlights the fact that these two important elastic parameters play an important role in the expression of microseismicity during hydraulic fracturing. The moment magnitude of a seismic event is positively correlated with the amount of energy released during that event. As stated above, a brittle material will absorb less energy and fail under smaller strain when compared to a plastic material, so it follows that the relationship seen in Figure 109 in which larger microseismic events fall in the less brittle zone of a PR-YM crossplot and vice versa exists.

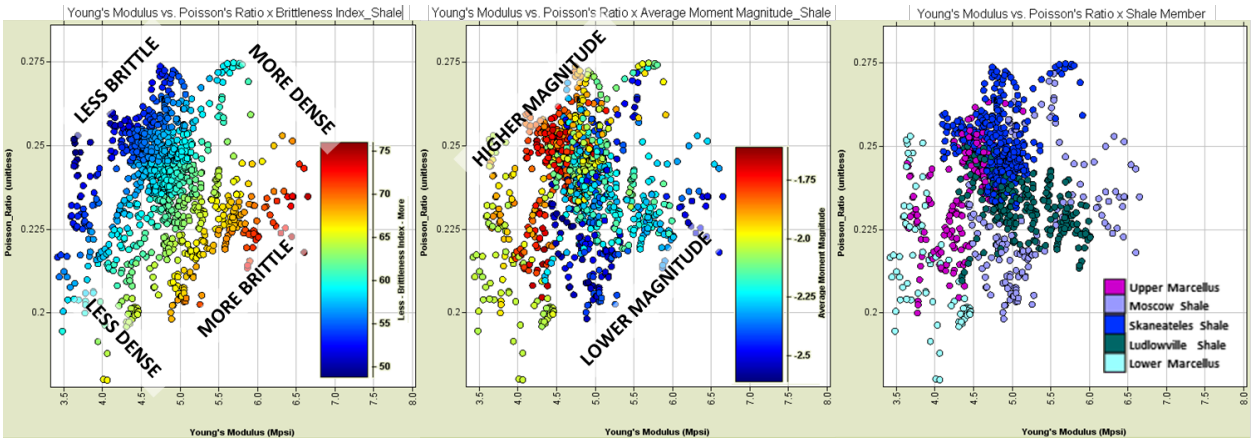

Figure 110 – PR versus YM colored by brittleness, moment magnitude, and shale member.

Figure 109 includes both shale and limestone lithologies, but if these two distinct rock types are viewed separately, the relationships become slightly refined (Figure 110; Figure 111). The far right portion of each figure shows the PR-YM crossplot colored by the shale or limestone member name. Comparison of the rock name with the magnitude distribution reveals that discreet stratigraphic units tend to plot in clusters on the PR-YM crossplot and microseismicity within each unit tends to be of the same general character. For example, in Figure 110 the magenta colored shale, the Upper Marcellus, tends to contain the highest magnitude events (red on the middle plot).

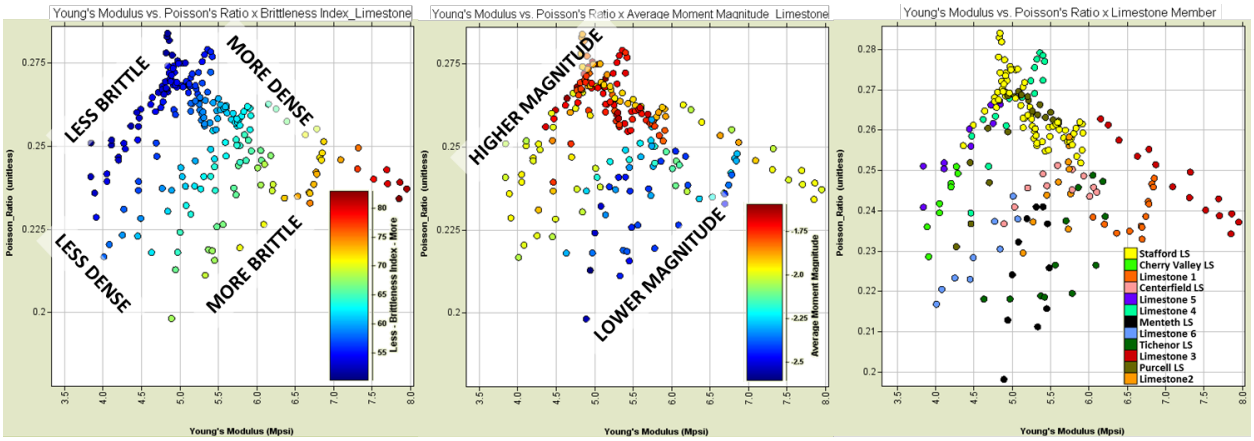

Figure 111 – PR versus YM colored by brittleness, moment magnitude, and limestone member.

Both YM and PR exert control over the magnitude of failure, but is one property more influential than the other? Plotting PR versus moment magnitude with color according to the lithologic member (Figure 112) shows a fairly poor correlation in the shale and a much better correlation in the limestone. Lewandowski, Wang et al. (2005) performed laboratory analysis on metallic glass samples to quantify their toughness and brittleness in terms of fracture energy, or the energy required to create a fracture. They found that fracture energy increases exponentially

as PR increases (Figure 113). One could readily make the connection between fracture energy and moment magnitude because the energy release of a seismic event increases exponentially with the seismic moment. YM versus magnitude (Figure 114) shows a slightly improved correlation in the shale and drastically reduced (essentially zero) correlation in the limestone. An even better correlation in the shale is achieved when brittleness is plotted versus magnitude (Figure 115). The outlying Lower Marcellus data points that appear in Figure 112 and Figure 114 are pulled in toward the overall trend-line in Figure 115 and the distribution appears to be more symmetrical about the trend-line.

Regarding the outlying Lower Marcellus Shale data, it is proposed here to be the consequence of very near-field pressure perturbation. Changes in the stress state can affect the elastic properties of the rock, becoming more or less elastic. The Lower Marcellus, acting as the host of the injection point, would experience a local and temporary increase in stress and homogenization of elastic properties. The geophysical logs used to generate all cross-plots were acquired prior to hydraulic fracturing and represent the in-situ conditions. Notice the very narrow range of moment magnitudes with the Lower Marcellus (Figure 112). This suggests the same style of brittle failure over and over again, even though Poisson's ratio varies between ~0.1 and ~0.35. It is concluded that these outlying data do not adversely affect the analyses presented here, but rather, the consistency of the microseismic response within the Lower Marcellus suggests a temporary stress-related "adjustment" of the elastic properties.

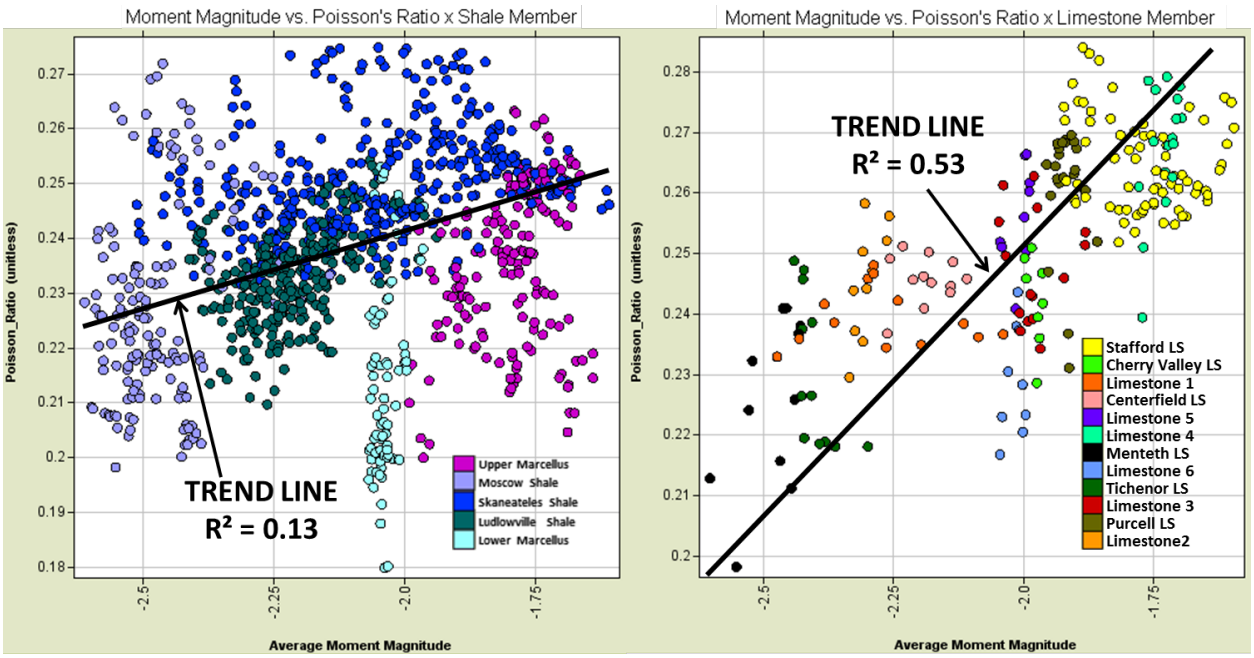

Figure 112 – PR versus moment magnitude colored by shale member and limestone member.

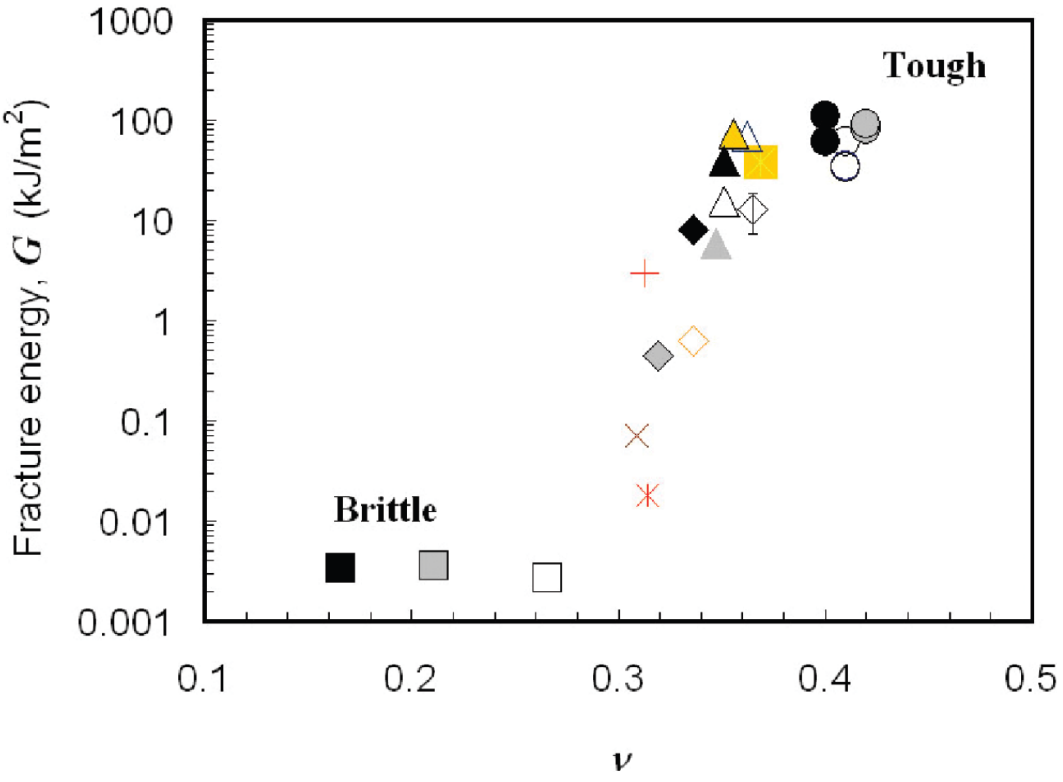

Figure 113 – Fracture energy versus PR showing the fracture toughness gradient. From Lewandowski, Wang et al. (2005).

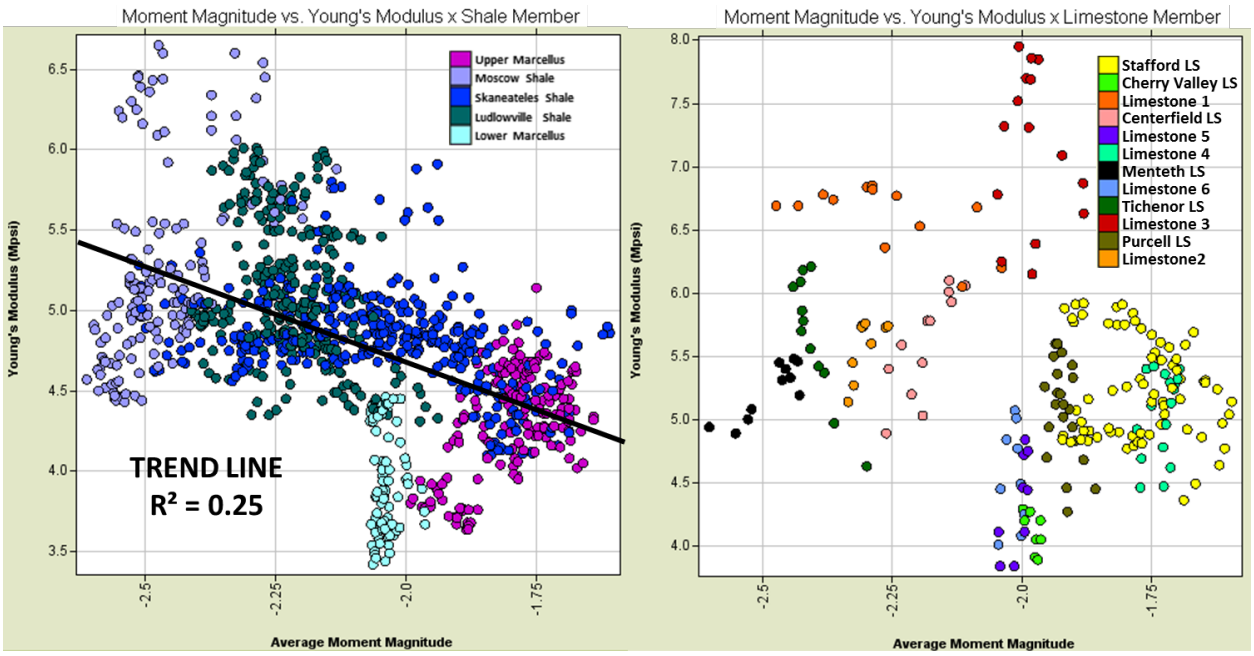

Figure 114 – YM versus moment magnitude colored by shale member and limestone member.

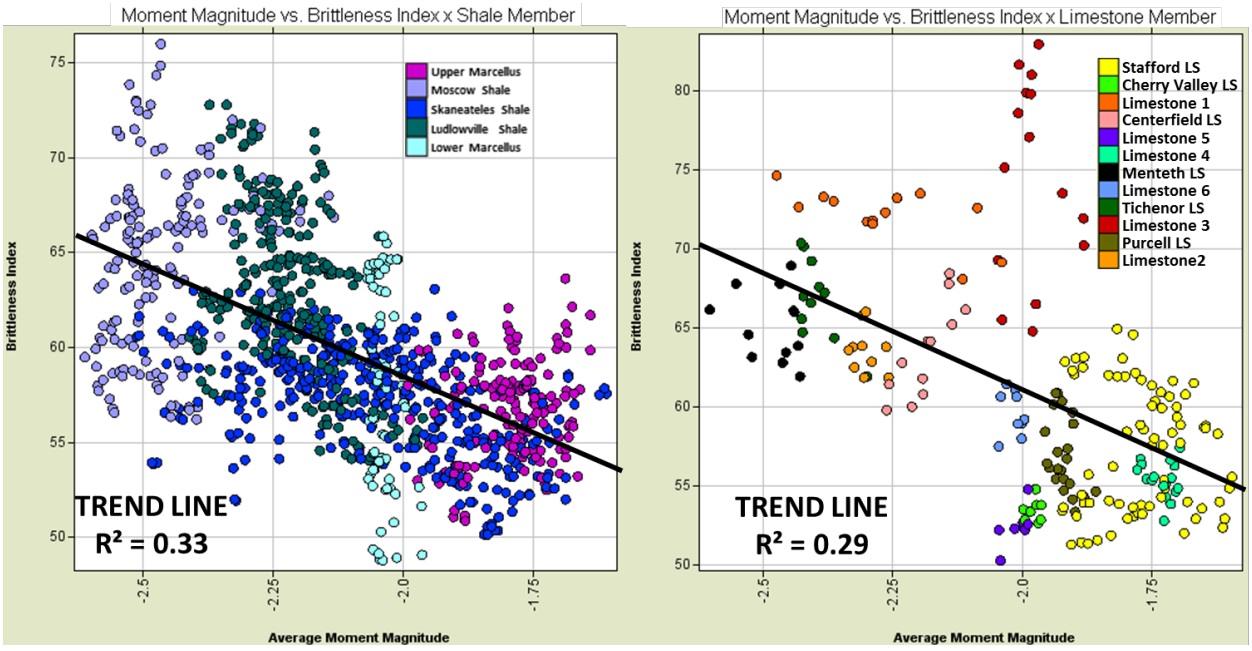

Figure 115 – Brittleness versus moment magnitude colored by shale member and limestone member.

The Gutenberg-Richter relationship, which explains the frequency-magnitude distribution for earthquake catalogs, was discussed in Section 3.1.1. It has been shown that this microseismic catalog follows this relationship, with event count increasing exponentially as event magnitude decreases.

Figure 112 showed that PR is not well correlated with magnitude in the shale rocks but better correlated in limestone. The correlation between brittleness and magnitude is ~ three times better in shale than PR. Since statistically, there are less large magnitude events than small magnitude events, PR and brittleness should have a relationship with event count and magnitude.

PR versus event count for shale colored by magnitude (Figure 116) shows an exponential increase in the number of events as PR decreases and the events become progressively smaller in magnitude. The shale members separate from each other in this cross-plot space; the Skaneateles Shale has the highest overall PR and the lowest overall event count, the Upper Marcellus has a slightly lower PR and the second highest event count, and the Ludlowville Shale has the third lowest PR and third highest event count. The Moscow Shale and Lower Marcellus Shale occupy large ranges in both PR and event count but generally follow the overall trend. Limestone (Figure 117) behaves similarly to shale in this cross-plot space but the number of sample points is much lower, resulting in a less well defined distribution.

In a brittleness versus event count crossplot, the magnitude gradient becomes better defined (Figure 118). The largest magnitude events are restricted to the low brittleness/low event count region of the plot, while the smallest magnitudes are restricted to the higher brittleness region. Small magnitude event count displays significantly more scatter than large magnitude count, likely due to detection limits of the instrumentation. If an event's magnitude is smaller

than the magnitude of completion for the catalog, then it is certain that that not all events of that magnitude were detected by the instrumentation.

The Mu·Rho-Lambda·Rho crossplot space (Figure 119 and Figure 120) correlates very well with magnitude in both the shale and limestone rocks, perhaps the best of all methods shown so far. The next section will focus on LMR for an analysis of microseismic variability in the Marcellus Shale alone.

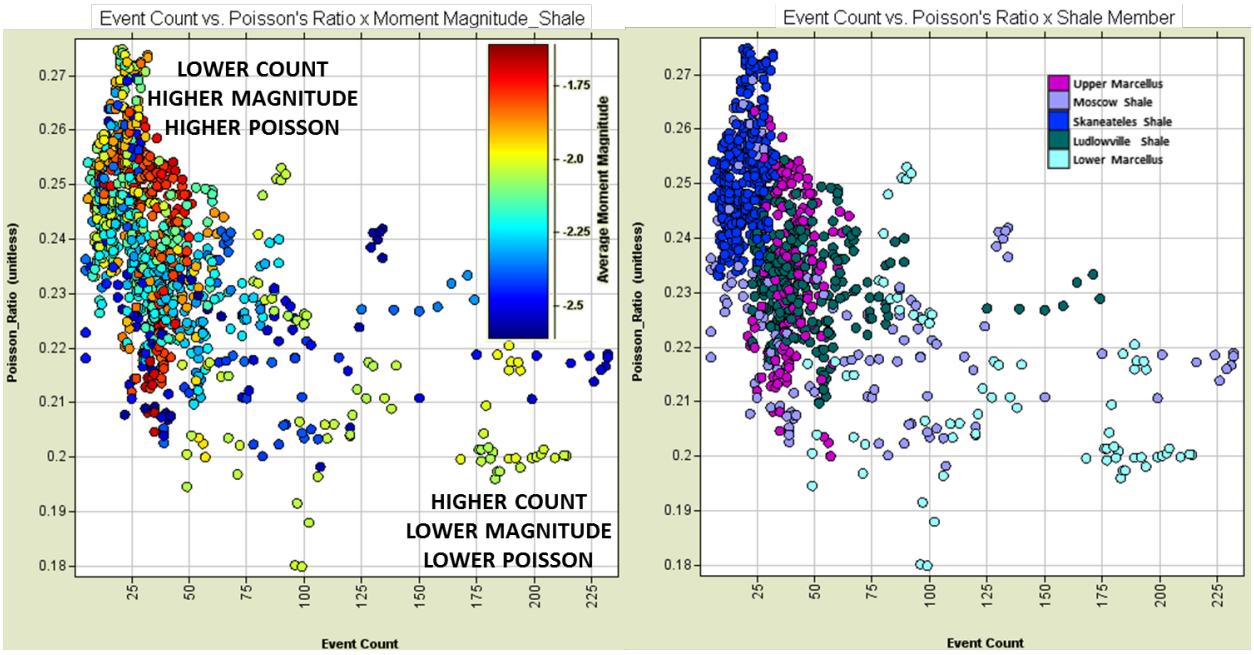

Figure 116 – PR versus microseismic event count colored by moment magnitude and shale member.

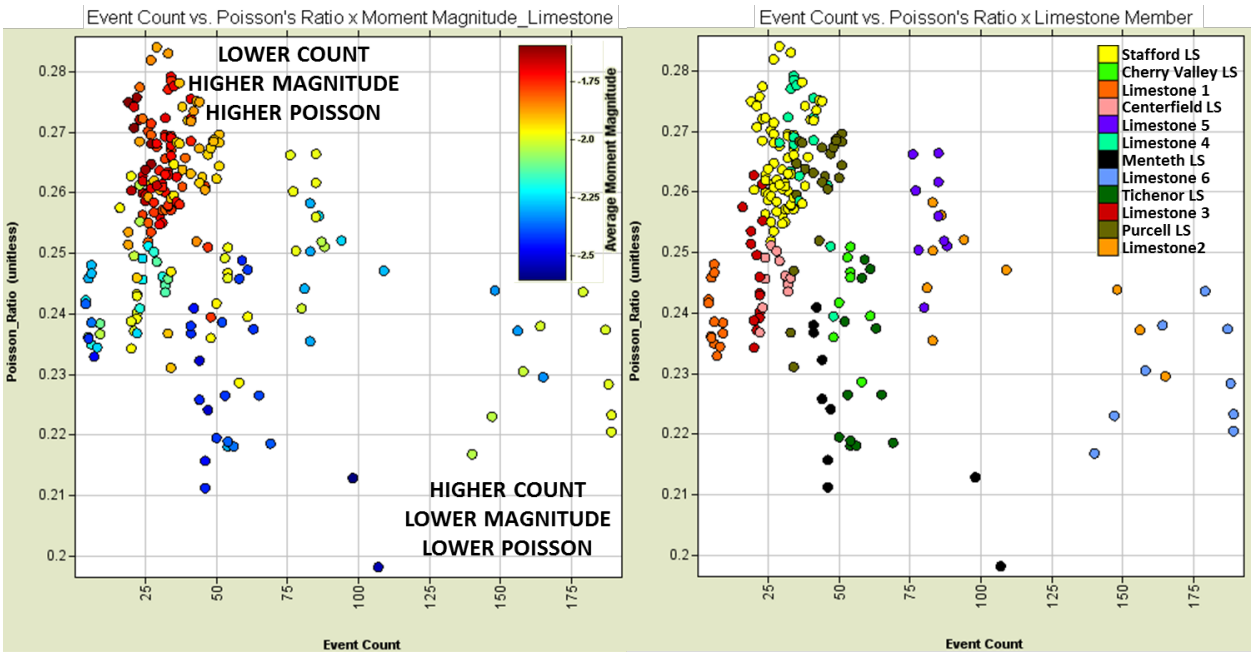

Figure 117 – PR versus microseismic event count colored by moment magnitude and limestone member.

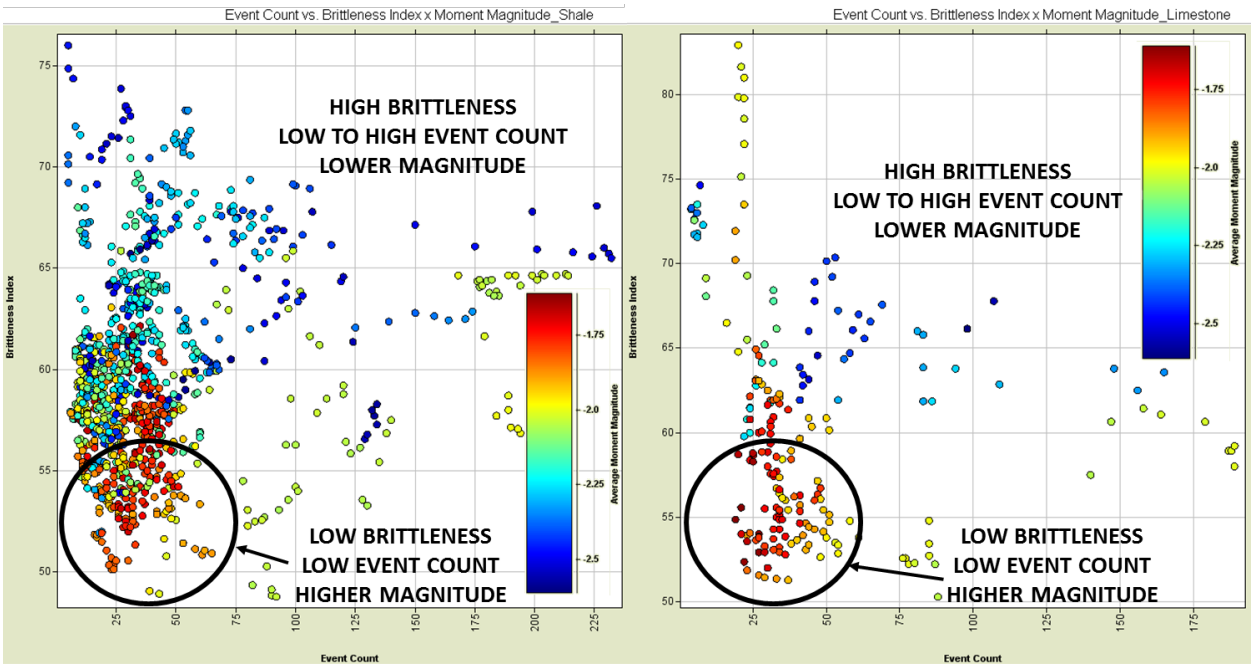

Figure 118 – Brittleness versus microseismic event count colored by moment magnitude for shale and limestone separately.

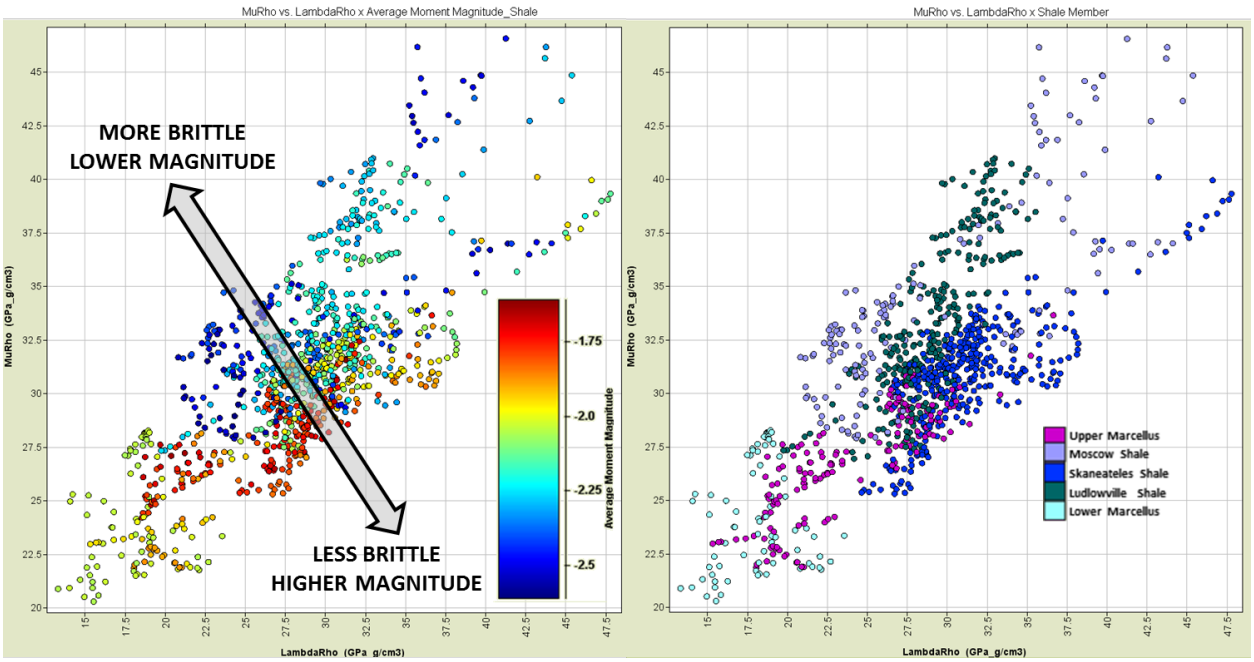

Figure 119 – MR versus LR colored by moment magnitude and shale member.

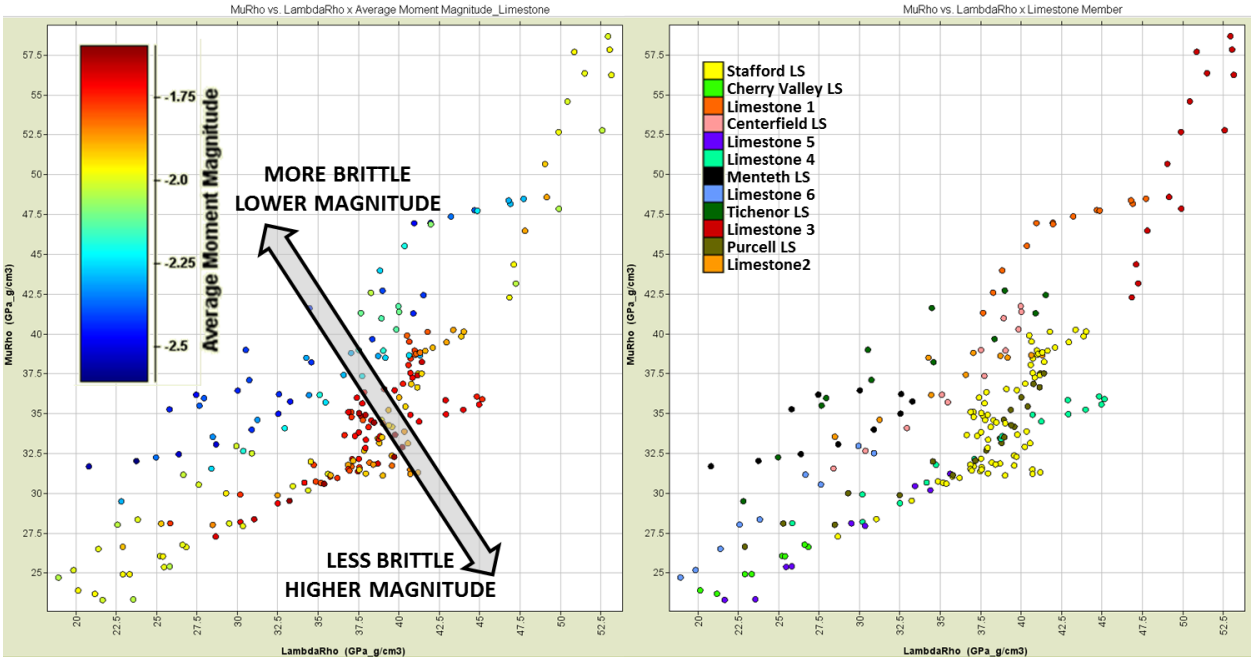

Figure 120 – MR versus LR colored by moment magnitude and limestone member.

3.3.6 Lateral Microseismicity Distribution

In the previous section, an apparent relationship was established between the elastic properties of rocks of the Hamilton Group and the corresponding microseismic response. Approximately 600 feet of vertical geophysical well logs were compared to the microseismic cloud distributed throughout the geologic column. The Marcellus Shale is sufficiently heterogeneous to test this hypothesis in a single geologic unit, utilizing the variation in elastic properties and microseismic attributes along the trajectory of the lateral section of the well bore. Using the methods described in Section 3.1.4.2, pseudo-logs of microseismic attributes, specifically moment magnitude and event count, were generated for comparison to traditional geophysical well logs (Figure 121).

Analysis of the lateral geophysical well logs shows that the Marcellus Shale at this study location falls in a less brittle space on an LMR crossplot (Figure 122) compared to reservoir rocks such as carbonate, sandstone, coal, and other shale rocks. There is agreement between the microseismic behavior of the Marcellus Shale in response to changing elastic properties and the microseismic behavior in the overlying Hamilton Group in general, described in the previous section.

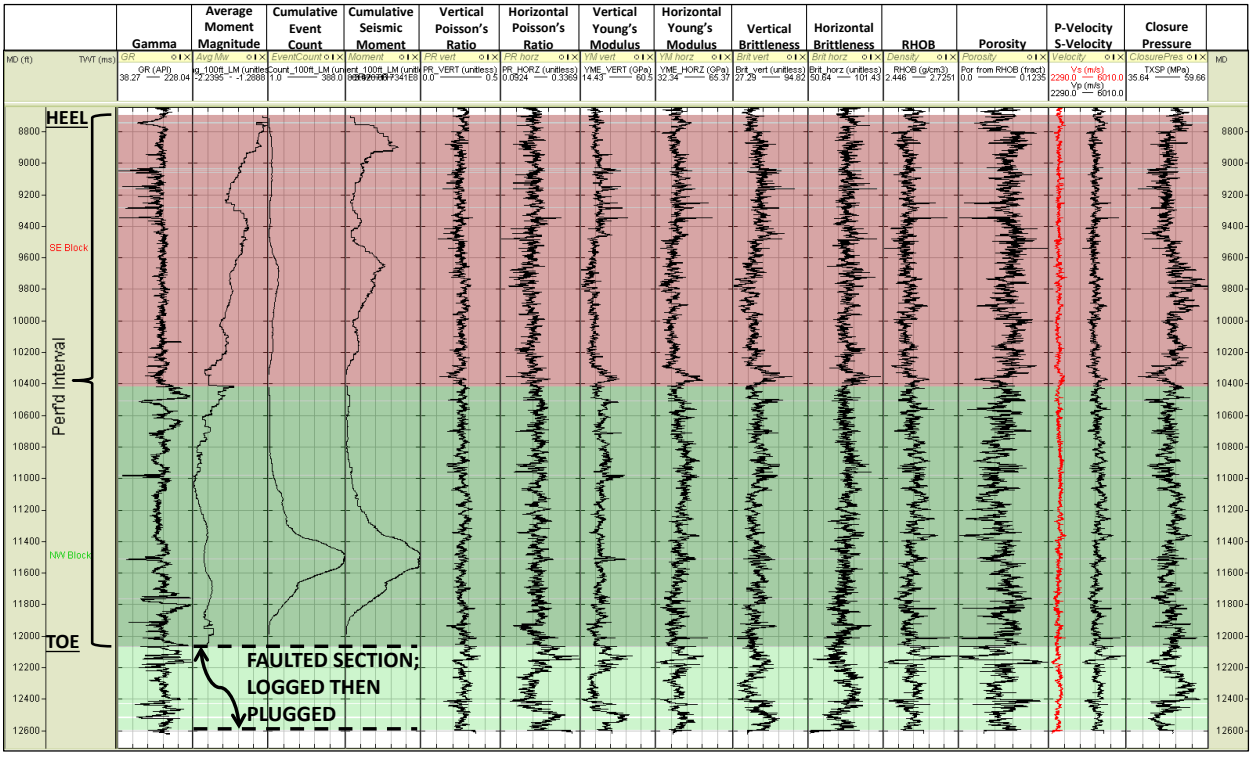

Figure 121 – Lateral geophysical well logs and microseismic pseudo-logs at Clearfield County.

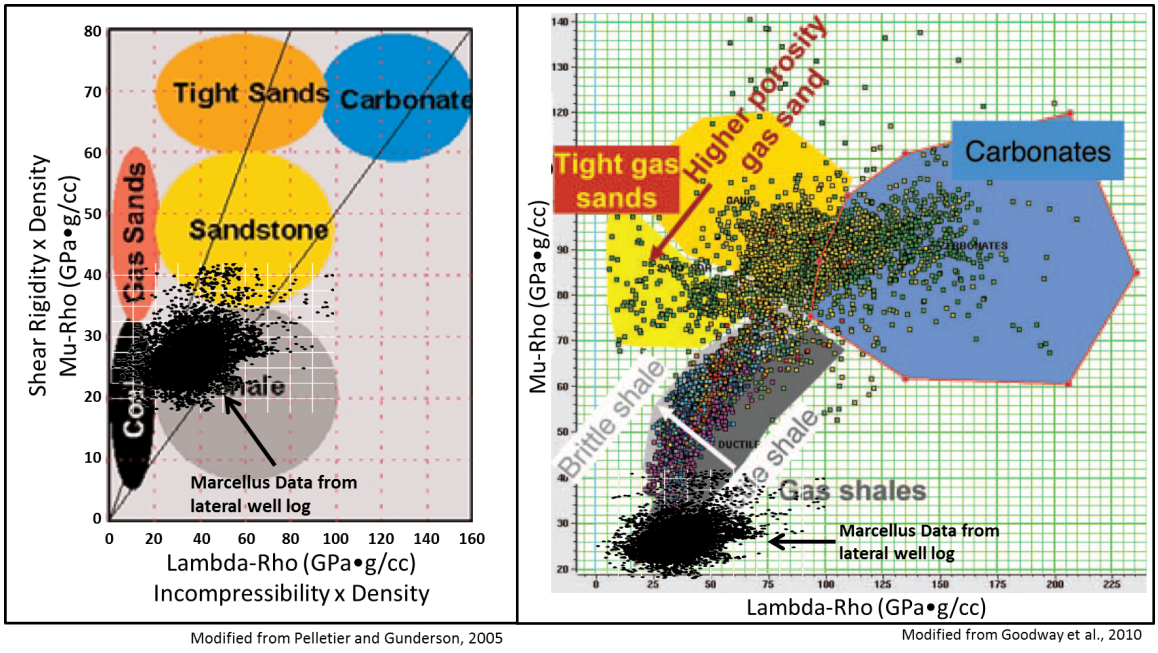

Figure 122 – Published MR versus LR lithology crossplots with Clearfield Marcellus Shale values superimposed. Modified from Pelletier and Gunderson (2005) and Goodway, Perez et al. (2010)

Section 3.3.7 will review evidence for a fault or discontinuity crossing the lateral well at approximately the midpoint. For the sake of the following discussion, there is a distinct change in the character of the microseismicity from what is being termed the "NW fault block" to the "SE fault block". The vertical extent of microseismicity is larger in the NW block but the overall event magnitude is lower and event density is higher. The lateral extent of microseismicity is larger in the SE block, but overall event magnitude is higher and event density is lower. In addition, there is a dearth of microseismicity across a lateral band sub-perpendicular to the well trajectory, hinting at a possible structure diverting hydraulic energy in this region.

Similar to the PR-YM cross-plots from the vertical well logs, LMR cross-plots colored by average event moment magnitude from the lateral well indicate that as brittleness increases, magnitude decreases. In other words, as the rock becomes more brittle, its ability to store potential energy before rupturing diminishes. There is an added dimension of information present in the lateral well log; horizontal and vertical (or fast and slow, respectively) velocity from which fast and slow moduli and higher order properties can be calculated. Shale will be stiffer in a direction parallel to bedding (Figure 123) (higher YM – large arrow, lower PR – small arrow) due to the added structural support on a micro-scale of grain alignment parallel to bedding. A lower YM and higher PR will be experienced perpendicular to bedding.

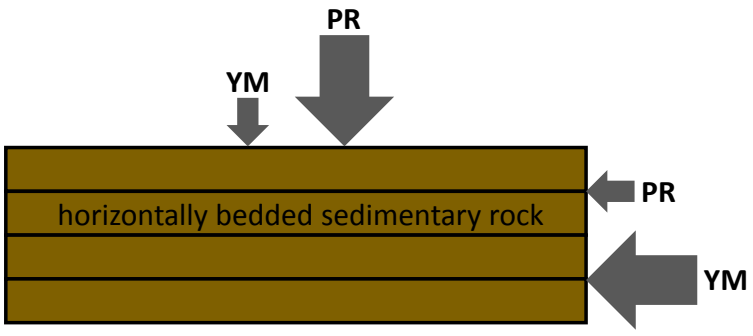

Figure 123 – Schematic diagram illustrating anisotropic effect of layering on elastic rock properties.

LMR cross-plotting for both sides of the fault indicates that the NW and SE blocks occupy two different spaces in the cross-plot. The NW block occupies a slightly more brittle space than the SE block (Figure 124). LMR characteristics of the rock change between the slow and fast (vertical and horizontal, respectively) orientations (Figure 125 and Figure 126). MR almost doubles from slow to fast, as one might expect because it is simply the shear impedance squared. The rock exhibits more plastic behavior in the vertical direction and more brittle behavior in the horizontal direction. LR, however, changes very little. LR is the difference between the compressional impedance squared and two times the shear impedance squared, so it is less sensitive to absolute changes in p and s-wave velocity and more sensitive to changes in the velocity ratio. Russell (2010) notes that MR gives insight into the matrix of the rock (i.e. brittleness or plasticity) and LR is a fluid indicator because fluids affect the p/s-wave velocity ratio.

The gradation of moment magnitude appears to be better defined on a cross-plot of slow MR versus slow LR than on a plot of fast MR versus fast LR (Figure 125 and Figure 126). This is especially evident in the SE block of the dataset. Observe the better definition and separation of magnitude on Figure 125 than in Figure 126, where the smallest and largest magnitude events appear to be almost evenly distributed throughout the cross-plot. The reason for this is unclear, but it is proposed here that the apparent strong influence of the vertical geomechanical properties of the shale on the observed magnitude has a larger implication. The Marcellus Shale is both fissile and naturally vertically fractured. These planar features are natural weaknesses for hydraulic fracturing to exploit in expanding a discrete fracture network. Fluid entering the horizontal bedding planes of the shale would exert a vertical force pushing the planes apart, causing a vertical shear at the fracture tip. Dilation of a vertical fracture would cause a lateral

shear at the fracture tip. Therefore, the vertical (slow) shear modulus would dictate how energetic a bedding plane failure is, while the horizontal (fast) shear modulus would determine the energy release from failure on a natural fracture. Given the lower correlation of magnitude with fast MR it is suggested that bedding plane failure is the dominant mechanism. Vertical propagation of the fracture network would be accomplished in a step-wise fashion as bedding planes are connected by vertical shearing and natural vertical fractures.

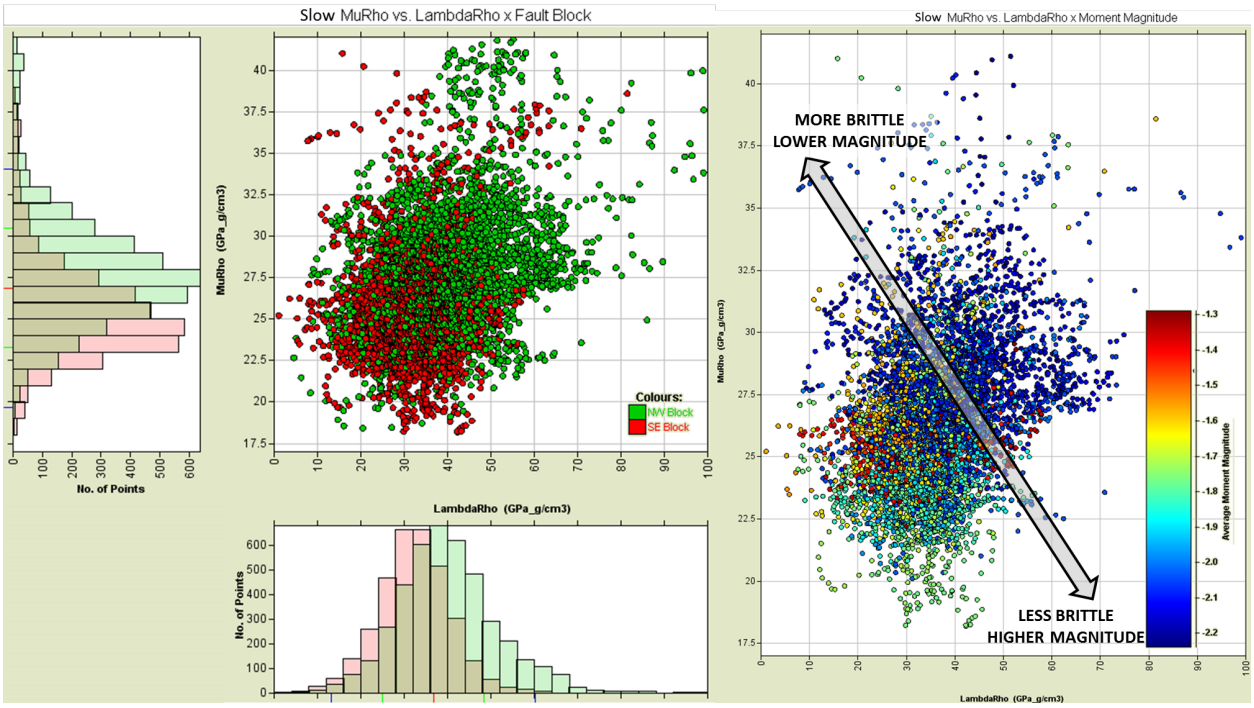

Figure 124 – Left – slow MR versus LR, separated by fault block. Right – slow MR versus LR colored by moment magnitude.

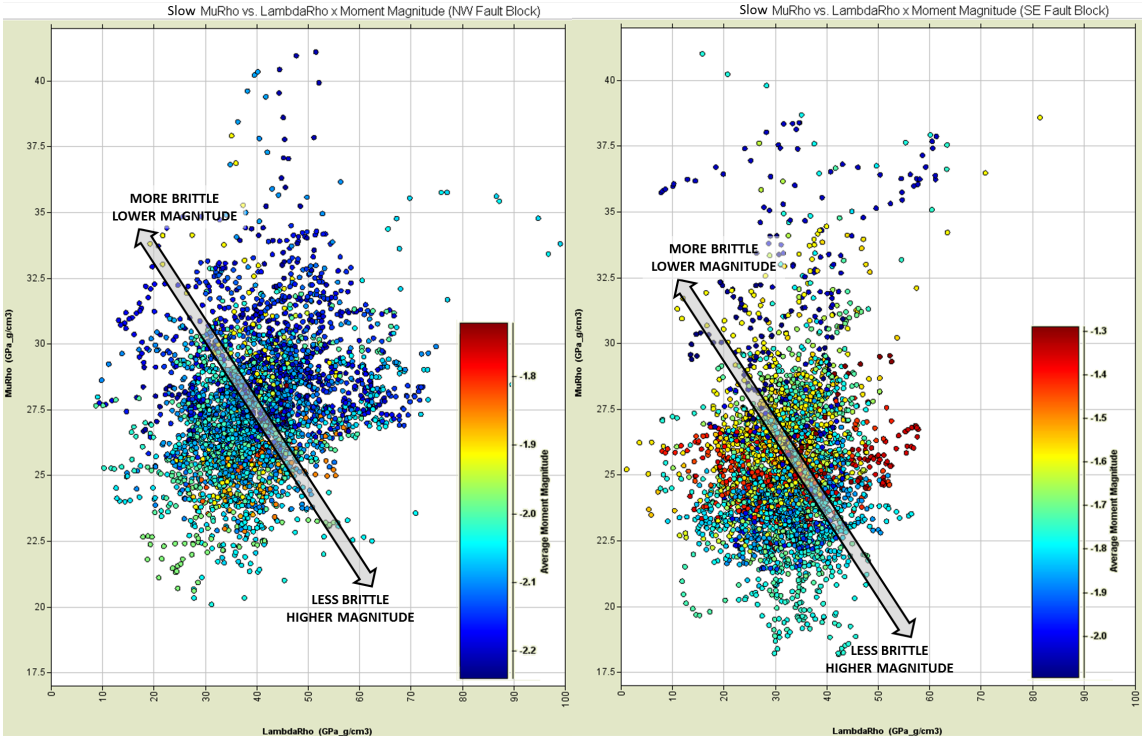

Figure 125 – Slow MR versus LR colored by moment magnitude; NW block (left), SE block (right).

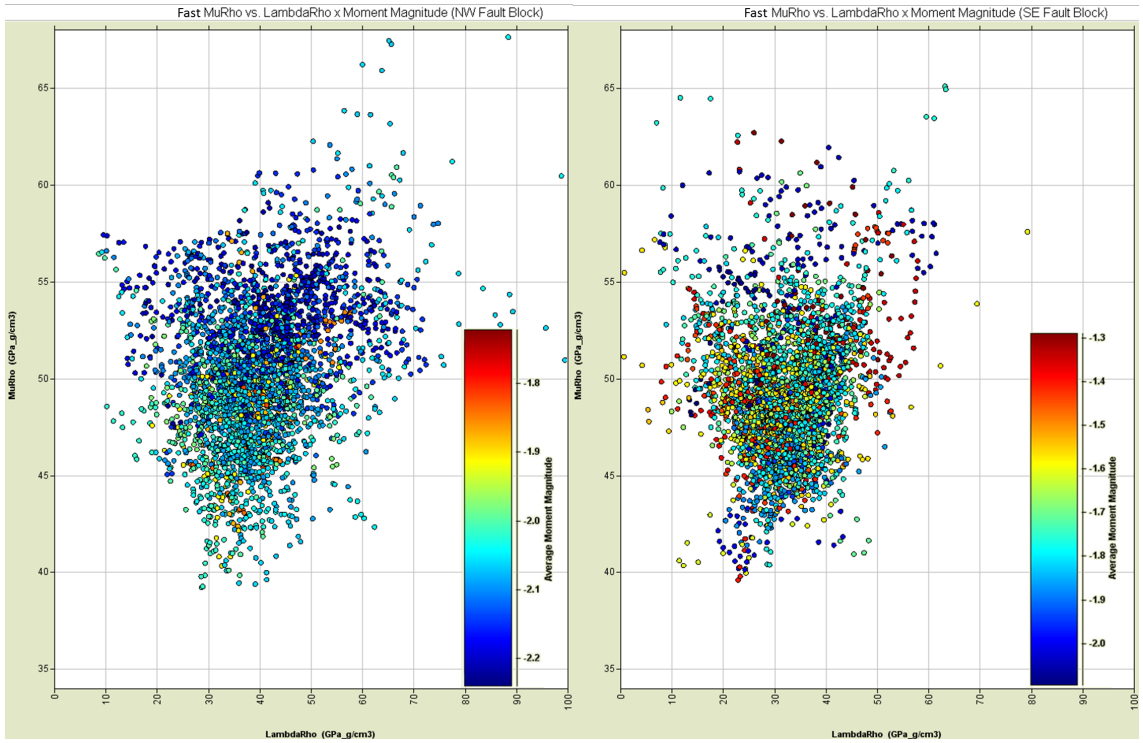

Figure 126 – Fast MR versus LR colored by moment magnitude; NW block (left), SE block (right).

Young's modulus, Poisson's ratio, seismic velocity, and density play an important role in dictating the microseismic expression that will be recorded during hydraulic fracturing. Prior knowledge of rock properties from well logs can enable operators to predict the microseismic response before they hydraulically fracture. Operators can expect low numbers of larger events in more elastic/plastic (high PR) rocks, and large numbers of small events in more brittle (low PR) rocks. In terms of the "fracability" of the reservoir, targeting low PR volumes will result in more microseismic activity; advantageous if this is taken as a proxy for increased stimulation and fracture network creation. Conversely, less brittle rocks may be more susceptible to aseismic deformation (slow-slip), potentially another important stimulation mechanism. This exercise showcases a novel approach to microseismic data, adding new and complimentary understanding to the knowledge of unconventional shale reservoirs. Key conclusions include:

1) Larger magnitudes tend to occur in high PR and low brittleness rocks.

2) Smaller magnitudes tend to occur in low PR and high brittleness rocks.

3) The large range in event count for low magnitude events is likely a result of detection limits. The microseismic catalog is complete only above the magnitude of completion, so smaller events will be detected in lower numbers.

4) PR by itself is a good predictor of event count and brittleness is a good predictor of event magnitude.

5) Event magnitude is best correlated with LMR, where high MR corresponds to a more brittle rock and smaller magnitude.

6) The stronger correlation of event magnitude with LMR measured in the vertical direction in the Marcellus Shale suggests a tendency toward bedding plane failure connected by vertical fractures and shearing.

3.3.7 Microseismic Characterization of an Unmapped Fault

The spatial distribution of the microseismic cloud is a first order indicator of interaction with linear features during hydraulic fracturing. The sharp truncation of microseismicity on the northeastern ends of each microseismic wing, for stages three and four, is the first indicator of fault interaction (Figure 127). Compare this to the southwestern ends, where microseismicity gradually becomes more diffuse. A fault can be sketched to follow the well-defined linear edge of the cloud, and simply extended across the stimulated volume. An examination of subsequent stages in the context of this linear feature shows that stages five, six, and seven cluster on the northwestern side of the proposed fault with very few events occurring on the southeastern side (Figure 128). One might be inclined to attribute this to detection limits, but it is important to note the location of one downhole array (GE COP 324 #4) is within this zone of low event density. Stages eight and nine cluster around the well bore on the southeastern side of the fault with some growth to the northwest (Figure 128).

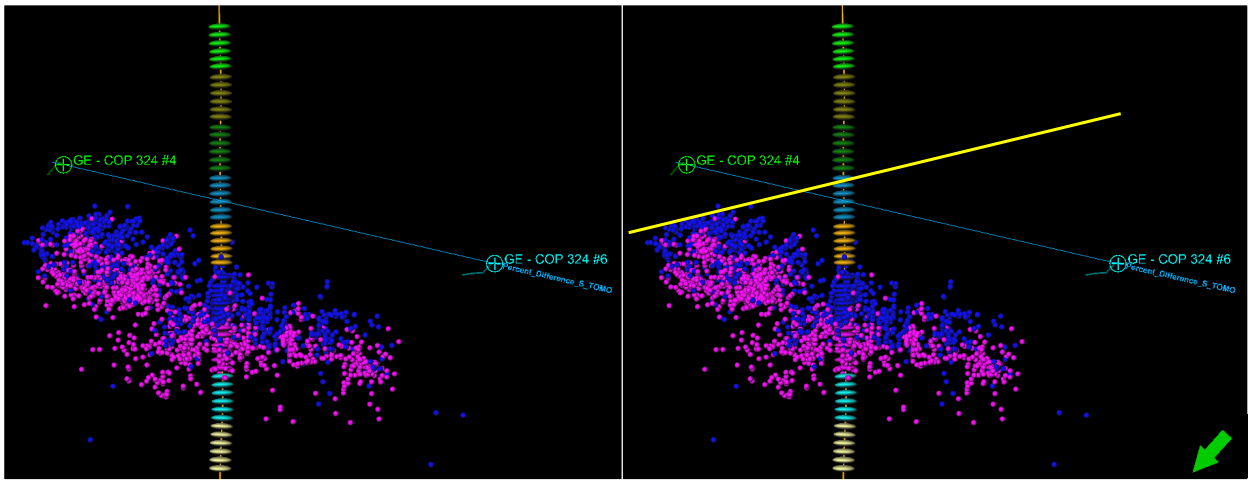

Figure 127 – Map view of Stage 3 (pink) and Stage 4 (blue) microseismic events with proposed fault (yellow).

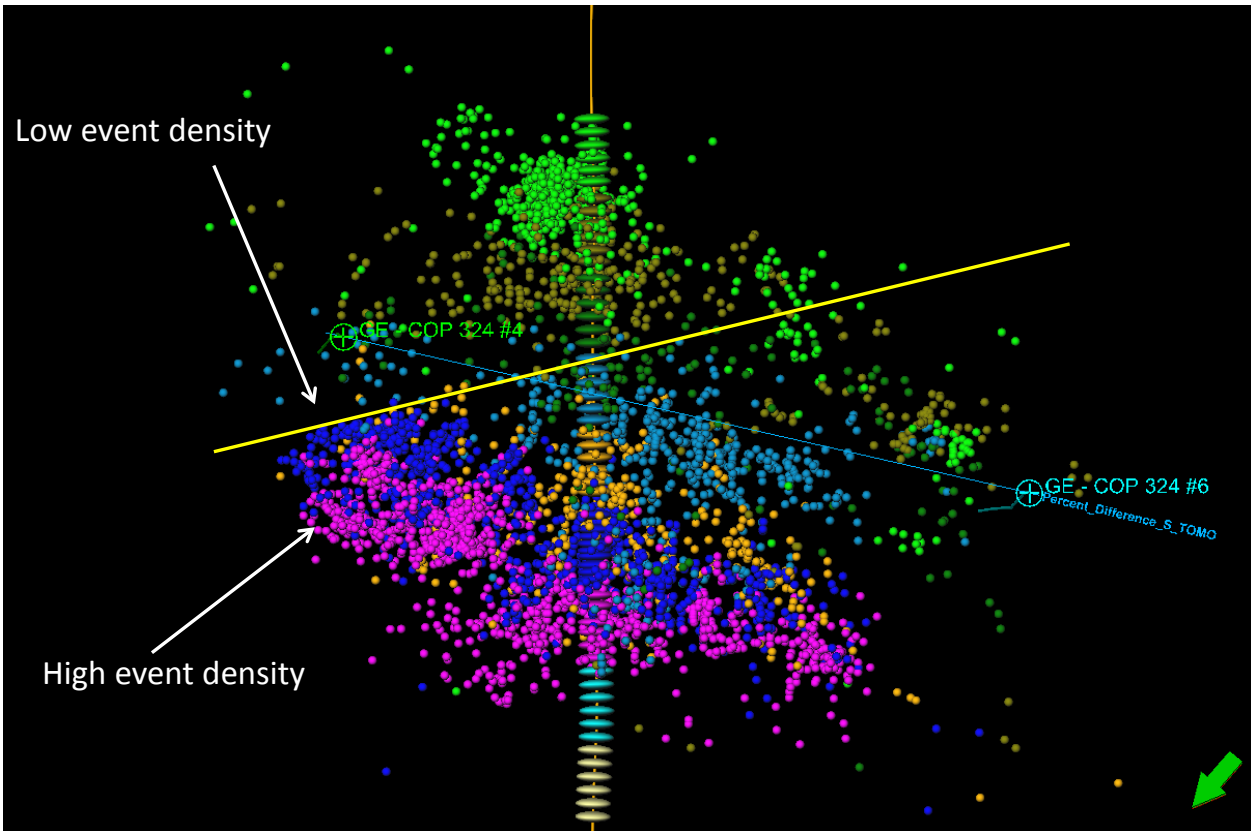

Figure 128 – Stage 3 to Stage 9 events showing zones of low and high event density and proposed fault.

As described in Section 3.1.4, the direction of $S_{h\text{-}max}$ can be inferred by the azimuth of the long axis of an ellipse fit around the microseismic events in a single stage. In a multi-stage hydraulic fracturing operation, the resulting microseismic cloud will give multiple estimates of $S_{h\text{-}max}$ orientation along the length of the well bore. Yale (2003) proposed that in a geologic setting where fault blocks are present and there is a relatively small horizontal differential stress, both of which are the case in the Appalachian Basin, the local stress field may rotate slightly from one fault block to the next. The World Stress Map of Heidbach, Reinecker et al. (2009) contains two $S_{h\text{-}max}$ measurements from borehole breakouts, both approximately 41 miles east of this project site, oriented 67° and 70°. In Stages 1-8, the average orientation of the microseismic clouds is N67.9°E; Stages 9-13 yield an average of N82.4°E (Figure 129). This is a relatively

abrupt change in the inferred direction of $S_{h\text{-}max,}$ and it is proposed here that there is a northeast trending, low-offset, sub-vertical fault present in the vicinity of the middle stages of the lateral well that causes this (likely) local perturbation it the stress field. Additional lines of evidence will be presented in the following pages.

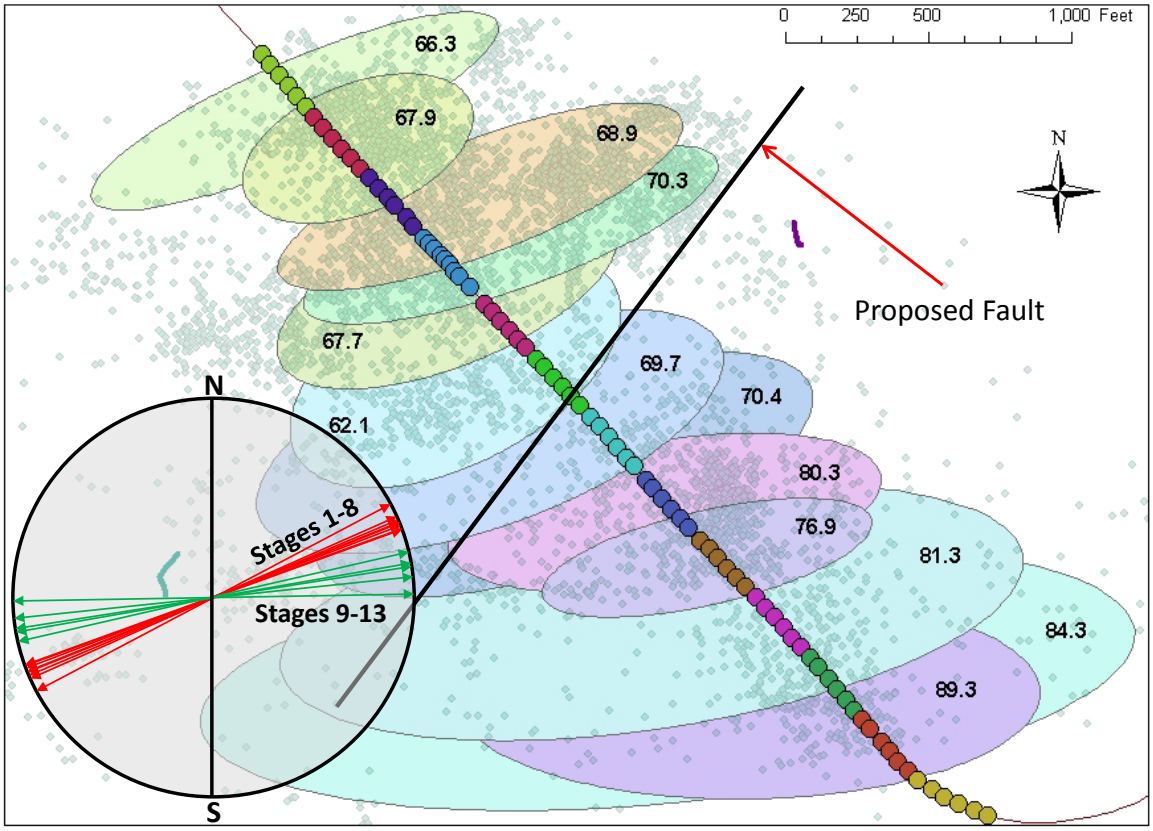

Figure 129 – ArcGIS® directional distribution ellipses for all stages at Clearfield. Ellipses are one standard deviation (contain 68% of features). Inset shows the compass orientation of ellipses (S_{h_max} orientation), highliting the distinct 10-15° rotation across the discontinuity.

The location and alignment of microseismic events in space is important, but the distribution of the properties of said events tells a more detailed story. Figure 130a and Figure 131a show a map view of the microseismic cloud displayed as a cellular moment density map. In

a three dimensional grid space the seismic moments of events within a single cell are summed, resulting in a single moment density for that cell; red is a high density and white is a low density. An immediately apparent feature of this map is the preponderance of low density cells on the northwest side of the proposed fault location. Given the geometry of the downhole detection arrays (shown as red and green "strings" of geophones) there is no reason to believe this is a product of detection bias. Seismic moment and energy exponentially increase as the magnitude incrementally increases, so if the data is filtered to remove these low density cells a better picture of the stimulated or "damaged" volume is revealed (Figure 130b and Figure 131b). After removal of the low density cells a feature becomes apparent. Goodway, Monk et al. (2012) document the absence of microseismicity in a linear arrangement as indicative of the presence of a fault. In this case it appears a fault is preventing a sufficient increase in pore pressure inside of it to cause substantial stimulation, while at the same time introducing a local stress field anomaly that is causing differing microseismic behavior on either side. The following discussion of spatial b-values will build upon this argument.

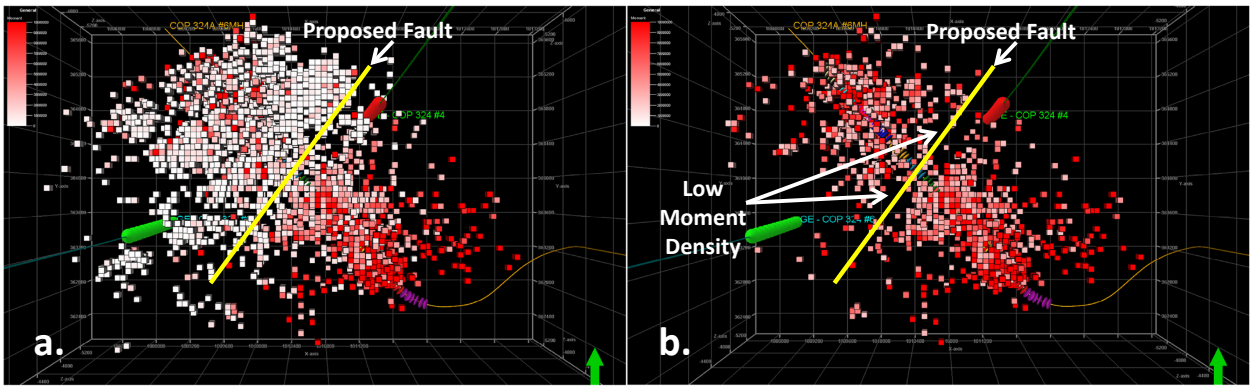

Figure 130 – 3 dimensional cellular moment density map. Zone of low deformation surrounds proposed fault location. Modified from Schlumberger (2013).

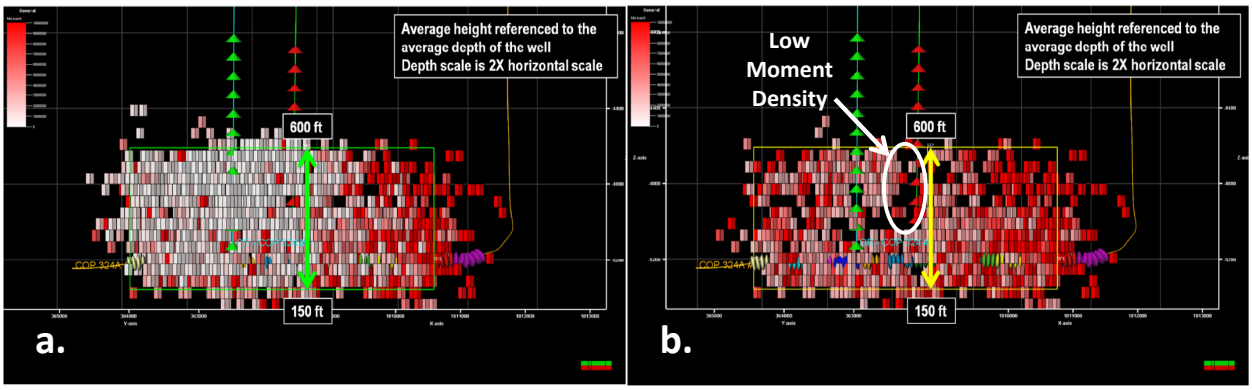

Figure 131 – 3 dimensional cellular moment density map. Zone of low deformation surrounds proposed fault location. Modified from Schlumberger (2013).

Figure 132a (inset) shows the map view of microseismic events at Clearfield and the locations of b-value cross sections through the seismic cloud. It is evident in the fence diagram of cross sections that there are spatial differences in the b-value throughout the cloud, both vertically and laterally. One must be careful in interpreting these changes, especially near the edges of the cloud and in areas of low event density. The three dimensional b-value calculations use a 250 event, variably-sized moving window, calculating a value for each 10 meter cell in the grid. For comparison a map view (Figure 132b) and detailed cross section (Figure 132c) were generated using a 100 meter search radius (constant size) on the same 10 meter grid size, with similar results in areas of high event density. The fixed search radius with an event minimum serves to eliminate calculations in areas of low data density, improving confidence in the interpretation.

The most notable feature of the b-value map and cross section is the volume of low b-values flanked by high b-values that crosses the lateral well along a northeast trajectory. This could be the result of a change in the local stress regime across a structural boundary such as a fault. Relatively speaking, a lower b-value indicates failure within a higher overall state of

driving stress (i.e. a larger differential stress). As such we can postulate that the northwest side of this apparent boundary, near the mid-point of the lateral well, is under a higher state of differential stress than the southeast side. Recall Figure 130 and Figure 131 which showed a much higher number of microseismic events, mostly of low magnitude, on the northwest block of the proposed fault. It is reasonable to conclude that the Mohr-Coulomb failure envelope has not changed radically across the fault, but rather the northwest block is simply closer to the envelope than the southeast block, leading to a propensity for brittle failure. While two and three-dimensional b-value calculations help to sharply define anomalies, the simplest approach of calculating a single b-value for each stage and creating a relatively low resolution time series can be enlightening as well (Figure 133). It is critical to compare these results with additional lines of evidence to rule out sampling bias and artifacts.

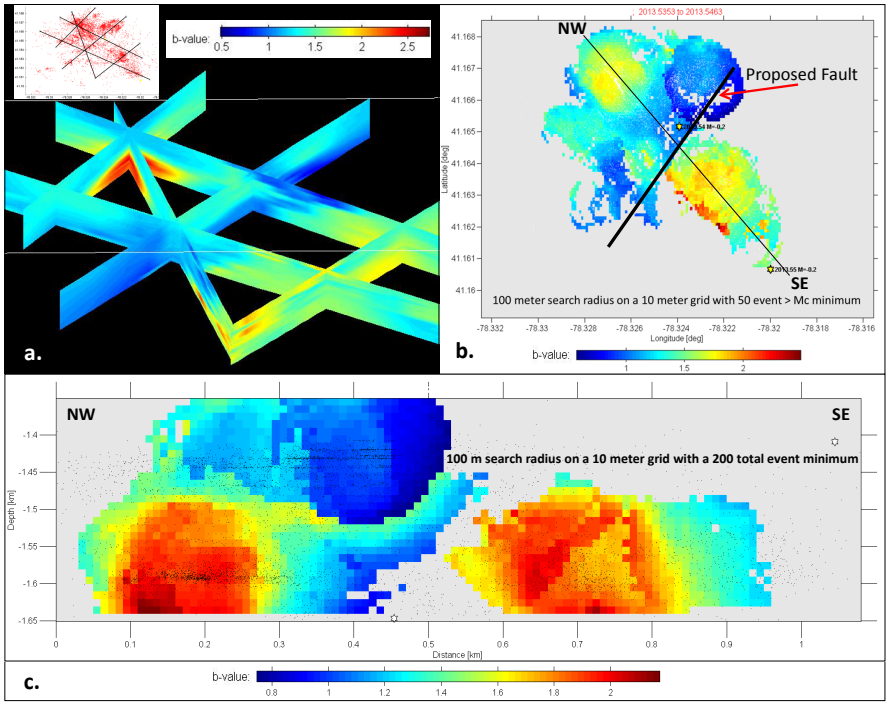

Figure 132 – (a) Fence diagram of b-value cross sections. (b) Map view of b-values. (c) NW-SE b-value cross section (location shown in (b)).

Recall Figure 77 and the comparison of temporal b- to D-values at the Clearfield site. Both the Clearfield results and results from a similar study by (Grob and van der Baan 2011) show that when the b-value is approaching 2 and highly variable, indicative of small magnitude events in a lower stress environment, the D-value is also variable, depending upon the complexity of the fracture network being stimulated. However, when a fault is stimulated, this lowers the b-value to ~1 and the D-value converges upon a value of 2. Figure 77 illustrates that this b- to D-value relationship exists during stages 5, 6, and 7, further supporting the use of fractal analysis as a fault identification tool.

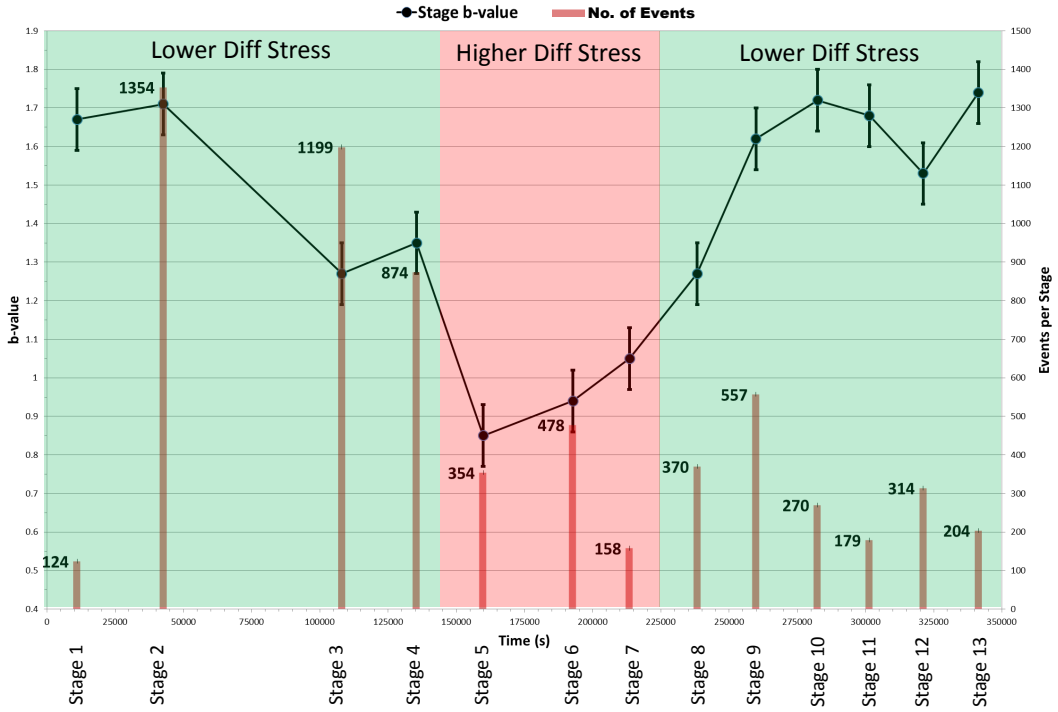

Figure 133 – Stage by stage b-value and event count, showing changing differential stress along wellbore.

Heretofore, the identification of this unmapped fault has relied solely on the spatial and seismological properties of the microseismic events. Two tomographic velocity profiles were acquired between the two monitoring wells, nearly orthogonal to the lateral well bore. The first

was acquired before hydraulic fracturing and the second was acquired after hydraulic fracturing but before the well was flown back. This is important, as the formation was under higher induced fluid pressure and the velocity profile should show a greater fluid effect where stimulation had occurred. Compressional waves (p-waves) travel through fluid and hence a saturated medium will have a lower p-wave velocity than the equivalent unsaturated medium. Shear waves (s-waves) do not travel through fluids, so any observed decrease in s-wave velocity is a result of a change in the ability of the solid component of the rock to transmit s-waves. This can occur when a rock is fractured or increased pore pressure decreases the density of grain contacts. This same phenomenon can also affect p-wave velocity (Mur, Ahmadov et al. 2015). In order to create a meaningful display of velocity change induced by hydraulic fracturing, the post-frac profile was subtracted from the pre-frac profile to give the velocity difference between the two profiles. The difference is then divided by the pre-frac profile to give a percent change between the two.

A p-wave velocity decrease of ~100 ft/second (~30 meters/second) is observed along the velocity profile (Figure 134). The anomaly appears as two separate areas that straddle the s-wave anomaly (Figure 135). The maximum s-wave velocity decrease is ~250 ft/second (~76 meters/second). These two anomalies occur in areas of relatively low event density, leading to the conclusion that they are not directly the product of increased fracture density. The proposed fault discussed in previous pages passes directly through the middle of the s-wave anomaly and between the two areas of p-wave anomaly. Fluid accumulation in a zone of relatively higher secondary porosity such as a fault would adversely impact the ability of the solid component of the rock to transmit seismic waves, due to dilation of the secondary pores and lower grain-to-grain contact area.

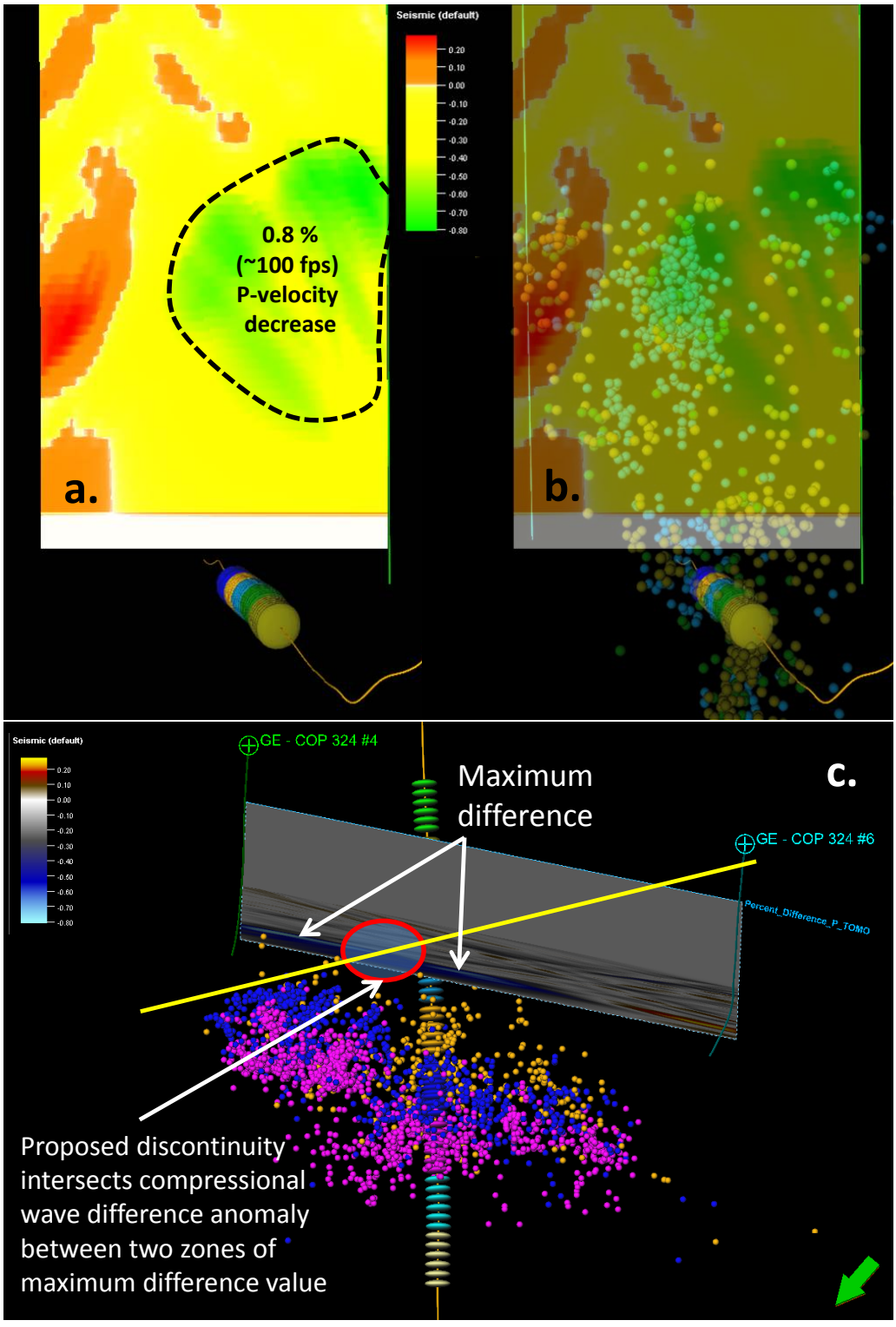

Figure 134 – (a) Crosswell tomographic P-wave velocity difference section. (b) Microseismic events generally do not cross into the lower velocity anomaly. (c) The 0.8 % decrease in P-wave velocity straddles the proposed location of a low offset fault controlling microseismicity.

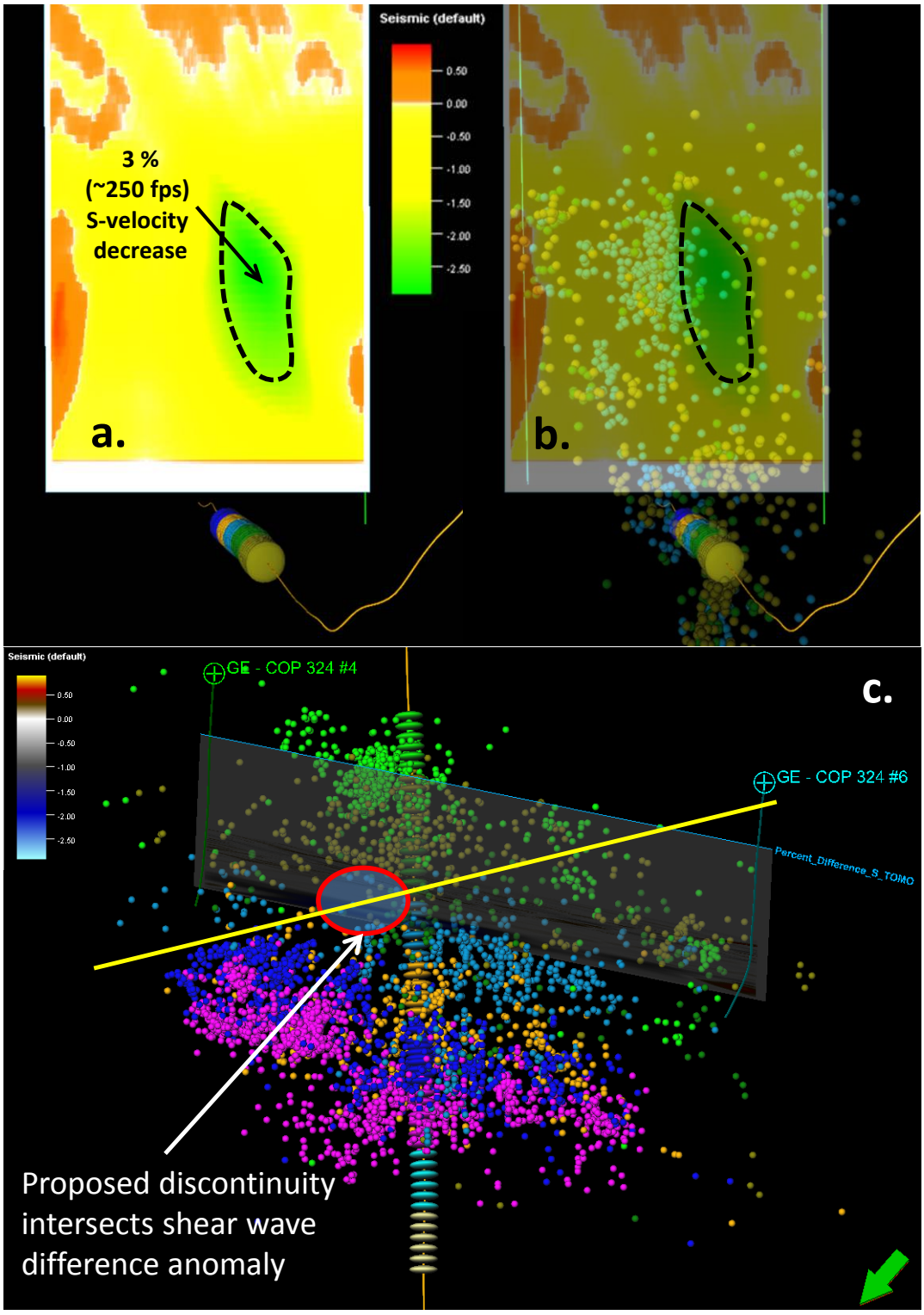

Figure 135 – (a) Crosswell tomographic S-wave velocity difference section. (b) Microseismic events generally do not cross into the lower velocity anomaly. (c) The 3 % decrease in S-wave velocity coincides with the proposed location of a low offset fault controlling microseismicity.

So far the evidence presented for the existence of an unmapped fault crossing the lateral well bore has been based upon microseismic and tomographic velocity data collected specifically for this well. A more regional view can show if local interpretations of geologic structure fit into the larger picture. A 30 mile^2 seismic survey was acquired in Clearfield County. Figure 136 is a map of seismically identified faults in the vicinity of the well bore, with sufficient throw to be resolved by a seismic survey (>~100 feet, at minimum). Roughly orthogonal normal faults are observed to be surrounding the well bore and it is reasonable to conclude that the fault to the northeast of the well, near the end of line A-A', continues to the southwest and terminates at the mapped crossing fault. Seismic Variance is a calculated attribute that represents lateral trace-to-trace variability over a specified sample interval. In laterally continuous sedimentary layers there is low amplitude variability from one trace to the next; however, faults and other cross cutting features introduce abrupt changes to seismic amplitudes that register as high values in a variance map. Because seismic attributes focus on variations in individual seismic traces, it is believed that they can enhance features below the overall seismic resolution (Chopra and Marfurt 2007). Variance was calculated on a time-slice through the Marcellus Shale (Figure 137), showing only very subtle features in the region between the two monitoring wells. It is possible that the lower reach of the fault is above the Marcellus, possibly in the lower Skaneateles Shale. Figure 107 and Figure 131 show the vertical b-value distribution and the cross section view of cellular moment density, respectively. Both the b-value and the density of microseismic events increase abruptly below the elevation of the lower Skaneateles Shale, indicating less interaction with a fault.

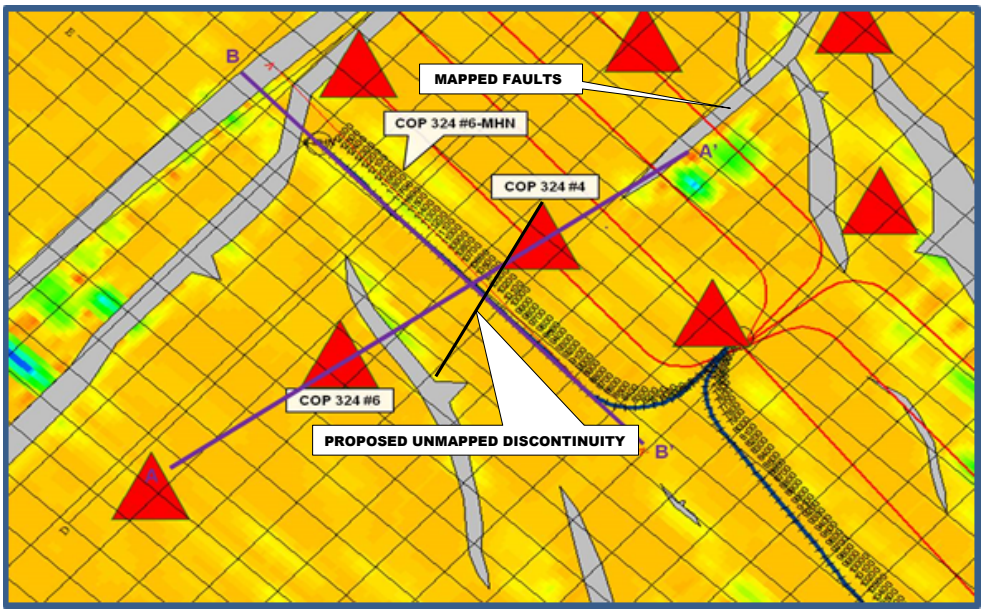

Figure 136 – Map of well location with respect to existing faults and the proposed fault. Modified from (Schlumberger 2013).

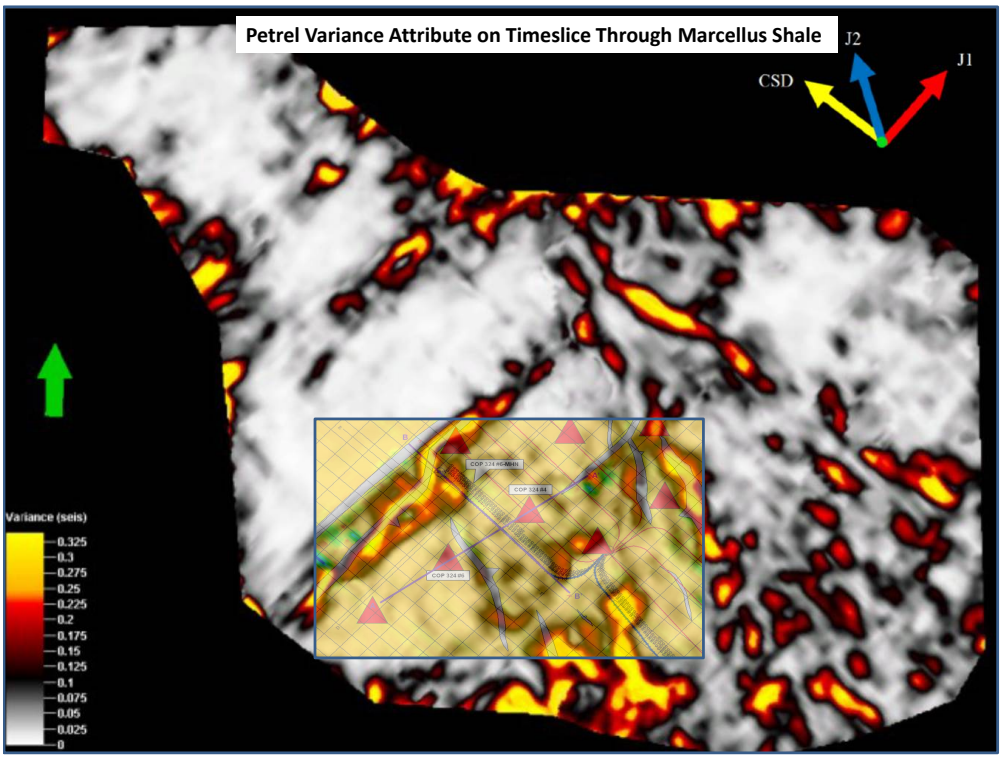

Figure 137 – Figure 137 superimposed upon a seismic variance attribute map shows no features in the area of the proposed fault. Modified from (Roberts 2013).

Five pieces of evidence to support the existence of an unmapped fault have been presented: the spatial arrangement of microseismicity, directional distribution of events by stage, moment density analysis, spatial b-value analysis, and the presence of post-frac velocity anomalies. Any one of these pieces treated as stand-alone proof of a fault would not offer a very convincing argument. It is the synthesis of multiple data attributes and data sources that lends strength to the conclusions presented here.

4.0 SUMMARY

In this thesis, two microseismic datasets from Pennsylvania have been analyzed in detail to provide a level of understanding that builds upon the traditional spatial analysis. Six lateral wells at Greene County and one lateral well at Clearfield County were hydraulically fractured in the Devonian Marcellus Shale. A single vertical string of down-hole geophones were used to monitor during fracturing at Greene County and two vertical strings were used at Clearfield. The so-called "dots in a box" approach equates the presence of microseismicity with stimulation of the rock volume. Although this approach is not being disputed here, it is shown to be too simplistic. It does not take into account the temporal, spatial, seismological, and geomechanical properties of the microseismic events and their ability to shed light on the style of failure, interaction with geological structures, changing stress states in the earth, and a host of other factors. For example, at Greene County, out of zone events that occurred early in a fracturing stage, far from the injection point, in a non-reservoir rock should not be included in the "stimulated reservoir volume" but definitely need to be studied to understand their nature. Using a variety of analyses and integrating the microseismic data with cross-well tomography, passive surface seismic, and geophysical well logs, four major enhancements were made to the understanding of hydraulic stimulation in the Marcellus Shale.

At both Greene County and Clearfield County, the comparison of event magnitude and source-to-event distance with fractal dimensions (b and D-values) and pumping data, in time,

shows that there are subtle relationships between the hydraulic energy input and the corresponding microseismic expression. D and b-values tend to be positively correlated at Greene County, indicating a causative relationship between the spatial distributions of the events (tight cluster, a line, a plane, or a diffuse cloud) and the frequency-magnitude distribution. A high D-value (diffuse) corresponds to a high b-value (small magnitude-dominated) and a low D-value (plane, line, point) corresponds to a low b-value (large magnitude-dominated). Research has shown that low b-values may indicate interaction with faults and failure in a relatively higher state of stress, which would serve to concentrate seismicity along distinct features. Excursions in the pumping pressure and/or pumping rate generally indicate a change in the flow regime downhole. A rapid spike in pressure could indicate fracture tip "screen-out" (sand plugging). A drop in pressure accompanied by a need to increase the rate to compensate could indicate erosion of the casing perforations or breakthrough of fracturing fluid into a high permeability fault or fracture system. The b and D-values generally adjust accordingly. During Stage 2 at Clearfield County, screen-out occurred, indicated by a rapid spike in pressure that caused the operator to decrease the flow rate. Shortly after decreasing flow, the operator returned to a state of increased flow and pressure. Prior to screening out, microseismicity was occurring infrequently and at distances of up to 1,300 feet from the perforation. After the rapid rate and pressure perturbations, very high density microseismicity began to occur very close to the wellbore, within 400 feet. The b-value reflects this change by shifting to higher values, suggesting failure in a previously fractured rock that is under lower stress.

Secondly, this thesis extends the study of slow slip seismicity (Long Period Long Duration, LPLD) into the Appalachian Basin and the Marcellus Shale. Previous studies have taken place in the Barnett Shale in Texas. The importance of slow slip deformation in organic

shales is only beginning to be understood, but it is suspected that aseismic processes account for up to 75% of reservoir stimulation during hydraulic fracturing. The radiated energy from microseismic events added to the theoretical energy required to create a fracture defined by the extent of microseismicity does not even account for 25% of the hydraulic energy pumped into the reservoir. Although there are obvious sources of energy loss such as friction, mechanical inefficiency, and high permeability zones, this still presents a surprising imbalance that can be rectified in part by invoking aseismic deformation. A single 2 to 80 Hz seismometer installed at the near-surface passively recorded seismic signals throughout the entire hydraulic fracturing operation at Greene County. Analysis of the seismogram alongside the pumping and microseismic data reveals that a low frequency tremor begins shortly after the first microseismic event and continues for an undetermined amount of time. A detailed look at the 1-hour power spectra from 20-hour time windows encompassing the beginning and end of fracturing at Wells 4,5, and 6, and Wells 1,2, and 3 shows a definite increase in power in the 3-20 Hz range during fluid injection over the pre-frac baseline. This LPLD signal, rather than abruptly disappearing at the conclusion of fluid injection, gradually decreases toward baseline levels over the course of ten hours, supporting the assessment of this signal as real and not noise contamination. However, a single-seismometer-study leaves something to be desired from a signal QC perspective. The appearance of similar signals at multiple stations would improve confidence that the waveform is a natural phenomenon.

The third major component of this thesis is an effort to define the geomechanical drivers of microseismic expression so that researchers and operators may understand their microseismic data in an engineering/geological context and perhaps design a fracturing program better suited to the rock properties. High quality vertical and lateral geophysical well logs are available in the

Clearfield County study. Microseismic data is sampled vertically through the cloud, crossing a variety of rock types including shale, limestone, sandstone, and chert, and also laterally, but restricted to microseismic data only within the Marcellus Shale. The sampling is completed such that the sampling interval matches that of the well logs but each sample overlaps the one above and below or on either side. This technique creates a high resolution microseismic "log" that shows subtle changes in microseismic properties and allows direct cross-plotting of microseismic logs against geophysical logs. As a starting point, laboratory experiments with amorphous solids (glasses) reveal that material with a high Poisson's ratio (PR) tends to require more energy to induce a fracture and release more energy when fractured than material with a lower PR. Low PR material tends to be brittle. An uncontrolled natural environment introduces several complicating factors including stress, material changes, and structural discontinuities but overall, the laboratory relationship is supported by the results of this study. The five geomechanical properties used are Young's modulus, Poisson's ratio, brittleness, lambda·rho (LR), and mu·rho (MR). Moment magnitude and event count are the microseismic parameters to which the geomechanical properties are related. Key observations are that larger magnitudes tend to occur in high PR and low brittleness rocks and smaller magnitudes tend to occur in low PR and high brittleness rocks. PR by itself is a good predictor of event count, and brittleness is a good predictor of event magnitude. Event magnitude is best correlated with LR-MR, where high MR corresponds to a more brittle rock and smaller magnitude. The stronger correlation of event magnitude with LMR measured in the vertical direction in the Marcellus Shale suggests a tendency toward bedding plane failure connected by vertical fractures and shearing. This study represents relationships established at one location in the Marcellus Shale. In order to validate

and build confidence in these correlations, more studies in the Marcellus and other unconventional reservoirs are critical.

The fourth main element of this thesis is aimed at identifying a suspected fault that had been previously unmapped when the operator performed hydraulic fracturing at the Clearfield site. This activity integrates multiple lines of evidence for the fault, starting with the spatial distribution of microseismicity, then the propagation direction of events as an indicator of a changing stress field, then heterogeneous moment density distribution, and multi-dimensional b-value analysis to highlight anomalies. Finally, pre- and post-frac cross-well velocity tomography provides evidence of a discrete shear wave velocity anomaly that appears to be a consequence of fluid intrusion into a fault structure. Previously published, seismically-derived fault maps provide a strong geological basis in which to interpret a new fault structure. Firstly, the spatial locations of the microseismic events initially help to define a linear feature in the Hamilton Formation above the Marcellus Shale, prompting further investigation. Events appear to "pile-up" along a linear/planar trend, resulting in a high concentration of events adjacent to a very low concentration of events. Detection limits can be effectively ruled out as a cause; this phenomenon is within the lowest magnitude detection radius around one of the monitoring wells. Based upon this observation, it appears this planar structure is preventing the transmission of fluid and/or pressure across itself. Secondly, due to the tendency of hydraulic fractures to propagate in the direction of the maximum horizontal stress, the alignment of microseismicity that is often seen in hydraulic fracturing studies gives insight into the orientation of the principal tectonic stresses. At this location in the Appalachian Basin, the maximum stress magnitude is oriented vertically, followed by northeast oriented horizontal stress, and then northwest oriented horizontal stress is the least principal stress. As such, hydraulic fractures tend to propagate

upward and downward and away from the perforation in a northeast-southwest direction. Published studies have documented changes in the horizontal stress orientation across the boundaries of discrete fault-bound blocks in tectonic settings with relatively small horizontal stress differential (maximum minus minimum). Using GIS, the directional distribution of microseismic events from each stage is consistent for the first eight stages (average N67.9°E) and then changes relatively abruptly in the last five stages (average N82.4°E). This ~15° shift in the alignment of microseismic events coincides with the proposed location of a fault crossing the lateral well. Next, the spatial distribution of seismic moment density highlights a dearth of deformation around a linear feature that coincides with the proposed fault location. It is postulated that the presence of this fault causes fluid to accumulate without a sufficient increase in pore pressure to cause brittle failure. The seismogenic b-value is used extensively throughout this thesis to measure relative changes in the state of stress and failure style. The b-value is measured vertically through the microseismic cloud, laterally along the wellbore, and spatially, in two dimensions and three dimensions. This multidimensional analysis converges upon the conclusion that there is a b-value anomaly approximately midway along the wellbore indicative of fault-controlled microseismicity. Evaluation of the b-value on a stage-by-stage basis and temporally shows that seismicity along ~2/3 of the wellbore (1/3 at the toe and 1/3 at the heel) is associated with failure along a discrete fracture network in a relatively solid rock-mass. The b-values fall between 1.3 and 1.8. The b-value anomaly develops in the middle third of the wellbore where values fall between 0.8 and 1.1, indicative of relatively less small magnitude events and, in conjunction with all other evidence presented heretofore, interaction with a fault structure. The two-dimensional b-value map further defines this structure as northeast striking, and the cross section and the pseudo-three dimensional fence diagram suggest that it is sub-

vertical. Both of these observations are consistent with the local structural trends. The vertical b-value "log" (contained in Figure 107) shows that there is an abrupt increase in b-value from an average of 0.93 to an average of 1.52 in the lower Skaneateles Shale. This suggests that the lower limit of the fault may lie at this transition, approximately 80 feet above the Upper Marcellus. Seismic fault maps support this interpretation; the variance attribute indicates a northeast trending discontinuity is present to the northeast of the proposed fault location, but only faint features are observed crossing the well. Finally, velocity tomography shows that the s-wave velocity decreases in a volume of rock above the Marcellus Shale as a direct result of hydraulic fracturing. The proposed fault trajectory intersects this -3.5% velocity anomaly. Microseismicity occurs around the anomaly but very few events occur within it. It is proposed that hydraulic fracturing fluid accumulated along the fault due to its high permeability, causing a change in the ability of the rock to transmit shear waves (and to a lesser extent, p-waves).

5.0 DISCUSSION

To treat microseismic data from hydraulic fracturing as simply a representation of where the stimulated fractures are (or inversely, where they are not), is a terrible waste of information. Seismological analysis of the catalog, geomechanical analysis through integration with well logs, and a variety of spatial analyses can open up new interpretations for both oil and gas operators and geoscientists in general. The primary goal of research, from the purely academic to industry driven, should be to advance the state of the art and the understanding of phenomenon, support existing studies, or add new studies and results to the existing pool of knowledge. This thesis serves all of these ends.

This thesis' effort to compare the fractal dimensions, b and D, to each other and to other microseismic properties and injection parameters follows a short list of studies that have resulted in mixed conclusions. Recall, the b-value is the slope of the frequency-magnitude distribution of the seismic catalog, and the D-value is the slope of the frequency-separation distance distribution of the seismic cloud. Earlier studies mostly focused on natural seismicity related to tectonic processes, but Hirata, Satoh et al. (1987) examined acoustic emissions resulting from hydraulic fracturing of granite. The found no correlation between the two parameters. A study by Hirata (1989) of natural seismicity in Japan found a negative correlation between b- and D-values, indicating that numerous small-magnitude events (high b-value) occurred in an ordered linear to planar geometry (low D-value), and vice-versa. Wang and Lin (1993) also found a negative

correlation between b- and D-values in western Taiwan. Henderson, Barton et al. (1999) studied induced seismicity associated with fluid injection at the Geysers geothermal field in California. They found that the correlation was negative during the initiation of injection but switched to a positive correlation once the injection pressure and rate because more constant. This suggests a shift from rapid stress loading that triggers many small events along defined structures, to slow stress loading and diffusion-dominated pore-pressure perturbation. Mandal and Rastogi (2005) presented similar findings to those of Henderson, Barton et al. (1999) in a natural earthquake aftershock sequence in India. Finally, Chen, Wang et al. (2006) reported a positive correlation between b and D during six months of aftershocks following the 1999 Chi-Chi earthquake in Taiwan. Grob and van der Baan (2011) found both positive and negative correlation between b- and D-values in a microseismic dataset from a months-long steam injection cycle in a Canadian heavy-oil field. Their analysis showed that a grouping of high D-values (>2), followed by low D-values (~1), followed again by high D-values (>2) corresponds temporally with b-values >1, then b-values ~1, then b-values <1. They concluded that when b-values were representative of interaction with a fault, the D-values indicated planar to linear event distribution. Otherwise, the interpretation of the b- to D-value relationship is difficult. We also observe this phenomenon at Clearfield, in which fault interaction causes the fractal dimensions to approach expected values, and more complex networks of small fractures cause heterogeneity in the fractal dimensions. These findings show that the b- to D-value comparison can be used as supporting evidence if fault interaction is suspected during hydraulic fracturing.

In addition to providing a set of analyses and guidelines to the microseismic researcher in general to help diagnose the presence of a fault or other energy-diverting, stress perturbing geologic structure, the identification of an unmapped fault at Clearfield has significance on a

local level as well. The well at Clearfield is a poor performer. The microseismic production was not as vigorous as the operator would have liked to see. The gas production has been lower than expected. A fault crossing the well, providing a high permeability conduit for fracturing fluid, would explain much of this poor performance.

Previous studies in the Barnett Shale in Texas, Horn River Basin in British Columbia, and a Canadian tight gas-sand have shown evidence of long-period, long-duration (LPLD) seismicity associated with hydraulic fracturing. We present the first evidence of LPLD seismicity in the Marcellus Shale of the Appalachian Basin. Microseismic monitoring of hydraulic fracturing in the Marcellus Shale is fast-becoming a common occurrence due to its relatively low cost and high informational return. The correlation between the generation of microseismic events and hydrocarbon production is inconclusive. The radiated energy from microseismic events falls woefully short in accounting for the amount of hydraulic energy pumped into the reservoir. Barring massive energy and fluid losses to friction, tortuous flow, and through-flow of fluid into faults, LPLD seismicity offers an explanation for the shortfall. If LPLD events can be located in space and time, and related to the occurrence of brittle failures represented by microseismic events, a more complete picture of the true stimulated rock volume can be achieved. This information is valuable to operators because they can forecast production more accurately, and gauge the effectiveness of their stimulation techniques.

We have shown a definitive link between microseismicity and the elastic properties of the host rock. A microseismic dataset that is statistically incomplete and well logs that only represent a small sample of the rock properties are still sufficient to reveal the strong link between elasticity and seismicity. The dependence of stimulation potential and style on elastic properties offers predictive power that may help operators to plan and forecast a play. However, operators

typically target brittle rocks (i.e., lower PR, higher YM) because of their perceived increased "fracability". While this is true in the context of brittle failure and microseismic productivity, the lower susceptibility of elastic rocks (i.e., high PR, low YM) to brittle failure may go hand in hand with a higher susceptibility to LPLD (slow slip) seismicity. Using these established relationships between engineering properties of the rock and the seismic expression of failure, operators may be able to target specific portions of the reservoir to have a desired effect. At the very least, they should not shy away from rocks traditionally thought of as poorly "fracable", as they may be missing out on another (possibly more effective) stimulation mechanism in slow-slip failure.

In closing, we have shown that the interpretation of microseismic data is greatly enhanced by integration with other information such as well logs and seismic. The microseismic user must examine the data from every angle, in every dimension, and cross-plot space, as unexpected relationships can be revealed. While microseismic monitoring of fluid injection has existed for almost 50 years, it is experiencing a renaissance in unconventional development. Now is the time for bold analysis and great advances. Its value to the industry will only increase from here.

BIBLIOGRAPHY

Abdalla, C. W., et al. (2011). "Marcellus Shale Wastewater Issues in Pennsylvania - Current and Emerging Treatment and Disposal Technologies." Penn State Cooperative Extension: 1-9.

Aki, K. (1967). "Scaling law of seismic spectrums." Journal of Geophysical Research **72**(4): 1217-1231.

Angus, D. A. and J. P. Verdon (2013). "Using Microseismicity to Estimate Formation Permeability for Geological Storage of CO2." ISRN Geophysics **2013**: 1-7.

Arroyo, J. L., et al. (2003). "Superior Seismic Data from the Borehole." Oilfield Review: 2-23.

Baisch, S., et al. (2002). "Probing the Crust to 9-km Depth: Fluid-Injection Experiments and Induced Seismicity at the KTB Superdeep Drilling Hole, Germany." Bulletin of the Seismological Society of America **92**(6): 2369-2380.

Barth, A., et al. (2008). Stress derivation from earthquake focal mechanisms. World Stress Map Project: Guidelines: Focal Mechanisms.

Boroumand, N. and D. W. Eaton (2012). Comparing energy calculations: Hydraulic fracturing and microseismic monitoring. GeoConvention 2012: Vision**:** 1-4.

Brown, D. W. (2009). Hot Dry Rock Geothermal Energy: Important Lessons from Fenton Hill; SGP-TR-187. Thirty-Fourth Workshop on Geothermal Reservoir Engineering, Stanford University, Stanford, California.

Brown, K., et al. (2005). "Correlated transient fluid pulsing and seismic tremor in the Costa Rica subduction zone." Earth and Planetary Science Letters **238**(1-2): 189-203.

Brune, J. N. (1970). "Tectonic stress and the spectra of shear waves from earthquakes." Journal of Geophysical Research **75**: 4997-5009.

Chen, C.-C., et al. (2006). "A correlation between the b-value and the fractal dimension from the aftershock sequence of the 1999 Chi-Chi, Taiwan, earthquake." Geophysical Journal International **167**(3): 1215-1219.

Chopra, S. and K. J. Marfurt (2007). Seismic Attributes for Prospect ID and Reservoir Characterization, Society of Exploration Geophysicists.

Cipolla, C. (2014). Microseismic Interpretations and Applications: Beyond SRV. SPE Paper 168596. MicroSeismic, Inc. User Group Meeting.

Cronin, V. (2010). "A Primer on Focal Mechanism Solutions for Geologists." Baylor University: 1-14.

Dohmen, T., et al. (2013). "A New Surveillance Method for Delineation of Depletion Using Microseismic and Its Application to Development of Unconventional Reservoirs," Paper SPE 166274. Society of Petroleum Engineers, Annual Technical Conference and Exhibition, 30 September - 2 October 2013. New Orleans, Louisiana, USA.

Duncan, P. M. and S. Williams-Stroud (2009). "Marcellus Microseismic." Oil and Gas Investor: 65-67.

Engelder, T., et al. (2009). "Joint sets that enhance production from Middle and Upper Devonian gas shales of the Appalachian Basin." AAPG Bulletin **93**(7): 857-889.

Fontaine, J. S., et al. (2008). "Design, Execution, and Evaluation of a "Typical" Marcellus Shale Slickwater Stimulation: A Case History," Paper SPE 117772 MS. Society of Petroleum Engineers, Eastern Regional/AAPG Eastern Section Joint Meeting, 11-15 October 2008 Pittsburgh, Pennsylvania, USA.

Gephart, J. W. and D. W. Forsyth (1984). "An improved method for determining the regional stress tensor using earthquake focal mechanism data: Application to the San Fernando Earthquake Sequence." Journal of Geophysical Research **89**(B11): 9305.

Gercek, H. (2007). "Poisson's ratio values for rocks." International Journal of Rock Mechanics and Mining Sciences **44**(1): 1-13.

Goertz-Allmann, B., et al. (2012). From observations of microseismic source parameters to reservoir geomechanics. AGIS Workshop. Zurich, Switzerland, Swiss Seismological Service, Swiss Federal Institute of Technology Zurich.

Goodway, W. (2009). "The Magic of Lamé." CSM Heiland Lecture - Colorado School of Mines - Student Geophysical Society - November 5th 2009.

Goodway, W., et al. (1997). Improved AVO fluid detection and lithology discrimination using Lamé petrophysical parameters; "λρ","μρ",&"λ/μ fluid stack", from P and S inversions. Society of Exploration Geophysicists Annual Technical Conference and Exhibition. Dallas TX USA.

Goodway, W., et al. (2012). "Combined microseismic and 4D to calibrate and confirm surface 3D azimuthal AVO/LMR predictions of completions performance and well production in the Horn River gas shales of NEBC." The Leading Edge **December**: 1502-1511.

Goodway, W., et al. (2010). "Seismic petrophysics and isotropic-anisotropic AVO methods for unconventional gas exploration." The Leading Edge **Special Section: Tight Gas Sands**: 1500-1508.

Grechka, V., et al. (2010). "Case History: Predicting permeability and gas production of hydraulically fractured tight sands from microseismic data." Geophysics **75**(1): B1-B10.

Grob, M. and M. van der Baan (2011). "Inferring in-situ stress changes by statistical analysis of microseismic event characteristics." The Leading Edge **Special Section: Canada, Arctic Technology**
1296-1301.

Grob, M. and M. van der Baan (2012). Statistics of microseismic events: implications for geomechanics. Geoconvention 2012: Vision.

Gutenberg, B. and C. F. Richter (1944). "Frequency of Earthquakes in California." Bulletin of the Seismological Society of America: 185-188.

Gutenberg, B. and C. F. Richter (1949). Seismicity of the Earth and Associated Phenomena. Princeton, NJ, USA, Princeton University Press.

Hammack, R., et al. (2014). "An Evaluation of Fracture Growth and Gas/Fluid Migration as Horizontal Marcellus Shale Gas Wells are Hydraulically Fractured in Greene County, Pennsylvania," NETL-TRS-3-2014. EPAct Technical Report Series, U.S. Department of Energy, National Energy Technology Laboratory, Pittsburgh, PA, USA**:** 1-76.

Hardy, H. R., et al. (1975). Feasibility of utilizing microseismic techniques for the evaluation of underground gas storage reservoir stability, Report L19725e. Pipeline Research Council International Inc.

Harper, J. A. and J. Kostelnik (2011) "The Marcellus Shale Play in Pennsylvania – Part 2: Basic Geology," http://www.dcnr.state.pa.us/cs/groups/public/documents/document/dcnr_007593.pdf. Pennsylvania Department of Conservation and Natural Resources, Pennsylvania Geological Survey.

Heidbach, O., et al. (2009). "The World Stress Map, Based on the database release 2008,equatorial scale 1:46,000,000." Commission for the Geological Map of the World.

Henderson, J. R., et al. (1999). "Fractal clustering of induced seismicity in The Geysers geothermal area, California." Geophys. J. Int. **139**: 317-324.

Hirata, T. (1989). "A correlation between the b value and the fractal dimension of earthquakes." J. Geophys. Res. **94**(B6): 7507-7514.

Hirata, T., et al. (1987). "Fractal structure of spatial distribution of microfracturing in rock." Geophys. J. R. astr. Soc. **90**: 369-374.

Hummel, N. and S. A. Shapiro (2012). Back front signatures of seismicity induced by nonlinear fluid-rock interaction. Istanbul International Geophysical Conference and Oil & Gas Exhibition. Istanbul, Turkey.

Hummel, N. and S. A. Shapiro (2016). "Back front of seismicity induced by non-linear pore pressure diffusion." Geophysical Prospecting **64**(1): 170-191.

Kaiser, J. (1950). Untersuchungen über das Auftreten von Geräuschen beim Zugversuch (Study on the occurence of noise in the tensile test), Technische Hochschule München. **PhD**.

Kanamori, H. (1977). "The energy release in great earthquakes." Journal of Geophysical Research **82**(20): 2981-2987.

Lewandowski, J. J., et al. (2005). "Intrinsic plasticity or brittleness of metallic glasses." Philosophical Magazine Letters **85**(2): 77-87.

Lombardi, A. M. (2003). "The Maximum Likelihood Estimator of b-Value for Mainshocks." Bulletin of the Seismological Society of America **93**(5): 2082-2088.

Majer, E. L. and T. V. McEvilly (1979). "Seismological investigations at The Geysers geothermal fiel." Geophysics **44**(2): 256-269.

Mandal, P. and B. K. Rastogi (2005). "Self-organized Fractal Seismicity and b Value of Aftershocks of the 2001 Bhuj Earthquake in Kutch (India)." Pure and Applied Geophysics **162**(1): 53-72.

Maxwell, S. (2013). "Beyond the SRV." E&P **November 2013**.

McClain, W. C. (1971). Seismic Mapping of Hydraulic Fractures - ORNL TM 3502, Oak Ridge National Laboratory.

McClain, W. C. (1971). Seismic mapping of hydraulic fractures, ORNL-TM-3502. Oak Ridge National Laboratory.

Milici, R. C. and C. S. Swezey (2006). "Assessment of Appalachian Basin Oil and Gas Resources: Devonian Shale–Middle and Upper Paleozoic Total Petroleum System," Open File Report Series 2006-1237. United States Department of the Interior, United States Geological Survey.

Montgomery, C. T. and M. B. Smith (2010). "Hydraulic Fracturing – History of an Enduring Technology." Journal of Petroleum Technology: 26-32.

Mooney, W. D. (1989). Seismic methods for determining earthquake source parameters and lithospheric structure. Geophysical framework of the continental United States. L. C. Pakiser and W. D. Mooney. Boulder, Colorado, Geological Society of America. **Memoir 172**.

Moos, D., et al. (2011). "Predicting Shale Reservoir Response to Stimulation in the Upper Devonian of West Virginia," Paper SPE 145849. Society of Petroleum Engineers, Annual Technical Conference and Exhibition, 30 October-2 November 2011. Denver, Colorado, USA.

Mur, A., et al. (2015). Personal Communication: A Webex Meeting Entitled "Geomechanics in the Marcellus" with ikon Science. E. Zorn.

Northrop, D. A., et al. (1989). Multiwell Experiment Final Report: IV. The Fluvial Interval of the Mesaverde Formation - SANDIA REPORT SAND89-2612/A • UC-132. Multiwell Experiment Project Groups - Sandia National Laboratory.

Öncel, A. O. and T. Wilson (2004). "Correlation of seismotectonic variables and GPS strain measurements in western Turkey." Journal of Geophysical Research: Solid Earth **109**(B11): n/a-n/a.

Pelletier, H. and J. Gunderson (2005). "Application of rock physics to an exploration play: A carbonate case study from the Brazeau River 3D." The Leading Edge **24**(5): 516-519.

Power, D. V., et al. (1976). "Detection of Hydraulic Fracture Orientation And Dimensions in Cased Wells." Journal of Petroleum Technology **28**(9): 1116-1124.

Rickman, R., et al. (2008). A Practical Use of Shale Petrophysics for Stimulation Design Optimization: All Shale Plays Are Not Clones of the Barnett Shale. Paper SPE-115258-MS. Society of Petroleum Engineers Annual Technical Conference and Exhibition. Denver, Colorado, USA.

Roberts, E. D. (2013). Structure Segmentation and Transfer Faults in the Marcellus Shale, Clearfield County, Pennsylvania: Implications for Gas Recovery Efficiency and Risk Assessment Using 3D Seismic Attribute Analysis. Eberly College of Arts and Sciences, Department of Geology and Geography. Morgantown, West Virginia, West Virginia University. **M.S.:** 92.

Rothert, E. and S. A. Shapiro (2003). "Microseismic monitoring of borehole fluid injections: Data modeling and inversion for hydraulic properties of rocks." Geophysics **68**(2): 685-689.

Russell, B. (2010). Making sense of all that AVO and inversion stuff! The Milton Dobrin Lecture.

Rutledge, J. T., et al. (2013). "Geomechanics of Hydraulic Fracturing Inferred from Composite Radiation Patterns of Microseismicity," Paper SPE 166370 MS. Society of Petroleum Engineers, Annual Technical Conference and Exhibition, 30 September–2 October 2013. New Orleans, Louisiana, USA.

Rutledge, J. T., et al. (1998). Microseismic mapping of a Cotton Valley hydraulic fracture using decimated downhole arrays. Society of Exploration Geophysicists, International Exposition and Sixty Eighth Annual Meeting, 13-18 September 1998. . **Expanded Abstracts:** 338-341.

Sasaki, S. and H. Kaieda (2002). "Determination of Stress State from Focal Mechanisms of Microseismic Events Induced During Hydraulic Injection at the Hijiori Hot Dry Rock Site." Pure and Applied Geophysics **159**: 489-516.

Schlumberger (2013). "Schlumberger Microseismic Services Evaluation Report; COP324A#6MH, Clearfield County, PA, Marcellus Shale; Prepared for URS Energy and Construction Inc., July 15, 2013 to July 19, 2013"**:** 1-106.

Shapiro, S. (2015). Fluid-Induced Seismicity. United Kingdom, Cambridge University Press.

Shapiro, S. A., et al. (1997). "Estimating the crust permeability from fluid-injection-induced seismic emission at the KTB site." Geophysics Journal International **131**: F15-F18.

Shapiro, S. A., et al. (2002). "Characterization of fluid transport properties of reservoirs using induced microseismicity." Geophysics **67**(1): 212-220.

Shuck, L. Z. (1974). The determination of direction and length of hydraulically induced fractures in petroleum reservoirs: A field experiment; Paper 5160. Proceedings, Society of Petroleum Engineers Annual Technical Conference.

Sorkhabi, R. (2014). "Fracture, Fracture Everywhere: Part II." GEOExPro **11**(4): 42-46.

Talwani, P. (2000). "Seismogenic properties of the crust inferred from recent studies of reservoir-induced seismicity – Application to Koyna." Current Science **79**(9): 1327-1333.

Urbancic, T. I., et al. (2002). "Identifying Fracture Growth Patterns Using Microseismicity." CSEG Geophysics: 1-2.

USGS (1993). "Petroleum Geology of the Devonian and Mississippian Black Shale of Eastern North America", United States Geological Survey, Bulletin 1909. J. B. Roen and R. C. Kepferle.

Vermylen, J. P. and M. D. Zoback (2011). "Hydraulic Fracturing, Microseismic Magnitudes, and Stress Evolution in the Barnett Shale, Texas, USA" Paper SPE 140507. Society of Petroleum Engineers, Hydraulic Fracturing Technology Conference and Exhibition, 24–26 January 2011. The Woodlands, Texas, USA.

Walker, R. N. (1997). Cotton Valley Hydraulic Fracture Imaging Project - Paper SPE-38577-MS. SPE Annual Technical Conference and Exhibition. San Antonio, Texas.

Wang, J.-H. and W.-H. Lin (1993). "A Fractal Analysis of Earthquakes in West Taiwan." TAO **4**(4): 457-462.

Warpinski, N. (2013) Microseismic Monitoring: Engineering Value and Validation. Presented at Society of Petroleum Engineers - Denver Section Meeting - 2013.

Warpinski, N. R., et al. (1998). An Interpretation of M-Site Hydraulic Fracture Diagnostic Results - SPE-39950-MS. SPE Rocky Mountain Regional/Low-Permeability Reservoirs Symposium and Exhibition. Denver, Colorado.

Wickstrom, L., et al. (2011). The Marcellus and Utica Shale Plays in Ohio. Ohio Oil and Gas Association Meeting, Ohio Department of Natural Resources, Division of Geological Survey.

Wiemer, S. (2001). "A Software Package to Analyze Seismicity: ZMAP." Seismological Research Letters **72**(2): 374-383.

Wikel, K. (2011). "Geomechanics: Bridging the Gap from Geophysics to Engineering in Unconventional Reservoirs." CSEG Recorder **May 2011**: 36-44.

Williams, J. H. (2011). "The Marcellus Shale Gas Play: Geology, Development, and Water-Resource Impact Mitigation." http://ny.water.usgs.gov/projectsummaries/CP30/Marcellus_Presentation_Williams.pdf. United States Geological Survey, New York Water Science Center.

Wilson, T. H., et al. (2015). "Interrelationships of Marcellus Shale gas production to frac-induced microseismicity, interpreted minor faults and fractures zones, and stimulated reservoir volume, Greene County, Pennsylvania." Interpretation **4**(1): T15-T30.

Wyss, M., et al. (2001) "ZMAP: A Tool for Analyses of Seismicity Patterns. Typical Applications and Uses: A Cookbook." http://www.seismo.ethz.ch/prod/software/zmap/box_feeder/cookbook.pdf. 1-64

Yale, D. P. (2003). "Fault and stress magnitude controls on variations in the orientation of in situ stress." Geological Society, London, Special Publications **209**: 55-64.

Zoback, M. D., et al. (2012). "The Importance of Slow Slip on Faults During Hydraulic Fracturing Stimulation of Shale Gas Reservoirs," Paper SPE 155476. Society of Petroleum Engineers, Americas Unconventional Resources Conference, 5–7 June 2012. Pittsburgh, Pennsylvania, USA.

Zorn, E. V., et al. (2014). "Time Dependent b and D-values, Scalar Hydraulic Diffusivity, and Seismic Energy from Microseismic Analysis in the Marcellus Shale: Connection to Pumping Behavior during Hydraulic Fracturing," Paper No. SPE-168647-MS. Society of Petroleum Engineers, Hydraulic Fracturing Technology Conference, 4-6 February 2014. The Woodlands, TX.